NOVEL EMI SHIELDING STRATEGIES FOR HYBRID FUNCTIONAL STRUCTURES

THESIS SUBMITTED TO AcSIR FOR THE AWARD OF THE DEGREE OF

DOCTOR OF PHILOSOPHY

IN CHEMICAL SCIENCES

By

DIJITH K. S.

Registration No: 10CC12A39012

Under the guidance of

Dr. K.P. SURENDRAN & Dr. SAJU PILLAI

MATERIALS SCIENCE AND TECHNOLOGY DIVISION

NATIONAL INSTITUTE FOR INTERDISCIPLINARY

SCIENCE AND TECHNOLOGY (CSIR-NIIST)

THIRUVANANTHAPURAM- 695 019

KERALA, INDIA

March 2019

Dedicated to

My Family & Friends...

DECLARATION

I hereby declare that the matter embodied in the Ph.D. thesis entitled "**Novel EMI shielding strategies for hybrid functional structures**" is the result of the investigations carried out by me at the Functional Materials Section, Materials Science and Technology Division, CSIR-National Institute for Interdisciplinary Science and Technology (CSIR-NIIST), Thiruvananthapuram, under the supervision of Dr. K. P. Surendran and Dr. Saju Pillai and the same has not been submitted elsewhere for any other degree, diploma or title.

In keeping with the general practice of reporting scientific observations, due acknowledgement has been made wherever the work described is based on the findings of other investigators.

Dijith K. S.

Thiruvananthapuram
March 2019

NATIONAL INSTITUTE FOR INTERDISCIPLINARY SCIENCE AND TECHNOLOGY
(NIIST)
(Formerly Regional Research Laboratory)
Council of Scientific & Industrial Research (CSIR)
Industrial Estate PO, Trivandrum – 695 019,
Kerala, INDIA

CERTIFICATE

*This is to certify that the work incorporated in this Ph.D. thesis entitled "**Novel EMI shielding strategies for hybrid functional structures**" submitted by **Mr. Dijith K. S.** to the Academy of Scientific and Innovative Research (AcSIR) in partial fulfillment of the requirements for the award of the **Degree of Doctor of Philosophy in Chemical Sciences** embodies original research work carried out by him under my supervision. I further certify that this work has not been submitted to any other University or Institution in part or full for the award of any degree or diploma. Research material obtained from other sources such as text, illustration, table etc., used in the thesis have been duly cited and acknowledged.*

Dr. Saju Pillai
(Co-Supervisor)

Dr. K. P. Surendran
(Supervisor)

Trivandrum
March 2019

Dijith K. S.
(Student)

Acknowledgements

It is with great pleasure that I extend my deep sense of gratitude to Dr. K.P. Surendran, my thesis supervisor for suggesting the research problem, for the valuable guidance, support and encouragement. There maintains a strong bond with my Co-Supervisor Dr. Saju Pillai, who provided help at any time during the entire period. I offer my sincere gratitude to Dr. M.T. Sebastian for the discussions at the beginning stage of my research work.

I would like to convey my gratitude to Dr. A. Ajayaghosh, Director, CSIR-NIIST, Thiruvananthapuram, Dr. Suresh Das and Dr. Gangan Prathap (former Directors, NIIST), for providing all the research facilities for my Ph.D. Work.

I wish to thank Dr. Harikrishna Bhat (Head, Materials Science and Technology Division, NIIST), Dr. P. Prabhakar Rao and Dr. M. L. P. Reddy for their help rendered during the course of this work.

I wish to express my sincere thanks to my doctoral committee members Dr. Bhoje Ghowd, and Dr. U. S. Hareesh and Dr. Narayan Unni for their understanding, encouragement and personal attention and suggestions during doctoral committee meeting which provided glimpse of new thoughts for my Ph.D work

I am deeply indebted to Dr. Luxmi Varma and Dr. Mangalam Nair (present and former AcSIR Co-ordinators). Sincere thanks to Dr Manoj Rama Varma, former APC Chairman and Dr. G. Subodh, Head, Depart ment of Physics, Kariavattom Campus, University of Kerala for their support. I am thankful to Dr. Prabhakaran K. Chemistry Department, IIST Valiyamala for extending facility for conducting some of the research work and Dr. Anoop Krishnan, Chemical Science Division, NCESS, Akkulam for allowing to carry out the CSIR 8oo work. I am thankful to T. P. D. Rajan, Dr. S. Shukla, Dr. M Vasundhara and Dr. K. G. Nishanth for their support. The support provided by other scientists of NIIST is also thankfully acknowledged.

I am extending my gratitude to Mr. Ajeesh Paulose, Mr. A. Peer Mohammed, Mr. M. R. Chandran, Mr. Kiran Mohan, Ms. Soumya, Mr. Prithviraj and Ms. Luci Paul for helping me in many ways. I am very thankful to all scientists, students and staff members of Materials Science and Technology Division for their help and support. I convey my special acknowledgments to Administrative section, Finance and Account section, Stores and Purchase Section, and Library and Information section for extending me various services to facilitate my research program.

My sincere thanks to my uncle Dr. Dileepkumar. The experience with him taught a lot of new lessons and my stay at Pappanamcode with him is ever rememberable. Special mentions and cheers for my overnight working partners, Dr. Vaisak S, Akshay V R, Arun S, Arun B, Suneesh. They made those days in NIIST a wonderful and adventurous. Thanks Mr. Sujith Vijayan and Mr. Vinu V Dev for the extended support during my Ph.D.

The valuable advices and helps given by my seniors in the lab, Dr. Dhanesh Thomas, Dr. Manu K. M., Dr. Abhilash P. (My volley ball guru), Dr. Deepa K. S., Dr. Jobin Varghese, Dr. Nina Joseph, Dr. Chameswari J., Dr. Namitha L. K., Dr. Neenulekshmi P. and Dr. Raji G. R. are greatly acknowledged.

My wholehearted gratitude to my colleagues: Ms. Gayathri T. H., Ms. Lekshmi D. R., Dr. Angel Mary Joseph, Dr. Induja I. J., Ms. Kanakangi S. Nair, Mr. K. Krishnakumar, Ms. Aparna, Ms. Sabitha Ann Jose, Ms. Revathy, Ms. Jasnamol P. P., Ms. Aswathy K., Ms. Aswathy V. S, Mr. Vishnu, Mr. Rojerce Brown Job, Ms, Roshni S. Babu, Mr. Hemanth A., Ms. Mini Varghese, Mr. Praveen Mathew, Ms. Sruthy, Ms. Ann Rose Sunny, Ms. Varsha Viswanath, Ms. Sreejitha Prajith, Ms. Heera Menon, Mr. Sikander Ahammed, Ms. Mitra R., Ms. Dhrisya, Mr. Vilesh, Ms. Sivabharathi, Ms. Anu Varkey with whom I have shared my lab days with memorable occasions and who have been very helpful and supportive both in personal and academic endeavours.

Sports is a passion for me and Team MSTD is always the spirit for that passion. Not mentioning by name, but my sincere thanks to all team members who lifted the spirit and made cheering moments during the past years @ NIIST.

I take this opportunity to sincerely acknowledge the University Grand Commission, Government of India, New Delhi, for providing financial assistance which supported me to perform my work comfortably.

I express my sincere gratitude to all my teachers and well-wishers of my college and school life. I express my deep love and thankfulness to my college/school friends and classmates for their love, care and moral support.

There are some one who always be remembered even though they are not there with you. They could have a special feel for you that nobody else can have. You could have been best explained by them in your achievements. I can feel those words and blessings. Last but not least, I would like to pay high regards and my heart-felt thanks to my mother Sreedevi Amma E, my brother Dinil K. S., my sister Deepa K. S.,my sister-in-law GangaKumari, and all my family members for their sincere encouragement, prayers and inspiration throughout my research work and lifting me uphill this phase of life. A special mention goes to my niece Chandana and nephew Chinmay. I express my deepest sense of gratitude to my wife's family members for their patience, care and understanding. Special mention here for Anila R, Karthik A and Ajay S.

Words are not enough to express the gratitude and love towards my wife Aiswarya R for her love, care, and valuable support to accomplish this goal. During the ups and downs, she was always with me to inspire me. Now we both had only one inspiration, that is the beautiful smile of Avnidiya. If I could have finished my Ph.D work on time, I may miss this wonderful opportunity to acknowledge this little charm. Besides this, I thank several people who have knowingly and unknowingly

helped me in the successful completion of this project and apologize for not mentioning all of them personally.

Dijith K S.

CONTENTS

Declaration i

Certificate ii

Acknowledgements iii

Contents vi

Preface x

Chapter 1: Electromagnetic Interference Shielding: Problems and Solutions 1

1.1 Introduction 3

1.2 Electromagnetic Interference 3

1.3 Requirement for EMI Shielding 4

1.3.1 Factors Enhancing EMI Problems 5

1.4 Concept of EMI Shielding 6

1.4.1 Electric and Magnetic Field Shielding Principles 7

1.4.2 Shielding Effectiveness 10

1.4.3 Absorption Shielding 11

1.4.4 Reflection Shielding 12

1.4.5 Multiple Reflections 14

1.4.6 Influence of Thickness of Shield and Distance from Source 14

1.4.7 Calculation of Shielding Effectiveness Using Scattering Parameters 14

1.5 Applications of EMI Shielding 15

1.6 Market Demand of EMI Shielding Materials 17

1.7 Materials for EMI Shielding 19

1.8. Materials Covered in the Present Thesis 21

1.8.1 Semiconducting Oxides 22

1.8.2 Perovskite Based Conducting Oxides 22

1.8.3 Macroporous Foams 24

1.8.4 Epoxy Based Composites in Microwave Shielding 26

1.8.5 Metallisation of Composite's Surface 27

1.8.6 Magnetic Nanomaterials in Shielding 28

1.8.7 Conductive Fabrics 30

1.8.7.1 Polymer Based Fabrics 30

1.8.7.2 Carbon Fibers and Fabrics 31

1.9 Scope of the Present Thesis 32

1.10 References 34

Chapter 2: $La_{0.5}Sr_{0.5}CoO_{3-\delta}$-Epoxy Composites and their Surface Modification Strategies for Effective EMI Shielding 47

2.1 Thermophysical and Microwave Shielding Properties of $La_{0.5}Sr_{0.5}CoO_{3-\delta}$ and Its Composite with Epoxy 49

2.1.1 Introduction 49

2.1.2 Materials and Methods 50

2.1.3 Results and Discussion 52

2.1.3.1 Structural, Electrical and EMI shielding properties of LSCO 52

2.1.3.2 Microstructure of the LSCO-Epoxy Composites 56

2.1.3.3 Thermophysical Properties of the Composites 57

2.1.3.4 Mechanical Properties of the Composites 60

2.1.3.5 AC Electrical Properties at Microwave Bands 61

2.1.3.6 EMI Shielding of LSCO-Epoxy composites 65

2.1.4 Conclusions 68

2.2 Screen Printed Silver Patterns on $La_{0.5}Sr_{0.5}CoO_{3-\delta}$-Epoxy Composite as a Strategy for Many-Fold Increase in EMI Shielding 70

2.2.1 Introduction 70

2.2.2 Materials and Methods 71

2.2.3 Results and Discussion 72

2.2.3.1 Improved Thermal, Mechanical and Dielectric properties 72

2.2.3.2 Modification Using Conductive Surface Designs 74

2.2.3.3 Structure and Microstructure of Surface Designs 75

2.2.3.4 AC Electrical Parameters of Surface Modified Composites 77

2.2.3.5 EMI shielding of modified composites 79

2.2.4 Conclusions 83

2.3 References 84

Chapter 3: $La_{0.5}Sr_{0.5}CoO_{3-\delta}$ Foam Structures and Nanowires for Microwave Shielding Applications 91

3.1 Conducting $La_{0.5}Sr_{0.5}CoO_{3-\delta}$ based Macroporous Foams for Harsh Condition Microwave Shielding 93

3.1.1 Introduction 93

3.1.2 Materials and Methods 95

3.1.3 Results and Discussion 97
3.1.3.1 Structural Evolution 97
3.1.3.2 Scanning Electron Microscopy 98
3.1.3.3 Mechanical Properties 100
3.1.3.4 Electrical Properties 101
3.1.3.5 EMI shielding properties 103
3.1.4 Conclusions 107
3.2 $La_{0.5}Sr_{0.5}CoO_{3-\delta}$ Nanowires for Microwave Shielding Applications 109
3.2.1 Introduction 109
3.2.2 Materials and Methods 110
3.2.3 Results and Discussion 111
3.2.3.1 Structural Characterization 111
3.2.3.2 Morphological analysis 112
3.2.3.3 Magnetic properties of LSCO nanowires 115
3.2.3.4 Electrical properties of LSCO nanowires 116
3.2.3.5 EMI shielding analysis 118
3.2.4 Conclusions 119
3.3 References 120
Chapter 4: Polyol Derived Ni and NiFe Alloys for Effective Shielding of Electromagnetic Interference 125
4.1 Introduction 127
4.2 Materials and Methods 129
4.3 Results and Discussion 130
4.3.1 Structural and Morphological Analysis 131
4.3.1.1 X-ray Diffraction Analysis 131
4.3.1.2 Transmission Electron Microscopy 133
4.3.1.3 X-ray Photoelectron Spectroscopy Analysis 135
4.3.1.4 Scanning Electron Microscopy 137
4.3.2 Magnetic Properties 139
4.3.3 Electrical Properties 143
4.3.4 EMI Shielding Effectiveness 146
4.4 Conclusions 152
4.5 References 155
Chapter 5:Metallized Flexible Fabrics for Microwave Shielding Applications 163

5.1 Nickel Electrodeposited Textile Fabrics for Microwave Shielding Applications 165
5.1.1 Introduction 165
5.1.2. Experimental Methods 168
5.1.3. Results and Discussion 169
5.1.3.1 WAXS and XRD Analysis 169
5.1.3.2 Morphological Characterizations 171
5.1.3.2.1 Photographic Images 171
5.1.3.2.2 Optical Microscopy 172
5.1.3.2.3 Scanning Electron Microscopic Analysis 173
5.1.3.2.4 Elemental mapping and EDAX 179
5.1.3.2.5 Dielectric Characterization of Fabrics 181
5.1.3.2.6 Electrical Conductivity 183
5.1.3.2.7 Magnetic Characterization 184
5.1.3.2.8 EMI Shielding Characterization 185
5.1.4. Conclusions 191
5.2 Nickel Electrodeposited Carbon Fabrics for Microwave Shielding Applications 193
5.2.1. Introduction 193
5.2.2. Materials and Methods 194
5.2.3. Results and Discussion 196
5.2.3.1 Scanning Electron Microscopy 196
5.2.3.2 Elemental Mapping 197
5.2.3.3 EMI Shielding Characterization 199
5.2.4. Conclusions 202
5.3 References 203
Chapter 6: Conclusions and Future Prospects 207
6.1 Conclusions 209
6.2 Scope for Future works 212
List of Publications 215

PREFACE

With the usage of electronic equipments on the high rise, electronic pollution is inevitable that affects every walks of life. Among various e-pollutions, a recently highlighted domain that has far reaching consequences, is the electromagnetic interference (EMI). EMI is the disruption of operation of an electronic device when it is in the vicinity of an electromagnetic field caused by another electronic or electric device. Since EMI reduces the lifetime and performance of the electronic instruments and even affects human health, it is highly crucial to protect sophisticated instruments and components from electromagnetic interference. Thus, electromagnetic compatibility (EMC) has great relevance in both consumer and defence electronics, which can be achieved by using suitably designed EMI shielding solutions at the emitter or susceptor. EMI shielding materials either reflect and/or absorb the electromagnetic radiation, which thereby acts as a shield against the penetration of the radiation through the shield. Earlier, the widely used materials for EMI shielding were metals, which being bulky, are discouraged these days for lightweight gadget applications. Intense research over three decades brought out a wide variety of materials including carbonaceous materials, conducting polymers, metamaterials etc. to the EMI shielding arena. The technological relevance of different shielding solutions and the science behind basic EM wave attenuation mechanism are outlined in the introductory **Chapter 1**. The consumer electronics and defense sectors are looking for surface patterned, ultra-lightweight, porous, flexible and wearable shielding structures which is highly challenging due to the lack of suitable materials available and the complex design & engineering involved. Against this background we have formulated some strategies. Our efforts to develop novel microwave shielding solutions involving conducting oxide perovskites are detailed

in the subsequent two working chapters and a couple of ferromagnetic metal based structures are described in the following two chapters.

Essentially**, Chapter 2** deals with developing a conducting composite based on $La_{0.5}Sr_{0.5}CoO_{3-\delta}$ as the filler and further modifying their surface for enhancing microwave attenuation. However, despite possessing relatively high electrical conductivity, research on perovskite structured protonic conductors is largely a grey area where not even a single material was qualified for promising EM wave absorber applications. Against this background, we have taken up a detailed investigation on the development of an all oxide EMI shielding solution based on the perovskite structured $La_{0.5}Sr_{0.5}CoO_{3-\delta}$ (LSCO). Interestingly, the sintered LSCO sheets were showing excellent microwave shielding properties up to 35-42 dB in the entire X and Ku bands. Towards getting a light weight and easily processable structure, we have accomplished a composite of LSCO with the easily mouldable polymer, epoxy. The thermal, dielectric and electromagnetic wave shielding properties of the composites were studied. The mechanical strength, thermal expansivity and thermal conductivity of the composites were progressively improved with LSCO addition. An improvement in the shielding effectiveness was observed with filler addition and attained a value of 10 dB in the range of 8.2 to 10 GHz for a maximum loaded LSCO-epoxy composite. However, the apparent EMI shielding ranges were not up to the level for practical applications which prompted us to introduce a novel strategy to augment the level of shielding. On top surface of the composite sheets, predesigned silver (Ag) patterns (mostly periodic structures including rectangular patterns parallel and perpendicular to the waveguide axis, mesh like patterns as well as blanket coating) were screen printed, which resulted in a dramatic 4-fold improvement in their EMI shielding effectiveness, with significant enhancements in the reflection and absorption shielding efficiency of the composite. Compared to the conventional way of adding silver to form

epoxy-silver 0-3 composite above its percolation, the present method of screen printing needs only lesser amount of the conductor to generate a maximum shielding efficiency of 99%, with considerable easiness of processing.

Chapter 3 is an investigation on LSCO based nanostructures and foam structures for EMI shielding applications. Herein, LSCO nanowires were synthesized using microemulsion method and investigated its electrical and magnetic properties. Being less conducting compared to its bulk counterpart, nanostructured LSCO showed lower EMI shielding properties. So we decided to explore with bulk LSCO for the creation of porous, high strength, and corrosion resistant lightweight EMI shielding structures. LSCO foams were prepared by emulsion freeze-gelcasting route using hydrogenated vegetable oil (HVO). LSCO foams with broad range of porosities (76.9 to 90.3%) and cell sizes (10 to 120 μm) having near spherical cells were obtained by drying and oil extraction, followed by sintering of gelled emulsion bodies prepared at various aqueous LSCO slurry (ALS) concentrations and HVO to ALS volume ratios. The LSCO foam bodies showed promising compressive strength and Young's modulus in ranges of 1–7 MPa and 57-428 MPa, respectively. The temperature dependency of electrical conductance was analysed and the metallic nature of LSCO was further evidenced. Impressive EMI shielding effectiveness as high as 33 dB has been achieved for LSCO foam prepared at HVO to ALS volume ratio of 1, at an ALS concentration of 10 vol.%. The specific shielding effectiveness observed for the foam is ~5 times that of dense LSCO ceramics. The newly developed LSCO foams are lightweight and capable of withstanding harsh environmental conditions, since they are free from oxidation and survivable enough at high temperature.

Chapter 4 deals with the synthesis, characterization and investigation of microwave shielding properties of Ni and NiFe alloys. The preparation followed a simple, surfactant-free polyol method. The morphological analysis demonstrated a uniform

spherical nature of the alloys, with size range ~10-30 nm. An undesirable thin oxide layer was found to be forming over the alloy nanoparticles (NPs) which is feebly visible in TEM and later confirmed by XPS analysis. The magnetic properties of the Ni and NiFe NPs were measured using a vibrating sample magnetometer (VSM) at room temperature. The saturation magnetization value was found to be lowest in Ni, but keeps on increasing with increasing Fe content in the composition. The resistivity, as revealed from I-V characteristics, was shown to be lowest for the permalloy ($Ni_{80}Fe_{20}$) phase, while the values increased with further increment in the Fe content. The microwave shielding properties of the Ni and its Fe alloy NPs were investigated in the Ku band range. Certainly, all of the NiFe alloy combinations we tested, were showing excellent EMI shielding above 30 dB, with significant enhancements in the absorption shielding efficiency. These alloys are good candidates for EMI shielding having the ability to attenuate 99.9 % of electromagnetic radiations.

EM attenuating metalized fabrics have great significance in defense sector since they are invisible to radar. They can be wearable, breathable to air, but at the same time act as a shield against the stray electromagnetic waves. **Chapter 5** sketches our efforts to develop wearable shielding solutions by electrodepositing Ni on surface modified fabrics without significantly deteriorating their flexibility. Herein we explored mainly three materials, linen, nylon- mesh and carbon fabric, to serve as substrates for metallization through electrodeposition. The fabrics were activated by platinum sputtering, followed by Ni deposition in Watts bath solution. A uniform deposition of the nickel was observed in the scanning electron micrographs, where the thickness of deposition increases as a function of deposition time. The magnetic and EMI shielding properties of the nickel deposited fabrics were investigated in detail. The shielding properties were excellent in linen after Ni deposition which can be attributed to the greater surface coverage and

specific woven geometry of linen. Surface modified carbon fabrics also showed excellent shielding after Ni deposition. Such a high level of shielding is difficult to achieve in fabrics, which qualify them for wide variety of applications including soldier's jackets and radar absorptive lining of war materials.

The salient features and conclusions of the research work described in four working chapters are described in **Chapter 6** which includes scope of future work, as well.

Chapter 1

Electromagnetic Interference Shielding: Problems and Solutions

This chapter outlines the concept of electromagnetic interference (EMI) shielding, which is emerged to be a grave issue in modern electronic industry. The problems related with the wave interference and the various aspects and mechanism of shielding are briefly discussed in this chapter. The available solutions to EMI problems and the applications of EMI shielding materials in various attributes are briefed. The chapter also gives brief introduction on conducting oxide based composites, macroporous foams, conductive fabrics, and ferromagnetic materials.

1.1 Introduction

With innovations happening at breath taking speeds, the electronic revolution is profoundly transforming every walks of our lives. The application horizon of mobile communication devices and systems is expanding even faster, with the addition of bleeding edge technologies like IoT (Internet of Things), 5G and LTE (Long Term Evolution).[1] When such mobile devices become increasingly compact and more complex in nature, shielding them against inevitable electromagnetic interference (EMI) becomes more challenging. EMI of an electronic device, in simple terms, is the noise disturbance generated by an external source that affects its constituent circuit through electromagnetic induction, conduction or electrostatic coupling. In addition to consumer electronics, devices operating in automotive transit systems, medical electronics and critical military infrastructure also face massive EMI threats that may lead to under performance of the circuit and are hazardous to human health as well. So mitigating or blocking the interfering EM signals is inevitable for healthy device management.

1.2 Electromagnetic Interference

The process by which there is a transmission of the disruptive electromagnetic energy between electronic devices is known as EMI.[2] Through shielding and filtering such transmission can be reduced or eliminated and this process is known as Suppression. Propensity of a device or a system to be damaged by the exposure of EMI to an incident signal or field is known as Susceptibility. Immunity indicates the ability of an electronic system to perform to the predefined performance level resisting the EMI exposure. Radiated immunity and conducted immunity implies the ability of the product in relative terms to defy the electromagnetic energy mediated through propagation on free space and penetration through external cables and I/O interconnects respectively. Electrostatic

potential difference between bodies could result in transfer of electric charge through vicinity or direct contact. Suppression, susceptibility and immunity are key concepts in understanding the dynamics of electromagnetic interference shielding and its expanding impact in the relevant domains of applications in industry. The expedient nature of EMI had instigated the industry and governments to prescribe the standards and persuade for efficacious results towards the development of Electromagnetic Compability (EMC) standards. EMC assures that the electronic systems, devices and equipments are functional in the specified electromagnetic environment within a prescribed safety margin and at efficient levels of performance or design, unaffected by the degradation resulting from EMI. EMC signifies that a compatible device is neither emanating EM energy that could result in EMI in devices that are placed in proximity to the source; nor inducing any kinds of incompatibility with its own electromagnetic environment.[3]

1.3 Requirement for EMI shielding

With the unprecedented growth of electrical and electronic devices in every sphere of human life, there arises the need for shielding against electromagnetic interference. Radio waves (30 kHz- 300 GHz) forms the low energy end of electromagnetic spectrum and are widely used for communication purposes (Fig. 1.1). Higher energy range of ultraviolet light, X-rays and gamma rays represent the ionising radiation segment of the electromagnetic spectrum.[3] Being long wavelength waves, communication occurs mainly in radio frequency domain of the electromagnetic spectrum, and hence is mostly affected by EMI problems. The interference may occur due to energy generated by computer circuits, electric motors, power lines and even lightening. Microwave region (300 MHz-300 GHz), a sub-class of radio waves, could be further classified into different frequency bands, based on the application technologies used to access them. Accordingly, L band (1-2 GHz) is used by wireless, local area network (LAN), radars, global positioning

system (GPS) and mobile communication systems.[4] Bluetooth, cordless telephone and Wireless Fidelity operates in the S band (2-4 GHz) and C band (4-8 GHz).[5] Satellite communication mainly employs X band and K band (8-40 GHz). Military operations and research activities are the major applications in V band (40-75 GHz) and W band (75-110 GHz).[4] EMI related issues in these frequency spectrums can lead to various levels of damages ranging from data loss in the case of communication system to human loss in the area of military applications.

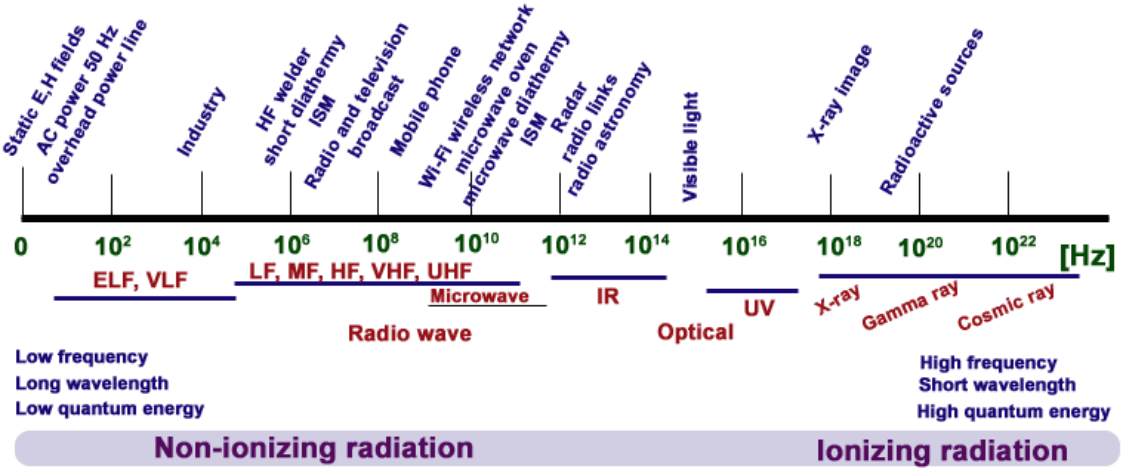

Fig. 1.1: Electromagnetic spectrum and their applications.

1.3.1 Factors Enhancing EMI problems

There are several factors that contribute to increase EMI problems.[6,7] The proliferation of smart gadgets have resulted in EMI problems mainly related to propagation paths and susceptibility. With regards to the impact of miniaturization of equipment, it contributed to the higher probability levels of interference arising out of shortened propagation path. While the component miniaturization has created improved avenues of portability and mobility, it inflicted high levels of susceptibility compared to equipments in a well-controlled space. With path breaking developments in the domain of chip interconnect technology, the EMI threshold is to be minimised through nanoengineering, in order to

avoid cross talk and maintain high clock speed. In all consumer electronic devices including mobile phones and laptops, EMC compliances and reliability are the key marketing features. Electrostatic discharge is a threat to the aircraft, automobiles and possess terminal damage to the microchips during the handling. The requirement for data security is another driving force of the shielding market. In the domain of military technology, EMI is an important challenge since the shield should maintain a minimal impact on factors such as size and weight. To strengthen the edifice of the military defence and communication systems, one has to confront this issue in an effective manner so as the base stands firm. Electromagnetic pulse and electronic eavesdropping are human made threats in the field of electromagnetic energy utilization. Electronic eavesdropping has been considered as a major issue in defence as well as commercial data storage and government agencies have taken several precautionary measures including programs for controlling radiations from devices containing crucial defence information.[8] Electromagnetic pulse is a type of electromagnetic wave which originates when a nuclear or chemical explosion occurs and could easily destroy the electromagnetic transmissions and unprotected devices as far as 500 km away from the source and the affected frequency range is the part of the electromagnetic spectrum below 100 MHz.

1.4 Concept of EMI Shielding

EMC is having three constituents namely source (emitter), propagation (coupling) path and susceptor. Reduction of EMI emissions from the source; modification or diversion in the propagation path; and improvisation of immunity of the susceptor are the EMI control methods. The type of propagation path determinates the dominance of EMI by radiation or conduction. With regards to shielding, the dominant radiated interference is relatively difficult to mitigate. Conducted EMI emissions relay on either differential mode or common mode of propagation. Radiated EMI emissions have E and H

propagation mechanisms. Thus the commonly accepted techniques to suppress interfering EM waves are derived from the methods to reduce the E and H fields.

1.4.1 Electric and Magnetic Field Shielding Principles

Electromagnetic shielding requires shielding of electrical and magnetic components present in the incoming radiation. Conductive materials attenuate the electric components while magnetic materials predominantly suppress the magnetic components of the waves. In a conductive shield enclosing electrical equipment, the interior electrical field is zero as demonstrated by Faraday cage experiment in 1821.[3] Faraday cage still forms the cornerstone of basic electric field shielding. The principle can be explained briefly as follows:

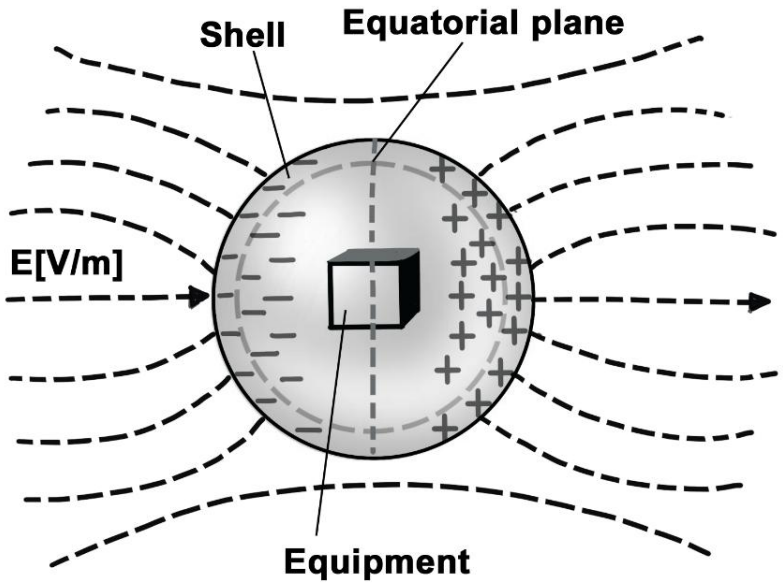

Fig. 1.2: Shielding of an equipment using a conducting spherical casing while placed in an electric field.

When a conductive spherical shield is placed in an electrical field as shown in Fig. 1.2, the electrical field cause polarisation along the shield which induces an opposing electric field, hence attenuating the incoming or source field. As the electric field or

current always prefers the least resistance path, the field will be restricted to the conductive surface, thus any void in the conductive shield may lead to poor shielding.[9,10]

In an analogous way, the magnetic field of the incoming radiation can be effectively shielded by soft magnetic materials which exhibit excellent permeability and low coercivity. When we consider a spherical magnetic enclosure as a shield, as explained by Fig. 1.3, the magnetic components in the EM wave will remain in the layer as it permeates the magnetic field and the magnetic reluctance will be very low inside the magnetic shield.[11]

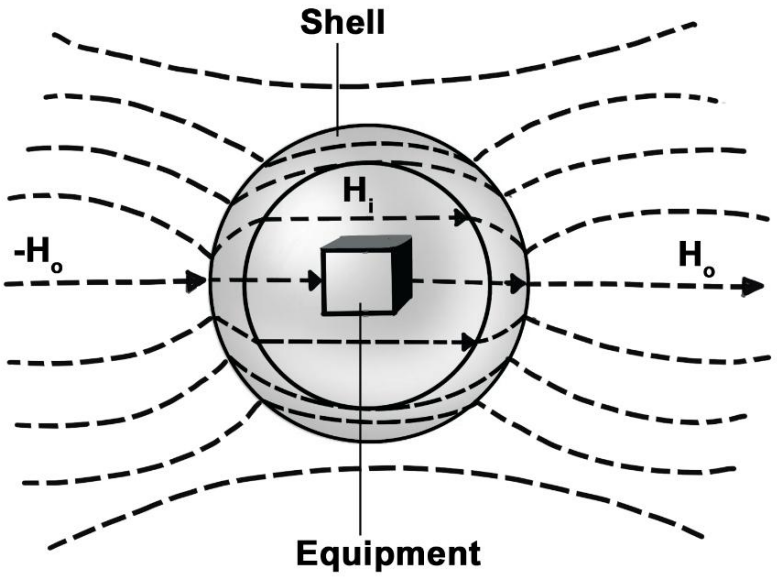

Fig. 1.3: Shielding of an equipment using a spherical casing having good permeability, located in an alternating magnetic field.

Electrical conductivity, in addition to magnetic permeability, is a characteristic trait that augments the effectiveness of magnetic shielding. This is exemplified in any of the magnetic field shielding solutions made with a highly conductive and low permeability thin shield. Fig. 1.4 shows the shielding mechanism of conducting spherical casing placed in a magnetic field. Here the principle is that, alternating magnetic fields induce Eddy currents in the adequately conducting shielding material which in turn

generate alternating magnetic fields in the opposite direction inside the shield. The opposing field generation is proportional to the increase in frequencies, resulting in effective shielding at high frequencies despite of the low permeability of the conductive material used in the fabrication of thin shield.[9]

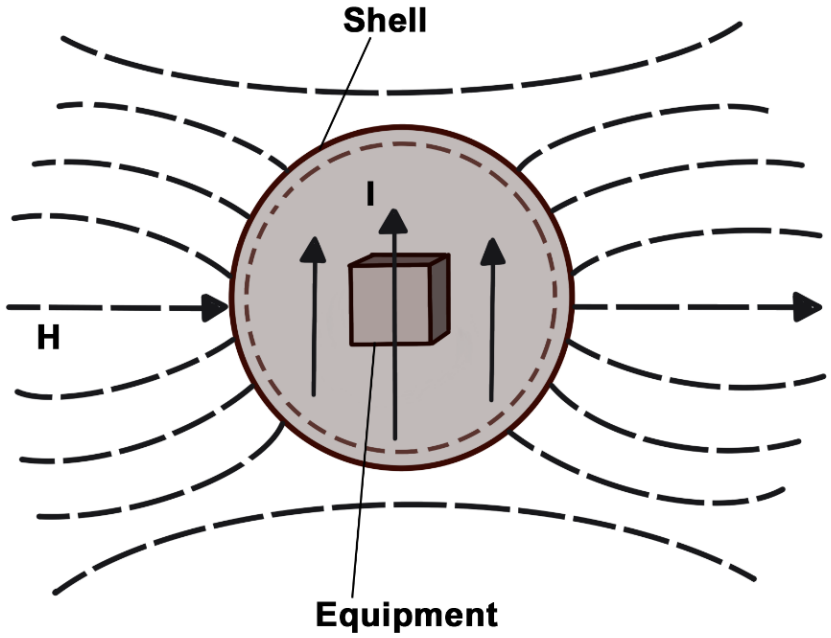

Fig. 1.4: Shielding of an equipment using a conducting spherical casing placed in an alternating magnetic field.

Low frequency shielding of magnetic fields is a highly difficult task to achieve.[8] However, there exists a few effective mechanisms for magnetic shielding at low frequency domain that includes flux shunting and eddy current cancellation.[12] In principle, a magnetic source induces magnetic fields that get redirected into the shield. These fields subsequently are shunted inside the material in a direction almost parallel to its surface, which eventually get discharged into the air, as shown in Fig. 1.5. Notwithstanding high efficiency, magnetic shielding is less popular since highly expensive thick shields are utilised for magnetic absorption. Apertures in the shield may affect the effectiveness as induced currents corresponding to the magnetic fields need paths without any obstacles.

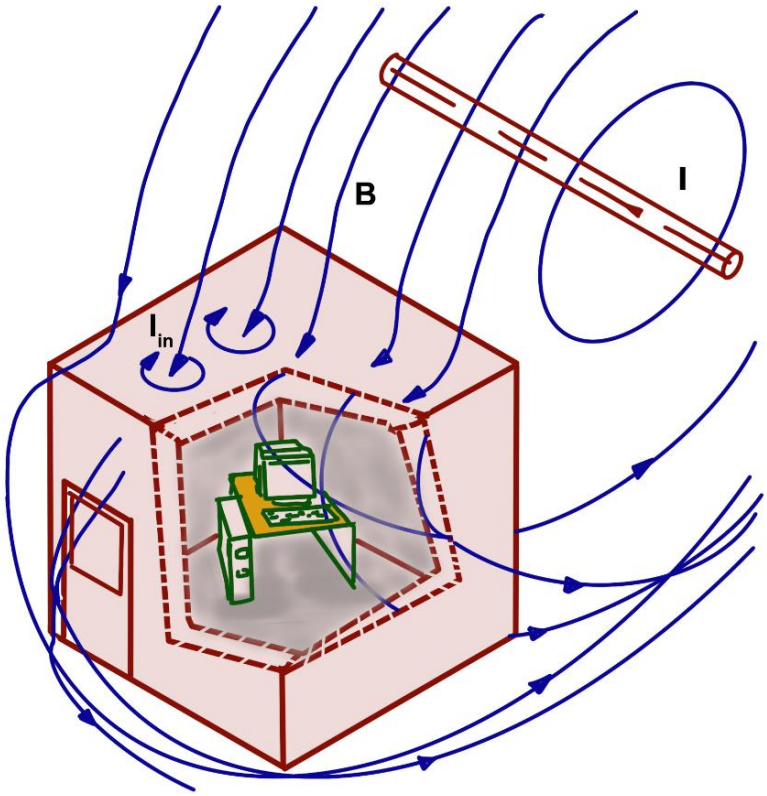

Fig. 1. 5: Low frequency shielding scenario for an electronic equipment kept near a current carrying source.

1.4.2 Shielding Effectiveness

Shielding efficiency of a material depends on its distance from the source, the thickness of the material, and frequency of the material. Shielding effectiveness (SE) measures the shielding efficiency of a material as a shield and its unit is decibels (dB). Shielding occurs by three main mechanisms: (i) reflection, (ii) absorption and (iii) multiple internal reflections (as shown in Fig. 1.6). Total shielding effectiveness is expressed as the sum of reflection shielding, absorption shielding and shielding due to multiple internal reflections.[13,14]

$$SE_T = SE_A + SE_R + SE_M \quad (1.1)$$

Multiple reflection factor can be neglected if absorption shielding exhibited by a shield is greater than 10 dB. Multiple reflection factor is not accounted for electric fields as well as

plane waves.

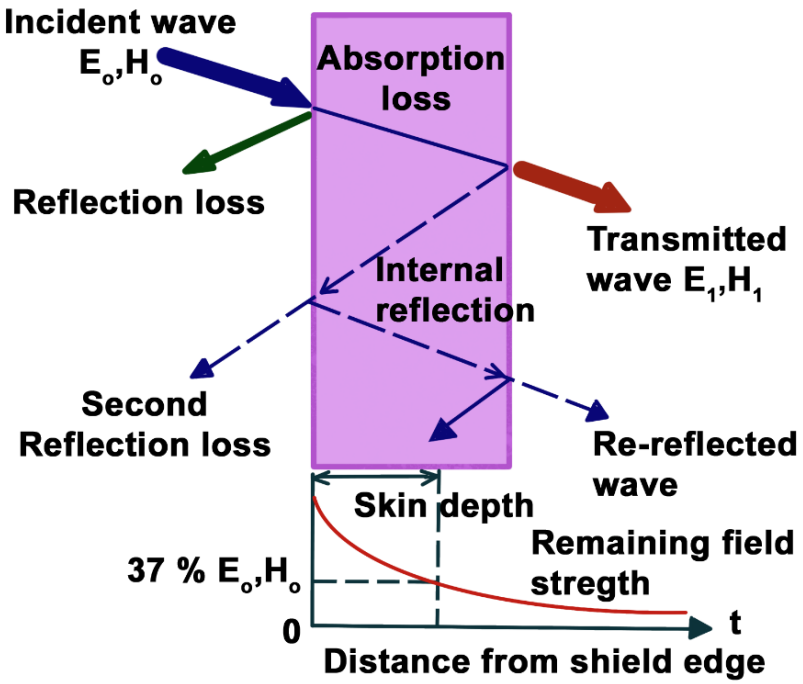

Fig. 1.6: Schematic of EMI shielding.

1.4.3 Absorption Shielding

A potent shield is supposed to absorb the incoming radiation and thereby protect the enclosed equipment. Absorption does not depend on the nature of source of radiation. Electromagnetic waves traversing through a shielding material cause opposing currents in the material. This results in ohmic losses which subsequently heat the shield. The attenuation of electric field as well as magnetic field is expressed as,

$$E = E_0 e^{-t/\delta} \quad (1.2)$$

$$H = H_0 e^{-t/\delta} \quad (1.3)$$

where E_0 and H_0 denote the amplitudes of the electric field as well as magnetic field, t denotes the thickness of the material, and δ denotes the skin depth of the material. Skin depth is an important parameter in shielding measurement and can be defined as the

distance required for the wave to reduce its initial amplitude to $1/e^{th}$ or 37 %. The skin depth, δ is calculated as,

$$\delta = \frac{1}{\sqrt{\pi f \mu \sigma}} \tag{1.4}$$

where f is the frequency of the electromagnetic wave expressed in MHz, μ denotes the relative permeability of the material and σ measures the conductivity of the material with respect to copper.

Absorption or penetration loss is expressed as,

$$A = 20\ \frac{t}{\delta} \log e = 131 t \sqrt{f \mu \sigma} \tag{1.5}$$

where t (in mm) indicates the thickness of the shielding material. Skin depth plays a major role in deciding the absorbance of the material. Thus the desirable qualities for a good EM wave absorbing material are high conductivity, high permeability and optimum thickness. Accordingly, highly conducting materials like copper exhibits good shielding performance at higher frequencies whereas magnetic materials like steel demonstrates commendable absorbance at lower frequencies.

1.4.4 Reflection Shielding

The impedance mismatch between incoming electromagnetic wave and the shielding material results in the reflection of the electromagnetic wave, traversing from air to the medium, at the surface of incidence. The electric field components of the incoming EM wave, usually exhibits high impedance (i.e. impedance > 377 Ω) compared to their magnetic counterparts. Conductive shields which offer very low resistance or impedance provide a mismatch to the electric fields and thus result in partial or total reflection of the incoming wave. The magnitude of reflection is dependent on the surface conductivity and can be estimated as[15,16],

$$SE_R = -10 \log_{10}\left(\frac{\sigma}{16 \varepsilon \omega \mu}\right) \tag{1.6}$$

Reflection shielding is the main way of protecting devices against electric fields. Impedance offered by magnetic fields is usually lower than 377 Ω. Hence the concept of impedance mismatch may not work well for magnetic fields. Magnetic fields are usually controlled by absorption shielding. The reflection shielding equations for electric field (R_E), magnetic field (R_H) and plane wave (R_P) are,[17]

$$R_E = 321.8 + 10 \log \frac{\sigma}{\mu f^3 r^2} \tag{1.7}$$

$$R_H = 14.6 + 10 \log \frac{\sigma f r^2}{\mu} \tag{1.8}$$

$$R_P = 168 - 10 \log \frac{\mu f}{\sigma} \tag{1.9}$$

where f is in Hz and r is the distance between source and shield in meters. If there is no mismatch in the impedance, the waves traverse without any loss through the material. So impedance mismatch is a necessary condition for reflection shielding.

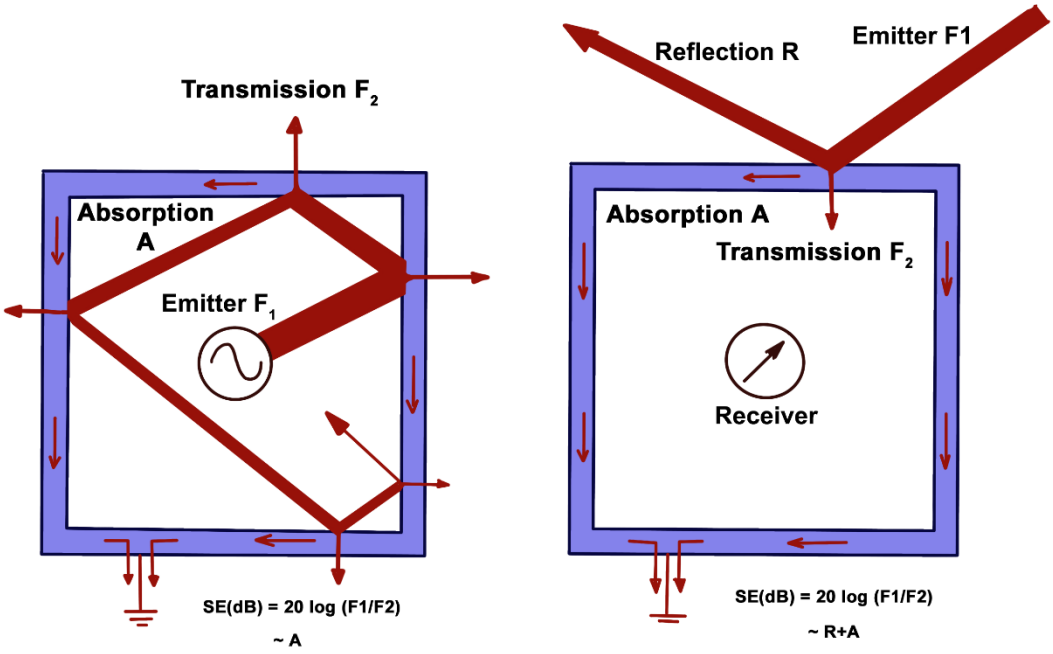

Fig. 1.7: Graphic representation of an EMI shielding enclosure shielding against (a) inside and (b) external EMI.

The absorption and reflection are important parameters in effective shielding. The action of an EMI shielding enclosure against internal and external electromagnetic stray waves is pictorially depicted in Fig. 1.7. For a least EM wave emitter, it is advised to use

a highly absorptive enclosure, since they can help reducing the intensity of the emitting waves by absorption loss. While in the case of protection from outside EM signals, the shield can be a combination of reflecting as well as absorbing, thereby avoiding the possibility of interaction of unwanted signals with the protected system.

1.4.5 Multiple Reflections

Multiple reflection factors are neglected for absorption less than 10 dB and mostly accounted for frequencies below 20 kHz when thin metallic shields are used for shielding purpose. The multiple reflection factor can be defined by the term B, given by,

$$B = 20\ log\left|1 - \frac{(K-1)^2}{(K+1)^2}\ 10^{-A/10} e^{-i227A}\right| \tag{1.10}$$

where K is the ratio of shield impedance to the incident magnetic field impedance. Even though the values of B can be negative or positive, for practical applications negative values are taken. For magnetic fields, shield impedance is negligible compared to incident field, multiple reflection term can be expressed as

$$B = 20 \log(1 - e^{-\frac{2t}{\delta}}) \tag{1.11}$$

1.4.6 Influence of Thickness of Shield and Distance from Source

Absorption shielding depends on the thickness of shield. When thickness of the shielding material increases, the amount of energy absorbed by the shield also increases. Magnetic fields decrease with distance from the source of origin. So for far field radiation, the dominant part constitutes the electric field and hence the main mechanism required for far field shielding will be reflection based. Reflection occurs at the surface of the shield and hence reflection shielding is independent of the thickness of the shield.

1.4.7 Calculation of Shielding Effectiveness Using Scattering Parameters

The response of a network to external communication devices could be quantified using scattering parameters.[18] Scattering parameters describe the relationship between input and output waves and is represented by the matrix,

$$S = \begin{bmatrix} S_{11} & S_{12} \\ S_{21} & S_{22} \end{bmatrix} \quad (1.12)$$

These parameters can be quantified using network analyzers which are electronic instruments for measuring amplitudes and phases of reflection as well as transmission coefficients. Four scattering parameters could be measured using network analyser. For a two port network analyser, S_{11} and S_{22} denote the reflection coefficients while S_{21} and S_{12} shows the transmission coefficients. Reflection coefficient and transmission coefficients could be calculated from the scattering parameters as,

$$R = |S_{11}|^2 = |S_{22}|^2 \quad (1.13)$$

$$T = |S_{21}|^2 = |S_{12}|^2 \quad (1.14)$$

Reflection and absorption shielding parameters effectiveness expressed in decibels could be calculated from the following equations;[19]

$$SE_R = -10 \log(1 - R) \quad (1.15)$$

$$SE_A = -10 \log\left(\frac{T}{1-R}\right) \quad (1.16)$$

1.5 Applications of EMI Shielding

EMI shielding finds applications in different areas such as automotive, defence, healthcare systems and communication devices (as shown in Fig 1.8). In electric vehicles, large volume of electronic and electrical components are present in different control units such as engine control and loading control and there is a great demand for EMI shielding in these vehicles. Usually, the microprocessors on circuit boards are protected by EMI covering caps and plastic housings by electrically conducting paints. Board level shielding is also employed for attenuating electromagnetic energy from digital devices. In transformers, Faraday cage is the usual shielding mechanism employed between primary and secondary windings; and thin conductive films are used for this purpose; whereas for

the high EMI levels, magnetic shielding enclosure is used for transformers and switched mode power supplies (SMPS).

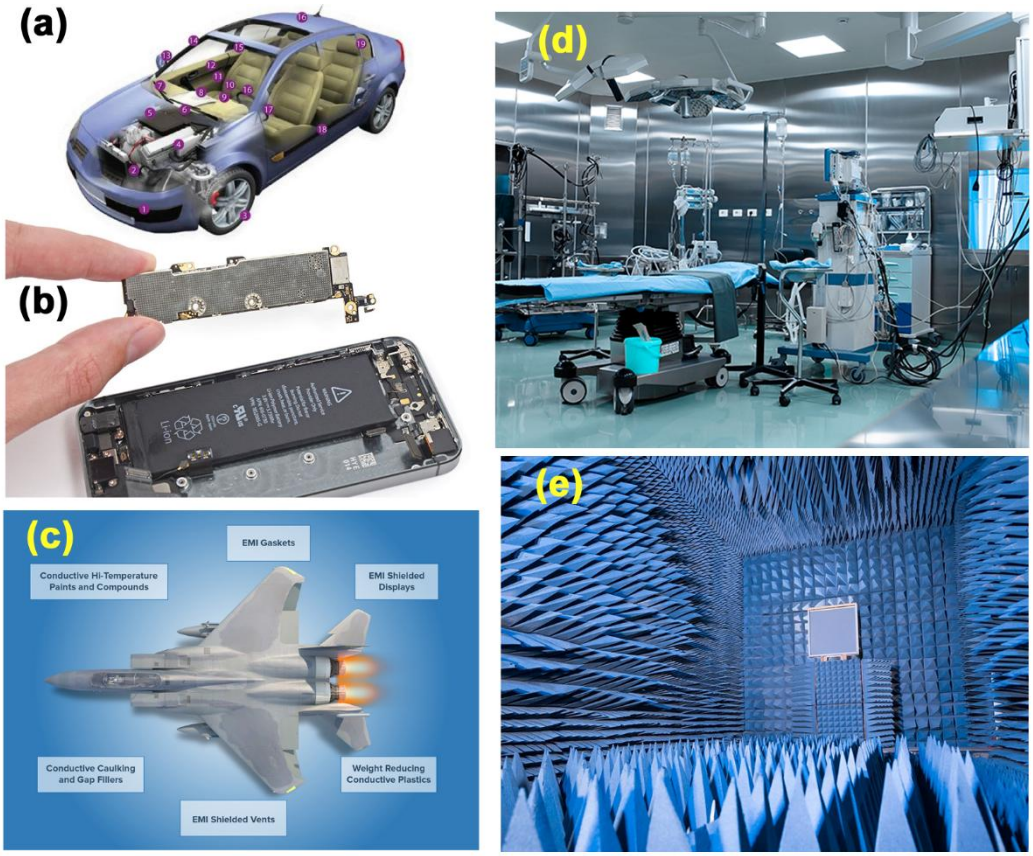

Fig. 1.8: A few applications of EMI shielding materials in (a) automobiles, (b) smart phone, (c) aerospace industry, (d) medical gaskets and (e) anechoic chambers.[20,21-23]

Armoured cars, battle tanks, drones, helicopter and control systems are equipped with various kinds of EMI shields. Battle tanks contain internal electrical components are shielded from outside static components by EMI barriers. Shielding of medical electronic equipments from unwanted EMI is an important area of application in healthcare systems. Conductive paint as well as autocatalytic selective painting are used for this application. Designs of connectors in electronic devices also take into consideration the problem of EMI shielding. Conventionally metal shells are used for shielding purposes which possess certain drawbacks such as heavy weight and high cost. Presently metal plated plastic

connectors provide better EMI shielding solutions. With the introduction of Wi-Fi, GPS, 3G, RFID, bluetooth and android cell phones, there is a rapid increase in EMI problems. EMI filtering circuits or internal EMI filters are presently attached to every device to mitigate the problem. PCB components are usually protected by employing shielding enclosures.[3]

In the arena of aerospace, cockpit radios and radar signals are affected by EMI generated by airborne devices like laptops, mobiles etc; leading to autopilot disconnects and erratic flight indications and hence shielding of various line replaceable units (LRU) are done for safe travel. These issues can be mitigated by employing suitable avionics packaging, enclosure shielding, radio packaging, window perimeters and structure gaps.[24] In stealth technology, radar is used for sending signals and detecting airborne objects. Microwave shielding has wide applications in defence sector in protecting the military aircrafts from the eyes of the radars and detectors. Shielding from radar is achieved through coating of radar absorbing materials, and executing novel design of stealth aircrafts which reflects the waves from radar in different direction. Microwave absorbing materials are also extensively used in anechoic chambers for testing antennas. One such example is carbon containing foam pyramids forming the lining of such chambers (see Fig. 1.8(e)).

1.6 Market Demand of EMI Shielding Materials

By 2022, a growth touching $7.38 billion is expected from the EMI market.[25] EMI shielding market is a rapidly growing economic domain and the key players include Chomerics, Laird Plc., PPG Industries Inc., Henkel AG & Co. KGaA, RTP Company and 3M Company. Some of the commercial products, constituents, suppliers, their performance, and their application frequency range along with cost analysis is included in Table 1.[26-27] As observed from the table, most of the commercially available products

constitute copper, nickel or silver as metallic components whereas polymer foams or textiles are chosen as the matrix for incorporating the conducting or magnetic components. But most of the fabrication techniques involve physical deposition processes which make the end products very expensive and time consuming.

Table 1. 1. Commercial products for EMI shielding application.

Sl No	Product	Components	Company	Frequency	SE
1	5770 series Conductive Foam	Polyurethene foam+ Copper/Nickel	Holland shielding materials	100 MHz-1 GHz	80- 83 dB
2	ECCOSORB®AN	Carbon loaded flexible foam	Laird	600 MHz-20 GHz	17 dB
3	4711 series Conductive textile	Nylon ripstop fabric, metallized with Cu/Ni	Holland shielding materials	10 GHz	80 dB
4	Conductive Fabric Tape 86749	Nickel/Copper metallized fabric with a conductive pressure sensitive adhesive	Laird	100 MHz	62 dB
5	CHO-MUTE™ 9005	Silicone elastomer matrix with ferrous filler	Parker Chomerics	3 GHz	20 dB
6	CHOFORM® 5538	Nickel –plated graphite particles in silicone elastomer	Chomerics	200 MHz - 10 GHz	60 dB
7	CHOFORM® 5528	Silver-plated copper particles in silicone elastomer	Chomerics	200 MHz - 10 GHz	70 dB
8	& CHOFORM® 5532	Conductive fabric (Polyester + Cu, Ni)	Holland shielding materials	10 GHz	87 dB
9	Eco Touch ™ Conductive Ripstop Fabric 3050-113	Copper	Laird	1 GHz-18 GHz	60 dB
10	Standard Shield 7000	Conductive textile	Holland shielding materials	10 GHz	87 dB
11	Conductive Silver coating 3830	Silver	Holland shielding materials	1 GHz	60 dB
12	Electrically Conductive Nickel coating 3800	Nickel	Holland shielding materials	100 MHz-1 GHz	40-60 dB

1.7 Materials for EMI Shielding

An ideal shielding structure is defined as a solid hollow sphere where no openings exists and such a model is practically not feasible.[3] From a theoretical perspective, the best shielding material would be a superconducting shell, which can expel magnetic fields also via Meissner effect. Recent years showed a resurged momentum in the search and development of materials that could be transformed as a shielding structure. With the paradigm shift to novel material synthesis techniques, we have more cost effective avenues to create such materials. Due to the influence of mechanical properties, ferromagnetic materials are the preferred choice of fabrication. Another option is the non-magnetic /standard conductive materials.[12]

Ferromagnetic materials are a class of magnetic materials that exhibits spontaneous magnetization below Curie temperature. The ferromagnetic materials are segmented into two type's namely, soft materials and hard materials which are classified on the basis of coercive fields.[28] Soft materials are having low-coercive fields whereas hard materials possess high-coercive fields. These high coercive fields are an integral requirement for permanent magnets. The sub-division of the soft magnetic materials consists of four broad families: iron-nickel (FeNi) or iron-cobalt (FeCo) alloys, electrical steels, amorphous metals and ferrites. Generally, Fe–(Ni, Co) is employed in shielding the materials with power-frequency magnetic fields. Mumetal, permendur, permalloy etc. are the distinctive members of the family extensively used in commercial EMI purposes, where high initial permeability and resistivity are beneficial.[12] Garnets and ferrites are two divisions of ferrimagnetic materials employed in high-frequency applications and they belong to certain class of ceramic materials.[4,29,30] The larger relative magnetic permeability values and larger losses make ferrites to possess excellent absorption properties and hence used in shielding applications.[31,32] The ferrites also have a higher

relative permittivity that may extend up to 15.[12] Yttrium iron garnets and barium ferrite based composites have been studied for their absorption shielding.[33]

In shielding problems, ferroelectric materials could be employed to diverge the electric displacement vector from an assigned region. The use of ferroelectric materials in diverging the electric displacement from the assigned region is having limited practical applications. For the purpose of absorption of incident EM energy, ferroelectric materials are often used due to their large values of the permittivity. The state of the art technology has produced thin films made of materials that could be available for shielding purposes. The thickness of the materials is having a definite range with the upper limit of 1 mm and the lower limit of tens of nm. This provides great advantages with regards to weight and cost, relatively with that of thick barriers.[3] It enables grounding or facilitates conductive paths to electrostatic discharges. The shielding performance of these layers is generally acceptable at a predefined limit of frequency and this limit is fixed to be higher than tens of MHz. Conductive layer's surface resistivity and point-to-point resistance are crucial elements in shielding. The four main technologies that are currently in use are conductive painting, electrolytic deposition, electroless plating[34] and vacuum metallizing.

Consequent to intense search, several novel materials were also qualified recently for EMI shielding applications including conductive polymers, smart papers (ferromagnetic or ferrimagnetic), conductive glasses and structural materials. Metamaterials and chiral materials have the potential to revolutionize the absorption shielding industry since they can be designed to create all absorbing laboratory level black holes. Metamaterials have typologies like backward-wave (BW) materials, negative-refractive index (NRI) materials, left-handed (LH) materials and double-negative (DNG) materials.[4] Another predominant member of this group of special materials is the composite materials of which the fibre reinforced composites are widely

adopted. Fibres with different orientations guarantee high structural strength and also mechanical behaviour that approximates to isotropy. Nanomaterials especially carbon nanotubes that portrays extraordinary strength along with unique electrical properties, are ideal for shielding applications. High electrical conductivity combined with thermo-mechanical properties qualify carbonaceous nanomaterials (including graphene quantum dots, graphene nanosheets, carbon nanotubes, and graphite) as first choice for shielding solutions.[35,36] Superconductors are another unharnessed group of special materials that possesses exemplary EM shielding which could be employed as effective shields against magnetic fields at the low frequency range.[37] Few high temperature superconductors such as $Bi_{1.8}Pb_{0.26}Sr_2Ca_2Cu_3O_{10+x}$ (Tc~108 K) are studied for their EMI shielding properties against magnetic fields as they could expel magnetic field due to their strong diamagnetic behaviour below critical temperature.[38]

A latecomer among high shielding materials is a new class of 2D materials, MXenes. They are two dimensional transition metal carbides and nitrides which could be represented as $M_{n+1}X_nT_x$ where M denotes a transition metal, X carbon or nitrogen and T_x represents surface moieties such as –OH,=O and –F.[39,40] The layered structure and low density in addition to exceptional electrical conductivity makes them useful as effective shielding materials.

1.8. Materials Covered in the Present Thesis

The microwave shielding materials' literature is flooded with carbon based nanomaterials and allotropes including quantum dots, nanosheets, nanotubes and graphite, primarily due to their exciting properties like high conductivity, high thermal conductivity, high tensile strength, low weight and flexibility. However, the present thesis is focussing mainly on conductive, semiconducting and magnetic structures which are devoid of carbon nanomaterials as a shield assisting constituent.

1.8.1 Semiconducting Oxides

Though metals and carbonaceous materials provide highly effective remedies for EMI shielding problems; high temperature, oxidising or corrosive environment fails them and demands new alternative solutions. Oxide conducting materials are useful here since they are resistant to oxidative corrosion. Several groups reported the applicability of zinc oxide in microwave attenuation applications primarily because of its radiation resistance in addition to higher breakdown voltages, lower electronic noise, and high-power and high-temperature operation. Aluminium doped zinc oxide films developed by atomic layer deposition method have been reported as transparent EMI shielding material with shielding effectiveness of 6.5 dB in the low frequency region 30 MHz to 1.5 GHz.[41] However, Ga doped ZnO by ion plating method using DC arc discharge demonstrated high shielding effectiveness of 47 dB for a frequency of 1.7-2.5 GHz.[42] Micro sized ZnO dispersed in nano gahnite displayed a reflection loss of -25 dB for X band shielding where the core shell topology was utilised.[43] ZnO dendritic structures fabricated by CVD process and composited with 50 vol. % paraffin showed a reflection loss of -42 dB at 3.6 GHz for a thickness of 5 mm.[44] ZnO nanotrees fabricated by two step CVD process achieved a reflection loss of -58 dB at 4.2 GHz for 60 wt.% loaded paraffin composites for 4 mm thick samples.[45] Nano needle like ZnO synthesised by a combustion technique displayed a reflection loss of -44 dB for 8 mm sample at 2 GHz and 373 K.[46] Inferior electrical conductivity due to its relatively large direct band gap (~3.3 eV) could be limiting factor for the wide band shield applications of ZnO.

1.8.2 Perovskite Based Conducting Oxides

Perovskites are crystalline ceramic oxide structures with structural formula ABO_3, where A is typically rare earth cation, B is transition metal cation and O is oxygen atom. The name perovskite originated from mineral called perovskite ($CaTiO_3$) named after

mineralogist Count Lev Aleksevich Von Perovski. Some of the lanthanum based rare earth perovskites possess high temperature stability and reasonably good conductivity, prompting their use as EMI shielding materials. Lanthanum strontium manganese oxide ($La_{1-x}Sr_xMnO_3$ or LSMO) based EMI shielding studies have been actively carried out by a handful of research groups.[47] LSMO is a low resistivity oxide material with rhombohedrally distorted perovskite structure and weak magnetic nature at room temperature. Introduction of Sr doping introduces Mn^{3+} and Mn^{4+} ions in the system leading to the electrical conduction due to electron transfer and introduction of ferromagnetism. $La_{1-x}Sr_xMnO_3$ (x = 0.4, 0.5, 0.6 and 0.7) samples when investigated for shielding performance, showed a maximum reflection loss of 25 dB for x=0.4 in X- band region and lowest values were obtained for x=0.7 ascribed to the increased resistivity of the system.[48] Core-shell structured $La_{0.6}Sr_{0.4}MnO_3$ nanoparticles synthesised by sol-gel method with amorphous shells owing to the low calcination temperatures reached a reflection loss of -41.1 dB at 8.2 GHz.[49] A maximum reflection loss of 23 dB was obtained for 80 wt.% loading of micron sized $La_{0.7}Sr_{0.3}MnO_3$ in epoxy matrix at a frequency of 10.5 GHz.[50] Sol gel derived $La_{0.7}Sr_{0.3}MnO_3$ particles showed a shielding effectiveness of 19 dB for X-band frequencies.[51] Microwave absorbers were developed by compositing solid state derived LSMO powder with 2 wt. % CNT/epoxy and demonstrated microwave absorption ability of -22 dB at 9.5 GHz for a conducting oxide loading of 80 wt. %. [52] Solid state process derived LSMO has also been composited with 5 wt. % carbon black and reflection loss of -23.63 dB at 7.87 GHz is reported.[47] Here, LSMO has contributed to the magnetic loss whereas dielectric loss was contributed by CNT in the former and carbon black in the latter cases, respectively. Solid state processed LSMO doped with Co, Ni and Fe have been studied as EMI shielding material and

$La_{0.7}Sr_{0.3}Mn_{0.8}Fe_{0.2}O_{3\pm\delta}$ possessed maximum reflection loss of -27.67 dB for a frequency of 10.97 GHz due to the increased ferromagnetic nature.[53]

Carbonyl iron/$La_{0.6}Sr_{0.4}MnO_3$ composites were reported with a reflection loss of -12.4 dB at 10.5 GHz for a thickness of 0.8 mm and weight ratio of 65:15.[54] $La_{0.6}Sr_{0.4}MnO_3$/polyaniline nanocomposites exhibited a reflection loss of -61.3 dB while nano $La_{0.6}Sr_{0.4}MnO_3$ showed a maximum loss of -64.6 dB at 16.4 GHz.[55] Studies on microwave absorbing properties of $La_{0.8}K_{0.2}MnO_3$ showed an increased dielectric loss compared to pure $LaMnO_3$ which contributed to a reflection loss greater than -20 dB for thickness ranging from 1.25 to 5 mm in the frequency range 2-18 GHz.[56] In short, the perovskite oxide conductors demands detailed investigation for harsh condition microwave protection applications due to their superior wear and corrosion resistance.

1.8.3 Macroporous Foams

Most commercially available shielding materials used in shielded rooms are based on different foam structures, since they are lightweight and have high specific shielding effectiveness.[57,58] Foams are high specific area, low density materials which offer exquisite physical, chemical and mechanical properties. Foams consist of basic units called cells created by gas bubbles. Cells have cell walls, plateau borders and nodes.[59] Plateau borders are intersection lines seen between two cell walls, and nodes are intersection point for plateau borders. Important parameters describing a foam structure are cell size, relative density, cell shape and topology.[60] Based on topology, solid foams can be categorised into closed celled foams with isolated or distinct cell structure and open celled foams with interconnected cell structure.[61] Solid foams generally are obtained from metals, carbonaceous materials and polymers.

Electrically conductive foams are formidable candidates for EMI shielding applications. They could be lightweight absorbers with high mechanical strength and low

thermal conductivity. In macroporous foams, the absorption of the unreflected radiation suffers multiple reflections at various interfaces within the shield, in addition to the conventional absorptive shielding. Yang et al, showed that CNT/polystyrene foam composite with 7 wt. % CNT loading demonstrated shielding effectiveness of around 20 dB, greater than that measured for a CNT/polystyrene composite.[62] One step fabricated flexible lightweight graphene/PDMS foams have been reported to exhibit an excellent shielding effectiveness of 20 dB in the X-band range and a higher value of 30 dB in the lower frequency region of 1.5 GHz even after undergoing bending cycles of upto 10000 times.[57]

Ultrathin graphene/polyimide foams with thickness 24 μm have been demonstrated by Li et al, where graphene stabilized the porous structure formation and assisted the graphitization process through the internal stress between the matrix and fillers.[63] In the same year, 3D reticulated titanium foams with low thermal conductivity and effective EMI shielding at low frequencies (0.3-3000 MHz) have been displayed.[64] Earlier, Aluminium foams were reported to offer shielding effectiveness of 25-75 dB in the lower frequency region of 130 MHz –1800 MHz for samples with porosity varying from 75.61 to 93.08 %.[65] One pot liquid foaming process derived silver nanowire hybrid polyimide composites showed a very low density of 0.014−0.022 g/cm^3 and high specific shielding values of 772 dBg^{-1}cm^3 in the frequency range of 800−1500 MHz.[66] 3D silver networks facilitate high speed electron transport which effects excellent specific shielding effectiveness even for a low Ag loading of 0.044 vol. %. Microcellular polyetherimide (PEI)/graphene nanocomposite foams fabricated by a foaming process considerably increased the value of specific shielding effectiveness from 17 to 44 dBg^{-1}cm^3, by effectively reducing the percolation threshold for electrical conductivity.[67] Lightweight polypropylene/stainless-steel fiber (PP−SSF) foamed composites showed effective SE of

75 $dBg^{-1}cm^3$ even for a filler loading of only 1.1 vol. % compared to 38 $dBg^{-1}cm^3$ of the solid PP−1.0 vol. % SSF composites.[68]

1.8.4 Epoxy Based Composites in Microwave Shielding

Poor mechanical properties, high density and corrosiveness of metals, limit their use as effective shielding materials. There arise the significance of polymer composites made of a polymer matrix and metallic or conductive filler. These composites incorporate the flexibility and low density of polymers and conductivity of metals; thereby providing durable low weight shielding solutions.[69] Though epoxies are highly insulating materials, their composites are widely used in commercial electromagnetic shielding solutions such as in Parker Chomerics CHO-SHIELD® 610 EMI coating; where low cost, mechanical stability, corrosion resistance and easy processing techniques gave them huge advantage over conducting polymers.[70]

Epoxy resins could be termed as low molecular weight thermosetting polymers containing more than one epoxide group of the form;

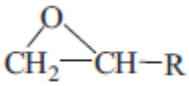

Curing agents required for epoxy resins could be categorized as amine-type curing agents, alkali curing agents, anhydrides and catalytic curing agents, based on their chemical compositions.[71] Epoxy resins display good toughness, appreciable resistance to moisture, chemical degradation and could be cured even at room temperature or by applying heat, which make them attractive option for industrial scale applications.[72] Various applications of epoxy resins include anticorrosive coating and decorative paints,[73] low cost adhesive in aerospace industry,[74] electronic packaging applications,[75] and biomedical applications.[76]

Performance of an epoxy composite as EMI shield depends on the inherent conductivity of the filler, interaction between the filler particles, interaction between the epoxy polymer and filler, proper dispersion of the filler in the matrix etc. in order to achieve a low percolation threshold.

Functionalised graphene/epoxy composite with a low conductive percolation threshold of 0.52 % is reported to show a shielding effectiveness of 21 dB; even for filler loading as low as 15 wt. % in X-band.[77] Single walled CNT/epoxy composites were studied as well and a shielding effectiveness of 20-30 dB was obtained in X band, for loading of 15 wt. %.[78] Fluorination effect on surface of multiwalled CNT on shielding efficiency of MWCNT/epoxy composite was studied in 800 MHz- 4 GHz range. It was found that better dispersion of MWCNT in epoxy matrix, due to fluorination, resulted in better shielding values.[79] In 2011, CNT embedded epoxy composite films were fabricated through a cost effective technique called three roll milling and the films were stacked to achieve a reflection loss of -10 dB.[80]

1.8.5 Metallisation of Composite's Surface

For decades, researchers used metallic mesh films with less thickness as effective shields in handheld gadgets like mobile phones, owing to the high electrical conductivity of the metallic films. In 2016, a sacrificial crackle template based metallic mesh of silver was fabricated Han et al., using a cost-effective lift-off method to obtain shielding effectiveness of ~26 dB, and optical transmittance of ~91 %.[81] Flexible and transparent EMI shield using Ag mesh pattern was fabricated through self-assembly and coupling method, which exhibited shielding effectiveness of -23 dB for frequency range of 1.5-10 GHz frequency with a transparency of 88 %.[82] Interestingly, copper mesh patterns with oxide layer formed by photolithographic methods on glass substrate even outperformed commercial ITO sample as EMI shield. Here, mesh patterns achieved a SE of 24 dB in

the Ku band while ITO samples could reach SE of only 18 dB for the same frequency range.[83] Chemical vapour deposition derived monolayer graphene transferred on metal mesh obtained by crackle template based technique showed SE of 14.12 dB in Ku band whereas graphene sheet could only exhibit a value of 1.88 dB.[84] Practical metamaterial design constraints and inability of thin film techniques to coat on conformal structures restrict researchers using designed surface metallisation, as a tool to improve EMI shielding.

1.8.6 Magnetic Nanomaterials in Shielding

Magnetic materials are preferred for absorption based shielding. Ferrites and metallic magnetic materials are widely used as microwave absorbers. Ferromagnetic metals exhibit high saturation magnetization and high permeability characteristic of efficient absorbers, even at high frequencies. The permeability of ferrites is found to be low at high frequencies according to the Snoek's law.[85] Fe-Ni alloys exhibit high permeability of 80000 at 150 kHz which makes perfect shielding solutions.[8] Microwave absorption of surface modified $Fe_{50}Ni_{50}$ is studied in quasi microwave region and an optimum reflection loss of -40 dB was reported at 1.1 GHz for sample with 2.3 mm thickness.[86] Gas atomized $Fe_{50}Ni_{50}$ samples after shape modification by planetary milling, have been analysed in the frequency range 1-4 GHz and maximum reflection loss of -8 dB was reported when measured in a polymer matrix.[87] In 2011, Fe–40 wt.% Ni alloy with flaky and granular structures were studied to deduce the effect of shape on absorption, and flaky samples exhibited better reflection loss of -23.8 dB at 0.8 GHz.[88] Urchin like nickel micro spherical structures were reported with reflection loss of -21.98 dB at 17.4 GHz due to enhanced magnetic loss.[89] Flower like Co superstructures/wax composites have also exhibited a reflection loss of -40.25 dB at 6.08 GHz owing to the high conductance, high magnetization and increased eddy current loss.[90] Zhao et al., in

2017 reported that Fe_3O_4 nanorings/paraffin composite with 20 wt. % filler loading showed a reflection loss of -17.4 dB at 18 GHz which was attributed to the enhancement in permeability caused by magnetic nanorings acting as plasmon structures.[91] In another study, 80 wt. % amorphous iron nanostructures/paraffin composites attained a reflection loss of -53.2 dB at 6.4 GHz caused by the enhanced resistivity, creating an impedance match and thereby contributing to the better absorbing properties.[92] For Fe nanoflakes with porous morphology, a reflection loss of -30.8 dB at 3.2 GHz was reported where the porous structure and oxygen vacancies increased the number of dipoles, thereby causing an increased absorption.[93] Fe_3O_4 nanocrystals/paraffin wax composites with 30 wt. % loading showed a reflection loss of -21.1 dB at 8.1 GHz for a thickness of 3 mm.[94] Samples of dendritic Fe_3O_4 microstructures and γ-Fe_2O_3 dendritic microstructures with 4 mm thickness were found to have a reflection loss of -53 dB and -50 dB respectively. The enhanced microwave absorbing properties could be due to the enhanced dielectric loss and magnetic loss and the decreased coercivity of the hierarchical structures.[95] Iron and nickel nanoparticles fabricated by DC arc discharge method displayed core-shell structure with metallic core and oxide shell of few nanometers, giving a reflection loss of -47.5 dB at 9.6 GHz for iron and -14.9 dB at 6.6 GHz for nickel. The higher performance in iron is ascribed to its orientational polarization mechanism, bringing about a higher dielectric loss.[96] A reflection loss of -45 dB at 8 GHz was reported for porous Ni/NiO disc like structures where the NiO/Ni boundaries as well as enhanced conductive loss play a crucial role in increasing the attenuation properties.[97] Wu et al. reported superior microwave absorbing properties of porous α-Fe_2O_3 nanosphere/paraffin composites (-25 dB at 13 GHz for 3.5 mm thick samples) in comparison to porous γ-Fe_2O_3 and Fe_3O_4 nanosphere/paraffin composites, obviously due to the higher permittivity of the former.[98] Porous carbonyl iron flakes showed maximum value of reflection loss of -41.8 dB at 4

GHz for thickness of samples varying from 0.9 to 4.5 mm, owing to porous structure of the samples.[99] The porous iron particles developed by corrosion technique showed a reflection loss of -42.2 dB at 13.2 GHz, compared to -36.3 dB at 9.6 GHz for carbonyl iron particles.[100] In 2014, Fe nanospheres and nanowires synthesised by Li et al., through a chemical reduction method which when composited in epoxy matrix resulted in reflection loss values of -33 dB for 5 mm samples and -32 dB for 3.5 mm samples respectively.[101] Prior to that, flake shape carbonyl iron obtained by ball milling of spherical carbonyl iron samples composited with epoxy resin, reported a reflection loss of -23 dB at 5.5 GHz for 3 mm thick samples.[102] Flake-shaped $Fe_{50}Ni_{50}$ alloy particles/paraffin composites exhibited a reflection loss of -39 dB at 55 MHz for 5 cm thick samples, due to the high permeability.[103]

1.8.7 Conductive Fabrics

1.8.7.1 Polymer Based Fabrics

Fabrics could be defined as integrated fibrous structures developed by fiber entanglement, yarn interlacing, multiaxial placement, intertwining, or interlooping.[104] Smart fabrics offer an exciting arena of research, by offering a platform for integrating technologies for sensing, storing or generating electronic signals. Developing microwave absorbing smart fabrics are extremely important for defence sector, since it can make the wearer 'radar invisible'. Lyocells with polyaniline/Co-Ni coatings were developed by two stage process which involves polymerization and electroplating whose synergetic effect resulted in shielding effectiveness values as high as 33.9–46.2 dB. Here the high shielding is attributed to the Co-N, Ni-N bondings, causing effective interphase interaction between PANI and Co-Ni coatings.[105] Polyimide fabric decorated with $NiFe_2O_4$@PANI core-shell particles demonstrated reflection loss of -19.2 dB at 16.1 GHz for a thickness of 1.5 mm, where the magnetic loss was originated from $NiFe_2O_4$ while

dielectric loss was from PANI shell.[106] Recently, Jiyong et al. shown that stretchable polytrimethylene terephthalatae coated with PANI and plated with Ni by electroless deposition technique could exhibit a shielding effectiveness of 43 dB for a low frequency range upto 2.5 GHz.[107] Electroless Ni plating on polypyrrole (Ppy) deposited linen fabric modified with 3-aminopropyltrimethoxysilane (APTMS) self-assembled monolayers (SAMs) could also attain shielding values as high as 43.51 dB. On the other hand, linen based fabrics, despite being durable and eco-friendly, showed inferior shielding properties. For example, linen/Ppy composite had a value of only 15 dB whereas linen/Ni showed about 20 dB at a frequency of 1000 MHz.[108] Since it is highly breathable with 5 fold heat dissipation performance to wool and 19 times of silk, more focussed research is required to develop efficient shielding cloths using linen.

1.8.7.2 Carbon Fibers and Fabrics

Carbonaceous materials offer exemplary solutions as microwave absorbing materials with low densities, superior mechanical properties and higher degrees of flexibility comparing to their metallic counterparts. Carbon fiber was brought into limelight when Thomas Alva Edison in 1880 filed a patent for its first application as filament for incandescent lamp after trying with 1600 types of materials.[109] Carbon fibers can be derived from polyacrylonitrile (PAN) based, pitch based or cellulose based precursors. PAN based carbon fibers are non-graphitic while pitch based carbon fibers are graphitic hence exhibit higher densities and thermal conductivities but lower mechanical strength. Non-twisted continuous carbon filaments ranging from 5 to 10 μm in diameter could be termed as a tow of carbon fibers.[110] Carbon fabrics could be categorized as woven or non-woven. In a woven fabric, warp is defined as the yarns parallel to the weaving direction while those transverse to that direction are termed weft (or picks, fills or woofs). Simplest category of 2D planar woven fabric is the plain weave pattern which

possesses excellent structural integrity as well as fiber stability necessary for any practical application.

Highly efficient carbon fiber nanomats were reported with properties superseding that of graphene or reduced graphene oxide aerogels; their shielding effectiveness reaching 52-81 dB at 1.5 GHz, for thickness ranging from 2.9 to 5.4 mm.[111] Ultrathin shielding materials made of Ni plated carbon fabrics covered with polycarbonate showed remarkable flexibility and excellent shielding effectiveness of 72.7 dB at 1.5 GHz.[112] Mussel inspired dopamine modified 3D carbon nanofiber mats coated solvothermally with Fe_3O_4 nanoparticles acquired shielding effectiveness of 62.6 dB in X-band region.[113] Chen et al. reported that reinforcement of carbon fiber with SiC caused an increase in flexural strength but a decrease in shielding effectiveness from 43 to 31 dB for X band frequency range; yet suggested as thermostructural material for corrosive environments.[114] Carbon fiber/carbonyl iron core-shell structures fabricated by metal organic chemical vapour deposition (MOCVD) process, reported a reflection loss greater than -10 dB for a frequency range of 2-18 GHz for 0.9-3.9 mm thick samples.[115] The increased dielectric loss and multiple reflections occurring at the core-shell interfaces are believed to have enhanced the microwave absorbance for core- shell architecture compared to the composites made between carbonyl iron and carbon fibers.[116] Technologically, carbon fibers are advantageous for aeronautical shielding applications, in addition to the fuel saving in aircraft due to their lower densities (1.6-2.0 g/cm^3), are easily processable through injection moulding. Hence, more research is needed to tap the high EM wave attenuation characteristics of carbon fibers through proper material design and engineering.

1.9 Scope of the Present Thesis

In accordance with the present huge market demand of over 6 billion US dollars annually, the development of novel EMI shielding solutions is a challenge due to the lack of suitable materials available as well as the complex design & engineering involved. As shown in the preceding discussion, the consumer electronic and defence sectors are currently looking for surface modified, ultra-lightweight, porous, flexible and wearable shielding structures. The present thesis is a gentle attempt to tackle some of these burning issues through process design and engineering. Given below are some of the broader objectives undertaken in this research through four working chapters:

- To develop a surface modification strategy to augment the EMI shielding properties of the composites which are otherwise engineered for good mechanical and thermal characteristics.
- To develop high temperature withstanding ultra-porous ceramic shield, which could save the material and energy with excellent stability.
- To develop materials for cavity resonance damping using high permeability materials which are conducting as well as magnetic, while possessing high stability.
- Developing a flexible and wearable fabric which can serve as microwave inhibitors and can have direct applicability in defence and consumer electronics.

1.10 References

(1) Lee, S.; Jo, I.; Kang, S.; Jang, B.; Moon, J.; Park, J. B.; Lee, S.; Rho, S.; Kim, Y.; Hong, B. H. Smart Contact Lenses with Graphene Coating for Electromagnetic Interference Shielding and Dehydration Protection. *ACS Nano* **2017,** *11* (6), 5318-5324.

(2) Montrose, M. I. *EMC and the Printed Circuit Board: Design, Theory, and Layout Made Simple*, John Wiley & Sons: Hoboken, New Jersey, 2004; Vol. 6.

(3) Tong, X. C. *Advanced Materials and Design for Electromagnetic Interference Shielding*, CRC Press: Boca Raton, 2016.

(4) Jaroszewski, M.; Thomas, S.; Rane, A. V. *Advanced Materials for Electromagnetic Shielding: Fundamentals, Properties, and Applications*, Wiley: New Jersey, 2018.

(5) Hasan, M. M.; Faruque, M. R. I.; Islam, M. T. Dual Band Metamaterial Antenna for LTE/Bluetooth/WiMAX System. *Sci. Rep.* **2018,** *8* (1), 1240.

(6) Molyneux-Child, J., EMC Shielding Materials–A Designer's Guide, Newnes. Oxford: 1997.

(7) Chatterton, P. A.; Houlden, M. A. EMC-Electromagnetic Theory to Practical Design. *NASA STI/Recon Technical Report A* **1992,** *93*, 17521.

(8) Hemming, L. H. *Architectural Electromagnetic Shielding Handbook: A Design and Specification Guide*, John Wiley & Sons: New Jersey, 2000.

(9) Bjorklof, D. Shielding for EMC. *Compliance Engineering* **1998,** *15* (5).

(10) Bridges, J. E. An Update on the Circuit Approach to Calculate Shielding Effectiveness. *IEEE Transactions on Electromagnetic Compatibility* **1988,** *30* (3), 211-221.

(11) Duffin, W.; Kelley, J. B. Advanced Electricity And Magnetism. *Physics Today* **1970,** *23*, 72.

(12) Celozzi, S.; Araneo, R.; Lovat, G. *Electromagnetic Shielding*, John Wiley & Sons: New Jersey, 2008; Vol. 192.

(13) Schelkunoff, S. A. *Electromagnetic Waves*, D. Van Nostrand: New York, 1943.

(14) Gooch, J. W.; Daher, J. K. *Electromagnetic Shielding and Corrosion Protection for Aerospace Vehicles*, Springer: 2007.

(15) Pawar, S. P.; Biswas, S.; Kar, G. P.; Bose, S. High frequency millimetre wave absorbers derived from polymeric nanocomposites. *Polymer* **2016,** *84*, 398-419.

(16) Bhattacharjee, Y.; Arief, I.; Bose, S. Recent trends in multi-layered architectures towards screening electromagnetic radiation: challenges and perspectives. *J. Mater. Chem. C* **2017,** *5* (30), 7390-7403.

(17) Ott, H. W. *Noise Reduction Techniques in Electronic Systems*, Wiley New York, 1988; Vol. 442.

(18) Chen, L.; Ong, C.; Neo, C.; Varadan, V.; Varadan, V. Microwave Theory and Techniques for Materials Characterization. . *Microwave Electronics: Measurement and Materials Characterization* **2004**, 37-141.

(19) Dhawan, S.; Ohlan, A.; Singh, K. Designing of Nano Composites of Conducting Polymers for EMI Shielding. In *Advances in Nanocomposites-Synthesis, Characterization and Industrial Applications*; InTech: 2011.

(20) Schenck, S. Apple Tipped to Give iPhone 7 Logic Board Individual-Chip Shielding. https://pocketnow.com/iphone-7-emi-shielding (accessed Mar 22, 2019).

(21) SOURCEBOOK^{TM} EMI Silicones for Sealing and Shielding in Medical Devices and Equipment. http://knowledge.sourcebookmaterials.com/emi-silicones-for-sealing-and-shielding-in-medical-devices-and-equipment (accessed Mar 22).

(22) Conet http://www.conet.in/index.php/anechoic-chambers-shielded-room-accoustic-chambers (accessed Mar 22, 2019).

(23) Parker Hannifin Corporation Latest Shielding, Thermal Management and Optical Display Technologies from Parker Chomerics at Paris Air Show. https://www.connectingindustry.com/Electronics/latest-shielding-thermal-management-and-optical-display-technologies-from-parker-chomerics-at-paris-air-show.aspx (accessed Mar 22, 2019).

(24) Nakauchi, E. Controlling the EMI Effects of Aircraft Avionics. https://www.aerospacemanufacturinganddesign.com/article/amd0415-aircraft-avionics-emi-effects/ (accessed Mar 22, 2019).

(25) Market Report Semiconductor and Electronics Market Research Reports & Consulting. https://semiconductorresearch.wordpress.com/2018/10/25/emi-shielding-market-is-expected-to-reach-7-38-billion-by-2022/ (accessed Mar 15, 2019).

(26) Laird™ EcoTouch Conductive Fabrics. https://pm.lairdtech.com/emi-shields-gaskets/metalized-conductive-fabrics/ecotouch-conductive-fabrics (accessed Mar 23, 2019).

(27) PArker Hannifin Corporation EMI Shielding. http://ph.parker.com/in/en/emi-shielding (accessed Mar 23, 2019).

(28) Spaldin, N. A. *Magnetic Materials: Fundamentals and Applications*, Cambridge University Press: Cambridge, 2010.

(29) Biswas, S.; Arief, I.; Panja, S. S.; Bose, S. Electromagnetic screening in soft conducting composite-containing ferrites: The key role of size and shape anisotropy. *Materials Chemistry Frontiers* **2017,** *1* (12), 2574-2589.

(30) Biswas, S.; Panja, S. S.; Bose, S. Physical Insight into the Mechanism of Electromagnetic Shielding in Polymer Nanocomposites Containing Multiwalled Carbon Nanotubes and Inverse-Spinel Ferrites. *J. Phys. Chem. C* **2018,** *122* (34), 19425-19437.

(31) Iqbal, S.; Shah, J.; Kotnala, R.; Ahmad, S. Highly Efficient Low Cost EMI Shielding by Barium Ferrite Encapsulated Polythiophene Nanocomposite. *J. Alloys Compd.* **2019,** *779*, 487-496.

(32) Bhattacharjee, Y.; Chatterjee, D.; Bose, S. Core–multishell heterostructure with excellent heat dissipation for electromagnetic interference shielding. *ACS Appl. Mater. Interfaces* **2018,** *10* (36), 30762-30773.

(33) Choudhary, H. K.; Kumar, R.; Pawar, S. P.; Anupama, A.; Bose, S.; Sahoo, B. Effect of Coral-Shaped Yttrium Iron Garnet Particles on the EMI Shielding Behaviour of

Yttrium Iron Garnet-Polyaniline-Wax Composites. *ChemistrySelect* **2018,** *3* (7), 2120-2130.

(34) Wang, Y.; Ni, L.-j.; Yang, F.; Gu, F.-q.; Liang, K.; Marcus, K.; Wan, Y.-d.; Chen, J.-j.; Feng, Z.-s. Facile Preparation of a High-Quality Copper Layer on Epoxy Resin via Electroless Plating for Applications in Electromagnetic Interference Shielding. *J. Mater. Chem. C* **2017,** *5* (48), 12769-12776.

(35) Lakshmi, N.; Tambe, P. EMI Shielding Effectiveness of Graphene Decorated with Graphene Quantum Dots and Silver Nanoparticles Reinforced PVDF Nanocomposites. *Compos. Interfaces* **2017,** *24* (9), 861-882.

(36) Zhou, E.; Xi, J.; Guo, Y.; Liu, Y.; Xu, Z.; Peng, L.; Gao, W.; Ying, J.; Chen, Z.; Gao, C. Synergistic Effect of Graphene and Carbon Nanotube for High-Performance Electromagnetic Interference Shielding Films. *Carbon* **2018,** *133*, 316-322.

(37) Gozzelino, L.; Gerbaldo, R.; Ghigo, G.; Laviano, F.; Truccato, M.; Agostino, A. Superconducting and Hybrid Systems for Magnetic Field Shielding. *Supercond. Sci. Technol.* **2016,** *29* (3), 034004.

(38) Denis, S.; Dusoulier, L.; Dirickx, M.; Vanderbemden, P.; Cloots, R.; Ausloos, M.; Vanderheyden, B. Magnetic Shielding Properties of High-Temperature Superconducting Tubes Subjected to Axial Fields. *Supercond. Sci. Technol.* **2007,** *20* (3), 192.

(39) Naguib, M.; Mochalin, V. N.; Barsoum, M. W.; Gogotsi, Y. 25th Anniversary Article: MXenes: A New Family of Two-Dimensional Materials. *Adv. Mater.* **2014,** *26* (7), 992-1005, DOI: doi:10.1002/adma.201304138.

(40) Shahzad, F.; Alhabeb, M.; Hatter, C. B.; Anasori, B.; Hong, S. M.; Koo, C. M.; Gogotsi, Y. Electromagnetic Interference Shielding with 2D Transition Metal Carbides (Mxenes). *Science* **2016,** *353* (6304), 1137-1140.

(41) Choi, Y.-J.; Gong, S. C.; Johnson, D. C.; Golledge, S.; Yeom, G. Y.; Park, H.-H. Characteristics of the Electromagnetic Interference Shielding Effectiveness of Al-Doped ZnO Thin Films Deposited by Atomic Layer Deposition. *Appl. Surf. Sci.* **2013,** *269*, 92-97.

(42) Yamada, T.; Morizane, T.; Arimitsu, T.; Miyake, A.; Makino, H.; Yamamoto, N.; Yamamoto, T. Application of Low Resistivity Ga-doped ZnO Films to Transparent Electromagnetic Interference Shielding Material. *Thin Solid Films* **2008,** *517* (3), 1027-1031.

(43) Kong, L.; Yin, X.; Ye, F.; Li, Q.; Zhang, L.; Cheng, L. Electromagnetic Wave Absorption Properties of ZnO-Based Materials Modified with $ZnAl_2O_4$ Nanograins. *J. Phys. Chem. C* **2013,** *117* (5), 2135-2146.

(44) Zhuo, R.; Feng, H.; Chen, J.; Yan, D.; Feng, J.; Li, H.; Geng, B.; Cheng, S.; Xu, X.; Yan, P. Multistep Synthesis, Growth Mechanism, Optical, and Microwave Absorption Properties of ZnO Dendritic Nanostructures. *J. Phys. Chem. C* **2008,** *112* (31), 11767-11775.

(45) Zhuo, R.; Qiao, L.; Feng, H.; Chen, J.; Yan, D.; Wu, Z.; Yan, P. Microwave Absorption Properties and the Isotropic Antenna Mechanism of ZnO Nanotrees. *J. Appl. Phys.* **2008,** *104* (9), 094101.

(46) Liu, J.; Cao, W.-Q.; Jin, H.-B.; Yuan, J.; Zhang, D.-Q.; Cao, M.-S. Enhanced Permittivity and Multi-Region Microwave Absorption of Nanoneedle-Like ZnO in the X-Band at Elevated Temperature. *J. Mater. Chem. C* **2015,** *3* (18), 4670-4677.

(47) Tsay, C.-Y.; Huang, Y.-H.; Hung, D.-S. Enhanced Microwave Absorption of $La_{0.7}Sr_{0.3}MnO_{3-\delta}$ Based Composites with Added Carbon Black. *Ceram. Int.* **2014,** *40* (3), 3947-3951.

(48) Li, G.; Hu, G.-G.; Zhou, H.-D.; Fan, X.-J.; Li, X.-G. Attractive Microwave-Absorbing Properties of $La_{1-x}Sr_xMnO_3$ Manganite Powders. *Mater. Chem. Phys.* **2002,** *75* (1-3), 101-104.

(49) Cheng, Y.; Dai, J.; Zhu, X.; Wu, D.; Yang, Z.; Sun, Y. Enhanced Microwave Absorption Properties of Intrinsically Core/Shell Structured $La_{0.6}Sr_{0.4}MnO_3$ Nanoparticles. *Nanoscale Res. Lett.* **2009,** *4* (10), 1153.

(50) Yang, R.; Tsay, C.; Liang, W.; Lin, C. Microwave Absorbing Properties of $La_{0.7}Sr_{0.3}MnO_3$ Composites with Negative Magnetic Susceptibility. *J. Appl. Phys.* **2010,** *107* (9), 09A523.

(51) Reshi, H. A.; Singh, A. P.; Pillai, S.; Yadav, R. S.; Dhawan, S. K.; Shelke, V. Nanostructured $La_{0.7}Sr_{0.3}MnO_3$ Compounds for Effective Electromagnetic Interference Shielding in the X-Band Frequency Range. *J. Mater. Chem. C* **2015,** *3* (4), 820-827, DOI: 10.1039/c4tc02040e.

(52) Tsay, C.; Yang, R.; Hung, D.; Hung, Y.; Yao, Y.; Lin, C. Investigation on Electromagnetic and Microwave Absorbing Properties of $La_{0.7}Sr_{0.3}MnO_{3-\delta}$/Carbon Nanotube Composites. *J. Appl. Phys.* **2010,** *107* (9), 09A502.

(53) Zhang, S.; Cao, Q. Electromagnetic and Microwave Absorption Performance of Some Transition Metal Doped $La_{0.7}Sr_{0.3}Mn_{1-x}TM_xO_{3\pm\delta}$ (TM= Fe, Co or Ni). *Materials Science and Engineering: B* **2012,** *177* (9), 678-684.

(54) Cheng, Y.; Dai, J.; Wu, D.; Sun, Y. Electromagnetic and Microwave Absorption Properties of Carbonyl Iron/$La_{0.6}Sr_{0.4}MnO_3$ Composites. *J. Magn. Magn. Mater.* **2010,** *322* (1), 97-101.

(55) Cui, K.; Cheng, Y.; Dai, J.; Liu, J. Synthesis, Characterization and Microwave Absorption Properties of $La_{0.6}Sr_{0.4}MnO_3$/Polyaniline Composite. *Mater. Chem. Phys.* **2013,** *138* (2-3), 810-816.

(56) Zhao, S.; Zheng, J.; Shi, B.; He, L.; Liu, Z. The Microwave Absorbing Properties of $La_{0.8}K_{0.2}MnO_3$ Synthesized by Sol–Gel Method. *J. Mater. Sci.: Mater. Electron.* **2017,** *28* (2), 1168-1173.

(57) Chen, Z.; Xu, C.; Ma, C.; Ren, W.; Cheng, H. M. Lightweight and Flexible Graphene Foam Composites for High-Performance Electromagnetic Interference *Adv. Mater.* **2013,** *25* (9), 1296-1300.

(58) Chung, B.; Chuah, H. Design and Construction of a Multipurpose Wideband Anechoic Chamber. *IEEE Antennas and Propagation Magazine* **2003,** *45* (6), 41-47.

(59) Koerner, C. *Integral Foam Molding of Light Metals:Technology, Foam Physics and Foam Simulation*, Springer Science & Business Media: Heidelberg, Germany, 2008.

(60) Ashby, M. F.; Evans, T.; Fleck, N. A.; Hutchinson, J.; Wadley, H.; Gibson, L. *Metal Foams: A Design Guide*, Elsevier: Amsterdam, 2000.

(61) Okolieocha, C.; Raps, D.; Subramaniam, K.; Altstädt, V. Microcellular to Nanocellular Polymer Foams:Progress(2004–2015) and Future Directions–A Review. *Eur. Polym. J.* **2015,** *73*, 500-519.

(62) Yang, Y.; Gupta, M. C.; Dudley, K. L.; Lawrence, R. W. Novel Carbon Nanotube−Polystyrene Foam Composites for Electromagnetic Interference Shielding. *Nano Lett.* **2005,** *5* (11), 2131-2134.

(63) Li, Y.; Shen, B.; Pei, X.; Zhang, Y.; Yi, D.; Zhai, W.; Zhang, L.; Wei, X.; Zheng, W. Ultrathin Carbon Foams for Effective Electromagnetic Interference Shielding. *Carbon* **2016,** *100*, 375-385.

(64) Liu, P.; Qing, H.; Hou, H.; Wang, Y.; Zhang, Y. EMI Shielding and Thermal Conductivity of a High Porosity Reticular Titanium Foam. *Mater. Des.* **2016,** *92*, 823-828.

(65) Xu, Z.; Hao, H. Electromagnetic Interference Shielding Effectiveness of Aluminum Foams with Different Porosity. *J. Alloys Compd.* **2014,** *617*, 207-213.

(66) Ma, J.; Zhan, M.; Wang, K. Ultralightweight Silver Nanowires Hybrid Polyimide Composite Foams for High-Performance Electromagnetic Interference Shielding. *ACS Appl. Mater. Interfaces* **2014,** *7* (1), 563-576.

(67) Ling, J.; Zhai, W.; Feng, W.; Shen, B.; Zhang, J.; Zheng, W. g. Facile Preparation of Lightweight Microcellular Polyetherimide/Graphene Composite Foams for Electromagnetic Interference Shielding. *ACS Appl. Mater. Interfaces* **2013,** *5* (7), 2677-2684.

(68) Ameli, A.; Nofar, M.; Wang, S.; Park, C. B. Lightweight Polypropylene/Stainless-Steel Fiber Composite Foams with Low Percolation for Efficient Electromagnetic Interference Shielding. *ACS Appl. Mater. Interfaces* **2014,** *6* (14), 11091-11100.

(69) Thomassin, J.-M.; Jerome, C.; Pardoen, T.; Bailly, C.; Huynen, I.; Detrembleur, C. Polymer/Carbon Based Composites as Electromagnetic Interference (EMI) Shielding Materials. *Materials Science and Engineering: R: Reports* **2013,** *74* (7), 211-232.

(70) Parker Hannifin Corporation CHO-SHIELD® 610 Electrically Conductive Silver Plated Copper Epoxy EMI Coating.

http://www.parker.com/Literature/Chomerics/Parker%20Chomerics%20CHO-SHIELD%20610.pdf (accessed Mar 22, 2019).

(71) Jin, F.-L.; Li, X.; Park, S.-J. Synthesis and Application of Epoxy Resins: A Review. *J. Ind. Eng. Chem.* **2015,** *29*, 1-11.

(72) Mittal, V.; Saini, R.; Sinha, S. Natural Fiber-Mediated Epoxy Composites–A Review. *Composites Part B: Engineering* **2016,** *99*, 425-435.

(73) Yang, C.-F.; Wang, L.-F.; Wu, S.-M.; Su, C.-C. Characterization and Curing Kinetics of Epoxy/Silica Nano-Hybrids. *Materials* **2015,** *8* (10), 7032-7040.

(74) Azeez, A. A.; Rhee, K. Y.; Park, S. J.; Hui, D. Epoxy Clay Nanocomposites–Processing, Properties and Applications: A Review. *Composites Part B: Engineering* **2013,** *45* (1), 308-320.

(75) Hu, Y.; Du, G.; Chen, N. A Novel Approach for Al_2O_3/Epoxy Composites with High Strength and Thermal Conductivity. *Compos. Sci. Technol.* **2016,** *124*, 36-43.

(76) Barua, S.; Chattopadhyay, P.; Aidew, L.; Buragohain, A. K.; Karak, N. Infection-Resistant Hyperbranched Epoxy Nanocomposite as a Scaffold for Skin Tissue Regeneration. *Polym. Int.* **2015,** *64* (2), 303-311.

(77) Liang, J.; Wang, Y.; Huang, Y.; Ma, Y.; Liu, Z.; Cai, J.; Zhang, C.; Gao, H.; Chen, Y. Electromagnetic Interference Shielding of Graphene/Epoxy Composites. *Carbon* **2009,** *47* (3), 922-925.

(78) Huang, Y.; Li, N.; Ma, Y.; Du, F.; Li, F.; He, X.; Lin, X.; Gao, H.; Chen, Y. The Influence of Single-Walled Carbon Nanotube Structure on the Electromagnetic Interference Shielding Efficiency of Its Epoxy Composites. *Carbon* **2007,** *45* (8), 1614-1621.

(79) Im, J. S.; Park, I. J.; In, S. J.; Kim, T.; Lee, Y.-S. Fluorination Effects of MWCNT Additives for EMI Shielding Efficiency by Developed Conductive Network in Epoxy Complex. *J. Fluorine Chem.* **2009,** *130* (12), 1111-1116.

(80) Nam, I.; Lee, H.; Jang, J. Electromagnetic Interference Shielding/Absorbing Characteristics of CNT-Embedded Epoxy Composites. *Composites, Part A* **2011,** *42* (9), 1110-1118.

(81) Han, Y.; Lin, J.; Liu, Y.; Fu, H.; Ma, Y.; Jin, P.; Tan, J. Crackle Template Based Metallic Mesh with Highly Homogeneous Light Transmission for High-Performance Transparent EMI Shielding. *Sci. Rep.* **2016,** *6*, 25601.

(82) Kim, M.-H.; Joh, H.; Hong, S.-H.; Oh, S. J. Coupled Ag Nanocrystal-Based Transparent Mesh Electrodes for Transparent and Flexible Electro-Magnetic Interference Shielding Films. *Curr. Appl. Phys.* **2019,** *19* (1), 8-13.

(83) Han, Y.; Zhong, H.; Liu, N.; Liu, Y.; Lin, J.; Jin, P. In Situ Surface Oxidized Copper Mesh Electrodes for High-Performance Transparent Electrical Heating and Electromagnetic Interference Shielding. *Adv. Electron. Mater.* **2018,** *4* (11), 1800156.

(84) Han, Y.; Liu, Y.; Han, L.; Lin, J.; Jin, P. High-Performance Hierarchical Graphene/Metal-Mesh Film for Optically Transparent Electromagnetic Interference Shielding. *Carbon* **2017,** *115*, 34-42.

(85) Snoek, J. Dispersion and Absorption in Magnetic Ferrites at Frequencies Above One Mc/s. *Physica* **1948,** *14* (4), 207-217.

(86) Wei, J.; Zhang, Z.; Wang, B.; Wang, T.; Li, F. Microwave Reflection Characteristics of Surface-Modified $Fe_{50}Ni_{50}$ Fine Particle Composites. *J. Appl. Phys.* **2010,** *108* (12), 123908.

(87) Feng, Y.; Qiu, T. Enhancement of Electromagnetic And Microwave Absorbing Properties of Gas Atomized Fe-50 wt% Ni Alloy by Shape Modification. *J. Magn. Magn. Mater.* **2012,** *324* (16), 2528-2533.

(88) Liu, J.; Feng, Y.; Qiu, T. Synthesis, Characterization, and Microwave Absorption Properties of Fe–40 wt% Ni Alloy Prepared by Mechanical Alloying and Annealing. *J. Magn. Magn. Mater.* **2011,** *323* (23), 3071-3076.

(89) Sun, Y.; Pan, Z.; Long, H.; Or, S. W.; Ho, S.; Feng, C.; Liu, X. Urchin-Like Ni Microspherical Structure with Enhanced Magnetic Loss for Thin Microwave Absorber at Gigahertz. *Nano* **2017,** *12* (03), 1750034.

(90) Tong, G.; Yuan, J.; Wu, W.; Hu, Q.; Qian, H.; Li, L.; Shen, J. Flower-like Co superstructures: Morphology and phase evolution mechanism and novel microwave electromagnetic characteristics. *CrystEngComm* **2012,** *14* (6), 2071-2079.

(91) Zhao, Y.; Liu, L.; Jiang, K.; Fan, M.; Jin, C.; Han, J.; Wu, W.; Tong, G. Distinctly enhanced permeability and excellent microwave absorption of expanded graphite/Fe_3O_4 nanoring composites. *RSC Adv.* **2017,** *7* (19), 11561-11567.

(92) Wang, Z.; Zuo, Y.; Yao, Y.; Xi, L.; Du, J.; Wang, J.; Xue, D. Microwave absorption properties of amorphous iron nanostructures fabricated by a high-yield method. *J. Phys. D: Appl. Phys.* **2013,** *46* (13), 135002.

(93) Wang, X.; Liu, Y.; Han, H.; Mølhave, K.; Sun, H. Enhanced high-frequency microwave absorption of Fe_3O_4 architectures based on porous nanoflake. *Ceram. Int.* **2017,** *43* (17), 16013-16017.

(94) Ni, S.; Lin, S.; Pan, Q.; Yang, F.; Huang, K.; He, D. Hydrothermal synthesis and microwave absorption properties of Fe_3O_4 nanocrystals. *J. Phys. D: Appl. Phys.* **2009,** *42* (5), 055004.

(95) Sun, G.; Dong, B.; Cao, M.; Wei, B.; Hu, C. Hierarchical dendrite-like magnetic materials of Fe_3O_4, γ-Fe_2O_3, and Fe with high performance of microwave absorption. *Chem. Mater.* **2011,** *23* (6), 1587-1593.

(96) Lu, B.; Dong, X.; Huang, H.; Zhang, X.; Zhu, X.; Lei, J.; Sun, J. Microwave absorption properties of the core/shell-type iron and nickel nanoparticles. *J. Magn. Magn. Mater.* **2008,** *320* (6), 1106-1111.

(97) Guo, Y.; Dong, S.; Liu, S.; Cheng, Y.; Zhang, Z.; Wang, H. Fabrication of porous disk-like Ni/NiO microwave absorber and its excellent broad frequency absorption performance. *J. Alloys Compd.* **2018,** *731*, 143-149.

(98) Wu, H.; Wu, G.; Wang, L. Peculiar porous α-Fe_2O_3, γ-Fe_2O_3 and Fe_3O_4 nanospheres: facile synthesis and electromagnetic properties. *Powder Technol.* **2015,** *269*, 443-451.

(99) Wang, A.; Wang, W.; Long, C.; Li, W.; Guan, J.; Gu, H.; Xu, G. Facile preparation, formation mechanism and microwave absorption properties of porous carbonyl iron flakes. *J. Mater. Chem. C* **2014,** *2* (19), 3769-3776.

(100) Tong, G.-X.; Wu, W.-H.; Hu, Q.; Yuan, J.-H.; Qiao, R.; Qian, H.-S. Enhanced electromagnetic characteristics of porous iron particles made by a facile corrosion technique. *Mater. Chem. Phys.* **2012,** *132* (2-3), 563-569.

(101) Li, X.; Guo, X.; Liu, T.; Zheng, X.; Bai, J. Shape-controlled synthesis of Fe nanostructures and their enhanced microwave absorption properties at L-band. *Mater. Res. Bull.* **2014,** *59*, 137-141.

(102) Yang, R.-B.; Liang, W.-F. Microwave properties of high-aspect-ratio carbonyl iron/epoxy absorbers. *J. Appl. Phys.* **2011,** *109* (7), 07A311.

(103) Li, W.; Zhou, X.; Ying, Y.; Jiang, L.; Che, S. Particle thickness effect on electromagnetic properties of flake-shaped FeNi alloy. *physica status solidi (a)* **2015,** *212* (12), 2944-2950.

(104) Andersson, C. Yarn handleability and weft insert warp knit non-crimp fabrics Proc. *TECHCOMP-2* **1994,** *13*.

(105) Zhao, H.; Hou, L.; Bi, S.; Lu, Y. Enhanced X-Band Electromagnetic-Interference Shielding Performance of Layer-Structured Fabric-Supported Polyaniline/Cobalt–Nickel Coatings. *ACS Appl. Mater. Interfaces* **2017,** *9* (38), 33059-33070.

(106) Wang, Y.; Wang, W.; Yu, D. Three-phase heterostructures f-$NiFe_2O_4$/PANI/PI EMI shielding fabric with high Microwave Absorption Performance. *Appl. Surf. Sci.* **2017,** *425*, 518-525.

(107) Jiyong, H.; Guohao, L.; Junhui, S.; Xudong, Y.; Xin, D. Improving the electromagnetic shielding of nickel/polyaniline coated polytrimethylene-terephthalate knitted fabric by optimizing the electroless plating conditions. *Text. Res. J.* **2017,** *87* (8), 902-912.

(108) Zhao, H.; Hou, L.; Lu, Y. Electromagnetic interference shielding of layered linen fabric/polypyrrole/nickel (LF/PPy/Ni) composites. *Mater. Des.* **2016,** *95*, 97-106.

(109) Edison, T. A. Electric lamp. US Patent 223,898, 1880.

(110) Morgan, P. *Carbon fibers and their composites*, CRC press: 2005.

(111) Hong, X.; Chung, D. Carbon nanofiber mats for electromagnetic interference shielding. *Carbon* **2017,** *111*, 529-537.

(112) Xing, D.; Lu, L.; Teh, K. S.; Wan, Z.; Xie, Y.; Tang, Y. Highly flexible and ultra-thin Ni-plated carbon-fabric/polycarbonate film for enhanced electromagnetic interference shielding. *Carbon* **2018,** *132*, 32-41.

(113) Zhan, Y.; Long, Z.; Wan, X.; Zhang, J.; He, S.; He, Y. 3D carbon fiber mats/nano-Fe_3O_4 hybrid material with high electromagnetic shielding performance. *Appl. Surf. Sci.* **2018,** *444*, 710-720.

(114) Chen, L.; Yin, X.; Fan, X.; Chen, M.; Ma, X.; Cheng, L.; Zhang, L. Mechanical and electromagnetic shielding properties of carbon fiber reinforced silicon carbide matrix composites. *Carbon* **2015,** *95*, 10-19.

(115) Yuan, L.; Xiangxuan, L.; Rong, L.; Wu, W.; Xuanjun, W. Design and fabrication of carbon fiber/carbonyl iron core–shell structure composites as high-performance microwave absorbers. *RSC Adv.* **2015,** *5* (12), 8713-8720.

(116) Min, D.; Zhou, W.; Qing, Y.; Luo, F.; Zhu, D. Highly oriented flake carbonyl iron/carbon fiber composite as thin-thickness and wide-bandwidth microwave absorber. *J. Alloys Compd.* **2018,** *744*, 629-636.

Chapter 2

$La_{0.5}Sr_{0.5}CoO_{3-\delta}$-Epoxy Composites and their Surface Modification Strategies for Effective EMI Shielding

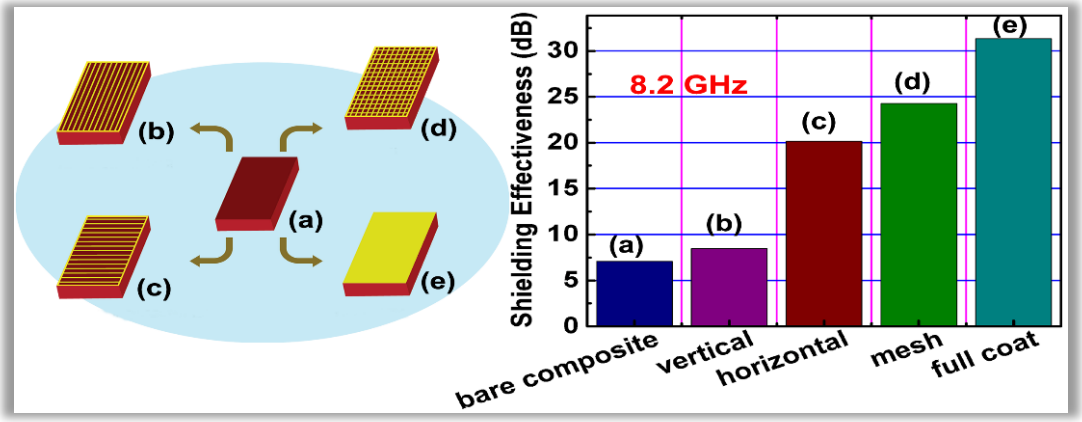

This chapter gives insight into the conducting perovskite $La_{0.5}Sr_{0.5}CoO_{3-\delta}$ and its epoxy composite for electromagnetic interference (EMI) shielding characteristics in the X and Ku-band (8.2-18 GHz), with special emphasis on their thermal, mechanical and dielectric properties. Perovskite $La_{0.5}Sr_{0.5}CoO_{3-\delta}$ are investigated for the first time and got excellent shielding effectiveness in the range of 35-42 dB, with 99.9 % of attenuation. The absorption dominant shielding mechanism is mainly attributed to the good conductivity values of $La_{0.5}Sr_{0.5}CoO_{3-\delta}$. When it was composited with epoxy for coating shield applications, the EMI shielding values plunged down to 10 dB, measured at 10 GHz. To augment the level of shielding, we have introduced a strategy of screen printing predesigned silver (Ag) patterns on top surface of the composite sheets. It resulted in a dramatic 4-fold improvement in their EMI shielding effectiveness, with significant enhancements in the reflection and absorption shielding efficiency of the composite. Compared to the conventional way of blending silver to form epoxy-silver 0-3 composite above percolation, the present method of screen printing needs only lesser amount of the conductor to generate a maximum shielding efficiency of 99 %, with considerable easiness of processing.

2.1 Thermophysical and Microwave Shielding Properties of $La_{0.5}Sr_{0.5}CoO_{3-\delta}$ and Its Composite with Epoxy

2.1.1 Introduction

As far as EMI shielding is concerned, the widely used materials were metals, due to their high electrical conductivity and reflectivity. Besides oxidation issues, their major disadvantages are poor wear and corrosion resistance.[1] Metal based EMI solutions are significantly heavy too. To overcome these problems, researchers have developed a series of conducting polymers and conducting oxides, fabricated in composite form. However, most of the conducting polymers suffer from stability and solubility issues that require the introduction of solubilizing substituents, which can further complicate the synthesis. To achieve effective EMI shielding, a widely accepted strategy is to develop various conductive fillers which can be conjugated with a polymer to get a processable composite form. So far as EMI shielding applications are concerned, metal based fillers in composites are becoming less attractive these days since they are heavy and stringent synthesizing conditions are required to control oxidation of the fillers. However, in real applications, the inclusion of metals in composite structures might cause problems due to the thermal expansivity difference between the metal and matrix. Oxide conductors have an advantage in this regard since they are free from oxidation-related issues. There were of course a few reports on semiconducting metal oxides, which are found useful in EMI shielding applications.[2-5] However, despite possessing relatively high electrical conductivity, research on perovskite structured protonic conductors is largely a grey area where not even a single material was qualified for promising EM wave absorber applications.

Against this background, we have taken up a detailed investigation on the development of an all oxide EMI shielding solution based on the perovskite structured $La_{0.5}Sr_{0.5}CoO_{3-\delta}$ (LSCO). It should be noted that the moderately high electrical conductivity (~1000 S/cm) for its cubic crystalline phase makes it suitable for various applications.[6,7] Obviously, this type of perovskite oxides were traditionally used for specific applications such as cathode material in solid oxide fuel cells,[8] catalyst in Li-air batteries,[9–11] oxygen separation membranes,[12] sensor materials[13,14] and so forth, but seldom used in EMI shielding applications. In the present investigation, for the purpose of further enhancing the applicability of LSCO as a mouldable coating, we have made a composite between LSCO and epoxy, by homogeneously dispersing the conducting oxide phase in the epoxy matrix. The epoxy resin was chosen from a galaxy of thermosetting polymers, because it has the advantage of high mechanical strength, water resistance and low cure shrinkage, besides enhanced processability. The correlation between electrical properties and EMI shielding of LSCO ceramic is probed in the present investigation. Further, the microstructure, thermal, mechanical, electrical and microwave dielectric properties of LSCO loaded-epoxy composites, along with EMI shielding effectiveness, were also investigated in this report.

2.1.2 Materials and Methods

LSCO ceramic powder was prepared by conventional solid-state reaction route. The constituent chemicals La_2O_3, $SrCO_3$ and Co_2O_3, (Aldrich, 99 %) were weighed stoichiometrically and mixed thoroughly in distilled water through ball milling using zirconia balls as the milling media, for 24 h. The uniform slurry, dried in a hot air oven at 100 ^oC, was pre-calcined at 800 ^oC for 2 h in a furnace followed by calcination at 1100 ^oC for 4 h. The phase pure LSCO powder was then ball milled again using zirconia balls, for 48 h. The

composite was prepared using a motorized mechanical stirrer by mixing LSCO powder with the room temperature curable epoxy resin (Huntsman resins; Araldite® GY 260) for 30 min in a steel vessel. Before proceeding to the next step of addition of curing agent, there involved a degassing procedure to eliminate the entrapped gas in the LSCO-epoxy matrix. Further step involved the addition of amine-based curing agent (Aradur® 1012) to the degassed matrix. The ratio of epoxy resin to the curing agent was kept to be in the ratio of 10:2.5 as suggested by the manufacturer. After thoroughly mixing the curing agent with the LSCO-epoxy matrix, it was then transferred to appropriate mould and kept at room temperature for 24 h for complete curing.

The phase formation and crystal structure of the LSCO ceramic were identified by X-ray diffraction analysis (PANalyticalX'Pert PRO diffractometer having Nickel filtered CuKα, Netherlands). The microstructure of the composites was analysed using a scanning electron microscope (SEM) (Jeol Model, JSM 5600LV). The DC conductivity of the samples was measured using four probe method, using a current source Aplab 9710 P and nanovoltmeter Keithley 2182 A. The EMI shielding testing was done using rectangular transmission waveguides operating at X (8.2–12.4 GHz) and Ku-bands (12.4–18 GHz). The dimension of samples for microwave characterisation at X-band is 22.86 x 10.10 mm, while that for Ku-band is 15.80 x 7.90 mm. The appropriately machined samples were inserted into the waveguide that was coupled to a vector network analyzer (Agilent E5071C). The error in microwave dielectric measurements using waveguide method is estimated to be between 3 and 5 %. Proper calibrations were performed prior to the measurement, in order to eliminate the errors due to directivity, source match, load match etc. The magnitude of complex scattering parameters (S_{11} and S_{21}) of these composites was measured using vector network analyzer.

From the measured S_{11} and S_{21} parameters, absorption shielding effectiveness (SE_A), reflection shielding effectiveness (SE_R) and the total EMI shielding effectiveness (SE_T), were calculated. The complex permittivity at microwave frequencies was determined using Agilent software 85071E from the measured scattering parameters. The thermal expansion measurements of the composites in the present work were performed using thermo mechanical analyser (SII Nanotechnology Inc., Tokyo, Japan). Thermal conductivity of the samples was measured by the laser flash technique[15] using thermal conductivity analyzer (Flash Line TM2000, Anter Corporation, USA). Mechanical tests were performed by a universal testing machine (Instron 5500 R Universal Testing Machine, USA) at a constant crosshead speed of 2 mm min^{-1}.

2.1.3 Results and Discussion

2.1.3.1 Structural, Electrical and EMI Shielding Properties of LSCO

The conducting oxide used in the present investigation, $La_{1-x}Sr_xCoO_{3-\delta}$ is a derivative of $LaCoO_3$ that belongs to the group of ABO_3 perovskites, with a trivalent rare earth in the A site (La) and a trivalent metal ion in the B site (Co). When the trivalent La^{3+} ions in $LaCoO_3$ are partially replaced by divalent Sr^{2+} ions to form $La_{1-x}Sr_xCoO_{3-\delta}$, an excess positive charge is generated. Because the Co^{z+} ions can have a different oxidation state, the charge neutrality is maintained by the formation of oxygen vacancies resulting in a change in the valence state of the Co^{z+} ions. Therefore, the complex oxide is believed to have an oxygen deficiency δ, due to the effect of oxygen vacancy mechanism. As the Sr doping reaches molarity level of $x > 0.4$ in $La_{1-x}Sr_xCoO_3$, there is a predominant change in crystal structure from rhombohedral to cubic. Fig. 2.1 (a) shows the X-ray diffraction (XRD) pattern of synthesized $La_{0.5}Sr_{0.5}CoO_{3-\delta}$ powder calcined at 1100 ^oC for 4 h. All the detected diffraction peaks of samples calcined at 1100 ^oC are indexed, indicating a complete formation of the phase $La_{0.5}Sr_{0.5}CoO_{3-\delta}$ (JCPDS: 48-0122).

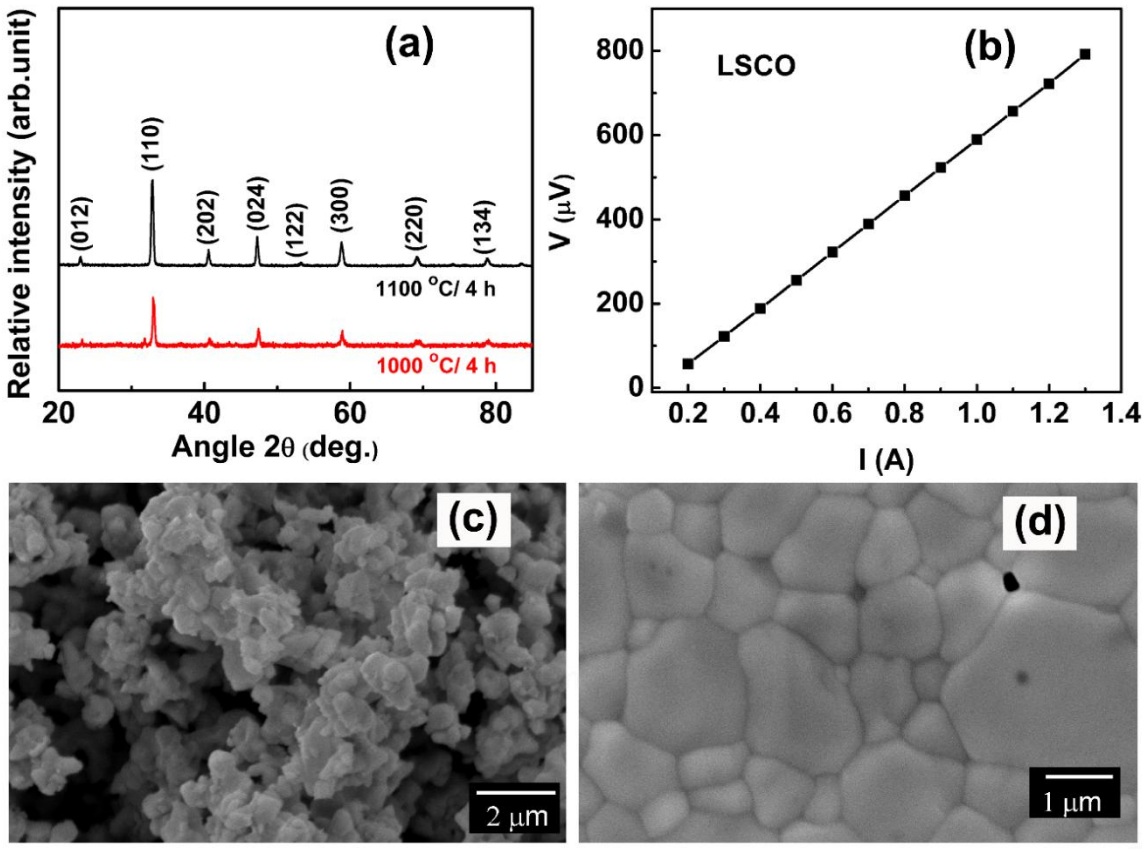

Fig. 2.1: (a) X- ray diffraction pattern of $La_{0.5}Sr_{0.5}CoO_{3-\delta}$ (LSCO) calcined at 1000 ºC and 1100 ºC, (b) I-V plot of sintered LSCO at room temperature, (c) and (d) SEM micrographs of calcined LSCO powder and the polished surface of sintered LSCO sheet.

LSCO, due to its desirable electrical properties and structural compatibility with ferroic perovskite oxides, has been widely used as an electrode material. In this investigation we have tested the dc electrical characteristics of sintered LSCO ceramics at room temperature. From the slope of the I-V plot, the resistance (R) value is obtained and the conductivity could be derived from the relation,

$$\sigma = \frac{l}{RA} \tag{2.1}$$

As given in I-V plot of Fig. 2.1(b), its apparent electrical conductivity is found to be in the range of 1400 S/cm, which is obviously two order less than the most conducting metals.[16,17]

The specific composition $La_{0.5}Sr_{0.5}CoO_{3-\delta}$, was previously reported to have moderately high electronic conductivity (>1000 S/cm). Its metallic behaviour can be explained based on the existence of an overlapped electron band structure in the Co-O-Co bond, as suggested by the itinerant electron model.[18,19] In order to investigate the EMI shielding properties of LSCO we used sintered LSCO blocks having precise dimension to fit to the wave guide port. The calcined LSCO powder was ground for one day in a tumbling ball mill and the average particle size of the ground LSCO powder is found to be 0.4-0.5 μm (see Fig. 2.1(c)). The ground LSCO powder was then pressed in a hydraulic press at 150 MPa in a 40 × 40 mm die. The LSCO sheets thus obtained were sintered in furnace at 1150 ^{o}C for 4 h, yielding 95 % dense sintered bodies. The SEM image of polished surface of the sintered LSCO sheet is shown in Fig. 2.1(d).

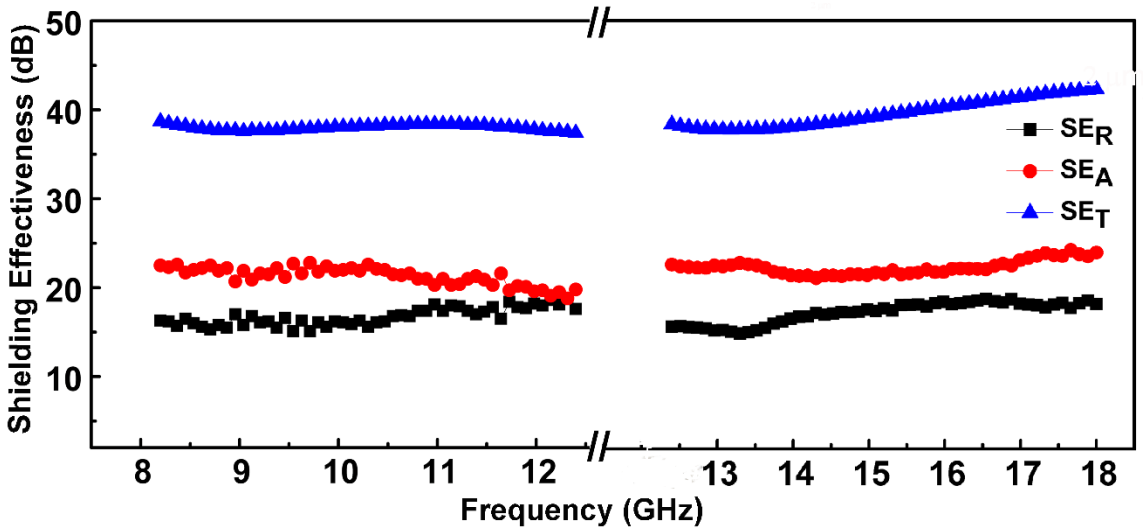

Fig. 2.2: The frequency dependent variation of total shielding effectiveness (SE_T), reflection shielding effectiveness (SE_R) and absorption shielding effectiveness (SE_A) of sintered LSCO at X and Ku band.

When an electromagnetic wave passes through a material, some part of it gets reflected, some get absorbed, while a part of it undergoes multiple internal reflections between various

filler components dispersed in a matrix.[20] The primary mechanism of EMI shielding is reflection where the shield must have mobile charge carriers (electrons or holes) that interact with the electromagnetic fields in the radiation. For significant absorption of radiation, which is considered as the secondary mechanism of EMI shielding, the shield should have electric and/or magnetic fillers that interact with the electromagnetic fields in the radiation. Thus, the total shielding effectiveness is the sum of reflection and absorption shielding effectiveness and the relation connecting these parameters are commonly presented in literature.[21,22] The reflection shielding efficiency, SE_R, and Absorption shielding efficiency, SE_A, are calculated using the scattering parameters S_{11} and S_{12} as given below;[23]

$$SE_R = -10\log(1 - {S_{11}}^2) \tag{2.2}$$

$$SE_A = -10\log\left(\frac{{S_{12}}^2}{1-{S_{11}}^2}\right) \tag{2.3}$$

and the total shielding effectiveness, $SE_T = SE_R + SE_A + SE_M$ (2.4)

Since the SE_T of LSCO is high, the contribution of SE_M is negligible and the final equation will be, $SE_T = SE_R + SE_A$ (2.5)

Interestingly, the EM wave shielding effectiveness of sintered LSCO samples were observed to be in the range of 35-42 dB, as shown in Fig. 2.2. Here, the inherent nature of high conductivity of LSCO plays a major role in achieving such a high value of shielding effectiveness. An SE_A value in the range of 20-30 dB itself depicts the absorption efficiency above 99 %, which is good for absorption based shielding applications. A relation connecting SE_A, SE_R, conductivity, frequency, permeability and thickness is shown.[24,25]

$$SE_R = -10log_{10}\left(\frac{\sigma}{16\varepsilon\omega\mu}\right) \quad (2.6)$$

$$SE_A = -8.68t\left(\sqrt{\frac{\sigma\omega\mu}{2}}\right) \quad (2.7)$$

While looking at the conductivity (σ) parameter in equations (2.6) and (2.7), it can be elucidated that the change in the conductivity value has a major influence to the SE_A value than SE_R value. From the above relation, we can state that the absorption dominant shielding effectiveness for LSCO sheet were due to the direct relation between the conductivity and SE_A. Noteworthy is the fact that a total shielding above 20 dB is well acceptable for practical EMI shielding application. In the present study, all the tested EMI shielding structures have a normalized thickness of 2 mm. Achieving a high shielding effectiveness above 35 dB means that 99.9 % of the incident radiation is getting attenuated.

2.1.3.2 Microstructure of the LSCO-Epoxy Composites

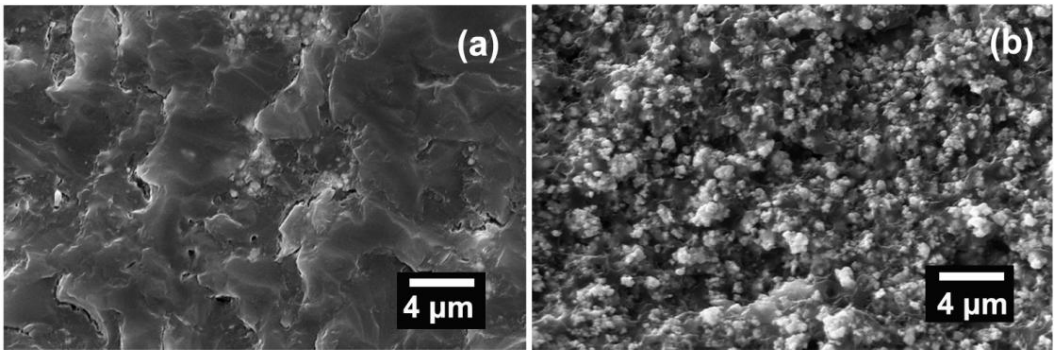

Fig. 2.3: SEM micrographs of fractured section of composite containing 10 wt. % LSCO and 70 wt. % LSCO filler

This high shielding LSCO powder has been employed in developing a light weight and easily processable shielding structure by adopting a composite approach with epoxy matrix. In the present investigation, the chosen polymer is a thermosetting epoxy resin, which has

proven advantages like weight reduction, design freedom, cost effectiveness and good physical properties like corrosion resistance as well as high strength to weight ratio. The composites were prepared by mixing different weight loading of LSCO powder (10-70 wt. %) to the epoxy matrix. The SEM micrograph in Fig. 2.3(a) shows fractured surface of least loaded (10 wt. %) composite, marked by more distinct dispersion of the filler. On the other hand Fig. 2.3(b) shows the fractogram of the maximum loaded epoxy (70 wt. % LSCO), in which there is enough evidence for some agglomeration of filler particles.

2.1.3.3 Thermophysical Properties of the Composites

High density electronic devices expand on significant heat build-up, which can compromise the performance and lifetime of computing devices and network systems. Thermo-mechanical management of composites are very critical for composites with good EMI shielding where high thermal conductivity is preferred to dispel away the heat generated. However, it is well-known that thermal conductivity of a composite depends on factors like polymer-filler interaction as well as filler characteristics, namely type and shape of the filler. In the present investigation, thermal conductivity (*TC*) of the LSCO-epoxy composites were computed using the relation $TC = \lambda \times C_p \times \rho$ where λ is the thermal diffusivity, C_p is the specific heat capacity at room temperature, and ρ is the density of the sample.[26,27] As seen in Fig. 2.4(a), the *TC* of the composite shows a gradual increment with the LSCO filler addition. This is understandable since the *TC* of pure epoxy is 0.25 W/m.K, which gets improved by 2.5 folds with the incorporation of 70 wt. % of filler $La_{0.5}Sr_{0.5}CoO_{3-\delta}$ that has higher reported *TC*.[28] Interestingly, the increment in *TC* is more predominant after 40 wt. % of LSCO addition. It is believed that more the amount of LSCO particles in the epoxy matrix, that forms an inter linking network that can sufficiently exchange the heat energy along the shorter interfaces.

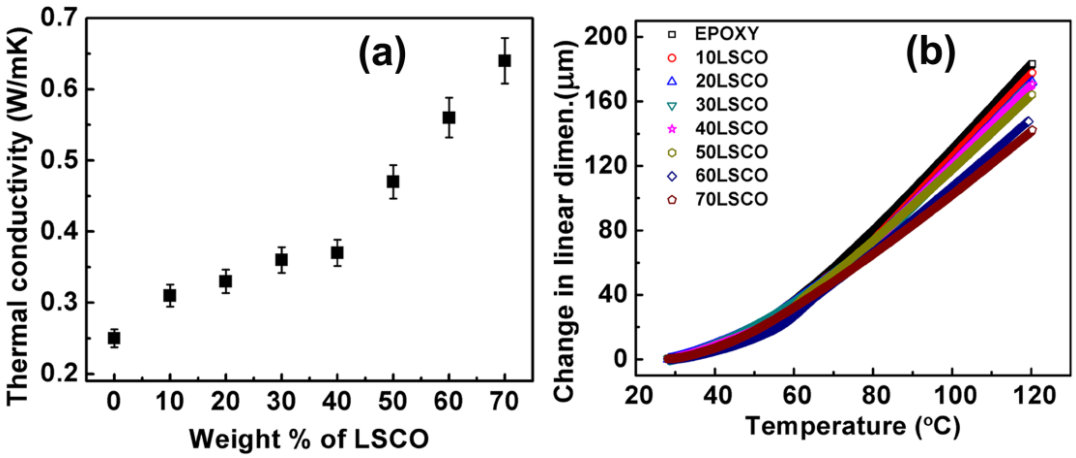

Fig. 2.4: (a) Thermal conductivity and (b) thermal expansion behaviour of various weight loaded LSCO-epoxy composite.

Table 2.1: The variation of CTE with weight loading of LSCO before and after glass transition temperature.

CTE of Epoxy-LSCO composite (ppm/°C)		
Wt. % of LSCO	**before T_g**	**after T_g**
0	76.9	181.1
10	75.0	178.0
20	73.2	176.0
30	71.1	174.0
40	69.5	168.0
50	62.2	160.0
60	53.4	154.0
70	67.8	132.0

Usually, polymers are likely to possess large coefficients of thermal expansion (*CTE*) in comparison to metals, semiconductors and ceramics. In real applications, the widely accepted strategy is to fabricate a 0-3 composite between the polymer and ceramic filler to tailor the high *CTE* of polymers, which can effectively manage the thermal stress. The mean *CTE* was computed by the equation, $CTE = \frac{l_2 - l_1}{l_0(T_2 - T_1)}$ where l_0 is initial length and l_1 and l_2

are the changes in length at temperatures T_1 and T_2, respectively. Fig. 2.4(b) shows the change in linear dimension of the composite with LSCO addition, as a function of temperature. In principle, uncured epoxy resins are noted for poor mechanical, chemical and heat resistance properties which usually improve upon curing with suitable curatives, thereby forming three-dimensional cross-linked thermoset structures. The glass transition temperature (T_g) of the linear epoxy resin used in the present study is 64.2 ^oC, obtained from the Fig. 2.4(b). The ultimate T_g of epoxy resin is influenced by several factors such as the chemical structure of the epoxy resin, the type of hardener used, the degree of cure etc. In *CTE* plots involving glass transition, the plot consists of two stages, characterized by different slopes: (i) thermal expansion before T_g (30-50 ^oC) and (ii) after T_g (80-120 ^oC). In both stages, the value of *CTE* is found to be decreasing with filler content. The calculated values of *CTE* of the composites were tabulated in Table 2.1. At lower temperatures, the value of *CTE* for LSCO loaded epoxy gradually decreases from 77 to 53 ppm/^oC with respect to the filler loading from 0 to 60 wt. % and at the maximum loading the value of *CTE* increased to 68 ppm/^oC which may be attributed to the agglomeration of filler particles. When the filler loading increases, the LSCO particles tend to agglomerate which results in the reduction of the interfacial area between LSCO and epoxy. The decrease in the interfacial area results in higher thermal expansion coefficient for highly loaded epoxy matrix.[29] Beyond T_g where it is believed that the mobility of the polymer chains increase significantly, the *CTE* varies from 181 to 133 ppm/^oC (Table 2.1). In general, with increasing amount of LSCO filler loading, the *CTE* is found to be gradually decreasing. This is due to the lower *CTE* of LSCO (which is about 16 ppm/^oC)[30] and increase in the interfacial area between the LSCO and epoxy matrix, which may pose restriction to the heat induced expansion of epoxy chain. The interface between filler and epoxy also have a crucial

role in transmitting the thermal stresses which can result in a reduction in the expansion of the matrix.[31]

2.1.3.4 Mechanical Properties of the Composite

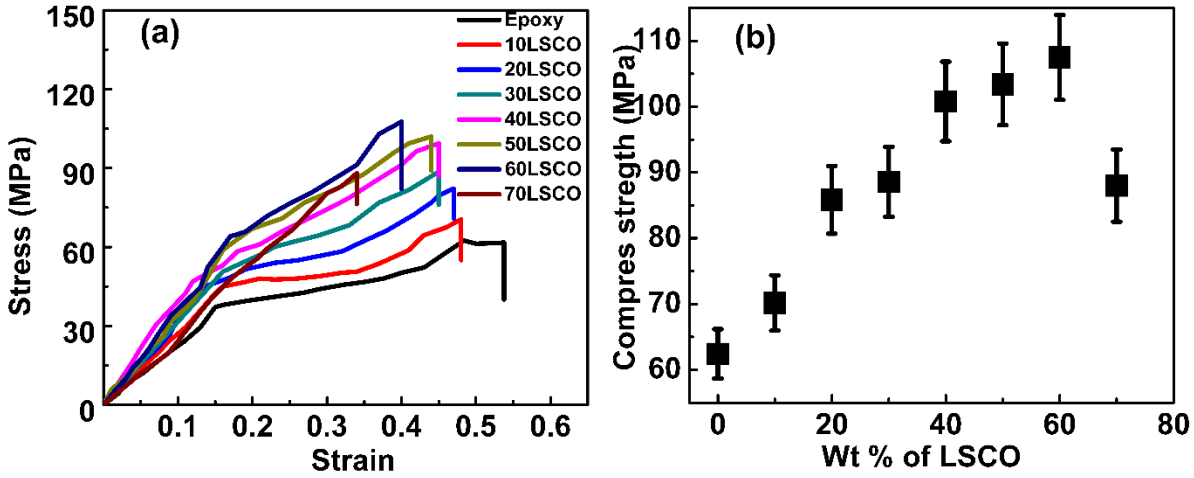

Fig. 2.5: (a) Stress-strain curves of LSCO-epoxy with varying weight loading of LSCO and (b) variation of compressive strength with weight loading of LSCO.

The strain behaviour of various epoxy-LSCO composites subjected to increasing compressive strains, is plotted in Fig. 2.5(a). Fig. 2.5(b) shows the compressive strength plotted as a function of the filler loading. The compressive strength of the composite is found to be improving with addition of filler. As shown, the stress-strain curve is slightly non-linear and mechanical failure occurs catastrophically in all cases. The pure epoxy has a compressive strength of 62 MPa which gets modified to 107 MPa with 60 wt. % LSCO loading. It is assumed that the interfacial bonding between the LSCO ceramic particles and the polymer matrix is strong enough and therefore, the ceramic could provide an efficient stress transfer to the matrix. This in turn causes an increase in the mechanical strength of the composites with increasing LSCO filler loading.[32] It should be noted that the mechanical strength need not increase proportionately for all ratios of filler loading. However, we observed a fall in the

compressive strength with higher filler loading (70 wt. %) that may have arisen from the chance for non-wettability of few filler particles which were agglomerated in the matrix, which are visible in the microscopic images also (see Fig. 2.3(b)). In this challenging case, the LSCO particles inside the agglomerates are not in direct contact with the epoxy matrix and thereby not involved in the reinforcement of the epoxy matrix.

2.1.3.5 AC Electrical Properties at Microwave Bands

Since the rationale being EMI shielding, estimating the microwave electrical parameters like permittivity (ε_r), loss tangent ($tan\delta$), AC conductivity and skin depths (δ) can provide vital information about the electromagnetic interference shielding efficiency of the composite. The real and imaginary part of permittivity (ε_r' and ε_r") and permeability (μ_r' and μ_r'') were derived by substitution of generated scattering parameters (S_{11} and S_{12}) in Nicolson–Ross-Weir equation.[33,34] From these parameters, the relative permittivity, $\varepsilon_r = \sqrt{\varepsilon_r'^2 + \varepsilon_r''^2}$ and the dielectric loss tangent, $tan\,\delta = \frac{\varepsilon_r''}{\varepsilon_r'}$ were further calculated and analyzed. For the sake of comparison, the optimum thickness of epoxy-LSCO composites was kept to be 2 mm throughout the study. The variation of ε_r and $tan\delta$ at 10 and 15 GHz as a function of the LSCO filler loading are given in Table 2.2. The dielectric parameters, ε_r and $tan\delta$ of epoxy-LSCO composites show an increasing trend with filler loading both in X and Ku band. At 10 GHz, the value of ε_r increases from 2.81 to 14.76 as the weight loading increases from 0 to 70 wt. % while the change is from 2.81 to 12.04 for 15 GHz. It should be noted that as the ceramic loading increases, the inter-particle distance between the LSCO particles in the epoxy matrix decreases, giving rise to a more effective conduction channel between the particles. This in turn may result in enhanced electromagnetic coupling between neighbouring particles due to cloud overlapping. Thus, above certain filler loading, the composite changes to a multipolar

system resulting in the overall enhancement of electrical conductivity and permittivity. Another feature contributing to the permittivity of the system is the polymer-ceramic interfacial effects.[35] With a change in the filler particle size, the surface area and hence the chemical structure of the interface will change, that also effect the dielectric permittivity of the medium.[36] Similar to permittivity, the dielectric loss tangent of epoxy-LSCO composites also show an increasing trend, as a function of the LSCO loading.

Table 2.2: The variation of ε_r and *tanδ* with LSCO addition at 10 and 15 GHz.

Wt. % of LSCO	ε_r		tanδ	
	10 GHz	15 GHz	10 GHz	15 GHz
0	2.810	2.810	0.025	0.027
10	3.080	3.079	0.029	0.032
20	3.366	3.365	0.031	0.034
30	4.204	4.296	0.031	0.039
40	4.957	5.250	0.032	0.035
50	6.032	6.080	0.044	0.044
60	10.098	7.880	0.081	0.061
70	14.759	12.042	0.156	0.098

As shown in Table 2.2, the value of *tan*δ increases from 0.02 to 0.156 at 10 GHz when the filler content increases from 0 to 70 wt. %. It is believed that the higher amount of protonic conductive component LSCO contributes to an aggravation of the dielectric loss since *tanδ* is proportional to the AC electrical conductivity. A combination of high AC conductivity and low skin depth are ideal for a typical EMI shielding material. Interestingly, the undoped

$LaCoO_3$ is a p-type semiconductor at temperatures below 800 °C which undergoes a phase transition from semiconducting rhombohedrally distorted perovskite (space group $R\bar{3}c$), to cubic perovskite (spacegroup Pm3m) when Sr is doped at the A-site based on $La_{1-x}Sr_xCoO_3$. Obviously in any microwave frequency band, the AC conductivity increases as a function of

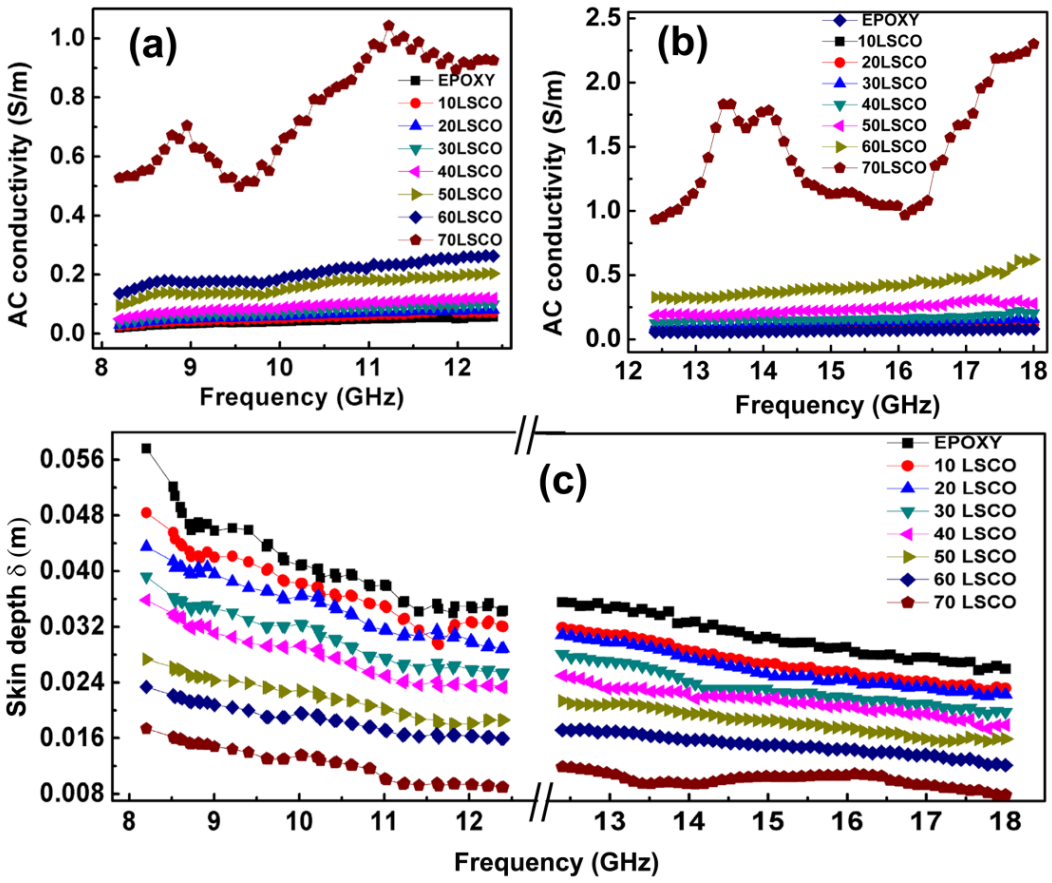

Fig. 2.6: (a) and (b) Variation of AC conductivity with different weight loading of LSCO in X and Ku band and (c) variation of skin depth with different weight percent of LSCO in X and Ku band.

the LSCO loading as shown in Fig. 2.6 (a) & (b) that shows the variation of conductivity for different loadings of LSCO in 8.2-18 GHz frequency ranges. The AC conductivity is directly related to loss factor ε'' and can be obtained from the relation, $2\pi f\varepsilon_o\varepsilon''$ where f is the frequency and ε_o is the relative permittivity of free space.[37,38] From the Fig. 2.6, it is clear that the AC

electrical conductivity shows an increasing trend as a function of filler loading. With filler loading increases from 0 to 70 wt. %, the conductivity varies from 0.05 to 0.65 S/m in the mid-X-band (10 GHz). Despite LSCO having a higher electrical conductivity in sintered ceramic form, the conductivity values of LSCO added polymer composites are not appreciably high for practical EMI shielding applications. The reasons for the observed low conductivity of the composite can be attributed to the high electrically insulating nature of the polymer matrix, along with the inferior electrical conductivities of oxide conductors in comparison with metals. However, as the weight percent of LSCO is increasing, the inter-particle distance is decreasing forming clusters of connected LSCO particles which span the entire volume to get high values of AC conductivity.

When electromagnetic radiation interacts with a conducting/semiconducting material, it penetrates only the near surface region of the material which is popularly known as the skin effect. Due to skin effect, a polymer-ceramic composite having conductive filler with a smaller particle size of the filler can shield electromagnetic waves better than one having a conductive filler with larger particles. In other words, for effective EMI shielding results, the unit size of the filler should be comparable to or less than the skin depth. From the SEM image (Fig. 2.1(c)), using the distribution analysis the particle size is found to be in the range of 0.4-0.5 μm. The skin depth (δ) is computed using the relation, $\delta = (\pi f \mu \sigma)^{-1/2}$, where f is the frequency, μ is the magnetic permeability, σ is the conductivity in S/m while $\mu = \mu_0 \mu_r$, $\mu_0 = 4\pi \times 10^{-7}$ H/m, and μ_r is the relative permeability. Fig. 2.6(c) shows the variation of skin depth for different LSCO loading as a function of microwave frequency in the 8.2-18 GHz range. From Fig. 2.6(c) it is analysed that at 10 GHz, the skin depth decreased from 0.04 to 0.02 m when LSCO content increases from 0 to 70 wt. %, while the corresponding change is from 0.03 to 0.01 m at 15

GHz. It is clear from the observations that, as the weight loading of LSCO increases, there is considerable improvement in the conductivity and permeability of the composite. Skin depth being inversely related to frequency and conductivity; it is natural that with increment of these parameters the skin depth is going to be lowering.

2.1.3.6 EMI Shielding of LSCO-Epoxy Composites

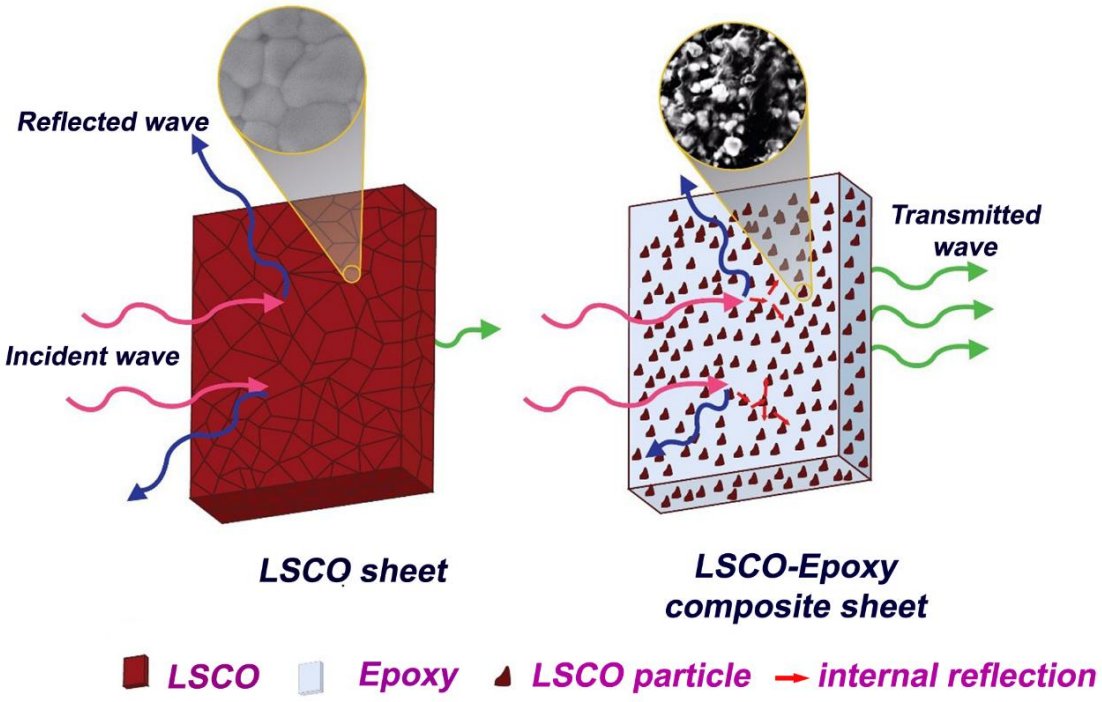

Fig. 2.7: Pictorial representation of EMI shielding mechanism of LSCO sheet and LSCO – epoxy composite.

Fig. 2.7 describes the overall shielding possibilities of bare LSCO and its epoxy composite. Transmission of EM wave is least in LSCO compared to composite, due to the favourable factors as mentioned in earlier section 2.1.3.1. The shielding effectiveness of the LSCO-epoxy composite was investigated in the same way as prescribed for sintered LSCO sheets. Specific parameters of the composite like geometrical shape of filler particles and filler/matrix interactions are also critical towards the effectiveness of shielding mechanism. The distribution

of the filler in epoxy medium is confirmed from the SEM micrograph (Fig. 2.3(b)), and improved mechanical strength for the composite are the result of good interfacial interactions between filler and matrix.

The frequency dependent behaviour of SE_R, SE_A and SE_T of the composites in the entire frequency range (8.2-18 GHz) for different loading of LSCO is given in Fig. 2.8. In the case of 70 weight loaded epoxy-LSCO composite at 9 GHz, the total SE of 9.8 dB is majorly contributed by reflection parameter, ie SE_R of 8.1 dB and that of SE_A is 1.7 dB only. A distinct domination of reflective shielding over absorptive shielding is evident for each and every composition of epoxy-LSCO composites (see Fig. 2.8(c) and 2.8(d)). It is interesting to note that, from the bare epoxy matrix showing a SE ~1 dB, a gradual improvement in shielding value is observed with LSCO filler addition and at 70 wt. % loading, SE attains values around 10 dB throughout the first half way range of X band, i.e. from 8.2 to 10 GHz. Fig. 2.9(a) shows the dependence of SE_R, SE_A and SE_T on the LSCO loading at mid X band region. All these parameters are showing a rising trend with increasing LSCO loading in the composite. A similar behaviour is observed at mid Ku band also (see Fig. 2.9(b)). At higher loading the inter particle distance between LSCO units decrease which creates a conduction path. In addition to that the composite become a multipolar system having greater interfacial areas between LSCO and epoxy matrix. This may ultimately add to the dielectric loss of the composite and observed enhancement in electromagnetic wave shielding. Furthermore, the multiple reflection possibilities from the far end of the LSCO composite surface can be another contributor to the total shielding effectiveness of the composite. The permittivity, dielectric loss, AC conductivity and skin depth values are showing optimum values for the maximum loaded composite which are in agreement with the observed shielding effectiveness values.

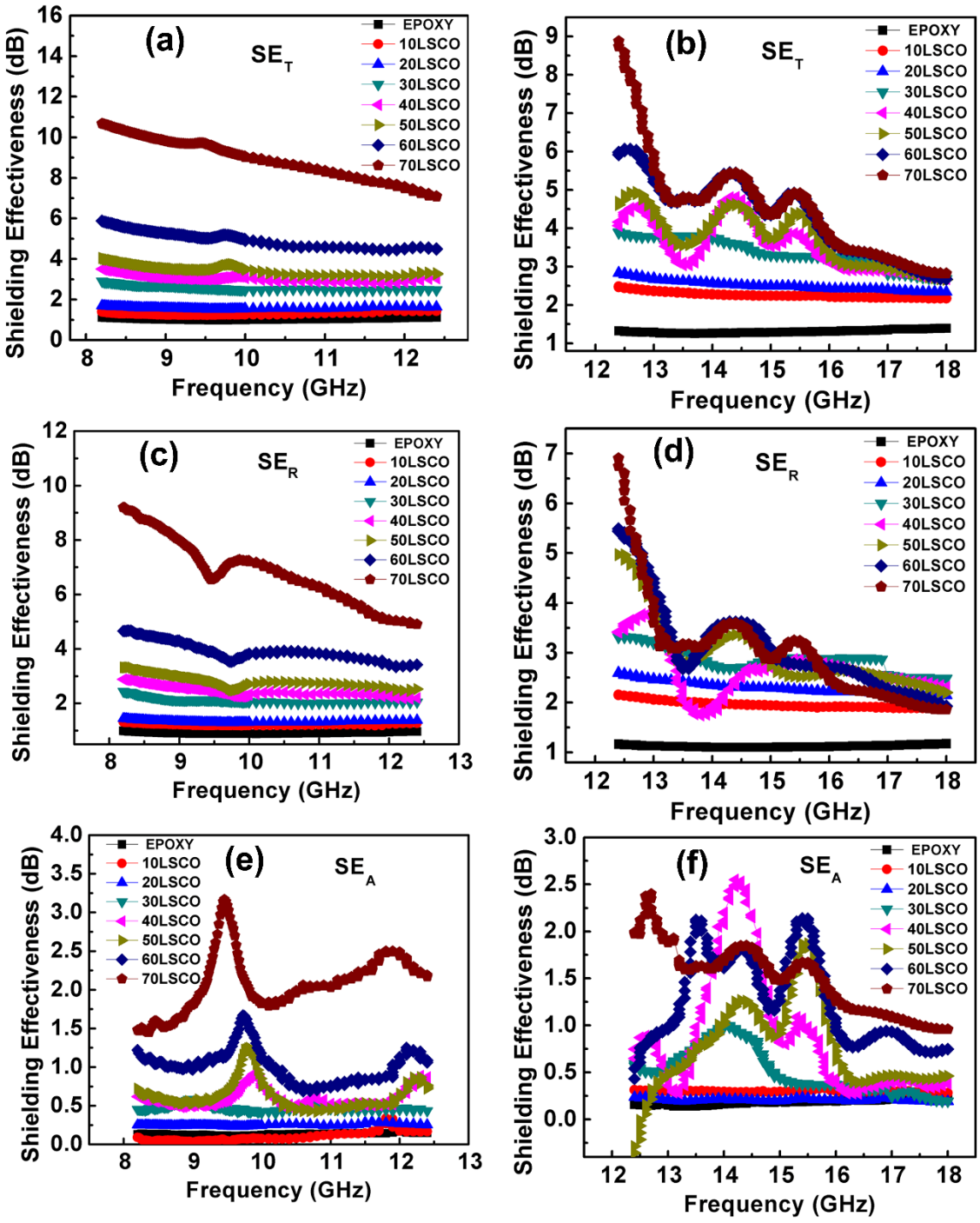

Fig. 2.8: (a) and (b) Frequency dependent variation of total EMI shielding effectiveness (SE_T), (c) and (d) variation of reflection shielding (SE_R) and (e) and (f) of absorption shielding (SE_A) of variously loaded LSCO-epoxy composites over X and Ku band frequency range (8.2–18 GHz).

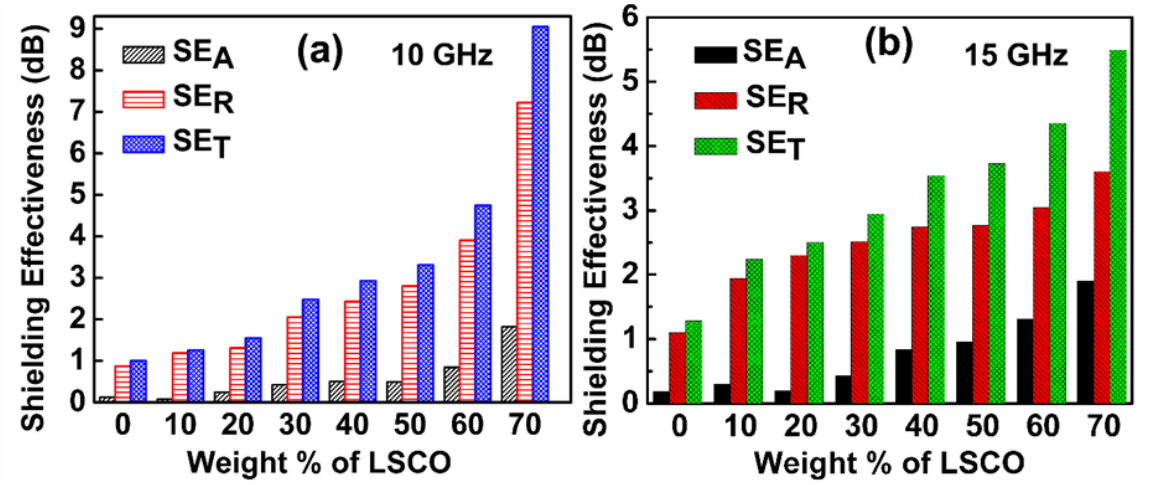

Fig. 2.9: (a) and (b) variation of total EMI SE (SE_T), absorption SE (SE_A), and reflection SE (SE_R) with LSCO loading at 10 & 15 GHz.

2.1.4 Conclusions

Perovskite conducting oxide, $La_{0.5}Sr_{0.5}CoO_{3-\delta}$ synthesized through solid state reaction technique, was investigated that was found to possess high EMI shielding effectiveness (35-42 dB in the 8.2-18 GHz range). The high microwave shielding where 99.9 % attenuation of the incident radiation occurred, was supplemented by its high dc conductivity (1400 S/cm) at room temperature. Further, LSCO was made 0-3 composite with epoxy, with purpose of improving its applicability on solid surfaces. The thermal conductivity, thermal expansivity and mechanical strength of the composite were improved as a function of LSCO filler loading. The gradual improvement in the shielding effectiveness was complemented by the gradual improvements in dielectric permittivity, dielectric loss and AC conductivity parameters, with increasing filler content. On the other hand, the AC skin depth values of the composites were decreasing, as a function of filler loading due to enhanced conductivity in both X and Ku bands. The maximum weight loaded (70 wt. % of LSCO) epoxy composite could provide a shielding efficiency around 10 dB in the 8.2-10 GHz range. However, the coefficient of thermal

expansivity and compressive strength were displaying anomaly at 70 wt. % LSCO loaded epoxy composite. Such mouldable EMI shielding structures are useful in electrostatic dissipation applications, where high mechanical strength, high thermal conductivity and low thermal expansivity are important.

2.2 Screen Printed Silver Patterns on LSCO-Epoxy Composite as a Strategy for Many-Fold Increase in EMI Shielding

2.2.1 Introduction

While searching for EMI shielding materials, a variety of materials can be suitable with wide range of properties like electrical conductivity, magnetic permeability and geometries. Metal based shielding materials are widely explored and are effective in reflective shielding.[39] The easy way to incorporate a shielding structure, say a metal, to a component is through the route of polymer composites. However, most of the polymers are insulators and are transparent to electromagnetic radiation.[40] To metalize the polymers, there are several techniques available. Some of the available techniques includes making composites of polymer with metallic particles, [41-43] making conductive coatings through various printing techniques, [44] direct metallization through vacuum metalizing, electro and electroless plating,[45-47] or establishment of intrinsically conductive polymers.[48-50] Among all, the composite approach and conductive coating through printing are seems to be cheaper than other techniques of metallization. Conductive filler incorporated composite is widely used in EMI shielding purpose and the metals used were silver, copper, aluminium, nickel, iron etc. Now the metals are replaced with conducting carbon based materials such as carbon black, carbon nanotube, graphene etc. which are advantageous in a way, as they are light weight and non-corrosive, compared to the metals. Thus it became evident that developing novel percolative composites has been a widely adopted strategy to achieve EMI shielding, and relatively less attention has been given to the surface modification of the composites.

Over the years, a few groups adopted screen printing of conducting pastes, especially carbon based pastes, as a means to improve their microwave absorbance on a variety of polymer surfaces.[51-53] EMI shielding filters made of Ag-conductive patterns printed on plasma display panels have recently been demonstrated in a few patents as well.[54,55] Designing and printing Ag-based metamaterial patterns on polymer substrates is another popular strategy to suppress certain selective frequency bands detrimental to the operating bands of specific devices.[56] Such structures are termed as frequency selective surfaces that can be easily applied as wallpaper on the walls of rooms without any structural loading issues to existing architecture. In another interesting work, silver oxide mesh patterns were bar-coated on a PET film with a thickness of 30 μm.[57] However, this method requires a curing at 150 ^{o}C and the synthesis procedure of silver neoalkanoates involves complex procedures. A few isolated studies have also been attempted to print metallic patterns on polymer, as a means to enhance the shielding effectiveness.[58,59] In the present work, LSCO - epoxy composites were employed as the platform for building up novel EMI shielding structures. In order to make a dramatic improvement in its EMI shielding characteristics, a unique approach of printing patterns of conductive Ag on top of the composite surface, was adopted. The microstructure, electrical and microwave dielectric properties of the various printed EMI shielding structures were investigated in this manuscript.

2.2.2 Materials and Methods

LSCO powders were prepared by conventional solid-state reaction route and later made in to a composite with epoxy as explained in section 2.1.2. The prepared composite sheets were polished to suitable dimension for EMI shielding studies. Screen printing technique were implied on small rectangular composite sheets using a home-made screen printer (Plastomek,

Kerala). For coating of the conductive metal patterns, a commercial grade silver ink (Metalon HPS-030LV, Novacentrix, USA) was used. The optimal level of Ag line width was adjusted to be ~300 µm and the same width was maintained for the vertical, horizontal lines as well as mesh designs. All the characterization techniques employed were same as that explained in section 2.1.2. Additionally, atomic force microscopy (AFM) imaging was performed in this research, using MultiMode 8 AFM equipped with NanoScope V controller (Bruker, Santa Barbara, CA, USA). Si cantilevers (NSG 01, NT-MDT) were used with force constants in the range of 2.5-10 N/m and with resonance frequency in the range of 120-180 kHz. The scan rate used was 0.5-1 Hz. Raw data were processed offline using Bruker's NanoScope Analysis image processing software. Surface roughness was reported both in average roughness, root mean square (RMS) values.

2.2.3 Results and Discussion

2.2.3.1 Improved Thermal, Mechanical and Dielectric properties

The effect of LSCO addition on the physical properties of the LSCO-epoxy composite has been detailed in the part 2.1 of chapter 2. That study revealed that the optimal mechanical and thermal properties of the composite were at 60 wt. % of LSCO loading.[60] For example, the thermal conductivity (TC) of pure epoxy was 0.25 W/m.K, which got improved by 2.3 folds with the incorporation of 60 wt. % of filler LSCO. On the other hand, a decreasing trend was observed for thermal expansion with filler loading and the least expansion was optimised to be for 60 weight loaded LSCO-epoxy composite (Fig. 2.10(a)). The lower coefficient of thermal expansion (*CTE*) of LSCO and increasing interfacial area were posing restrictions to the heat induced expansion of epoxy chain. The mechanical behavior of pure epoxy and 60 wt. % LSCO

loaded epoxy composites (60 LSCO), subjected to increasing compressive strains, is plotted in Fig. 2.10(b).

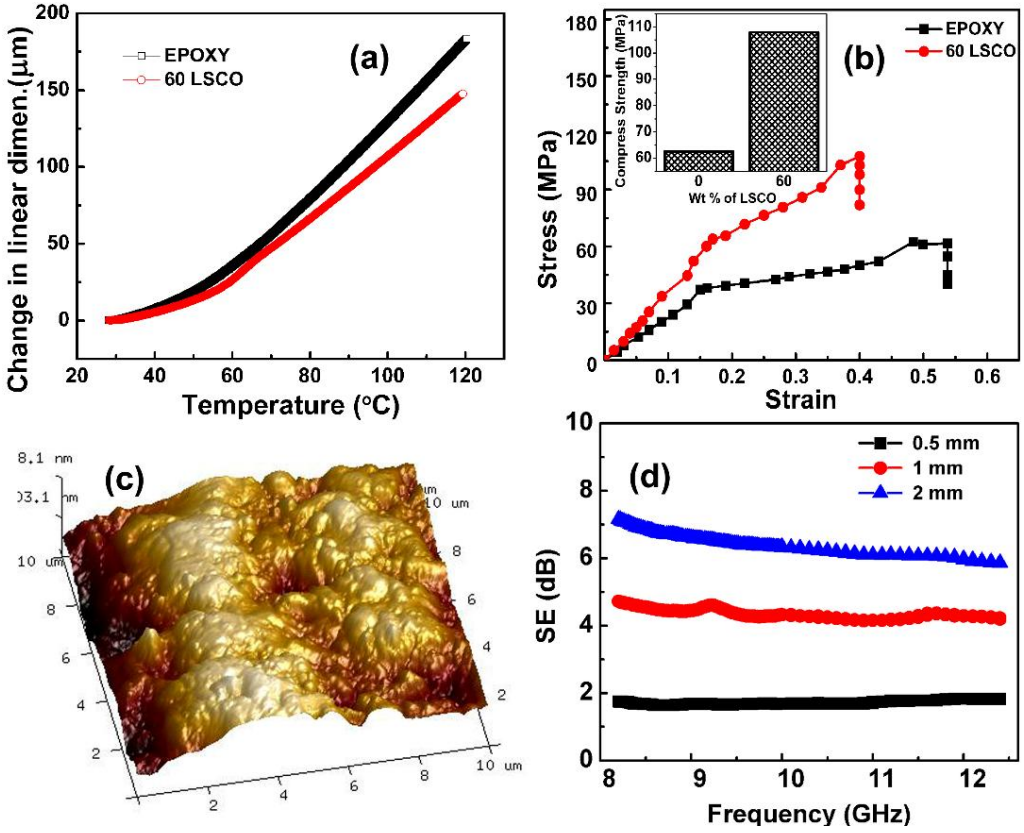

Fig. 2.10: (a) Thermal expansion behaviour of neat epoxy and 60 wt. % LSCO loaded epoxy composite, (b) Stress-strain curve of pure epoxy and that of 60 wt. % of LSCO loaded one. Inset figure showing improved compressive strength with 60 wt. % of LSCO. Fig. 2.10: (c) AFM surface topography images (3D) of the 60 wt. % LSCO loaded epoxy composite surface and (d) SE of 60 wt. % LSCO loaded epoxy composite, as a function of varying thickness.

The compressive strength of the composite was found to be improving with addition of LSCO and observed a maximum compressive strength for the composite with 60 wt. % loading. Further addition of filler keeps the compressive strength decreasing due to the inevitable filler agglomeration. The inset of Fig. 2.10(b) shows the compressive strength of bare epoxy and that of 60 LSCO. Evidently, the value of 62 MPa for pure epoxy got improved to 107 MPa with 60 weight percent of LSCO filler addition. The strong interfacial interaction

between LSCO and epoxy matrix with an effective stress transfer between them contributes to the observed trend.[61,62] The AFM (3D) surface topography images of the polished surface of the 60 LSCO is shown in Fig. 2.10(c). From the analysis of the AFM image, it is clear that the average and the root mean square (RMS) roughness values of the surface obtained are 144 and 179 nm, respectively.

2.2.3.2 Modification Using Conductive Surface Designs

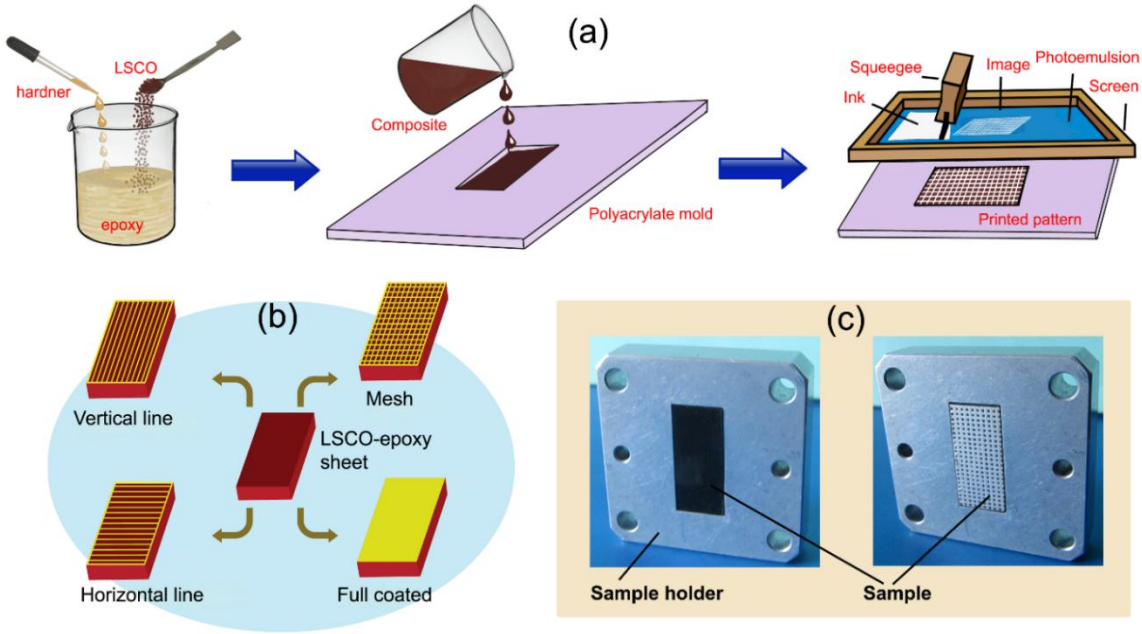

Fig. 2.11: (a) Schematic representation of the development of Ag coated LSCO-epoxy composite, (b) various patterns screen printed on the LSCO-epoxy composite and (c) photographic images of sample holder of the waveguide with bare composite and Ag pattern printed composite.

Even though various physical properties such as thermal, mechanical and dielectric parameters of epoxy matrix got improved with 60 wt. % loading, the improvement in EMI shielding values were feeble and this situation demands for further modification of the already developed composite. A simple strategy was implemented, which involved the introduction of

conductive coating on the surface of composite. A schematic representation of the different processes involved in the development of Ag coated LSCO-epoxy composite, is briefed in Fig. 2.11(a). The different schemes of silver patterns printed on top of LSCO-epoxy composite are pictorially represented in Fig. 2.11(b). Photographic images of sample holder of the waveguide with bare composite and Ag pattern printed composite were given in Fig. 2.11(c). A commercially available silver ink (Metalon HPS-030LV) was chosen for screen printing. Composite sheets with optimum thickness (2 mm) and solid loading (60 wt.% LSCO) have been selected for implementing the patterns, based on the EMI shielding measurements made on specimens with varying thickness (Fig. 2.10(d)). The line patterns of silver ink on the composite surface can be assumed as vertical and parallel rectangles (see Fig. 2.11(b)), with respect to their position in the rectangular slot of the wave guide. Mesh patterns, in a way, is a combination of vertical and parallel rectangular lines, one laid over the other, while the final choice was the blanket coating of ink over the composite surface.

In addition to silver screen printing, for the sake of comparison, we have attempted an alternative strategy which was the direct mixing of silver to the LSCO-epoxy matrix. Only one combination was tested, where out of the total additive, fifty weight percent of the composite filler was silver powder while the other fifty weight percent was filled by LSCO powder. In other words, the 1:1 combination of LSCO:Ag means that out of total filler content in epoxy, each filler is in 1:1 proportion which is equal to 60 wt. % of the epoxy matrix.

2.2.3.3 Structure and Microstructure of Surface Designs

Fig. 2.12(a) shows the top view of the printed silver mesh patterns. It is clear from the images that the width of the lines is 300 μm and is equally spaced on the surface layer. From

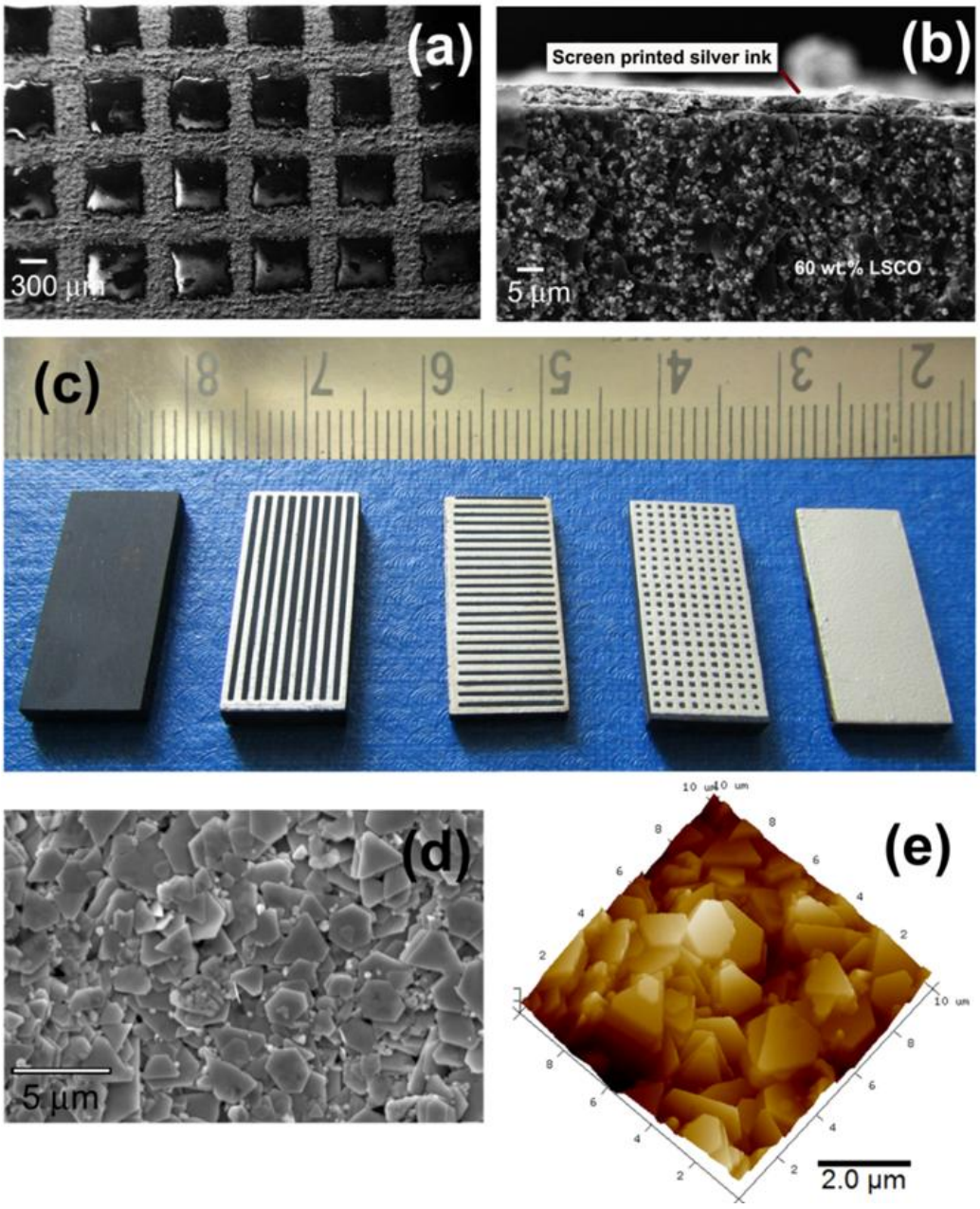

Fig. 2.12: (a) & (d) The SEM images of silver coated surface under different magnifications, (b) cross section of the LSCO composite with silver screen printed over the surface, (c) photographic image of the different silver patterns screen printed on the sample sheets and (e) shows the AFM surface topography images (3D) of the silver printed layer (10 x 10 µm).

the cross-section electron micrographs (Fig. 2.12(b)), the average thickness of silver pattern is estimated to be around 2-4 µm. The actual photographic image of the different patterns of

silver screen printed on the composite sample sheets is depicted in Fig. 2.12(c). Fig. 2.12(d) and (e) are the SEM and AFM (3D) surface topography images recorded from the conductive silver layer. From the AFM image, it is clear that silver particles possess broken plate-like morphology with feature sizes in the range of 1-4 µm. The average and the root mean square (RMS) roughness values of the surface obtained are 115 and 142 nm, respectively. The surface kurtosis of 2.628 highlights the uneven nature of the silver layer with skewness of -0.049 nm points the majority of shallowness of the surface.

2.2.3.4 AC Electrical Parameters of Surface Modified Composites

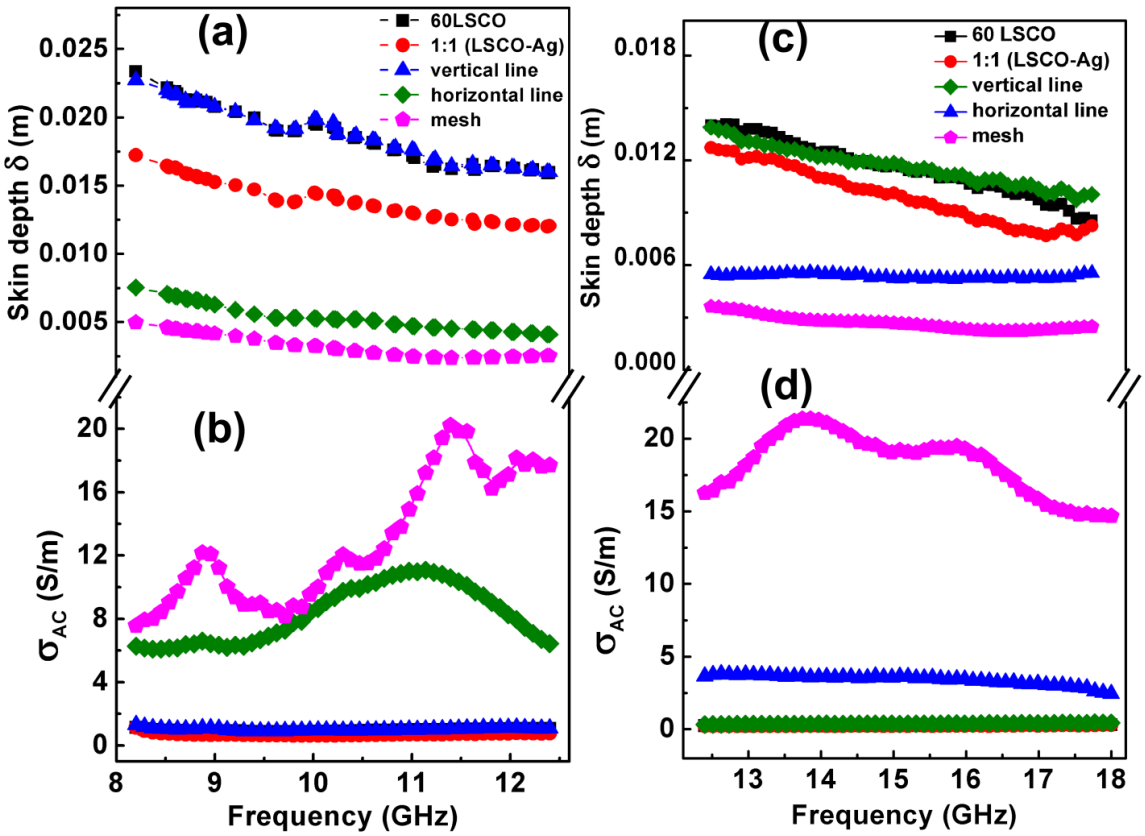

Fig. 2.13: The frequency dependent variation of (a) skin depth (δ) and (b) AC conductivity (σ_{AC}) of composites with various screen printed patterns, at X band. The variation of (c) skin depth and (d) AC conductivity at Ku band for various samples of 60 wt.% loaded LSCO-epoxy sheets which were modified differently using silver patterning.

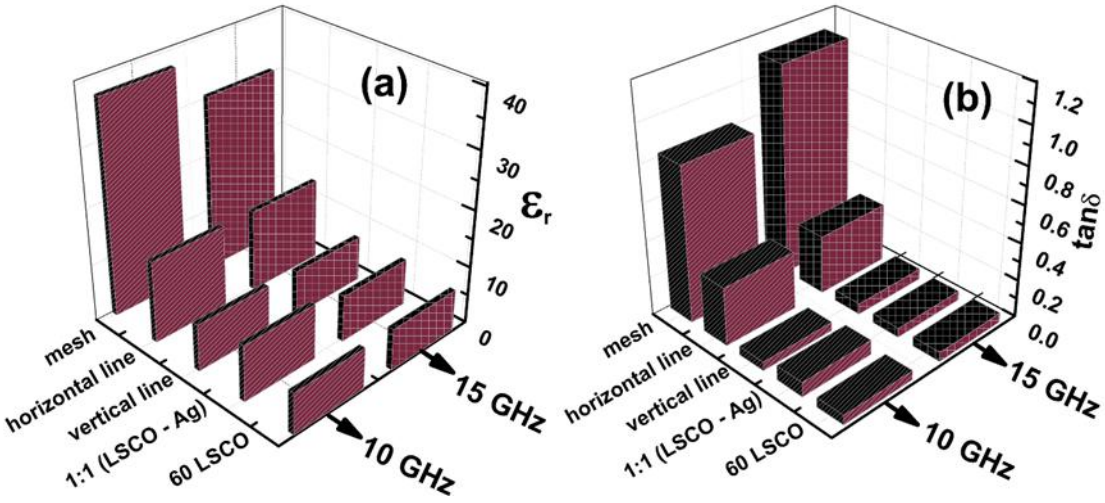

Fig. 2.14: (a) and (b) variation of ε_r and tanδ with Ag modification at mid X and Ku band.

The microwave electrical parameters like permittivity (ε_r), loss tangent ($tan\delta$), AC conductivity (σ_{AC}) and skin depths (δ) were crucial in determining the electromagnetic interference shielding efficiency of the modified composite. The frequency dependent variation of skin depth and AC conductivity of the composites with various screen printed patterns, at X band. Ku bands are depicted in Fig. 2.13. In the earlier work on LSCO-epoxy composites, it was observed that the AC conductivity for pure epoxy at mid X band, was 0.05 S/m and an enhanced value of 0.5 S/m for 60 wt. % LSCO loaded composite. Later, with the additional silver incorporation into the matrix in such a way that half of the LSCO filler when replaced with silver, there was no remarkable change in the AC conductivity. In sharp contrast to this, screen printing of silver patterns on 60 wt. % LSCO loaded composite resulted in enhancing the AC conductivity values to a greater extent (see Fig. 2.13). This noticeable variation is believed to have come from the difference in connectivity in the two approaches. Evidently, the screen printed silver particles were well connected to form a continuous coating. On the other hand, in the case of dispersed silver in the matrix, the connectivity between Ag particles may be insufficient to form a conductive pathway. This was evident at 10 GHz, where

the AC conductivity value of 0.5 S/m for 60 wt. % LSCO–epoxy composite got enhanced to 10.9 S/m with Ag mesh coating. With the increase of connectivity between silver line patterns, the loss factor (ε'') was also found to be increasing, similar to AC conductivity.

Evidently, the performed modifications with silver ink designs resulted in enhancing the AC conductivity and lowering the skin depth, which can be beneficial for EMI shielding. Fig. 2.14(a) and (b) shows the variation of ε_r and $tan\delta$ at 10 and 15 GHz for different silver pattern incorporation schemes made on the 60 wt. % LSCO loaded composite. As shown, the apparent dielectric permittivity has improved from 7.3 to 37.6 (at 10 GHz) with mesh design coating. Obviously, the AC conductivity observed a 60-fold increase while the dielectric loss increased by 15 times. The enhancement of the electromagnetic parameters and SE values especially the absorption shielding (SE_A) values are accounted by the maximum interconnected conducting channels with optimum coverage of the composite surface with silver coating. The skin depth drops from 0.0196 m to 0.0033 m range at 10 GHz, indicating how well the electromagnetic waves were attenuated at a shorter range on the surface of silver modified composite. It is obvious that the electromagnetic radiation can penetrate only the surface layer of a conductor. Thus it was important to examine whether the above-mentioned surface modifications with silver ink designs resulted in improving the SE value of the LSCO-epoxy composite.

2.2.3.5 EMI shielding of modified composites

The optimally loaded 60 wt. % LSCO-epoxy composite, which shows better mechanical and thermal properties, were analyzed for EMI shielding at varying thickness as given in Fig. 2.10(d).

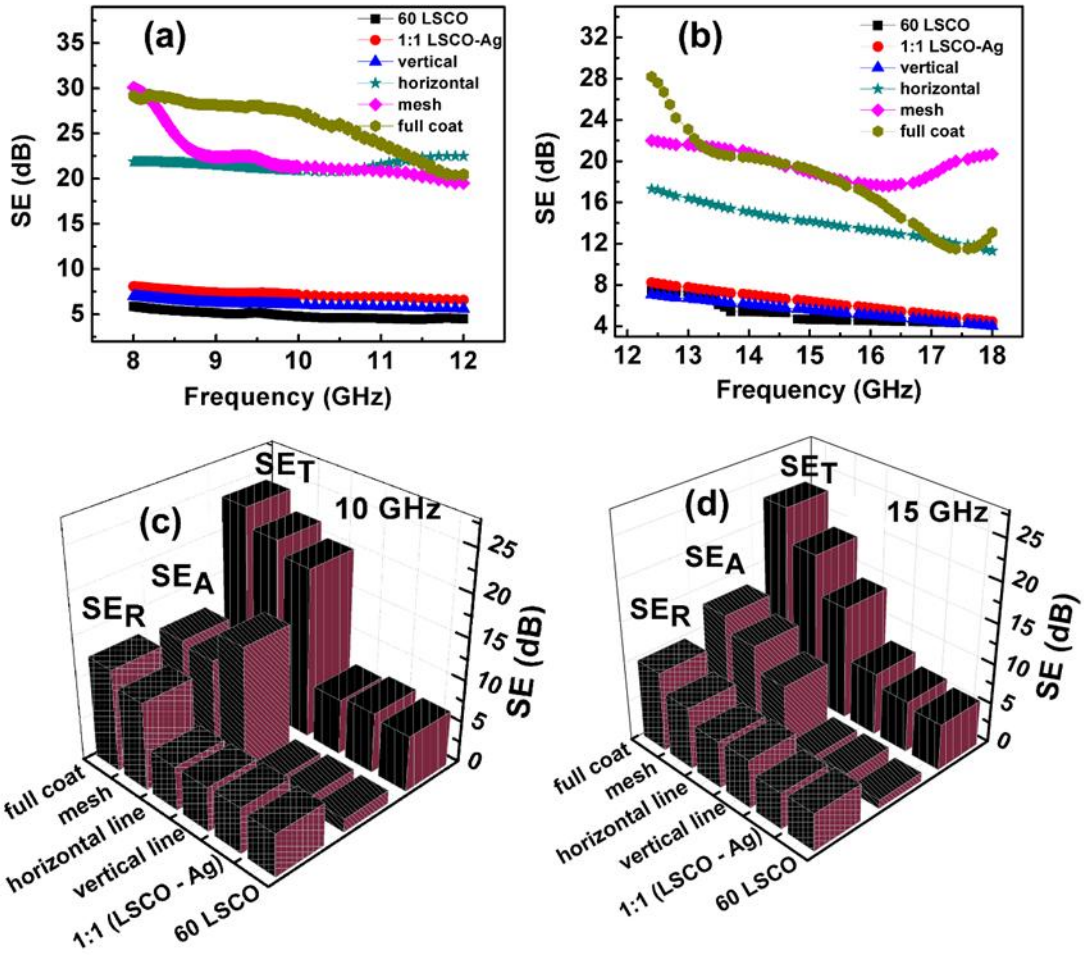

Fig. 2.15: (a) and (b) are shielding effectiveness of variously modified LSCO-epoxy composite with silver, in the X band and Ku band. (c) and (d) Improvement of total shielding effectiveness (SE_T), reflection shielding effectiveness (SE_R) and absorption shielding effectiveness (SE_A) with silver pattern modification at 10 and 15 GHz.

As the thickness increased from 0.5 to 2 mm, the SE value improved from 1.8 to 7.0 dB. From equation (2.7) it is clear that EMI shielding by absorption, depends mainly on the material thickness and electrical conductivity. Hence for the same composition, the increase in SE_A with increase in shield thickness, is obvious. Thus far, the maximum EMI shielding for epoxy-60 wt. % LSCO composite, 7 dB, is not appreciably high for useful practical applications. Some of the feasible strategies for the betterment of EMI shielding in composites are (a)

introduction of conductive coatings (b) compounding with conductive fillers or (c) replace the polymer with intrinsically conductive polymers.[63] As hinted before, the principal reason behind the inefficiency of the LSCO-epoxy composite to achieve high shielding efficiency, lies in the fact that the intrinsic conductivity of LSCO fall below three orders of magnitude to that of most conducting metals like silver and copper. In order to enhance the shielding efficiency to practical application levels, the aforementioned modification strategy involving printing of metallic patterns onto the optimally developed composite, has been adopted. Here the principal mechanism of EMI shielding is reflection which requires the presence of mobile charge carriers that interact with electromagnetic radiation and the electromagnetic field thus undergo ohmic losses due to the presence of these carriers.[64]

Though a conducting polymer could act as an electromagnetic wave shield, a high electrical conductivity is not the scientific pre-requisite for shielding, since conduction requires connectivity in the conduction path, whereas shielding does not. With the introduction of the silver patterns on the LSCO-epoxy composites, its EMI shielding efficiency improves dramatically. For example, the composites bearing mesh design and those with complete coating enhance the SE values to three to four-fold than uncoated ones. The SE of mesh coated and fully coated composite are 22 dB and 24 dB respectively at 10 GHz which are ideal for practical applications (see Fig. 2.15(c)). A total shielding effectiveness of 31.3 dB (at 8.2 GHz) is the maximum EMI shielding observed in this investigation for LSCO-epoxy composite specimen whose surface is blanket coated with silver, as shown in Fig. 2.15(a). As the area of the conductive surface coating is increasing, its AC conductivity is improving and the maximum is expected for full coated surface. From equation (2.7), it is clear that electrical conductivity (σ) and SE_A are directly related. Eventually that will be reflected in the overall

shielding effectiveness of the blanket coated sample. Interestingly enough, the composites bearing rectangular patterns horizontal to the major axis of the shim, gives better shielding of 21 dB than those of 7 dB for vertical pattern to the major axis of the shim, probably due to the more number of rectangles per unit area. The values in the range of 14-20 dB (at 10 GHz) for horizontal line printed composites can also be qualified for practical applications. Interestingly, though the horizontal and vertical line patterns improve the overall conductance of the shielding structure, they are obviously having inferior surface conductivity than mesh patterns, due to the higher connectivity among the conductive lines. Notwithstanding the fact that shielding does not require connectivity, it is largely enhanced by it which is the main reason behind the high EMI shielding of the composite structure where mesh type pattern was printed on top of them. The shielding effectiveness of silver printed LSCO-epoxy composites at Ku band (12.4-18 GHz) is given in Fig. 2.15(b). In general, of all the silver modified LSCO-epoxy composites considered in the present investigation, two distinct specimens namely mesh-patterned and full-coated ones showed a high shielding efficiency (> 20 dB) consistently in a broad frequency range (8.2-18 GHz).

Also for a comparison, we have made a composite in the conventional way by mixing silver along with LSCO filler (see the bar diagram for 1:1 LSCO-Ag in Figs 2.15(c) and (d)), in the epoxy matrix. However, this strategy is proven to be ineffective in improving the overall SE of the composite in comparison with surface coated specimens. In fact, 2D printing techniques requires much lesser amount of conductive materials for achieving good EMI shielding, than a typical 0-3 polymer-metal composite with filler loading above the percolation threshold. Hence using these innovative surface level modifications, one can transform

traditional composites with moderate EMI shielding into highly shielding structures, which is ideal for light weight aeronautical EMI shielding applications.

2.2.3.6 Conclusions

With the objective of achieving higher shielding efficiency, a novel surface modification strategy was adopted wherein predesigned silver patterns were screen printed on the surface of the LSCO loaded epoxy composite. Upon this, a dramatic 4-fold increment in the shielding efficiency (22-31 dB SE in the X and Ku-band 8.2-18 GHz) was observed with visible enhancements in the reflection as well as absorption shielding values. For example, the EMI shielding values of 4.7 dB (at 10 GHz) was remarkably enhanced to 24 dB with printing of Ag patterns on top of optimally loaded LSCO-epoxy composite structures. For silver design printed composites, this high shielding has been authenticated by visible increments in the AC conductivity, relative permittivity, and dielectric loss as well as a corresponding lowering of skin depths. Interestingly, instead of screen printing, the incorporation of silver powder replacing even up to 50 wt. % of LSCO in the matrix to form a 0-3 composite could not fetch any visible improvement in the EMI shielding effectiveness. While moving from simple line pattern to mesh design to full coating, the EMI shielding effectiveness is found to be progressively increasing, reaching up to 31 dB (at 8.2 GHz). The present strategy of introducing screen printing based design structures on composites can be used as a precursor for achieving the high SE values on materials with mediocre shielding habits. Such structures are ideal for absorber applications in aeronautical engineering where a combination of lightness, high mechanical strength, high thermal conductivity, and low thermal expansivity, in addition to high EMI shielding are needed.

2.3 References

(1) Wang, Y.; Jing, X. Intrinsically Conducting Polymers for Electromagnetic Interference Shielding. *Polym. Adv. Technol.* **2005**, *16* (4), 344–351.

(2) Hutagalung, S. D.; Sahrol, N. H.; Ahmad, Z. A.; Ain, M. F.; Othman, M. Effect of MnO_2 Additive on the Dielectric and Electromagnetic Interference Shielding Properties of Sintered Cement-Based Ceramics. *Ceram. Int.* **2012**, *38* (1), 671–678.

(3) Kong, L.; Yin, X.; Ye, F.; Li, Q.; Zhang, L.; Cheng, L. Electromagnetic Wave Absorption Properties of ZnO-Based Materials Modified with $ZnAl_2O_4$ Nanograins. *J. Phys. Chem.* **2013**, *117* (1), 2135–2146.

(4) S.Al-Ghamdi, A. A. Vanadium Sesquioxide Nanocomposite. US Patent, US 2010/0321147 A1, **2010**.

(5) Singh, R.; Kulkarni, S. G. Nanocomposites Based on Transition Metal Oxides in Polyvinyl Alcohol for EMI Shielding Application. *Polym. Bull.* **2014**, *71*, 497–513.

(6) Ohbayashi, H.; Tetsuichi Kudo, T. G. Crystallographic, Electric and Thermochemical Properties of the Perovskite-Type $Ln_{1-x}Sr_xCoO_3$ (Ln: Lanthanoid Element). *Jpn. J. Appl. Phys.* **1974**, *13*, 1–7.

(7) Petrov, A. N.; Kononchuk, O. F.; Andreev, A. V.; Cherepanov, V. A.; Kofstad, P. Crystal Structure, Electrical and Magnetic Properties of $La_{1-x}Sr_xCoO_{3-y}$. *Solid State Ion.* **1995**, *80*, 189–199.

(8) Endo, A.; Wada, S.; Wen, C. J.; Komiyama, H.; Yamada, K. Low Overvoltage Mechanism of High Ionic Conducting Cathode for Solid Oxide Fuel Cell. *J. Electrochem. Soc.* **1998**, *145* (3), L35–L37.

(9) Li, W. W.; Hu, Z. G.; Li, Y. W.; Zhu, M.; Zhu, Z. Q.; Chu, J. H. Growth, Microstructure, and Infrared-Ultraviolet Optical Conductivity of $La_{0.5}Sr_{0.5}CoO_3$ Nanocrystalline Films on Silicon Substrates by Pulsed Laser Deposition. *ACS Appl. Mater. Interfaces* **2010**, *2* (3), 896–902.

(10) Suntivich, J.; Gasteiger, H.; Yabuuchi, N.; Shao-Horn, Y. Electrocatalytic Measurement Methodology of Oxide Catalysts Using a Thin-Film Rotating Disk Electrode. *J. Electrochem. Soc.* **2010**, *157* (8), B1263.

(11) Wang, Y.; Fan, H. J. Improved Thermoelectric Properties of $La_{1-x}Sr_xCoO_3$ Nanowires. *J. Phys. Chem. C* **2010**, *114* (32), 13947–13953.

(12) Kovalevsky, A. V; Kharton, V. V; Tikhonovich, V. N.; Naumovich, E. N.; Tonoyan, A. A.; Reut, O. P.; Boginsky, L. S. Oxygen Permeation through $Sr(Ln)CoO_{3-l}$ (Ln = La, Nd , Sm , Gd) Ceramic Membranes. *Mater. Sci. Eng. B* **1998**, *52*, 105–116.

(13) Liu, W.; Wang, S.; Chen, Y.; Fang, G.; Li, M.; Zhao, X. Zhong. $La_{0.5}Sr_{0.5}CoO_{3-\delta}$ Nanotubes Sensor for Room Temperature Detection of Ammonia. *Sensors Actuators, B* **2008**, *134* (1), 62–65.

(14) Parry, J. M.; Raccah P. Method of Manufacturing a Gas Sensor. US Patent, US4221827, **1978**.

(15) Parker, W. J.; Jenkins, R. J.; Butler, C. P.; Abbott, G. L. Flash Method of Determining Thermal Diffusivity, Heat Capacity, and Thermal Conductivity. *J. Appl. Phys.* **1961**, *32* (9), 1679–1684.

(16) De Vries, A. J.; Kooij, E. S.; Wormeester, H.; Mewe, A. A.; Poelsema, B. Ellipsometric Study of Percolation in Electroless Deposited Silver Films. *J. Appl. Phys.* **2007**, *101* (5), 053703.

(17) Lu, L.; Shen, Y.; Chen, X.; Qian, L.; Lu, K. Ultrahigh Strength and High Electrical Conductivity in Copper. *Science.* **2004**, *304* (5669), 422–426.

(18) Todd, M. G.; Shi, F. G. Characterizing the Interphase Dielectric Constant of Polymer Composite Materials: Effect of Chemical Coupling Agents. *J. Appl. Phys.* **2003**, *94* (7), 4551.

(19) Park, S. H.; Theilmann, P.; Yang, K.; Rao, A. M.; Bandaru, P. R. The Influence of Coiled Nanostructure on the Enhancement of Dielectric Constants and Electromagnetic Shielding Efficiency in Polymer Composites. *Appl. Phys. Lett.* **2010**, *96* (4), 2008–2011.

(20) Li, B. W.; Shen, Y.; Yue, Z. X.; Nan, C. W. Enhanced Microwave Absorption in Nickel/Hexagonal-Ferrite/Polymer Composites. *Appl. Phys. Lett.* **2006**, *89* (13), 132504 1-3.

(21) Saini, P.; Choudhary, V.; Singh, B. P.; Mathur, R. B.; Dhawan, S. K. Polyaniline-MWCNT Nanocomposites for Microwave Absorption and EMI Shielding. *Mater. Chem. Phys.* **2009**, *113* (2–3), 919–926.

(22) Joseph, N.; Varghese, J.; Sebastian, M. T. A Facile Formulation and Excellent Electromagnetic Absorption of Room Temperature Curable Polyaniline Nanofiber Based Inks. *J. Mater. Chem. C* **2016**, *4* (4), 999–1008.

(23) Joseph, N.; Sebastian, M. T. Electromagnetic Interference Shielding Nature of PVDF-Carbonyl Iron Composites. *Mater. Lett.* **2013**, *90*, 64–67.

(24) Kumar, G. S.; Vishnupriya, D.; Joshi, A.; Datar, S.; Patro, T. U. Electromagnetic Interference Shielding in 1-18 GHz Frequency and Electrical Property Correlations in Poly(Vinylidene Fluoride)-Multi-Walled Carbon Nanotube Composites. *Phys. Chem. Chem. Phys.* **2015**, *17* (31), 20347–20360.

(25) Xu, Y.; Li, Y.; Hua, W.; Zhang, A.; Bao, J. Light-Weight Silver Plating Foam and Carbon Nanotube Hybridized Epoxy Composite Foams with Exceptional Conductivity and Electromagnetic Shielding Property. *ACS Appl. Mater. Interfaces* **2016**, *8* (36), 24131–24142.

(26) Youngblood, G. E.; Senor, D. J.; Jones, R. H.; Kowbel, W. Optimizing the Transverse Thermal Conductivity of 2D-SiCf/SiC Composites. *J. Nucl. Mater.* **2002**, *62*, 1120–1125.

(27) Yung, K. C.; Zhu, B. L.; Yue, T. M.; Xie, C. S. Preparation and Properties of Hollow Glass Microsphere-Filled Epoxy-Matrix Composites. *Compos. Sci. Technol.* **2009**, *69* (2), 260–264.

(28) Sebastian, M. T.; Menon, C. P.; Philip, J.; Schwartz, R. W. Thermal Properties of $La_{0.5}Sr_{0.5}Co_{1-x}Ni_xO_{3-\delta}$ Ceramics Using Photopyroelectric Technique. *J. Appl. Phys.* **2003**, *94*

(5), 3206–3211.

(29) Zhu, B. L.; Ma, J.; Wu, J.; Yung, K. C.; Xie, C. S. Study on the Properties of the Epoxy-Matrix Composites Filled with Thermally Conductive AlN and BN Ceramic Particles. *J. Appl. Polym. Sci.* **2010**, *118*, 2754–2764.

(30) Chen; Yu; Adler, S. B. Thermal and Chemical Expansion of Sr-Doped Lanthanum Cobalt Oxide ($La_{1-x}Sr_xCoO_{3-\delta}$). *Chem. Mater.* **2005**, *17* (17), 4537–4546.

(31) Holliday, L.; Robinson, J. Review: The Thermal Expansion of Composites Based on Polymers. *J. Mater. Sci.* **1973**, *8* (3), 301–311.

(32) Gorninski, J. P.; Dal Molin, D. C.; Kazmierczak, C. S. Strength Degradation of Polymer Concrete in Acidic Environments. *Cem. Concr. Compos.* **2007**, *29* (8), 637–645.

(33) Nicolson, A. M.; Ross, G. F. Measurement of the Intrinsic Properties of Materials by Time-Domain Techniques. *IEEE Trans. Instrum. Meas.* **1970**, *19* (4), 377–382.

(34) Weir, W. B. Automatic Measurement of Complex Dielectric Constant and Permeability. *Proc. IEEE* **1974**, *62* (1), 33–36.

(35) Deepa, K. S.; Shaiju, P.; Sebastian, M. T.; Gowd, E. B.; James, J. Poly(Vinylidene Fluoride)–$La_{0.5}Sr_{0.5}CoO_{3-\delta}$ Composites: The Influence of LSCO Particle Size on the Structure and Dielectric Properties. *Phys. Chem. Chem. Phys.* **2014**, *16* (32), 17008–17017.

(36) Señarís-Rodríguez, M. A.; Goodenough, J. B. Magnetic and Transport Properties of the System $La_{1-X}Sr_xCoO_{3-Delta}$ ($0 < x \leq 0.50$). *J. Solid State Chem.* **1995**, 323–336.

(37) Al-Saleh, M. H.; Sundararaj, U. X-Band EMI Shielding Mechanisms and Shielding Effectiveness of High Structure Carbon Black/Polypropylene Composites. *J. Phys. D. Appl. Phys.* **2013**, *46* (3), 035304.

(38) Deepa, K. S.; Sebastian, M. T.; James, J. Effect of Interparticle Distance and Interfacial Area on the Properties of Insulator-Conductor Composites. *Appl. Phys. Lett.* **2007**, *91* (20), 202904.

(39) Lee, H.-C.; Kim, J.-Y.; Noh, C.-H.; Song, K. Y.; Cho, S.-H. Selective Metal Pattern Formation and Its EMI Shielding Efficiency. *Appl. Surf. Sci.* **2006**, *252* (8), 2665–2672.

(40) Markham, D. Shielding: Quantifying the Shielding Requirements for Portable Electronic Design and Providing New Solutions by Using a Combination of Materials and Design. *Mater. Des.* **1999**, *21* (1), 45–50.

(41) Gamble, J.; Yats, L. D. EMI Shielding Composites. US Patent, US5399295, **1994**.

(42) Bigg, D. M.; Stutz, D. E. Plastic Composites for Electromagnetic Interference Shielding Applications. *Polym. Compos.* **1983**, *4* (1), 40–46.

(43) Simon, R. M. EMI Shielding Through Conductive Plastics. *Polym. Technol. Eng.* **1981**, *17*, 1–10.

(44) Perelaer, J.; Hendriks, C. E.; de Laat, A. W. M.; Schubert, U. S. One-Step Inkjet Printing of Conductive Silver Tracks on Polymer Substrates. *Nanotechnology* **2009**, *20* (16), 165303.

(45) Wang, H. B.; Wei, Q. F.; Wang, J. Y.; Hong, J. H.; Zhao, X. Y. Sputter Deposition of Nanostructured Antibacterial Silver on Polypropylene Non-Wovens. *Surf. Eng.* **2008**, *24* (1), 70–74.

(46) Sahu, D. R.; Lin, S.-Y.; Huang, J.-L. Improved Properties of Al-Doped ZnO Film by Electron Beam Evaporation Technique. *Microelectronics J.* **2007**, *38* (2), 245–250.

(47) J.N.Balaraju; Radhakrishnan, P.; V.Ezhilselvi; Kumar, A. A.; Chen, Z.; K.P.Surendran. Studies on Electroless Nickel Polyalloy Coatings over Carbon Fibers/CFRP Composites. *Surf. Coatings Technol.* **2016**, *302*, 389–397.

(48) Jing, X.; Wang, Y.; Zhang, B. Electrical Conductivity and Electromagnetic Interference Shielding of Polyaniline/Polyacrylate Composite Coatings. *J. Appl. Polym. Sci.* **2005**, *98* (5), 2149–2156.

(49) Niu, Y. Electromagnetic Interference Shielding with Polyaniline Nanofibers Composite Coatings. *Polym. Eng. Sci.* **2008**, *48* (2), 355–359.

(50) Erdoğan, M. K.; Karakişla, M.; Saçak, M. Preparation, Characterization and Electromagnetic Shielding Effectiveness of Conductive Polythiophene/Poly(Ethylene Terephthalate) Composite Fibers. *J. Macromol. Sci. Part A* **2012**, *49* (6), 473–482.

(51) Wang, L.-L.; Tay, B.-K.; See, K.-Y.; Sun, Z.; Tan, L.-K.; Lua, D. Electromagnetic Interference Shielding Effectiveness of Carbon-Based Materials Prepared by Screen Printing. *Carbon.* **2009**, *47* (8), 1905–1910.

(52) Lee, S. W.; Kim, K. K.; Cui, Y.; Lim, S. C.; Cho, Y. W.; Kim, S. M.; Lee, Y. H. Adhesion Test of Carbon Nanotube Film Coated onto Transparent Conducting Substrates. *Nano* **2010**, *05* (03), 133–138.

(53) Wang, W. D.; Xu, Q.; Zhou, S. X.; Deng, W. W. Preparation of Waterborne Graphite Conductive Coating and Study of Its Electromagnetic Shielding Performance. *Appl. Mech. Mater.* **2013**, *313–314*, 241–244.

(54) Lim, J. Method of Manufacturing Electromagnetic Interference (EMI) Shielding Filter for Plasma Display Panel and EMI Shielding Filter for Plasma Display Panel Using the Same. US Patent, US 8198810 B2 (2012), **2012**.

(55) Lim, J. Method of Manufacturing Electromagnetic Interference (Emi) Shielding Filter for Plasma Display Panel and Emi Shielding Filter for Plasma Display Panel Using the Same. US Patent, US 2010/0164354 A1, **2010**.

(56) Salam, B.; Lai, W. L.; Albert, L. C. W.; Keng, L. B. Low Temperature Processing of Copper Conductive Ink for Printed Electronics Applications. *IEEE 13th Electron. Packag. Technol. Conf. EPTC 2011* **2011**, No. 1, 251–255.

(57) Chun, S.; Grudinin, D.; Lee, D.; Kim, S. H.; Yi, G. R.; Hwang, I. Roll-to-Roll Printing of Silver Oxide Pastes and Low Temperature Conversion to Silver Patterns. *Chem. Mater.* **2009**, *21* (2), 343–350.

(58) Wang, L. B.; See, K. Y.; Zhang, J. W.; Salam, B.; Lu, A. C. W. Ultrathin and Flexible Screen-Printed Metasurfaces for EMI Shielding Applications. *IEEE Trans. Electromagn. Compat.* **2011**, *53* (3), 700–705.

(59) Jan Ziaja, Grzegorz Szafran, M. J. Impact of Technology on the Shielding Effectiveness of Barrier Materials Damping Frequency Selected Electromagnetic Fields. In *PIERS Proceedings*; **2013**.

(60) Dijith, K. S.; Pillai, S.; Surendran, K. P. Thermophysical and Microwave Shielding Properties of $La_{0.5}Sr_{0.5}CoO_{3-\delta}$ and Its Composite with Epoxy. *J. Electron. Mater.* **2017**, *46* (8), 5158–5167.

(61) Guo, Q.; Fan, G.; Xiong, D.-B.; Zhang, D.; Li, Z.; Tan, Z.; Cao, M. Graphene-and-Copper Artificial Nacre Fabricated by a Preform Impregnation Process: Bioinspired Strategy for Strengthening-Toughening of Metal Matrix Composite. *ACS Nano* **2015**, *9* (7), 6934–6943.

(62) Thi, P.; Mai, T.; Chau, C. N.; Boi, L. Van; Hoan, N. X.; Martin, I.; Carriere, P. The Role of Epoxy Matrix Occlusions Within $BaTiO_3$ Nanoparticles on the Dielectric Properties of Functionalized $BaTiO_3$ / Epoxy Nanocomposites. *Compos. Part A Appl. Sci. Manuf.* **2016**, *90*, 528–535.

(63) Geetha, S.; Satheesh Kumar, K. K.; Rao, C. R. K.; Vijayan, M.; Trivedi, D. C. EMI Shielding: Methods and Materials-A Review. *J. Appl. Polym. Sci.* **2009**, *112* (4), 2073–2086.

(64) Saini, P.; Choudhary, V. Enhanced Electromagnetic Interference Shielding Effectiveness of Polyaniline Functionalized Carbon Nanotubes Filled Polystyrene Composites. *J. Nanoparticle Res.* **2013**, *15* (1), 1415.

Chapter 3

$La_{0.5}Sr_{0.5}CoO_{3-\delta}$ Foam Structures and Nanowires for Microwave Shielding Applications

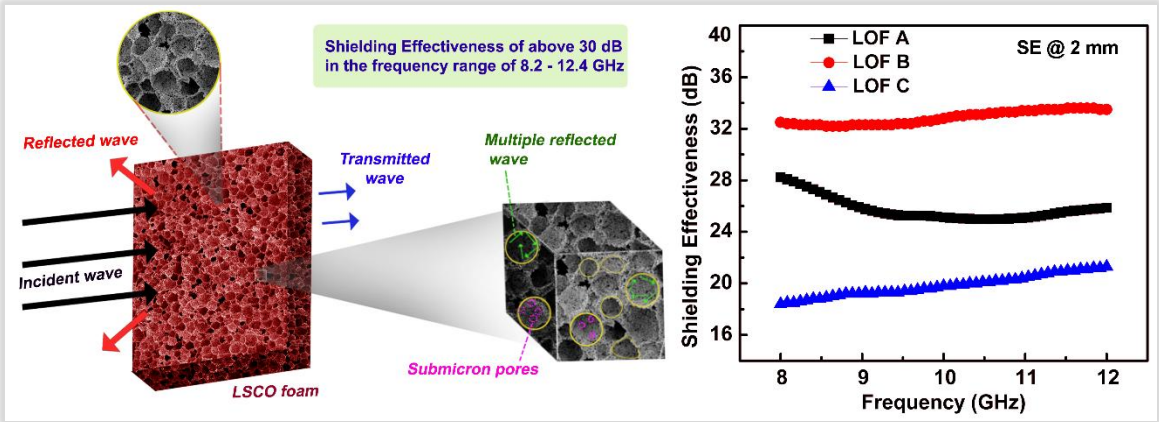

$La_{0.5}Sr_{0.5}CoO_{3-\delta}$ foams with broad range of porosities (76.9 to 90.3 %) having near spherical cells were prepared through emulsion freeze gelcasting route. The LSCO foams have compressive strength and Young's modulus in ranges of 1 to 7 MPa and 57 to 428 MPa, respectively. Impressive EMI SE as high as 33 dB has been achieved for LSCO foams prepared at a porosity level of 80 % with 10 vol. % LSCO in the composition. The developed LSCO foams are lightweight and capable of withstanding harsh environmental conditions, since they are free from oxidation and survivable enough at high temperature. Alternatively, in an attempt to investigate the trend in the physical characteristics of LSCO based nanosystems, a microemulsion technique was adopted to synthesis the LSCO nanowires. The as-grown nanowires having a diameter range of 15-35 nm, exhibited a room temperature conductivity of 120 S/cm and T_C of 225 K. LSCO nanowires also exhibited promising SE in the range of 28.5-32 dB, which is near to a shielding efficiency of 99.9 %. The non-corrosive, high temperature withstanding LSCO nanowires can be used as fillers for flexible and bendable EMI shielding solutions after suitable chemical engineering.

3.1 Conducting $La_{0.5}Sr_{0.5}CoO_{3-\delta}$ Based Macroporous Foams for Harsh Condition Microwave Shielding

3.1.1 Introduction

As far as satellite and aeronautical applications are considered, light weight porous ceramic EMI solutions are more suitable since they can save materials and energy. These porous ceramic structures possess several advantages over traditional metal and carbon-based EMI shielding materials, thanks to former's high mechanical strength and thermal stability, which could guarantee their smooth functioning at harsh environments. Among different porous structures, foams are unique since they possess well connected conductive network structure with low density, thermal insulation and enhanced microwave absorption properties. In the context of microwave shielding applications, metal oxides (either conducting or magnetic) can be a promising candidates; since they are free from oxidation and can withstand high temperatures. There are a few reports on conducting oxides which are investigated for EMI shielding applications.[1-4] Although perovskite oxides are regarded as the benchmark materials for high proton conductivity oxides, noteworthy attempts aimed at exploring their EM wave management, are feebly less. This can be partly due to the brittleness and high density nature of these oxides in hard ceramic form, which are some difficult challenges in EM shielding coatings. A possible solution is polymer composite way, which can circumvent some of the above mentioned drawbacks at the cost of diminished EMI shielding performance. Rather than compositing, a promising strategy will be making foam structures, which will lower both the density and thermal conductivity while maintaining the EMI shielding nature of the material to the required level. In this way, creative introduction of systematic porosity

augments the applicability of conductive ceramic materials, which are already having EMI wave attenuation properties.

Due to the wide usage of porous ceramics for aeronautic and avionic applications, a lot of research is going on in the direction of tuning the sizes, shapes, amounts and interconnections of distributed pores. Depending on the pore diameter porous materials are classified as macro (pore diameter ($d > 50$ nm), meso ($d = 2$ to 50 nm) and micro ($d < 2$ nm) porous foams.[5] Macro porous ceramics are ideal for harsh environment EMI shielding applications. In a macro porous shielding foam[6], multiple internally reflected waves enable prolonged path lengths, thereby creating an increased opportunity for EM wave absorption.[7,8]

In the present investigation, our interest was to develop a novel macroporous system derived from the conducting pervoskite oxide $La_{0.5}Sr_{0.5}CoO_{3-\delta}$ (LSCO). These oxides possess moderately high electrical conductivity (>1000 S/cm) for their cubic phase, that entitle them suitable applications in lithium-air batteries[9-11] solid oxide fuel cells,[12] and sensor materials.[13,14] Until recently their microwave absorbing abilities are unknown, wherein our group developed an EMI shielding composite employing LSCO as the filler in epoxy matrix.[15] Usually macroporous ceramic architectures are realized mainly through one of the following routes- direct foaming, partial sintering, sacrificial fugitives and replica template route. Herein, we followed an emulsion route which is simple, low cost and environmental friendly.[5] This was achieved by systematically introducing macropores in the LSCO matrix, yielding better microwave absorption and specific shielding characteristics. This is the first report on the EM wave attenuating characteristics of high temperature stable pervoskite based conductive oxide foams whose synthesis do not require any special atmosphere, as we do in carbonaceous foams.

3.1.2 Materials and Methods

The oil phase which has a melting range of 40–41 ^{o}C, is a food grade hydrogenated vegetable oil (HVO) (Dalda, Bunge India Pvt. Ltd., India) procured from local market. Sodium dodecyl sulphate (SDS) (Merck) and carrageenan (Sigma–Aldrich) were used as emulsifying agent and gelling agent, which are of analytical reagent (AR) grade. An aqueous ammonium poly(acrylate) solution – 35 wt. % (Darvan 821A, Vanderbilt company Inc. Norwalk, CA) was selected as a dispersant. AR grade toluene (Merck) served as the solvent.

LSCO was prepared from the precursor oxides through solid state route, as reported in Chapter 2.[15] Solid state derived LSCO powder was milled in a tumbling ball mill for 24 h using distilled water and zirconia balls with powder to ball ratio of 1: 3. The fine slurry obtained was dried to get the fine LSCO powder. This LSCO powder was used as the precursor for the preparation of LSCO foam. The synthesis of LSCO foam involves two stages: Stage I involves the slurry preparation, where the LSCO powder, ammonium poly(acrylate) dispersant and distilled water were mixed according to the required volume ratio (20 or 10 vol. %) and ball milled for 12 h. Since the volume percentage of aqueous LSCO slurries (referred hereafter as, ALS) were maintained as 20 and 10 in the present case the corresponding dispersant concentration was kept to be 1 wt. % of that of LSCO powder loading. After 12 h of mixing the slurry was transferred to a round bottom (RB) flask which was kept in a water bath at 90 °C. The gelling agent which is 1.5 wt. % of the water content in the aqueous slurry was added to the RB and kept for mechanical stirring using a Teflon paddle for half an hour. The stage II, involving mixing of both HVO and SDS in a separate beaker in a water bath at 85 °C. The amount of oil phase is fixed according to the volume percentage of aqueous phase. It can be in 1:1 or 1:2 ratios with the aqueous phase as per the composition in consideration. The amount

of SDS was 0.4 wt. % of oil phase. The molten HVO containing SDS was transferred to the aqueous LSCO suspension kept at 85 ^{o}C. The stirring was continued for half an hour to get a stable emulsion. Later the emulsion was cast into a suitable mould and cooled under 5 ^{o}C in a refrigerator for half an hour. The gelled bodies were dried at room temperature. Next process involves removal of HVO from the dried body using toluene solvent in a soxhlet extraction set up. The oil free samples obtained after soxhlet extraction were sintered in a high temperature furnace at 1150 ^{o}C for 4 h. The heating rate was kept to be 1 ^{o}C /min up to 700 ^{o}C and 5 ^{o}C thereafter. There was a dwell at 300 ^{o}C for the removal of residual oil or solvent. The porosity of the sintered samples was calculated from the density measurements.

Table 3.1: Given the composition and properties of the three LSCO foam compositions.

Material code	Composition of foam samples	Green foam density (g/cm^3)	Sintered foam density (g/cm^3)	Porosity (in %) (Archimedes method)
LOF A	20 vol % LSCO Oil to water ratio = 1 : 1	0.75	1.41	76.8
LOF B	10 vol % LSCO Oil to water ratio = 1 : 1	0.61	1.16	80.9
LOF C	10 vol % LSCO Oil to water ratio = 2 : 1	0.31	0.59	90.3

In the current study by varying the volume percentage of LSCO powder as well as by changing the ratio of oil phase in the composition of slurry, three different LSCO foams having diverse porosities and densities are derived. Hereafter, the LSCO foam prepared from 20 vol.% ALS with HVO to ALS volume ratio of 2, is termed as LSCO Foam Sample-A (LOF A) and those prepared from 10 vol.% ALS with HVO to ALS volume ratios of 1 and 2 are termed as LSCO Foam Sample-B (LOF B) and LSCO Foam Sample-C (LOF C), respectively. The density

observed for sintered LOF A, LOF, B and LOF C are 1.41, 1.16 and 0.59 g/cm^3, respectively. The corresponding porosities are 76.8 %, 80.9 % and 90.3 %, respectively. The three studied emulsion compositions are given in Table 3.1.

3.1.3 Results and Discussion

3.1.3.1 Structural Evolution

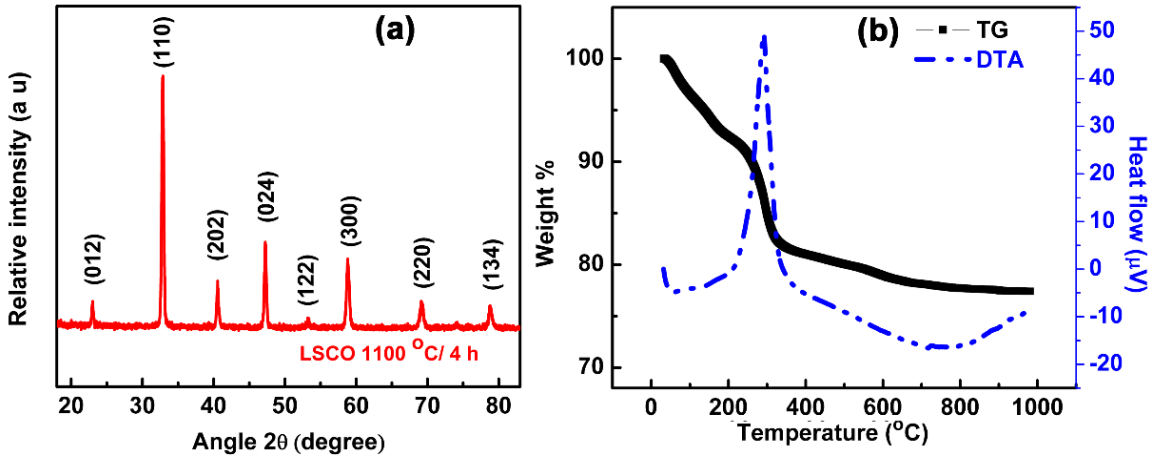

Fig. 3.1: (a) X-ray diffraction pattern of $La_{0.5}Sr_{0.5}CoO_{3-\delta}$ (LSCO) calcined at 1100 ºC and (b) gives the thermogram of green LSCO foam.

The conducting oxide, $La_{1-x}Sr_xCoO_{3-\delta}$ is derived by the substitution of Sr^{2+} with the La^{3+} ions in the parent compound $LaCoO_3$. Among the various Sr^{2+} doped $LaCoO_3$ systems, $La_{0.5}Sr_{0.5}CoO_{3-\delta}$ shows the best conductivity value,[16] which brought the system to the broad arena of EMI shielding applications recently.[15,17] Fig. 3.1(a) shows the X-ray diffraction (XRD) pattern of synthesized $La_{0.5}Sr_{0.5}CoO_{3-\delta}$ ceramic calcined at 1100 ºC for 4 hours. All the detected diffraction peaks could be indexed with JCPDS: 48-0122, signifying a complete phase formation of LSCO.

The prepared LSCO powder disperses well in aqueous medium using the ammonium poly(acrylate) dispersant to form slurries. The HVO containing the SDS disperses well in the aqueous LSCO suspension upon mechanical mixing to form a stable emulsion. The emulsions cast in a mould undergo gelation on cooling due to the freezing of HVO and physical cross-lining of carrageenan. The gelled bodies upon drying at ambient condition followed by oil extraction using toluene, produces porous green LSCO foam bodies of densities 0.75, 0.61 and 0.31 g/cm^3. These green bodies were analyzed for thermal characteristics. Fig. 3.1(b) shows the thermogram of green LSCO foam. The first region between 35 to 220 ^{o}C having 8 % weight loss may be due to the escape of moisture and solvent trapped inside the porous network. The second region i.e., from 220 to 320 ^{o}C, consists of about 8.9 % weight loss as a result of the burning of carrageenan network from the green foam. The LSCO green foam undergoes uniform shrinkage during sintering due to densification. As mentioned, there can be multiple microstructural transformations happen during heating and the final sintered body is expected to be stronger than the initial green bodies.

3.1.3.2 Scanning Electron Microscopy

Micrographs for all the studied composition give a clear indication about the kind of foam structure we derived. The open cellular foam with macroporous structure is clearly visible in Fig. 3.2. The LOF A shows a very low cell size in the range of 8 to 15 μm, whereas the LOF B and LOF C shows relatively large cell sizes of 15 to 30 and 60 to 90 μm, respectively. That is, a large increase in cell size was observed by decreasing the ALS concentration while keeping the HVO to ALS volume ratio same (LOF B) and later by increasing the HVO to ALS volume ratio at a constant ALS concentration (LOF C). Another interesting feature of the foam structure is that, within the micron sized pores (see Fig. 3.2(h))

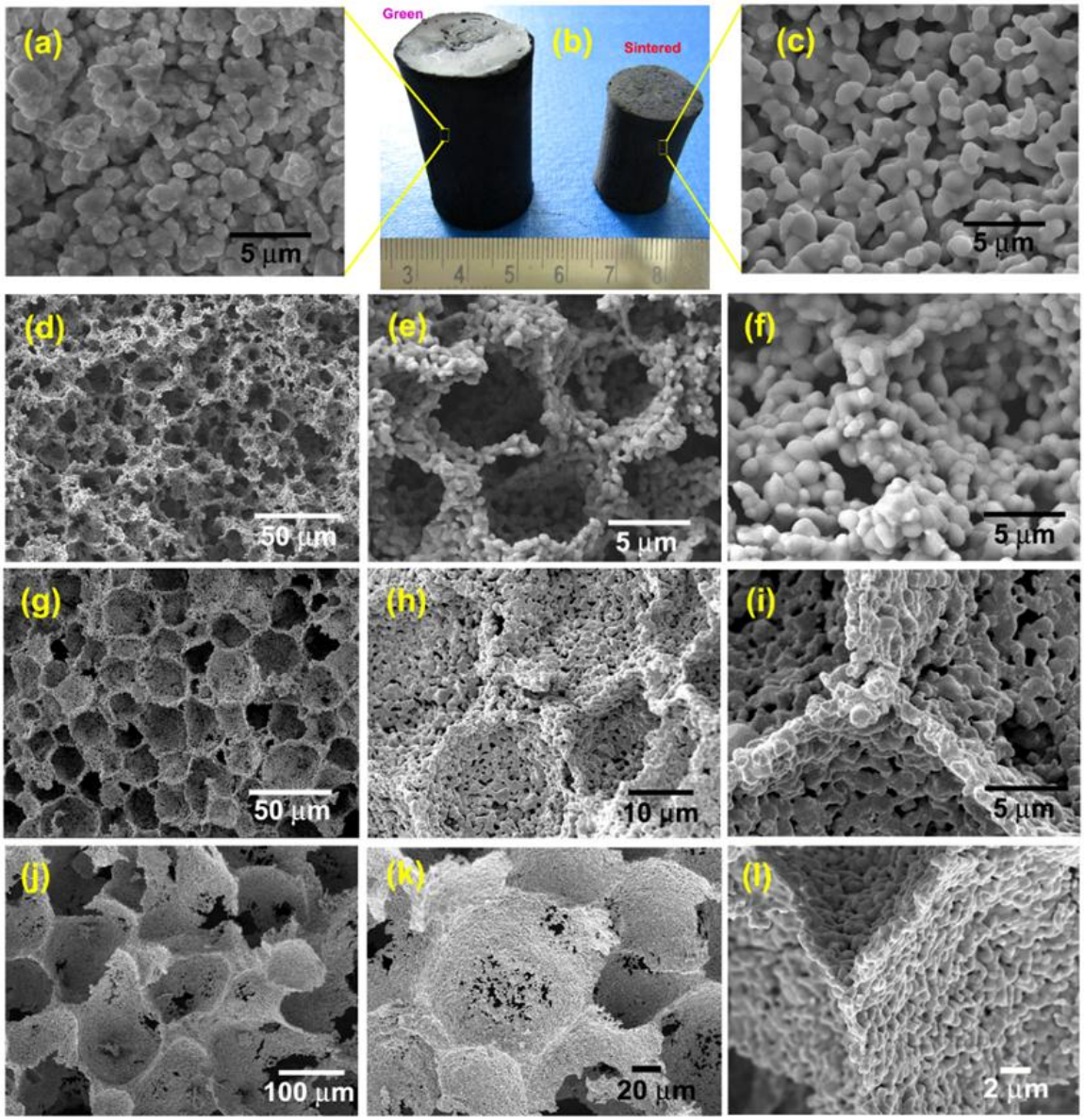

Fig. 3.2: (a) and (c) are the micrographs and (b) is the photograph of green and sintered foam (d) and (e) are scanning electron micrographs of different magnification of LOF A, (g) and (h) are of LOF B sample, (j) and (k) are different magnification of LOF C samples. (f), (i) and (l) indicates the strut region of three foam samples.

there are noticeable submicron sized pores which may have arisen due to the escape of oil phase. Such submicron sized pores are more predominant in the LOF C composition. Fig. 3.2(h) clearly portrays macropores with cells having numerous submicron sized pores within

each cells, which are ultimately the openings between the fused LSCO particles left by the thermally evaporated oil phase. These connected particles inside the cells is having a major role in enhanced physical characteristics. Fig. 3.2(j) clearly indicates the larger cells, and improper connectivity between particles are visible in each cells of Fig. 3.2(k). The strut region in all the foam samples are shown in Figs 3.2(f), (i) and (l). Strut regions are pronounced in the case of LOF A and LOF B samples, while they are lesser and thinner in LOF C samples.

3.1.3.3 Mechanical Properties

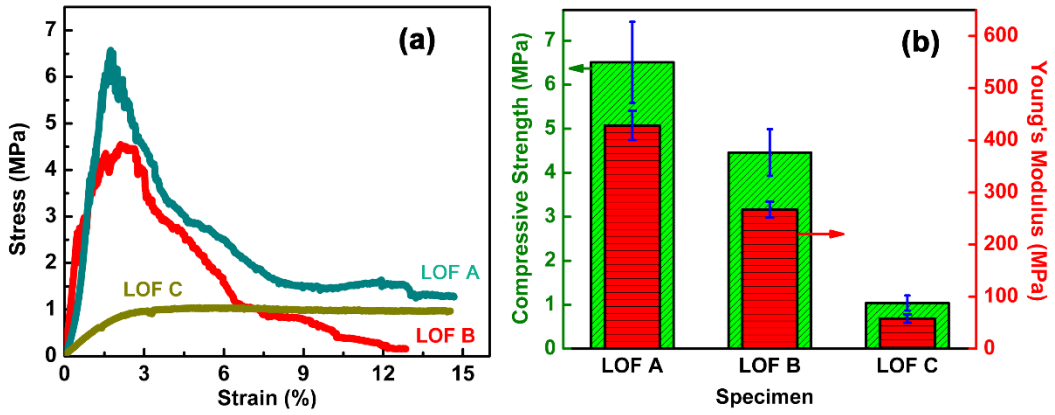

Fig. 3.3: (a) Stress–strain graph of the LSCO foams prepared at various weight loading of filler and HVO to ALS volume ratios. (b) The effect of various weight loading and HVO to ALS volume ratio on the compressive strength and Young's modulus of the LSCO foam.

The mechanical strengths of the three foams were investigated using standard ASTM protocols. Fig. 3.3(a) shows the stress–strain plot of the LSCO foams prepared at different HVO to ALS volume ratios. The macroporous LSCO foam prepared from 20 vol.% aqueous LSCO slurry shows higher compressive strength. For LOF A and LOF B the stress-strain behavior is similar to a brittle solid. That is, the stress rapidly declined after reaching a maximum value. On the other hand, the foam with the highest porosity (~ 90) showed a plateau region after the peak stress value characteristic of a brittle elastic foam material. The effect of

various weight loading and HVO to ALS volume ratio on the compressive strength and Young's modulus of the macroporous LSCO ceramics are shown in Fig. 3.3(b). The highest stress value in the stress–strain graph is the compressive strength, which has got considerably lowered with increasing porosity. That is, from LOF A to LOF C, the porosity changes from 76.9 to 90.3 % and the corresponding change in the average compressive strength value is from 6.51 to 1.04 MPa. On the other hand, the average Young's modulus decreases from 428.39 to 57.95 MPa with increment in porosity. The highest strength is observed for LOF A sample which is attributed to the strong connectivity of small spherical cells through thicker strut regions. But the least dense LOF C foam is having lowest strength among the three, since the porosity is on the highest side with pore size in the sub millimeter range. In a nut shell, the compressive strength and Young's modulus exhibited a monotonous relationship with porosity as expected.

3.1.3.4 Electrical Properties

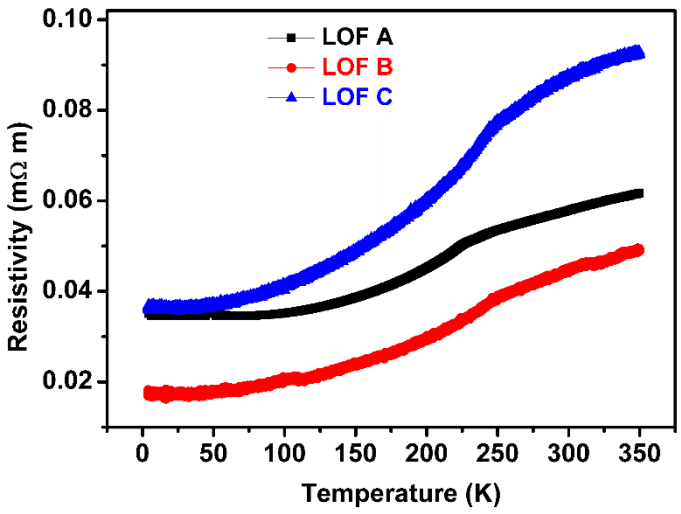

Fig. 3.4. R-T analysis of various LSCO foams in the temperature range of 4 K to 350 K.

Solid state derived LSCO is reported to have a metallic nature.[18] The perovskite structured $La_{0.5}Sr_{0.5}CoO_3$ was previously reported to possess high electronic conductivity (>1000 S/cm).[18-20] The metallic behavior of these oxides can be explained on the basis of existing overlapped electron band structure in the Co–O–Co bond, detailed in the itinerant electron model.[21,22] Fig. 3.4 shows temperature dependent electrical resistivity studies for LSCO foam samples in a temperature range from 4 K to 350 K, recorded at 0 T. As for all metallic structures, the electrical conductivity of LSCO decreases with increasing temperature.[23] Electrical conductivity of foams depends on various parameters like foam topology (whether open or closed structure) and pore size.[24] Interfacial area and thickness of the cell wall plays a major role on determining the electrical conductivity for open cell foams. A bump is visible over 210 - 260 K representing ferromagnetic to paramagnetic transition due to the change in the spin state of cobalt ions.[16] In porous LSCO samples, the resistivity depends on the connectivity between conductive grains. For LSCO foam samples, air act as insulating interfaces between the particles. Here the least resistance is observed in the case of LOF B. As observed in the micrographs, the stronger strut region and well-connected grains in each cell make the LOF B unit a better conductor than the rest. In the complex perovskite $La_{0.5}Sr_{0.5}CoO_3$, divalent Sr^{2+} ions partly replace trivalent La^{3+} ions, thereby inducing a transition from Co^{3+} to Co^{4+} and this [Co^{4+} Co^{3+}] species contribute to the electrical conductivity. Obviously, $La_{0.5}Sr_{0.5}CoO_{3-\delta}$ is a p-type conductor, since conduction mechanism is dictated by holes. The important characteristics of these oxides are high density of electrons through low conductivity and existence of metallic state for even $\sigma << \sigma_{MOTT}$ or could be considered as systems with low electron diffusivity.[25]

3.1.3.5 EMI Shielding Properties

The EMI shielding values of the LOF series having 2 mm thickness are shown in Fig. 3.5(a). The highest SE value was observed for LOF B samples, i.e. 32 - 33 dB and for LOF A and LOF C the values are in the range of 25 - 28 dB and 18 - 21dB. The trend in the conductivity (as seen the earlier Fig. 3.4) follows the order LOB > LOF A > LOF C and so are their EMI shielding values.

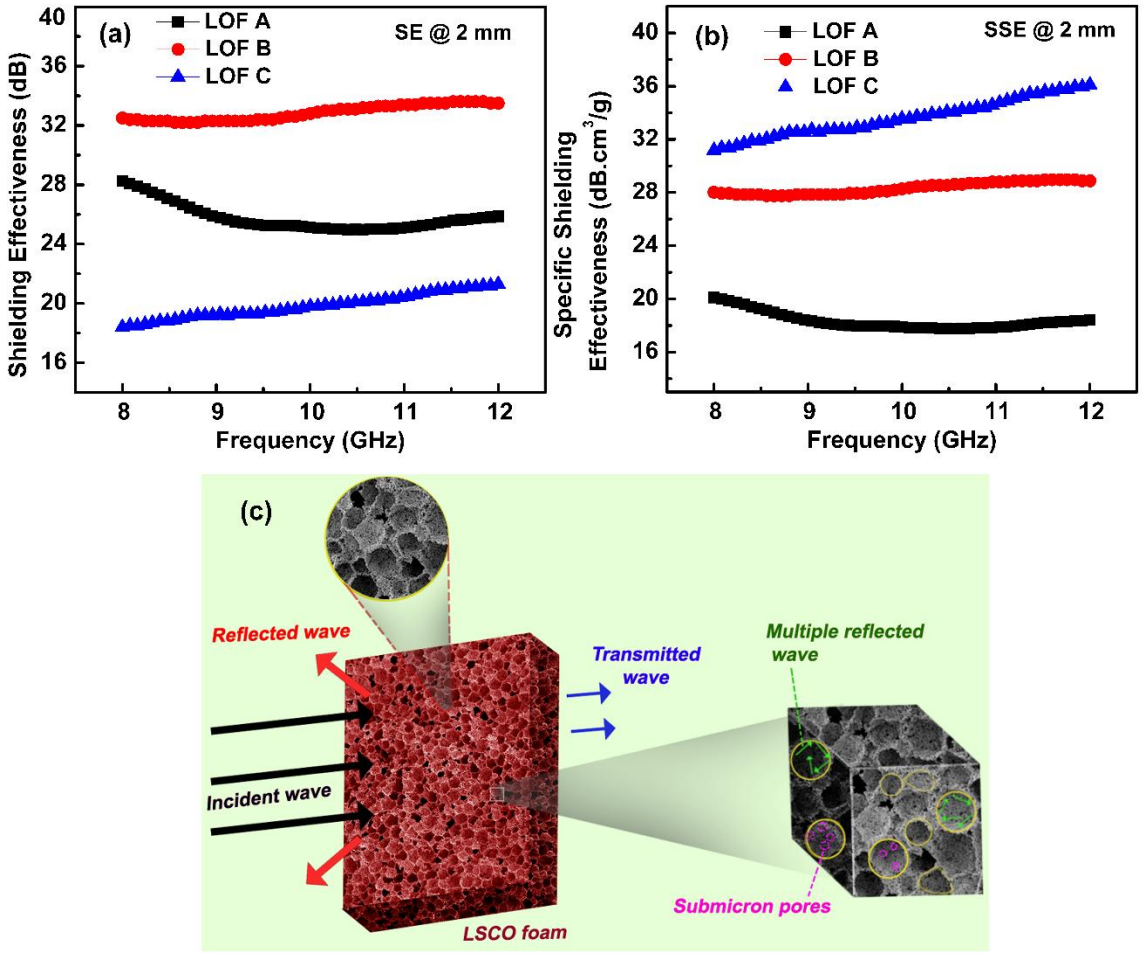

Fig. 3.5: (a) Shielding effectiveness and (b) specific shielding effectiveness of developed macroporous LSCO foams having 2 mm thick in the X band. (c) is a schematic representation of the electromagnetic wave attenuation mechanism inside the macroporous LSCO.

Our earlier investigation revealed that dense 2 mm thick LSCO sheets showed an EMI SE of 38 - 40 dB.[15] As expected, foam samples possess porosities ranging from 76 to 90 % when we move from LOF A to LOF B to LOF C. Out of the total shielding effectiveness of all the studied LSCO foams, the absorption shielding overwhelms the reflection. The hierarchical structural skeleton of the foams may favor the observed trend. For example, in the dense materials, the incoming EM wave will be facing greater impedance mismatch at the interface between material and air than they do in foam structure. In the current foam structures, the porosity varies from 76 to 90 %, which means the majority of the shield's volume is filled with air. A schematic representation of the interaction of LSCO foam with EM wave, alongwith the possible shielding mechanisms especially the multiple reflection possibilities are depicted in Fig. 3.5(c). Inside the foam, the EM wave is encountering obviously more interactive surfaces than the dense material (see Fig. 3.5 (c)). So when EM waves enters into pores, there created a low impedance path for them which undergo multiple internal reflections. It will definitely add to the absorption shielding efficiency of the system. The electrical conductivity and EM wave shielding can be theoretically correlated by the following equations,[26,27]

$$A = at(f\mu_r\sigma_r)^{1/2} \quad (3.1)$$

$$R = b\text{-}10 \log (f\mu_r/\sigma_r) \quad (3.2)$$

$$B = 20 \log (1- e^{-2t/\delta}) \quad (3.3)$$

where A, R and B are absorption, reflection and multiple reflection factors. a and b are constants while f, μ_r, σ_r, δ and t are the frequency, permeability, conductivity, skin depth and thickness respectively. From the above relations, it is clear that the electrical conductivity plays a major contribution to the absorption shielding mechanism. As the system is conductive in

nature, there is a possibility for micro-current generation inside the system on exposure to the EM waves. This will eventually damp the incoming wave. Furthermore, the higher microwave dielectric loss nature of the LSCO system will be promising in its wave attenuation nature.[28]

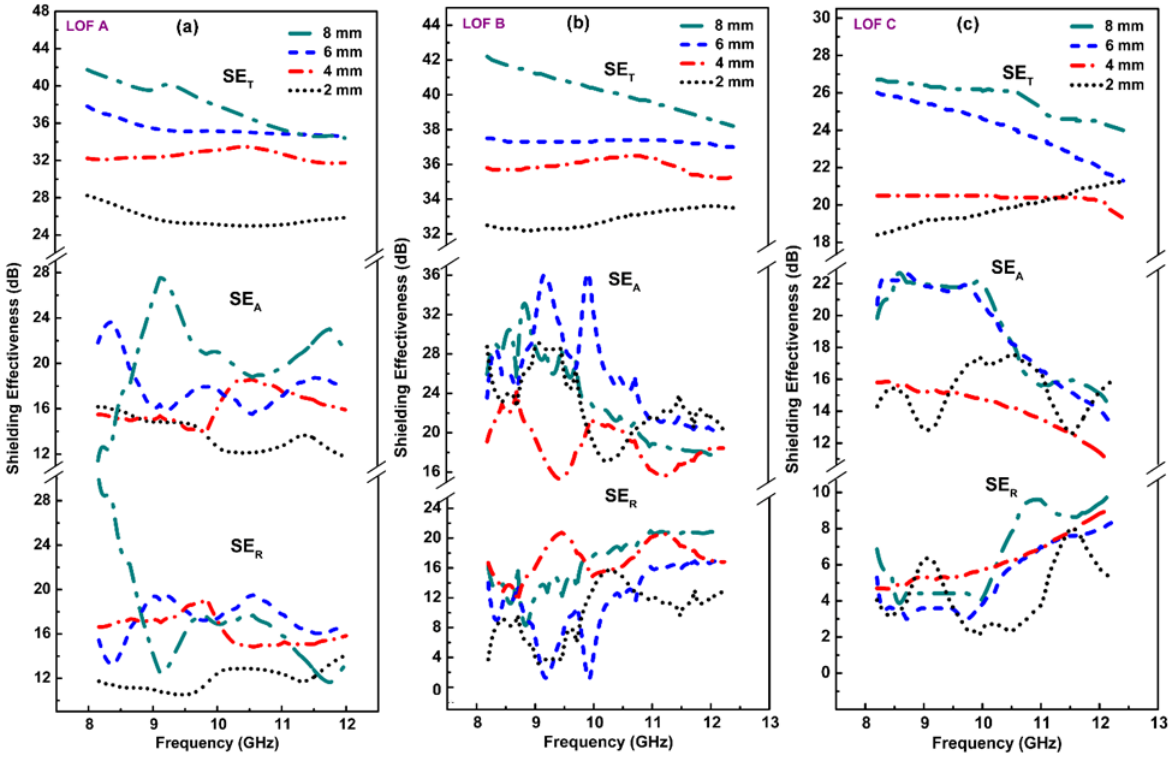

Fig. 3.6: Frequency-dependent variation of total EMI shielding effectiveness (SE_T), absorption shielding effectiveness (SE_A), and reflection shielding effectiveness (SE_R) of various thickness of developed LSCO foams over the entire X band frequency range (8.2–12.4 GHz).

Another peculiarity of the foam materials is their higher specific shielding effectiveness (SSE), which is defined as the SE per density of the material. The current system of LSCO foam, compared to the parent dense LSCO, possess promising SSE values. The calculated SSE values of foam structures of the LSCO are shown in the Fig. 3.5(b). The maximum SSE of 32 - 36 dB.cm^3/g is observed in the case of least dense LOF C sample, where the density is only 9.7 % of its parent material. The dense LSCO sample is showing a SSE value of 6 - 6.5 dB.cm^3/g. The SSE of LOF C is 5 times greater than that of dense LSCO.

Table 3.2: Comparison of high temperature withstanding ceramic foam for microwave shielding applications (RL: return loss).

	Material	Method of preparation	Nature of pore/Pore size	Measured frequency range	Thickness	EMI SE/RL	Ref.
1	Three-Dimensional Honeycomb SnO_2	Template method using polystyrene beads	Macroporous size 148 nm	4- 18 GHz	2 mm	> - 30 dB at 16-18 GHz range	[29]
2	Hierarchical Porous SiC Foam	Carbothermal reduction of carbonized dried dough	Macro-meso-micro pores coexist	8.2 – 12.4 GHz	3 mm	>- 20 dB at 8.2 – 12.4 GHz	[30]
3	3D porous Mn_2O_3 network	Hydrothermal route and subsequent annealing.	Macroporous size 50–100 nm	1 - 18 GHz	6 mm	- 27.1 dB at 3.1 GHz	[31]
4	Porous YSZ/SiC composite	Chemical vapor infiltration	Macroporous	8.2 - 12.4 GHz	3 mm	- 20.3 dB at 15 - 18 GHz	[6]
5	Zr/Si/C/O Ceramic Foams	Self-sacrificial template method	Mesoporous	1 - 18 GHz	7 mm	- 30 dB at 4 - 5 GHz	[32]
6	Porous Si_3N_4–SiC composite ceramic	Chemical vapor infiltration (CVI)	Macroporous size 0.5–1 μm	8.2 - 12.4 GHz	3.8 mm	- 30 dB at 8.7 GHz	[33]
7	Macroporous $La_{0.5}Sr_{0.5}CoO_{3-\delta}$	Emulsion freeze gelcasting route	Macroporous size 10 – 120 μm	8.2 - 12.4 GHz	2 mm	>- 32 dB at 8.2 - 12.4 GHz	current work

As the density changes from 6.10, 1.41, 1.16 to 0 .59 g/cm^3 the corresponding change in the average SSE value is 6, 18, 28 and 33 dB.cm^3/g at 10 GHz. Another observed trend in the results is that the increase in the SE value with the increase of the thickness of the LSCO foam

having the same pore-size distribution and porosity. Here the variation of SE with thickness is shown in the Fig. 3.6. The trend can be clearly explained on the basis of equations (3.1) and (3.3), where an increase in the thickness is observed to be influencing the absorption and multiple reflection loss simultaneously. For a system with same porosity, the larger thickness of the sample indicates more solid content and larger effective surface area. This in turn will provide more opportunities to EM wave to interact with the lossy LSCO and the attenuation will be more effective.

A comparative table of EMI shielding performance of the best attenuating ceramic foams are given in the Table 3.2. Here we have deliberately excluded carbonaceous foams for the sake of ease of comparison. As seen from the Table, the total shielding effectiveness of the shield largely depends on its thickness. In the case of porous structure like foams, the incoming EM wave must spend at least a wavelength in the absorber, in order to obtain reasonable absorption. Thus, thicker shields will have high attenuation since they could accommodate more wavelengths. Interestingly, the present shielding material, $La_{0.5}Sr_{0.5}CoO_{3-\delta}$ foam, outperform most of its ceramic foam counterparts, even at a normalized thickness of 2 mm. Such porous ceramic EMI solutions are ideal for satellite and aeronautical applications, where lightness and high thermal stability are critical.

3.1.4 Conclusions

In this study, macroporous forms derived from proton conductive perovskite ceramics are being reported for the first time. $La_{0.5}Sr_{0.5}CoO_{3-\delta}$ foams with tunable range of porosity and cell sizes were prepared through an emulsion freeze-gel casting route. The compressive strength of foams shows a dependency on their tailorable skeletal structure and porosity. Temperature dependent resistance studies convey their metallic nature. The *SE* of 32 - 33 dB

for the low density LSCO foam candidate having 2 mm thickness is excellent. For the studied samples, the variation trend in the EMI shielding values follows the same order of their respective electrical conductance. Here the major contribution to the total shielding is provided by the absorption component which is supplemented by the conducting nature of LSCO, as well as the peculiar void structure of the foam that enable multiple reflection possible at each cell. The SSE parameter of the LSCO foams were found to be better than their dense counterparts. Overall, the foaming procedure qualifies any oxide conductor to the broad domain of light weight EMI shielding applications. Such lightweight EM attenuating structures are most suitable for satellite and aeronautical structures that are subjected to under harsh environmental conditions where polymer composites fail, while macroporous ceramics can save materials and energy.

3.2 $La_{0.5}Sr_{0.5}CoO_{3-\delta}$ Nanowires for Microwave Shielding Applications

3.2.1 Introduction

Nanotechnology has contributed tremendously to the development of smart devices with fascinating electronic, optical, mechanical and thermal properties.[34] Nanowires, nanorods and nanotubes are different classes of 1D nanomaterials and they outperform the nanoparticles in many electronic applications, due to their interconnected nature; hence used in the fabrication of interconnects in smart devices. Smooth surfaces promote easier paths for electronic conduction and conducting polymers based nanowires and metal oxide derived nanowires have been largely reported in this regard. Most of the metal nanowire synthesis were based on template method; while electropolymerization technique was also widely employed for developing nanowires based on conducting polymers.[35] High surface area and connectivity are two important attributes that make them useful for multitude of applications. Metal and polymer based nanostructures suffer from oxidation and stability issues when used in high temperature applications. Hence ceramic based nanostructures are gaining wide attention in the context of high temperature EMI shielding applications. Last year, W. Zhou *et al*. investigated silicon nitride modified with silicon carbide nanofibers prepared by catalysis chemical vapour deposition through a gel casting procedure and reported a moderate SE in the range of 9.31 dB.[36] Perovskites nanomaterials are better choices for industrial applications due to their high conductivity in addition to the chemically inert and corrosion resistant nature.[37] There were only very few reports on perovskite nanowires as EMI shielding solutions. Recently, Liu *et al.* reported 2D nanocomposites with amorphous carbon and lanthanum ferrite, showing promising EMI shielding properties. These cation deficient composites exhibited a

SE of −26.6 dB at 9.8 GHz, for sample thickness of 2.94 mm.[38] As we discussed in Chapter 1, only a few conducting oxide nanostructures were reported to achieve 99.9 % shielding efficiency throughout the high frequency bands at a practical thickness limit of 2 mm.[39-42] As we have already observed EMI trends in LSCO bulk and foam structures which were found to have promising microwave attenuation, a detailed investigation is performed here on EMI properties of LSCO based nanostructures, prepared through microemulsion route.

3.2.2 Materials and Methods

Conducting perovskite LSCO nanowires were synthesized employing a microemulsion route. Microemulsion system consists of 30 mL isooctane, 6 mL butanol and 6 g CTAB, which form a miscible solution at ambient temperature (~60 ^{o}C). The prepared solution was divided into two portions. To the first portion, $La(NO_3)_3$, $Sr(NO_3)_2$ and $Co(NO_3)_2$ were added according to the stoichiometric ratio of the final composition. In the second portion KOH were added which would serve as the precipitating agent. After 15 min stirring, both these solutions were mixed together and vigorously stirred for few hours. Further the solution was kept at low stirring rate for 6 h at ambient temperature. Metal hydroxides precipitated inside the miscelle were retrieved by washing continuously with ethanol and deionised water. After thorough washing, the dried residue was calcined at 850 °C by slow heating at the rate of 1 °C/min in argon atmosphere to obtain perovskite LSCO nanowires. Thermogravimetric analysis was done to study the changes in precursor as well as phase formation. The phase purity of the synthesized nanowires was studied using XRD. The morphology and elemental mapping was performed using SEM and the lattice spacing, selected area diffraction patterns and energy dispersive spectroscopy of the nanowires were analyzed using TEM. The magnetic properties

of the nanowires were studied using VSM probe in PPMS and electrical conductivity was measured using four probe method.

3.2.3 Results and Discussion

3.2.3.1 Structural Characterization

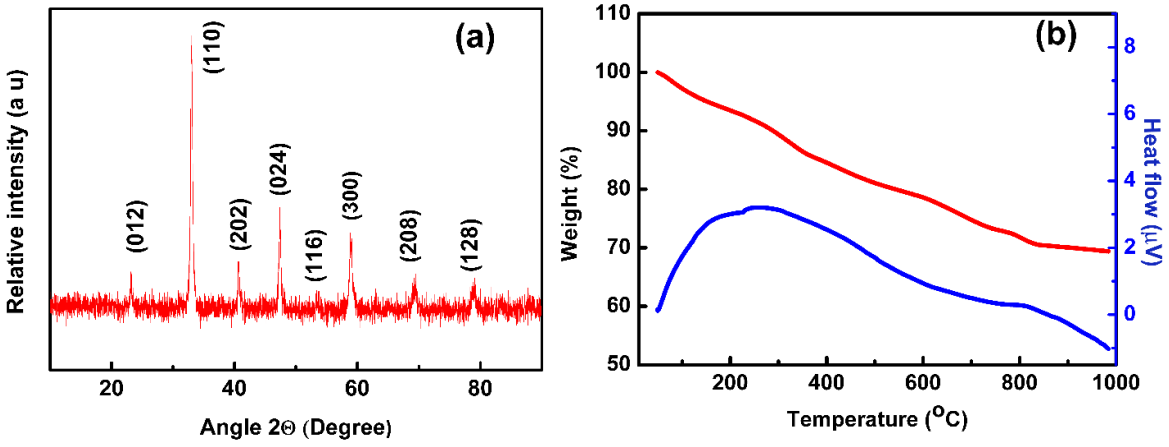

Fig. 3.7: (a) X- ray diffraction pattern of $La_{0.5}Sr_{0.5}CoO_{3-\delta}$ (LSCO) calcined at 850 °C and (b)TGA-DTA of LSCO nanowires.

The phase purity of the LSCO nanowires synthesized by microemulsion method is examined using XRD. Fig. 3.7(a) shows the XRD peaks of synthesized LSCO nanowires calcined at 850 °C. The peaks of the nanowires could be well indexed using JCPDS file no. 48-0122. The peaks are visibly broader than those obtained for solid state derived LSCO shown in Chapter 2.1, which may be due to their nanostructure. Thermogravimetric studies carried out for temperature range of 30-1000 °C depicted in Fig. 3.7(b), explain the formation stages of LSCO nanowires. A steady weight loss is observed from 30 to 825 °C, which includes the removal of solvents, burning of surfactants and crystalline phase formation. After 825 °C, there is no major visible weight loss which confirms the complete phase formation. The diffused exotherm around 150 to 350 °C comes from the decomposition/oxidation of residual

surfactants and co surfactants. The second exotherm is at 825 ^{o}C, which arises due to the crystalline phase formation of LSCO nanowires.

3.2.3.2 Morphological analysis

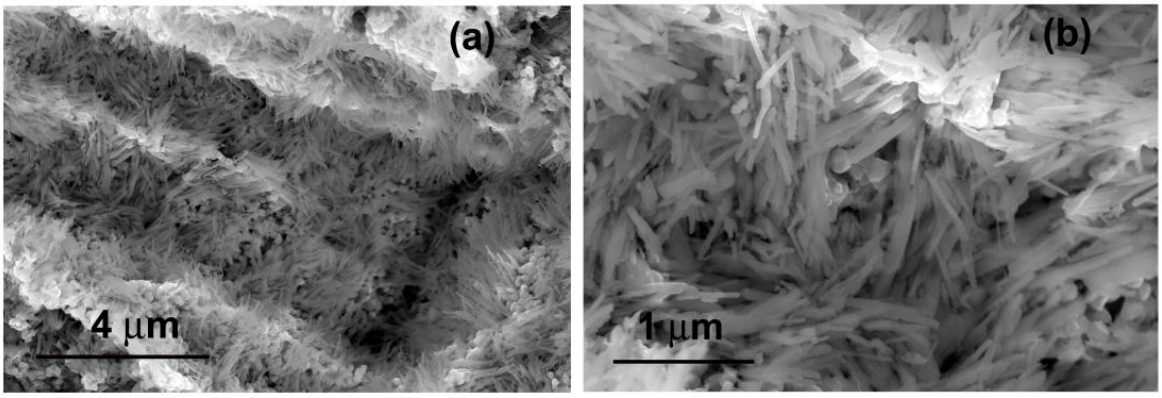

Fig. 3.8: (a) SEM micrographs of calcined LSCO nanostructures at low magnification and (b) at high magnification.

Cross section micrographs of pelletized LSCO nanowires are given in Figs 3.8(a) and (b). Aggregated nanowires with very few nanoparticles are seen in the micrographs. From the high magnification image in Fig. 3.8(b), the diameters are found to be in the nanometer range (< 50 nm). Elemental mapping has been performed on different sections of pelletized sample and representative image is shown in Figs 3.9(a-e). Fig. 3(a) shows the distribution of all the constituent elements in LSCO nanowires. The elemental distribution corresponding to La, Sr, Co and O are individually shown in Figs 3.9(b), (c), (d) and (e) respectively. Morphology of the nanowires obtained from TEM is depicted in Figs 3.10(a) and (b). From the low magnification image in Fig. 3.10 (a), it could be observed that nanorods are connected to each other forming a nanowire structure. The image analysis was done using ImageJ software and the diameter of the nanowires were obtained in the range of 15-35 nm. Using HRTEM (High Resolution TEM), their microstructure was further studied which is presented in Fig. 3.10(c).

As shown, the spacing between the periodic fringes is 0.27 nm which represents the (110) peak. This result matches well with the d spacing obtained for (110) peak from X-ray diffraction analysis.

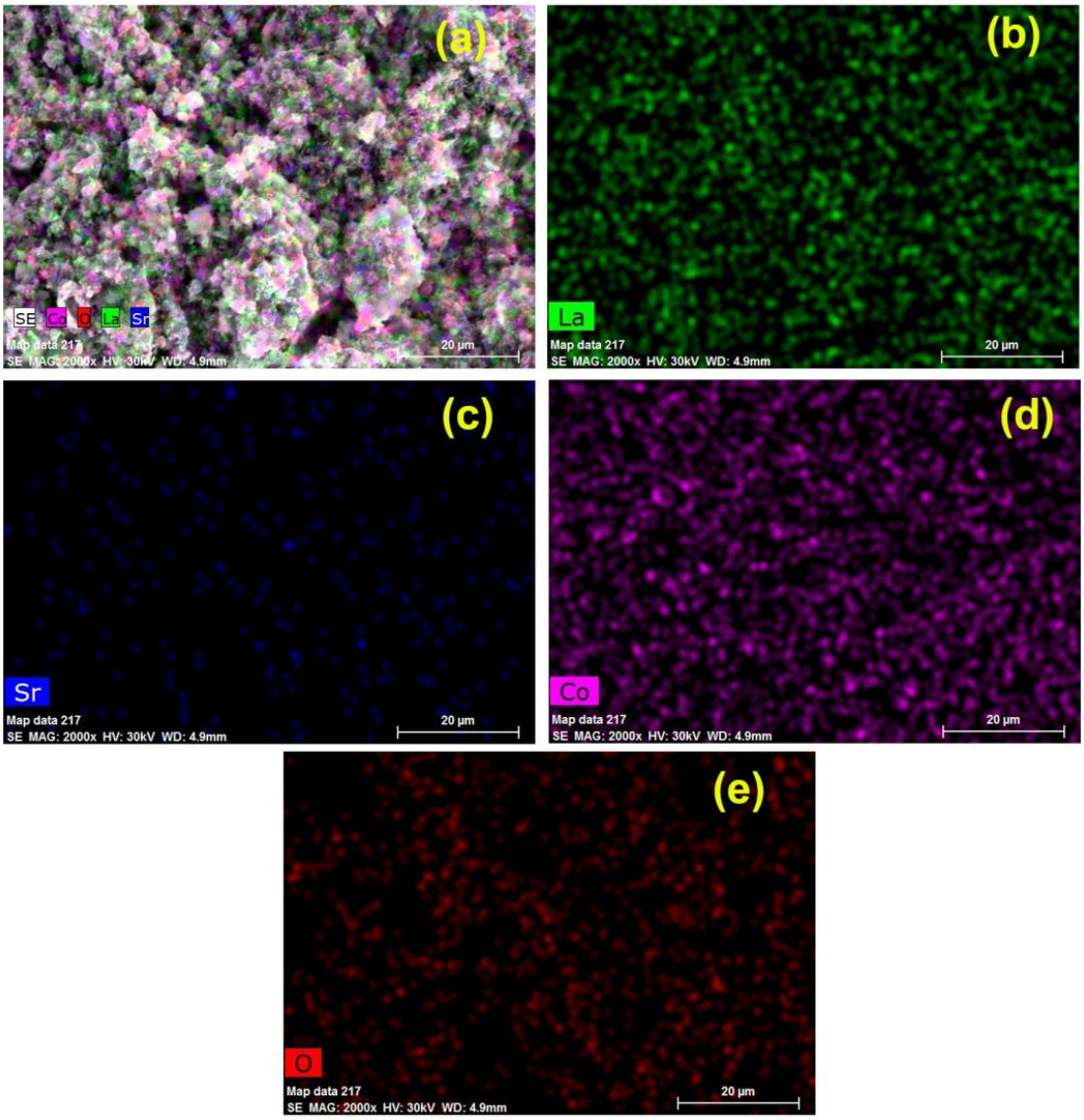

Fig. 3.9: (a) SEM micrograph with elemental mapping of LSCO nanowires. Figs 3.9(b), (c), (d) and (e) Mapping of La, Sr, Co and O respectively.

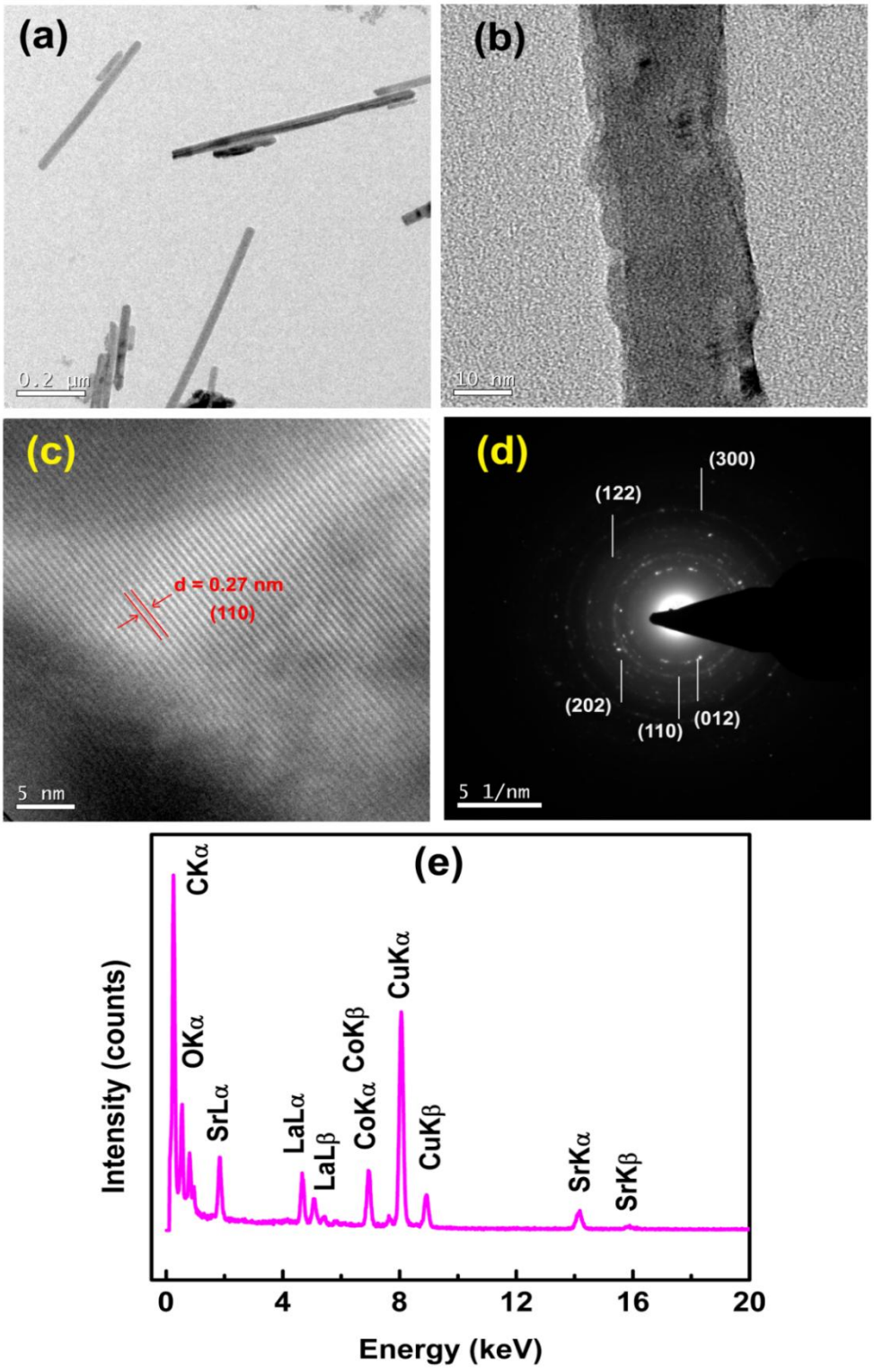

Fig 3.10: (a) Low and (b) high magnification TEM micrographs of LSCO nanowires, (c) HRTEM of nanowires showing lattice fringes, (d) SAED of LSCO nanowires and (e) TEM EDAX spectrum of the LSCO.

Fig. 3.10(d) shows the selected area diffraction pattern of the nanostructure and the diffraction spots represents the polycrystalline nature of the sample. Here the bright diffraction spots could be indexed using Gatan software. Fig. 3.10(e) shows the elemental analysis obtained from TEM. In the graph, Cu peak arises from the copper grid employed for dispersing the nanowire samples. The energy peaks corresponding to La, Sr, Co and O are clearly indexed in the spectrum.

3.2.3.3 Magnetic Properties of LSCO Nanowires

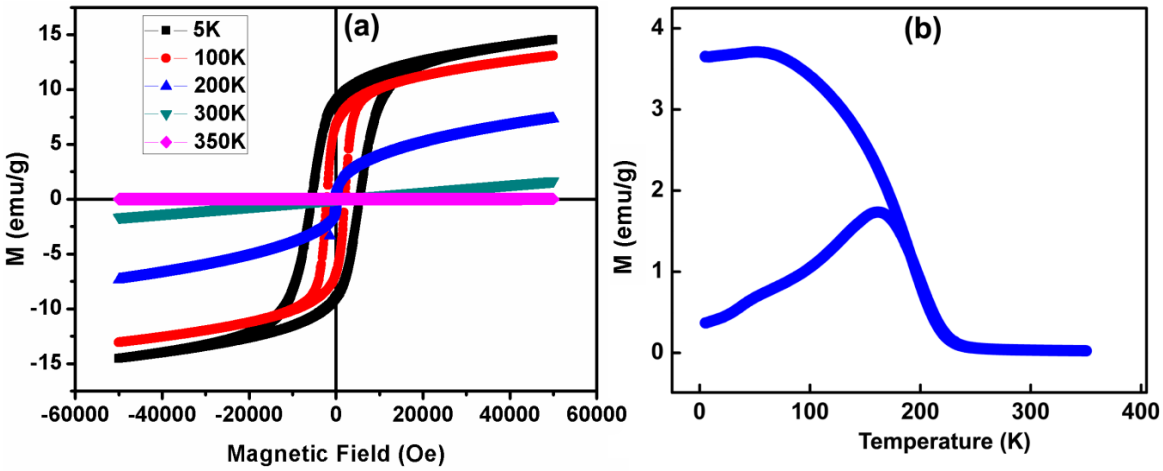

Fig. 3.11: (a) Magnetization vs magnetic field (M-H) curves of LSCO nanowires for various temperatures and (b) magnetization vs temperature curve of LSCO nanowires.

Magnetic analysis on the nanowires was done in the magnetic field ranging from -50 kOe to 50 kOe. The magnetization curves for 5 K, 100 K, 200 K, 300 K and 350 K were recorded and shown in Fig. 3.11(a). At 350 K and 300 K, LSCO nanowires shows straight line behaviour typical for a paramagnetic material. The same trend has been reported for bulk samples. When the temperature is lowered to 200 K; the behaviour changes from paramagnetic to ferromagnetic nature. At 5 K, hysteresis loop is clearly visible corresponding to the ferromagnetic interaction in the system.

The magnetism of one dimensional LSCO structures should be understood in details. In the original LSCO perovskite structure, there exists two sublattices containing (111) planes; one being rich in high spin state trivalent cobalt ions and other with low spin tetravalent cobalt ions. The trivalent cobalt ions give rise to antiferromagnetism and ferromagnetic interaction occurs due to the interaction between low spin (tetravalent) and high spin (trivalent) ions. The intermediate oxygen ion mediates the magnetic exchange interaction in these types of perovskite structures. From its M-H plots, it is evident that the transition temperature lies between 200 and 300 K. For understanding the transition, M-T analysis was done and field cooling (FC) and zero field cooling (ZFC) magnetization studies are depicted in Fig. 3.11(b). LSCO belongs to cluster glass phase. The difference between M_{FC} and M_{ZFC} is much higher in the cluster glass phase compared to the spin glass phase at sufficiently low temperature, indicating the presence of short range ferromagnetic ordering with in a cluster. The Curie temperature(T_C) of the calcined nanowires was obtained to be 225 K. For bulk LSCO, the reported T_C is 240 K. In the case of nanostructures, due to the finite size effect, there is an increase in the disorder of magnetic moments which may be one of the reasons behind lowering of T_C. Another factor that affects the transition temperature is the number of interfaces in a given volume, which increases for nanomaterials. Hence, the thermal energy could overcome the magnetic ordering, at a still lower temperature than for the bulk LSCO.

3.2.3.4 Electrical Properties of LSCO Nanowires

Among the perovskite oxides, systems with La at A-site, exhibit better conducting properties than other rare earths. One of the prominent reasons is the high ionic radius of La that contributes to increased structural symmetry, resulting in the formation of cubic or rhombohedral structure.[43] Another contributing factor is the absence of 4f electrons, which

with high effective mass could have deteriorated the conduction phenomenon. As seen earlier, the electrical conductivity of the shielding nanostructure, is an important criterion for developing highly efficient EMI shields.

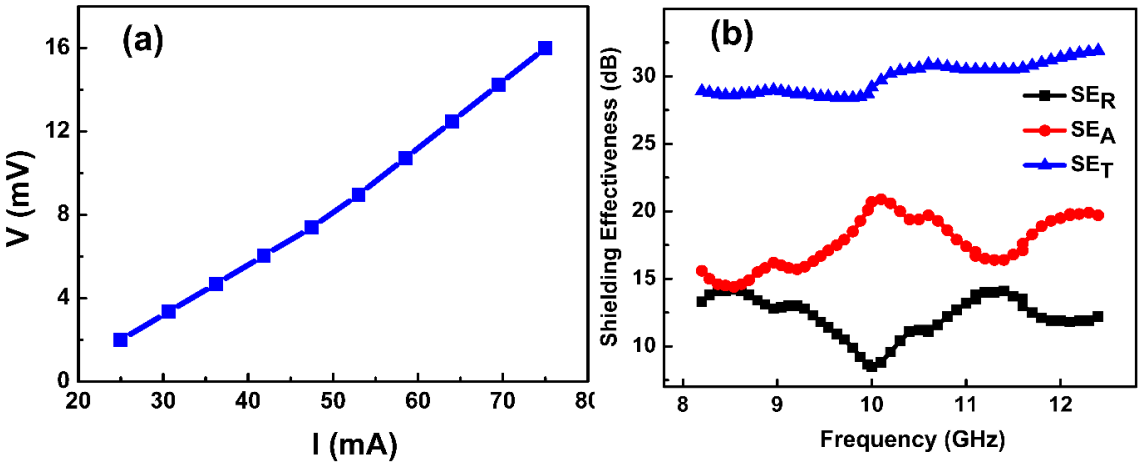

Fig. 3.12: (a) I-V plot of calcined LSCO nanowires at room temperature. Fig. 3.12(b) Frequency dependent variation of total shielding effectiveness (SE_T), reflection shielding effectiveness (SE_R) and absorption shielding effectiveness (SE_A) of LSCO nanowires at X band.

Conduction mechanism in bulk LSCO could be explained by the presence of itinerant electrons. The system is described as a hole doped semiconductor owing to the increase in the amount of Co^{4+} content for the partial substitution of La^{3+} by Sr^{2+} which increases the number of itinerant electrons. The four probe measurement shows linear behaviour typical for metallic structures (as shown in Fig. 3.12 (a)). The conductivity of the LSCO nanowires is calculated to be 120 S/cm which is obviously one order less than that obtained for bulk LSCO.[20] For nanomaterials, the surface area to volume ratio is high and the number of interfaces is also much more. These factors contribute to the increased surface scattering, which causes a reduction in DC electrical conductivity, compared to the bulk. Conventionally, materials with electrical conductivity value greater than one S/cm are desirable for effective EMI shielding.[37] In the present work, better conductivity of 120 S/cm is reported which satisfy one of the

shield's essential criterion. Nevertheless, the approximate diameter of the intertwined nanowire structure is only 15-35 nm, which should have further reduce the conductivity. There are several physical reasons to assume that the conductivity of nanowire will be inferior to that of the corresponding bulk material. In principle, there is high chance of scattering from the wire boundaries, and this phenomenon will be aggravated when the nanowire's width is below the free electron mean free path of the bulk material.

3.2.3.5 EMI Shielding Analysis

As discussed in Chapter 2, when the *SE* is high enough, the contribution of SE_M is negligible and the total shielding effectiveness is given by equation, $SE_T = SE_R + SE_A$. EM wave *SE* of LSCO nanowire samples were observed to be in the range of 28.5-32 dB, as shown in Fig. 3.12 (b), which is less than that observed for bulk LSCO. Here, the reduction could be attributed to the reduced conductivity exhibited by the nanowires. Mobile charge carriers play an important role in the conduction phenomenon in LSCO. In the case of nanowires with very small diameter 15-35 nm, the walls of the nanowires act as boundaries which scatter the mobile electrons. Hence the number of collisions increases with the number of interfaces available in a particular volume.[44] All these factors decrease the electronic conductivity in one dimensional structures. Still when the nanowires form closely inter-connected systems, as shown in SEM in Fig. 3.8. The connectivity of the sample causes better electrical conduction. Here also inherent nature of high conductivity of LSCO is an important factor in achieving high value of shielding effectiveness. Compared to metallic systems such as copper where the nanowires or particles suffer from poor conductivity due to oxidation issues except in inert conditions, the LSCO nanowires could exhibit stable values even at high temperatures applications without suffering corrosion.

LSCO nanowires exhibited SE_A values in the range of 14.4-20.7 dB, which showcase them as feasible candidates for absorption based shielding applications. As elucidated in Chapter 2.1, it could be concluded that the absorption dominant shielding effectiveness for LSCO nanowires are due to the direct relation between their electrical conductivity and SE_A. SE_R of the samples is in the range of 8.5 to 14 dB at X-band. In the present study, the tested EMI shielding structures have an optimum thickness of 2 mm. Achieving a high SE above 30 dB (99.9 %) qualifies these nanowire systems for high corrosive, high temperature coating applications.

3.2.4 Conclusions

La based perovskite nanowires of diameter 15-35 nm were synthesized by microemulsion technique. The LSCO nanowires achieved room temperature conductivity of 120 S/cm and T_C of 225 K. Compared to their bulk counterparts, there observed a lowering of DC conductivity in nanowires which is attributed to the high chance of electron scattering from the wire boundaries and this phenomenon is more at dimensions below the free electron mean free path of the bulk. Despite this, LSCO nanowires exhibited *SE* of 28.5-32 dB which corresponds to a shielding efficiency of > 99 %. Thus these nanowires could be proposed as an excellent candidate for nanoscale EMI shielding coatings under corrosive environments and high temperature conditions, where most metallic and polymer based nanowires fail.

3.3 References

(1) Al-Ghamdi, A. A. S.; El-Tantawy, F. M.; Aal, N. A. Vanadium Sesquioxide Nanocomposite. US Patent US20100321147A1, 2010.

(2) Kong, L.; Yin, X.; Ye, F.; Li, Q.; Zhang, L.; Cheng, L. Electromagnetic Wave Absorption Properties of ZnO-Based Materials Modified with $ZnAl_2O_4$ Nanograins. *J. Phys. Chem. C* **2013,** *117* (5), 2135-2146.

(3) Hutagalung, S. D.; Sahrol, N. H.; Ahmad, Z. A.; Ain, M. F.; Othman, M. Effect of MnO_2 Additive on the Dielectric and Electromagnetic Interference Shielding Properties of Sintered Cement-Based Ceramics. *Ceram. Int.* **2012,** *38* (1), 671-678.

(4) Singh, R.; Kulkarni, S. G. Nanocomposites Based on Transition Metal Oxides in Polyvinyl Alcohol for EMI Shielding Application. *Polym. Bull.* **2014,** *71* (2), 497-513.

(5) Vijayan, S.; Narasimman, R.; Prabhakaran, K. Freeze Gelcasting of Hydrogenated Vegetable Oil-in-Aqueous Alumina Slurry Emulsions for the Preparation of Macroporous Ceramics. *J. Eur. Ceram. Soc.* **2014,** *34* (16), 4347-4354.

(6) Yin, X.; Xue, Y.; Zhang, L.; Cheng, L. Dielectric, Electromagnetic Absorption and Interference Shielding Properties of Porous Yttria-Stabilized Zirconia/Silicon Carbide Composites. *Ceram. Int.* **2012,** *38* (3), 2421-2427.

(7) Li, S.; Tan, Y.; Xue, J.; Liu, T.; Zhou, X.; Zhang, H. Electromagnetic Interference Shielding Performance of Nano-Layered Ti_3SiC_2 Ceramics at High-Temperatures. *AIP Adv.* **2018,** *8* (1), 015027.

(8) Zhao, S.; Zhang, H.-B.; Luo, J.-Q.; Wang, Q.-W.; Xu, B.; Hong, S.; Yu, Z.-Z. Highly Electrically Conductive Three-Dimensional $Ti_3C_2T_x$MXene/Reduced Graphene Oxide Hybrid Aerogels with Excellent Electromagnetic Interference Shielding Performances. *ACS Nano* **2018,** *12* (11), 11193-11202.

(9) Wang, Y.; Fan, H. J. Improved Thermoelectric Properties of $La_{1-x}Sr_xCoO_3$ Nanowires. *J. Phys. Chem. C* **2010,** *114* (32), 13947-13953.

(10) Suntivich, J.; Gasteiger, H. A.; Yabuuchi, N.; Shao-Horn, Y. Electrocatalytic Measurement Methodology of Oxide Catalysts Using a Thin-Film Rotating Disk Electrode. *J. Electrochem. Soc.* **2010,** *157* (8), B1263-B1268.

(11) Li, W.; Hu, Z.; Li, Y.; Zhu, M.; Zhu, Z.; Chu, J. Growth, Microstructure, and Infrared-Ultraviolet Optical Conductivity of $La_{0.5}Sr_{0.5}CoO_3$ Nanocrystalline Films on Silicon Substrates by Pulsed Laser Deposition. *ACS Appl. Mater. Interfaces* **2010,** *2* (3), 896-902.

(12) Endo, A.; Wada, S.; Wen, C. J.; Komiyama, H.; Yamada, K. Low Overvoltage Mechanism of High Ionic Conducting Cathode for Solid Oxide Fuel Cell. *J. Electrochem. Soc.* **1998,** *145* (3), L35-L37.

(13) Parry, J. M.; Raccah, P. Method of Manufacturing a Gas Sensor. US Patent 4,221,827, 1980.

(14) Liu, W.; Wang, S.; Chen, Y.; Fang, G.; Li, M.; Zhao, X.-z. $La_{0.5}Sr_{0.5}CoO_{3-\delta}$ Nanotubes Sensor for Room Temperature Detection of Ammonia. *Sens. Actuators, B* **2008,** *134* (1), 62-65.

(15) Dijith, K. S.; Pillai, S.; Surendran, K. P. Thermophysical and Microwave Shielding Properties of $La_{0.5}Sr_{0.5}CoO_{3-\delta}$ and Its Composite with Epoxy. *J. Electron. Mater.* **2017,** *46* (8), 5158-5167.

(16) Senarıs-Rodrıguez, M.; Goodenough, J. Magnetic and Transport Properties of the System $La_{1-x}Sr_xCoO_{3-\delta}$ ($0< x\leq 0.50$). *J. Solid State Chem.* **1995,** *118* (2), 323-336.

(17) Dijith, K. S.; Pillai, S.; Surendran, K. P. Screen Printed Silver Patterns on $La_{0.5}Sr_{0.5}CoO_{3-\delta}$-Epoxy Composite as a Strategy for Many-Fold Increase in EMI Shielding. *Surf. Coat. Technol.* **2017,** *330*, 34-41.

(18) Cheung, J. T.; Morgan, P. E. D.; Lowndes, D. H.; Zheng, X. Y.; Breen, J. Structural and Electrical Properties of $La_{0.5}Sr_{0.5}CoO_3$ Epitaxial Films. *Appl. Phys. Lett.* **1993,** *62* (17), 2045-2047.

(19) Cheng, X.; Fabbri, E.; Nachtegaal, M.; Castelli, I. E.; El Kazzi, M.; Haumont, R.; Marzari, N.; Schmidt, T. J. Oxygen Evolution Reaction on $La_{1-x}Sr_xCoO_3$ Perovskites: A Combined

Experimental and Theoretical Study of Their Structural, Electronic, and Electrochemical Properties. *Chem. Mater.* **2015,** *27* (22), 7662-7672.

(20) Raccah, P.; Goodenough, J. A Localized-Electron to Collective-Electron Transition in the System (La, Sr)CoO_3. *J. Appl. Phys.* **1968,** *39* (2), 1209-1210.

(21) Todd, M. G.; Shi, F. G. Characterizing the Interphase Dielectric Constant of Polymer Composite Materials: Effect of Chemical Coupling Agents. *J. Appl. Phys.* **2003,** *94* (7), 4551-4557.

(22) Park, S. H.; Theilmann, P.; Yang, K.; Rao, A. M.; Bandaru, P. R. The Influence of Coiled Nanostructure on the Enhancement of Dielectric Constants and Electromagnetic Shielding Efficiency in Polymer Composites. *Appl. Phys. Lett.* **2010,** *96* (4), 043115.

(23) Madhukar, S.; Aggarwal, S.; Dhote, A.; Ramesh, R.; Krishnan, A.; Keeble, D.; Poindexter, E. Effect of Oxygen Stoichiometry on the Electrical Properties of $La_{0.5}Sr_{0.5}CoO_3$ Electrodes. *J. Appl. Phys.* **1997,** *81* (8), 3543-3547.

(24) Cuevas, F.; Montes, J.; Cintas, J.; Urban, P. Electrical Conductivity and Porosity Relationship in Metal Foams. *J. Porous Mater.* **2009,** *16* (6), 675.

(25) Rajeev, K.; Shivashankar, G.; Raychaudhuri, A. Low-Temperature Electronic Properties of a Normal Conducting Perovskite Oxide ($LaNiO_3$). *Solid State Commun.* **1991,** *79* (7), 591-595.

(26) Verma, P.; Saini, P.; Malik, R. S.; Choudhary, V. Excellent Electromagnetic Interference Shielding and Mechanical Properties of High Loading Carbon-Nanotubes/Polymer Composites Designed Using Melt Recirculation Equipped Twin-Screw Extruder. *Carbon* **2015,** *89*, 308-317.

(27) Al-Saleh, M. H.; Sundararaj, U. Electromagnetic Interference Shielding Mechanisms of CNT/Polymer Composites. *Carbon* **2009,** *47* (7), 1738-1746.

(28) Deepa, K.; Shaiju, P.; Sebastian, M.; Gowd, E. B.; James, J. Poly(Vinylidene Fluoride)–$La_{0.5}Sr_{0.5}CoO_{3-\delta}$ Composites: The Influence of LSCO Particle Size on the Structure and Dielectric Properties. *Phys. Chem. Chem. Phys.* **2014,** *16* (32), 17008-17017.

(29) Zhao, B.; Fan, B.; Xu, Y.; Shao, G.; Wang, X.; Zhao, W.; Zhang, R. Preparation of Honeycomb SnO_2 Foams and Configuration-Dependent Microwave Absorption Features. *ACS Appl. Mater. Interfaces* **2015,** *7* (47), 26217-26225.

(30) Liang, C.; Wang, Z.; Wu, L.; Zhang, X.; Wang, H.; Wang, Z. Light and Strong Hierarchical Porous SiC Foam for Efficient Electromagnetic Interference Shielding and Thermal Insulation at Elevated Temperatures. *ACS Appl. Mater. Interfaces* **2017,** *9* (35), 29950-29957.

(31) Yan, D.; Cheng, S.; Zhuo, R.; Chen, J.; Feng, J.; Feng, H.; Li, H.; Wu, Z.; Wang, J.; Yan, P. Nanoparticles and 3D Sponge-like Porous Networks of Manganese Oxides and Their Microwave Absorption Properties. *Nanotechnology* **2009,** *20* (10), 105706.

(32) Zhang, Q.; Gou, Y.; Wang, H.; Jian, K.; Wang, Y. A New Simple Way to Polyzirconocenesilane for Lightweight Polymer-Derived Zr/Si/C/O Ceramic Foams with Electromagnetic Wave-Absorbing and High Temperature-Resistant Properties. *Mater. Des.* **2017,** *120*, 90-98.

(33) Li, X.; Zhang, L.; Yin, X.; Feng, L.; Li, Q. Effect of Chemical Vapor Infiltration of SiC on the Mechanical and Electromagnetic Properties of Si_3N_4–SiC Ceramic. *Scr. Mater.* **2010,** *63* (6), 657-660.

(34) Park, M. S.; Wang, G. X.; Kang, Y. M.; Wexler, D.; Dou, S. X.; Liu, H. K. Preparation and Electrochemical Properties of SnO2 Nanowires for Application in Lithium-ion Batteries. *Angew. Chem., Int. Ed.* **2007,** *46* (5), 750-753.

(35) Ramanathan, K.; Bangar, M. A.; Yun, M.; Chen, W.; Mulchandani, A.; Myung, N. V. Individually Addressable Conducting Polymer Nanowires Array. *Nano Lett.* **2004,** *4* (7), 1237-1239.

(36) Zhou, W.; Yin, R.-M.; Long, L.; Luo, H.; Ding, Y.-h.; Li, Y. SiC Nanofibers Modified Si_3N_4 Ceramics for Improved Electromagnetic Interference Shielding in X-Band. *Ceram. Int.* **2018,** *44* (2), 2249-2254.

(37) Reshi, H. A.; Singh, A. P.; Pillai, S.; Yadav, R. S.; Dhawan, S. K.; Shelke, V. Nanostructured $La_{0.7}Sr_{0.3}MnO_3$ Compounds for Effective Electromagnetic Interference Shielding in the X-Band Frequency Range. *J. Mater. Chem. C* **2015,** *3* (4), 820-827, DOI: 10.1039/c4tc02040e.

(38) Liu, X.; Wang, L.-S.; Ma, Y.; Zheng, H.; Lin, L.; Zhang, Q.; Chen, Y.; Qiu, Y.; Peng, D.-L. Enhanced Microwave Absorption Properties by Tuning Cation Deficiency of Perovskite Oxides of Two-Dimensional $LaFeO_3$/C Composite in X-Band. *ACS Appl. Mater. Interfaces* **2017,** *9* (8), 7601-7610.

(39) Zhuo, R.; Qiao, L.; Feng, H.; Chen, J.; Yan, D.; Wu, Z.; Yan, P. Microwave Absorption Properties and the Isotropic Antenna Mechanism of ZnO Nanotrees. *J. Appl. Phys.* **2008,** *104* (9), 094101.

(40) Liu, J.; Cao, W.-Q.; Jin, H.-B.; Yuan, J.; Zhang, D.-Q.; Cao, M.-S. Enhanced Permittivity and Multi-Region Microwave Absorption of Nanoneedle-like ZnO in the X-Band at Elevated Temperature. *J. Mater. Chem. C* **2015,** *3* (18), 4670-4677.

(41) Tsay, C.-Y.; Huang, Y.-H.; Hung, D.-S. Enhanced Microwave Absorption of $La_{0.7}Sr_{0.3}MnO_{3-\delta}$ Based Composites with Added Carbon Black. *Ceram. Int.* **2014,** *40* (3), 3947-3951.

(42) Cheng, Y.; Dai, J.; Wu, D.; Sun, Y. Electromagnetic and Microwave Absorption Properties of Carbonyl Iron/$La_{0.6}Sr_{0.4}MnO_3$ Composites. *J. Magn. Magn. Mater.* **2010,** *322* (1), 97-101.

(43) Kozuka, H.; Ohbayashi, K.; Koumoto, K. Electronic Conduction in La-Based Perovskite-Type Oxides. *Sci. Technol. Adv. Mater.* **2015,** *16* (2), 026001.

(44) Cheng, Z.; Liu, L.; Xu, S.; Lu, M.; Wang, X. Temperature Dependence of Electrical and Thermal Conduction in Single Silver Nanowire. *Sci. Rep.* **2015,** *5*, 10718.

Chapter 4

Polyol Derived Ni and NiFe Alloys for Effective Shielding of Electromagnetic Interference

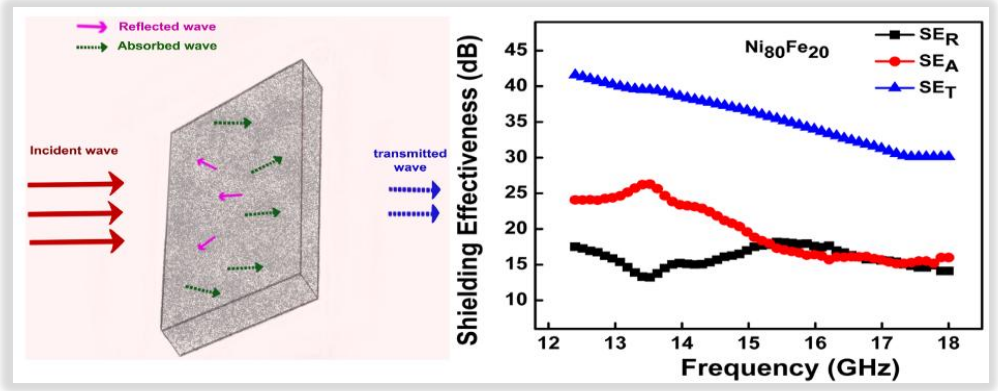

Ni and NiFe alloys with different compositions have been successfully synthesized through a simple, surfactant-free polyol method. The morphological analysis demonstrated a uniform spherical nature of the alloys, with size range ~10-30 nm. A very thin oxide layer was found to be forming over the alloy nanoparticles (NPs) which is feebly visible in TEM and later confirmed by XPS analysis. The saturation magnetization value was found to be lowest in Ni that keeps on increasing with increasing Fe content in the composition. The resistivity, as revealed from I-V characteristics, was shown to be lowest for the permalloy ($Ni_{80}Fe_{20}$) phase, while the values increase with further increment in the Fe content. All of the alloys tested in this investigation, showed excellent microwave shielding properties ranging from 21 to 41 dB in the entire Ku bands, for ~1 mm thick samples. The lowest EMI shielding range (21 to 29 dB) was noted for Ni NPs while the highest was observed in the case of permalloy (30 to 41 dB). These alloys are good candidates for EMI shielding applications having the ability to attenuate 99.9 % of electromagnetic radiations.

4.1 Introduction

The most used traditional shielding materials are metal based systems; among them magnetic metals span a major regime. A magnetic material with high permeability ($\mu >> 1$) and magnetic loss can create high magnetic field attenuation by providing a low reluctance path for the magnetic field. The magnetic shielding material will develop an alternating magnetic field that generates eddy current on the shield, making a nullifying field in the opposite orientation. For practical cavity resonance damping applications, the magnetic absorbers are found to be ideal since the magnetic field is maximum on the conductive surface where the absorber is placed. In general, for magnetic absorber-based EMI solutions, the shielding effectiveness increases as a function of frequency. Synthetic soft magnetic materials made the pathway for the development of high-density electronic circuits, to operate at high frequencies. They are widely used as magnetic cores in downsized inductors and as electromagnetic noise absorbers.[1] The pronounced absorptive nature of magnetic materials like ferrites and metallic alloys has been originated from their effective magnetic and dielectric loss properties.[2] These nanomagnetic materials have novel chemical, magnetic, electrical and electromagnetic properties, which are often different from their bulk counter parts because of the smaller sizes and larger specific surface areas. Iron, nickel, cobalt and their alloys are well known soft ferromagnets which exhibit high magnetization and low coercivity, which are widely being applied in EMI shielding and microwave absorption applications.[3]

Among various soft ferromagnets, permalloy ($Ni_{80}Fe_{20}$) that possesses extremely high magnetic permeability, low coercive force, nominal core losses with low remanence, is useful for efficient magnetic shielding applications where ultra-low fields than earth's magnetism are needed. Further, its small magnetostriction is befitting for industrial thin film applications,

where variable stresses don't affect the magnetic characteristics. Various synthesis procedures are available for the synthesis of Ni and NiFe nanoparticles, like mechanical alloying,[4] hydrothermal method,[5] sonochemical method,[6] reverse micelle techniques,[7] hydrogen plasma reaction method[8] etc. Most of these synthesis routes involving usage of different surfactants, reducing agents, special reaction conditions etc. which further makes the process complex. However, the present study follows a simple polyol method by making use of the polymer polyethylene glycol (PEG) as the solvent cum reducing agent. The polyol-based synthesis is frequently used in the synthesis of magnetic nanoparticles due to the method's control over composition and size of nanoparticles, through the capping effect of glycol-family solvents and nucleating agents.[9] Here PEG is serving multiple roles - as a versatile dispersant, high boiling solvent, effective reductant, and also as a stabilizer which controls the particle growth and avoids aggregation of precursors due to steric interactions. Ferromagnetic nanomaterials (Ni, Fe, NiFe alloys etc.) and other metallic nanoparticles are widely synthesized using this polyol method.[10–14] It is highlighted in the literature that the polyol process will result in the generation of monodisperse, highly crystalline and uniform sized nanoparticles.[15]

Here in this chapter, we report the synthesis and electric/magnetic/electromagnetic properties of Ni and its alloys with Fe using a simple PEG-mediated polyol method, without the need for any inert atmospheres during chemical synthesis. The prepared nanoparticles were formed into thin sheets and densified through hydrogen annealing which was further analyzed for their magnetic, electrical properties and EMI shielding characteristics. The microwave shielding properties of the series of polyol derived nano NiFe alloys ($Ni_{80}Fe_{20}$, $Ni_{50}Fe_{50}$, and $Ni_{20}Fe_{80}$) are being reported for the first time.

4.2 Materials and Methods

The chemicals used, nickel chloride hexahydrate ($NiCl_2.6H_2O$) and polyethylene glycol 400 (PEG) were procured from Aldrich, while iron chloride tetrahydrate ($FeCl_2.4H_2O$), sodium hydroxide (NaOH) and ethyl alcohol were procured from Merck. All the chemicals are of analytical grade purity. Nano nickel (Ni) and its alloys with iron (Fe) based on compositions $Ni_{20}Fe_{80}$, $Ni_{50}Fe_{50}$ and $Ni_{80}Fe_{20}$ were prepared by polyol method.[15] The first step involves proper mixing of the precursor salts ($FeCl_2.4H_2O$ and $NiCl_2.6H_2O$) in PEG dispersing media, in a bath sonicator. Throughout the study, the concentration of precursor in the solution was kept to be 0.2 M and pH was kept in the range of 10 to 11 by adding sodium hydroxide before proceeding to reduction process. Then the PEG metal salt solution was heated to 200 ^oC for 30 min, to remove moisture trapped in the mixture. Finally, the mixture was further reflexed at 300 ^oC for 2 h with constant stirring. The mixture was subsequently washed with water and ethanol to remove the filtrate. The residue after repeated washing was collected and kept in a vacuum oven overnight to get the dry precursor powder. Final annealing (at T = 600 ^oC) was performed in a tube furnace under hydrogen atmosphere for 3 h, to yield the phase pure metal and its alloys in nano powder form. A similar polyol procedure was also adopted for the preparation of iron nanoparticles from iron chloride but ended up in iron oxide (Fe_2O_3) rich phase and the product shown exaggerated grain growth during hydrogen annealing with micron-sized particles. It is a common practice to use polyol method for the production of iron oxide from precursor salt,[16–19] whereas only a few reports were available on iron nanoparticle synthesis, with modified synthesis procedures. This is because, during the polyol reduction process where polyethylene glycol acts as a reductant as well as a surface protecting agent for

Ni-Fe compounds, is inefficient to prevent the oxidation of iron. The concentration of oxide phase will depend upon the reducibility of the polyols.

The morphology and size of the grains were directly investigated by high-resolution transmission electron microscopy, HR-TEM (FEI Tecnai G2 30S-TWIN, FEI Co., Hillsboro, OR, USA). Energy dispersive spectroscopy was done to analyze the elemental composition. The chemical composition was analyzed using X-ray Photoelectron Spectroscopy (XPS) (PHI 500 Versa Probe 2 with Al Kα radiation). The Ni and NiFe alloys were uniaxially pressed (at ~ 100 MPa) into rectangular sheets/blocks for electric, magnetic and electromagnetic characterization. These samples were subsequently sintered at 600 ^{o}C for 3 h in the H_2 atmosphere, in order to improve their densification and mechanical strength. The magnetic properties of the samples were measured using a VSM probe in physical property measurement system (PPMS, Quantum Design Inc., USA). Here, the magnetic field was varied from -5 T to +5 T at 300 K and the magnetization of the samples were studied. M-T measurements were carried out for a temperature range of 300 K to 900 K at a magnetic field of 200 Oe. The required level of machining was carried out using a Struers polishing machine (Struers Tegramin - 25) to make the sample suitably fit to the waveguide and electromagnetic characterization is performed at Ku band.

4.3 Results and Discussion

Fig. 4.1 briefly describes the main steps in preparing the EMI shielding nanopowders, starting from precursors to the development of machined compacts suitable for transmission waveguide shielding measurement. No inert atmosphere was employed during chemical synthesis except annealing of the powder later after compaction, which was done at 600 ^{o}C in hydrogen.

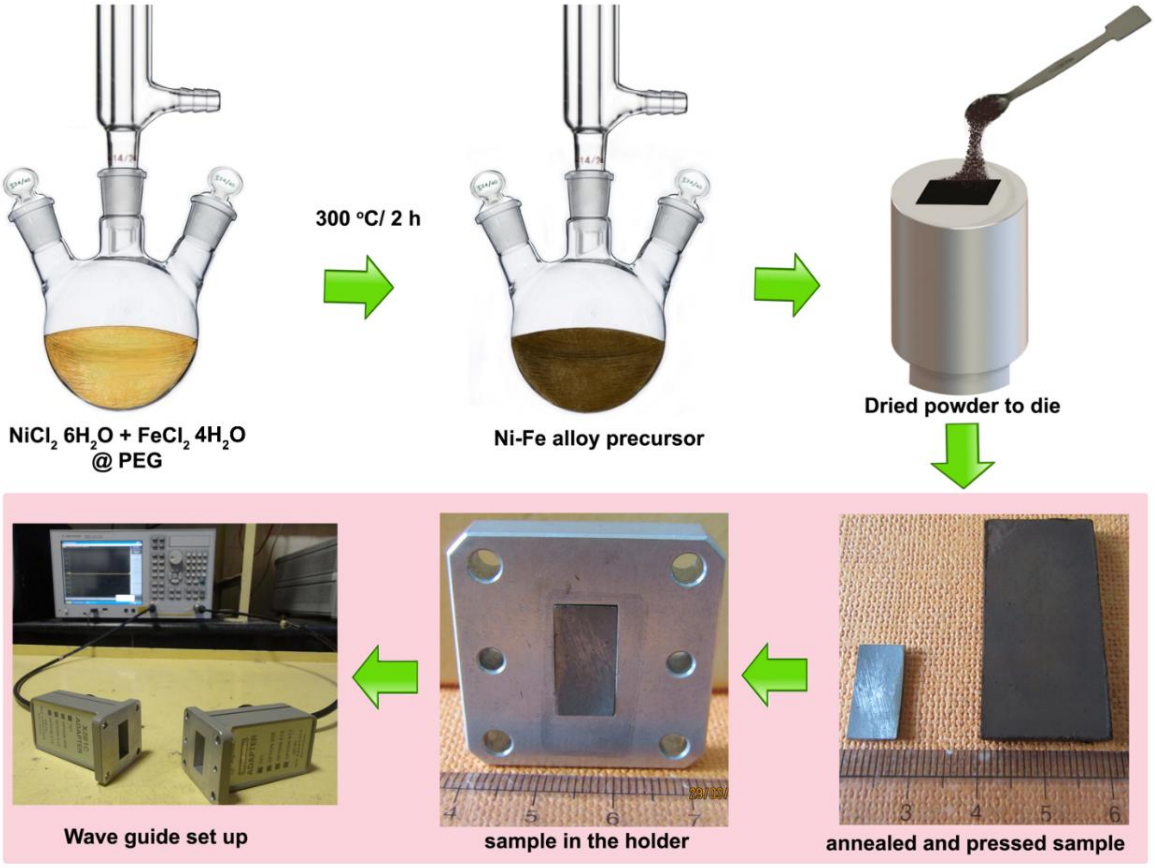

Fig. 4.1: Process flow of preparation of samples for EMI shielding characterization.

4.3.1 Structural and Morphological Analysis

4.3.1.1 X-ray Diffraction Analysis

PEG could effectively reduce both iron and nickel metal salts into metal nuclei which then nucleate to form metal nanoparticles. Fig. 4.2 shows the XRD patterns for Ni, $Ni_{80}Fe_{20}$, $Ni_{50}Fe_{50}$ and $Ni_{20}Fe_{80}$ nanoparticles synthesized by polyol method. As shown, the diffraction peaks can be indexed for crystal planes (111), (200) and (220) which match with the face-centered cubic structure of Ni (JCPDS no 00-004-0850) and bulk NiFe alloy. The lattice parameter a could be calculated from the d-spacing values of major intensity peaks as given by $a = \sqrt{3}d$ for fcc structure and $a = \sqrt{2}d$ for bcc structure.[20] The average lattice parameter

increases from a=3.523 Å for Ni to a=3.547 Å for permalloy as the atomic radius for Fe is greater than that for Ni. The same trend continues as there is an increase in lattice parameter to 3.585 for $Ni_{50}Fe_{50}$. For $Ni_{20}Fe_{80}$, there is a visible transition from fcc to bcc structure corresponding to Fe rich phase as observed from the XRD pattern. Clearly, the diffraction line (111) has shifted to higher 2θ angles as a consequence of decreased d-spacing since the unit cell lattice accommodated a higher percentage of iron.

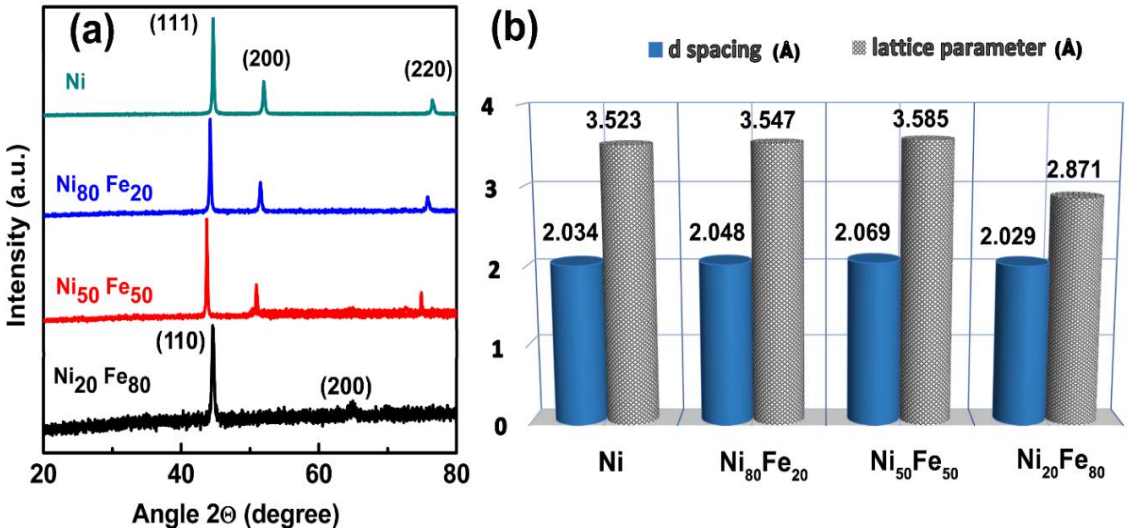

Fig. 4.2: (a) X-ray diffraction patterns of the nickel and its alloy with iron. (b) Variation of d spacing and lattice parameter, for different Ni and NiFe alloys.

Further, the diffraction line (200) at 2θ ~ 51.9° disappeared when x=50 changes to x=80 in $Ni_{100-x}Fe_x$, while another peak corresponding to the bcc structure of Fe arised at 65°. The peaks at 2θ ~ 44.5° and 65° respectively correspond to (110) and (200) planes of the bcc structured Fe. The lattice parameter showed a rapid decrease with fcc to bcc transition. The variation of lattice parameter and d-spacing for different percentages of iron addition is plotted in Fig. 4.2(b).

4.3.1.2 Transmission Electron Microscopy

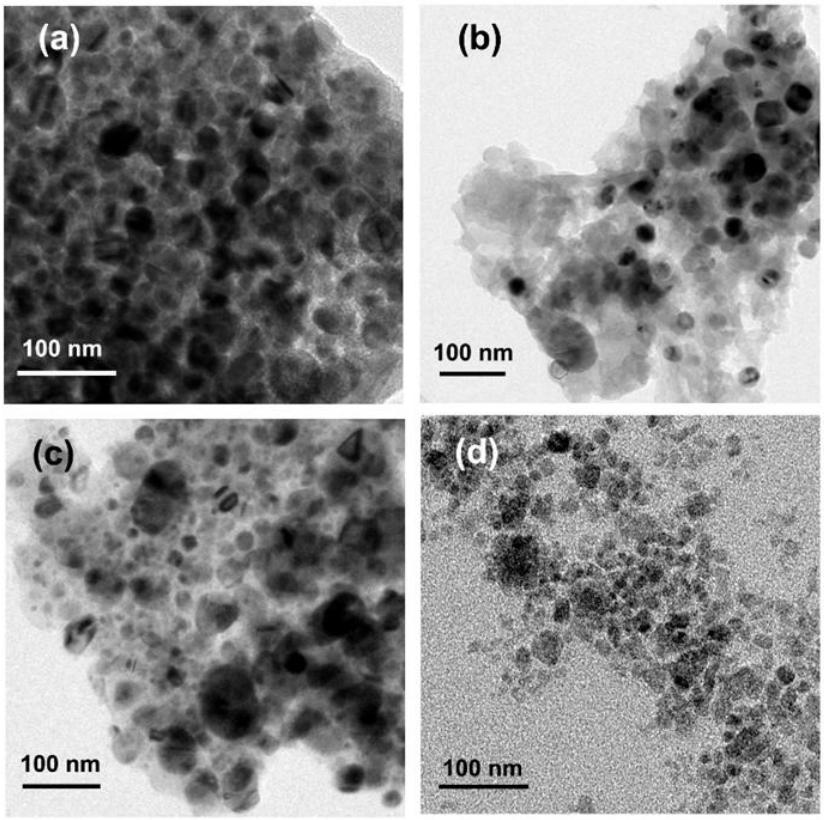

Fig. 4.3: Low resolution TEM micrographs of (a) Ni (b) $Ni_{50}Fe_{50}$ (c) $Ni_{80}Fe_{20}$ and (d) $Ni_{20}Fe_{80}$.

Even though the X-ray diffraction presented a complete phase purity for the samples synthesized through polyol method, diffraction techniques are inadequate to study the surface degradation of ferromagnetic nanoparticles. Hence we performed a detailed TEM analysis coupled with EDAX elemental analysis. The low-resolution images of Ni, $Ni_{80}Fe_{20}$, $Ni_{50}Fe_{50}$ and $Ni_{20}Fe_{80}$ are given in Fig. 4.3, which present spherical microstructural features of the nano metals and alloys. The magnified TEM micrographs in Fig. 4.4 clearly display the spherical nature of the Ni and its alloy series with particle size ranging from 10-30 nm. A thin oxide layer is associated with the particles is vaguely visible in the micrographs.

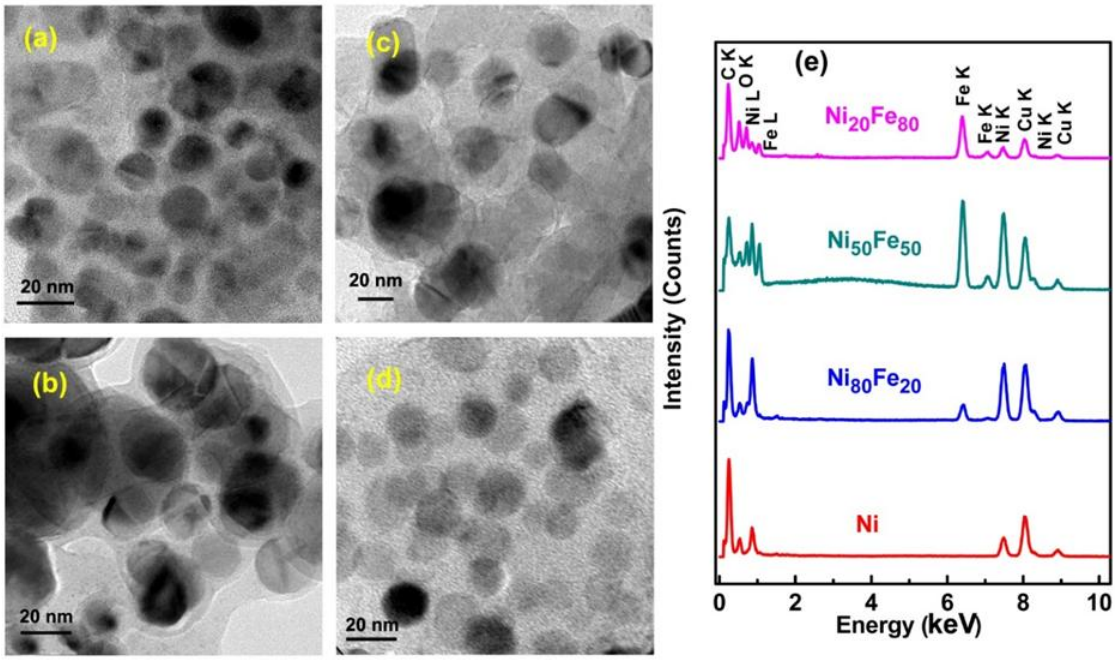

Fig. 4.4: TEM micrographs of (a) Ni (b) $Ni_{50}Fe_{50}$ (c) $Ni_{80}Fe_{20}$ and (d) $Ni_{20}Fe_{80}$ and (e) TEM EDAX spectrum of the Ni and its alloys.

In order to elucidate the elemental composition and to conform the presence of oxide layer, EDAX analysis was performed. In EDAX spectrum of Ni (Fig. 4.3(e)), all the relevant energy spectrum of Ni nanoparticles is identified.[21] But in the context of the present study, the characteristic Fe lines start appearing in $x \geq 20$ in $Ni_{1-x}Fe_x$ alloys and its intensity grows with x, obviously. The spectral peak in the EDAX analysis at 0.525 keV corresponds to oxygen, is a clear indication of the surface degradation due to oxide layer formation covering the nanoparticles. Since minor oxidation is unavoidable in ferromagnetic nanoparticles, and they can influence the magnetic characteristics of the parental compound since Ni_2O_3 is weakly magnetic, NiO is antiferromagnetic while Fe_2O_3 is ferromagnetic.[22,23] An earlier report by Islam *et al*., on the oxide formation in polyol method, is concurrent with the present observation. According to them, this oxide layer formation is beneficial since it will prevent further oxidation which is advantageous in biological applications.[15]

4.3.1.3 X-ray Photoelectron Spectroscopy Analysis

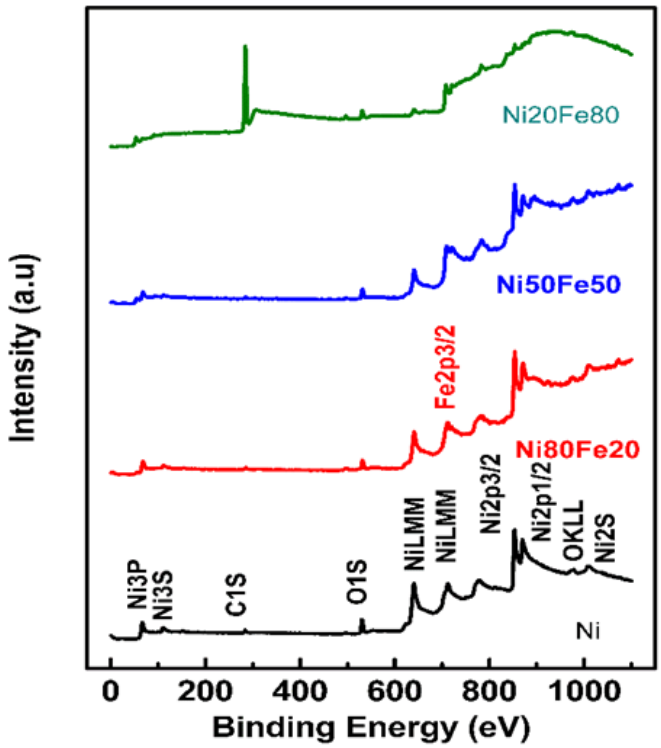

Fig. 4.5: XPS survey spectrum of Ni, $Ni_{80}Fe_{20}$, $Ni_{50}Fe_{50}$ and $Ni_{20}Fe_{80}$.

We further investigated the surface chemistry of Ni and $Ni_{100-x}Fe_x$ nanoparticles with a more surface sensitive spectroscopic technique, XPS. As shown, the Ni 2p and Fe 2p spectra presented in Fig. 4.6 give more insight into the formation of possible iron and nickel oxides on the surface region. In order to explore the various chemical states of nickel and iron in the experimental spectra, the Fe 2p and Ni 2p core levels were curve-fitted with a non-linear least square fitting program (XPS Peak 4.1 version). Prior to analysis, a correction should be done in order to elucidate the secondary electron background. The most recent and well-established Shirley background correction method was applied in the current investigation. After curve fitting, various oxidation levels of both nickel and iron were visible. From the XPS survey spectrum of alloys the presence of Ni, Fe, O and C are identified as given in Fig. 4.5.

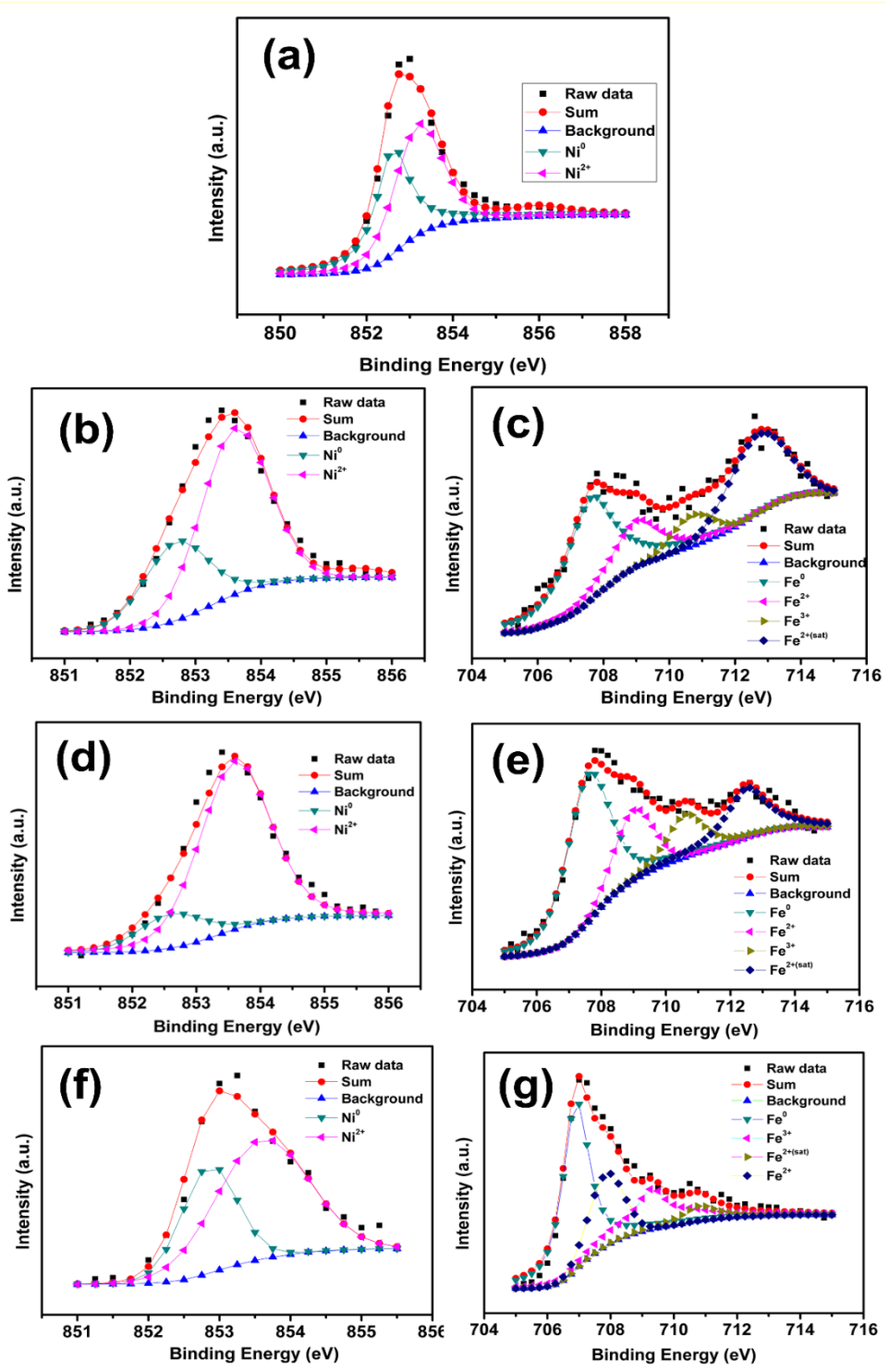

Fig. 4.6: Reconstruction of the experimental (open dots) Ni (2p) and Fe (2p) spectrum of nickel and their iron alloys. Fig. 4.6(a), 4.6(b), 4.6(d) and 4.6(f) are of Ni 2p; Fig. 4.6(c), 4.6(e) and 4.6(g) are of Fe 2p spectrum of samples Ni, $Ni_{80}Fe_{20}$, $Ni_{50}Fe_{50}$ and $Ni_{20}Fe_{80}$ respectively.

Fig. 4.6(a) depicts binding energy spectrum of pure nickel sample. The peak at 852.7 eV corresponds to the pure Ni (Ni^0) which is in agreement with literature data.[24] The oxide peak at 853.6 eV can be attributed to the Ni^{2+} oxidation state.[25] The same peaks are observed in the case of Ni $2p_{3/2}$, of the rest of the nickel-iron alloys series ($Ni_{80}Fe_{20}$, $Ni_{50}Fe_50$ and $Ni_{20}Fe_{50}$). In the case of Fe $2p_{3/2}$, the apparent peak position (707.6 eV) is believed to be shifted marginally from that of the pure Fe, which was reported to have a peak at 706.9 eV.[26] The energy shift can be attributed to the electron charge transfer between nickel and iron in the alloy combination.[27] The rest of the fitted peaks were at 709, 710.6 and 712.5 eV, which corresponds to Fe^{2+}, Fe^{3+} and Fe^{2+} satellite peaks, are concurrent with observed values in literature.[28] The existence of Ni^0 and Fe^0 peak in all the nickel-iron alloy combination reiterate the fact that the oxide layer is marginally lighter. On a closer examination of XPS results, it can be concluded that, in the polyol synthesis of ferromagnetic metals and alloys, a thin oxide layer formation is inevitable under ordinary synthesis conditions. This oxide layer is vaguely visible in TEM images (see Fig. 4.4), which further confirms the above observation.

4.3.1.4 Scanning Electron Microscopy

SEM micrographs of fractured surface of the Ni, $Ni_{80}Fe_{20}$, $Ni_{50}Fe_{50}$ and $Ni_{20}Fe_{80}$ are shown in the Fig. 4.6. Obviously, there are a lot of voids observed in the fractured area (see Fig. 4.7), which are believed to have formed consequent to the escape of residual PEG which remained in the precursor stage. As observed in SEM the particles are spherical and the nanoclusters of the magnetic nanoparticles have been coalesced together throughout the structure, results in the hetero structured microstructure.

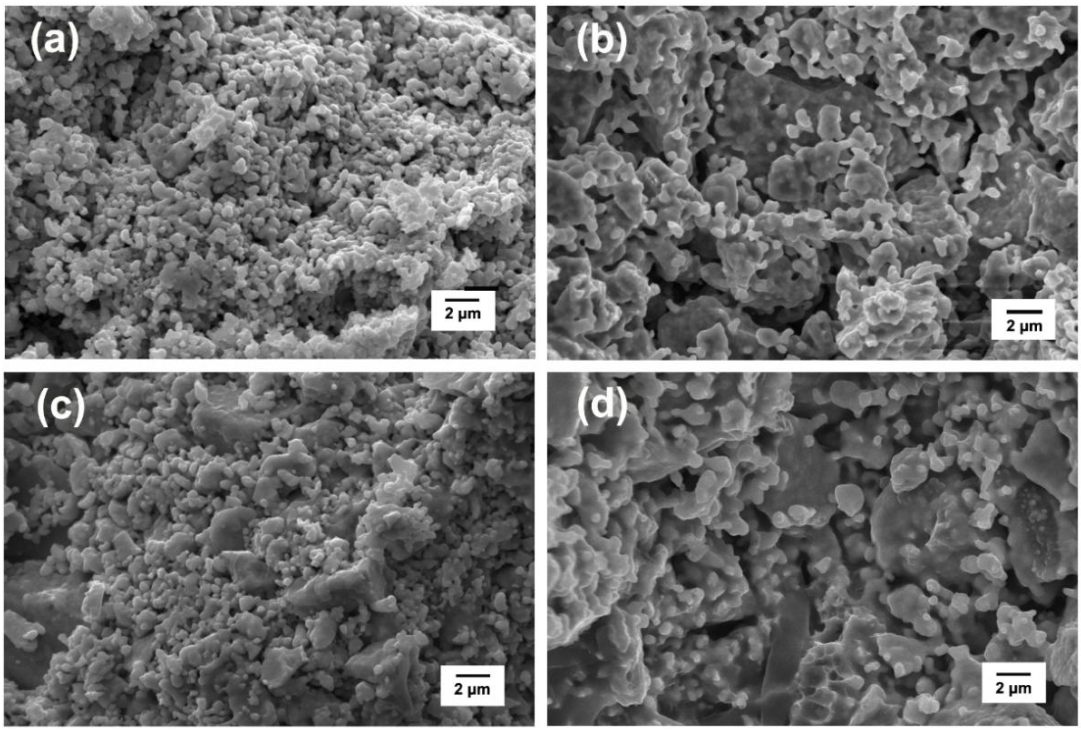

Fig. 4.7: Low magnification SEM micrographs of fractured surface of (a) Ni (b) $Ni_{80}Fe_{20}$ (c) $Ni_{50}Fe_{50}$ and (d) $Ni_{20}Fe_{80}$.

It should be noted no sintering aids were used in the powder compacts, for the fear of diamagnetic contamination. Fig. 4.8 shows the micrographs with elemental mapping of the fractured surface of Ni and NiFe alloy series, annealed at 600 ^{o}C. Here it is clear from the illuminated microstructure that the Ni and Fe distributions have depth difference according to the concentration of each constituent in the composition. Fig. 4.8(a) is micrograph of pure Ni and fully illuminated illustration of Ni is well visible. As the Ni concentration is lowering in the remaining Fe alloy composition, there is visible evidence of lowering of illuminated view of corresponding element in the following composition. Since the $Ni_{20}Fe_{80}$ combination is more prone to oxidation due to the higher concentration of iron, there is only a few illuminated area is visible under the mapping image.

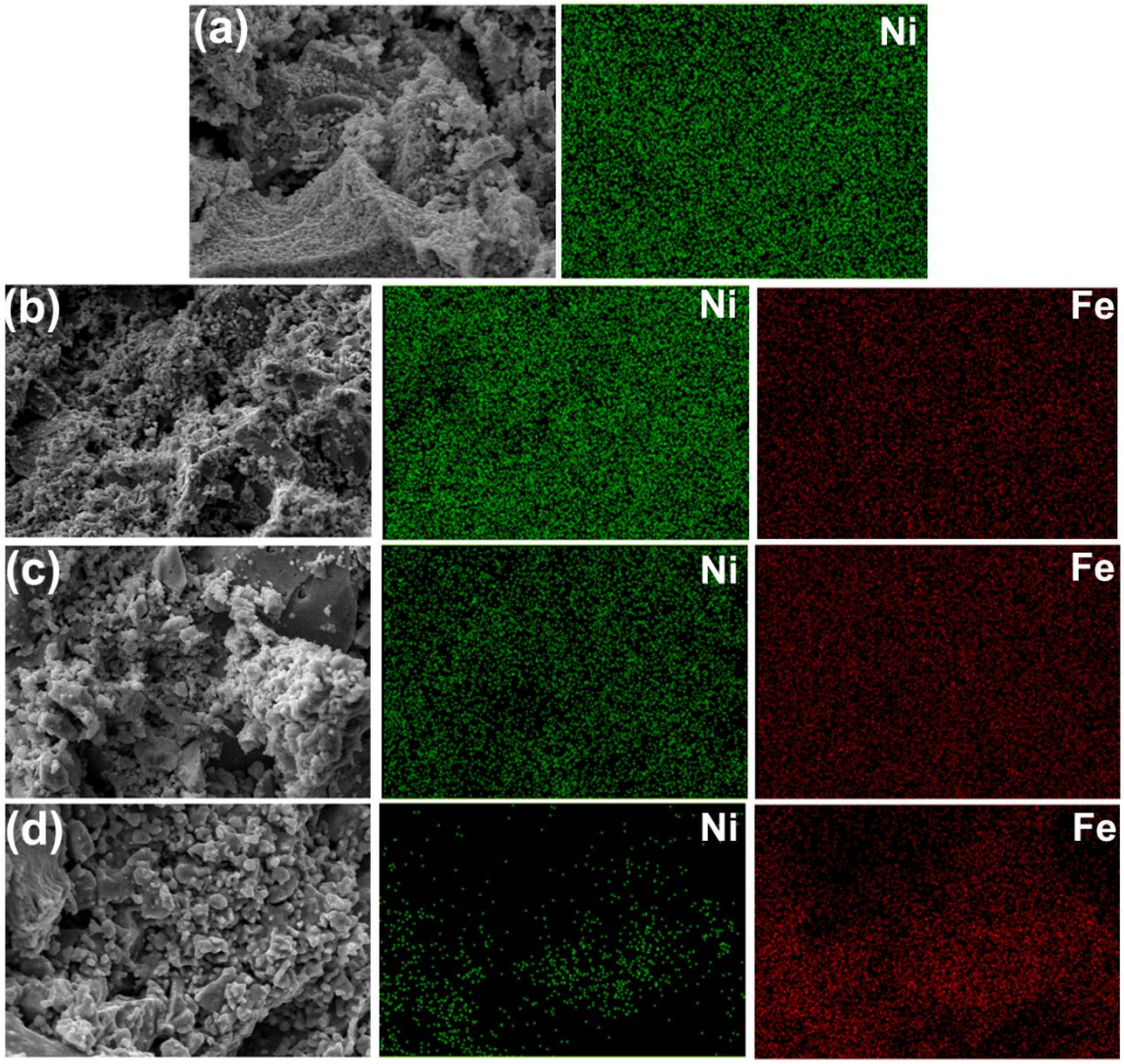

Fig. 4.8: SEM micrographs with elemental mapping of fractured surface of (a) Ni (b) $Ni_{80}Fe_{20}$ (c) $Ni_{50}Fe_{50}$ and (d) $Ni_{20}Fe_{80}$.

4.3.2 Magnetic Properties

The magnetic properties of nanostructured nickel alloys suffer dramatic changes compared to bulk, which is mainly due to the variations in domains. Obviously, at the nanometre scale, the magnetic anisotropy energy, dipolar interactions, and packing density play crucial roles consequent to the transition to single domain regime.[29] Fig. 4.9(a) illustrates

the dependence of magnetization of Ni and NiFe alloys, for the applied magnetic field at a temperature of 300 K.

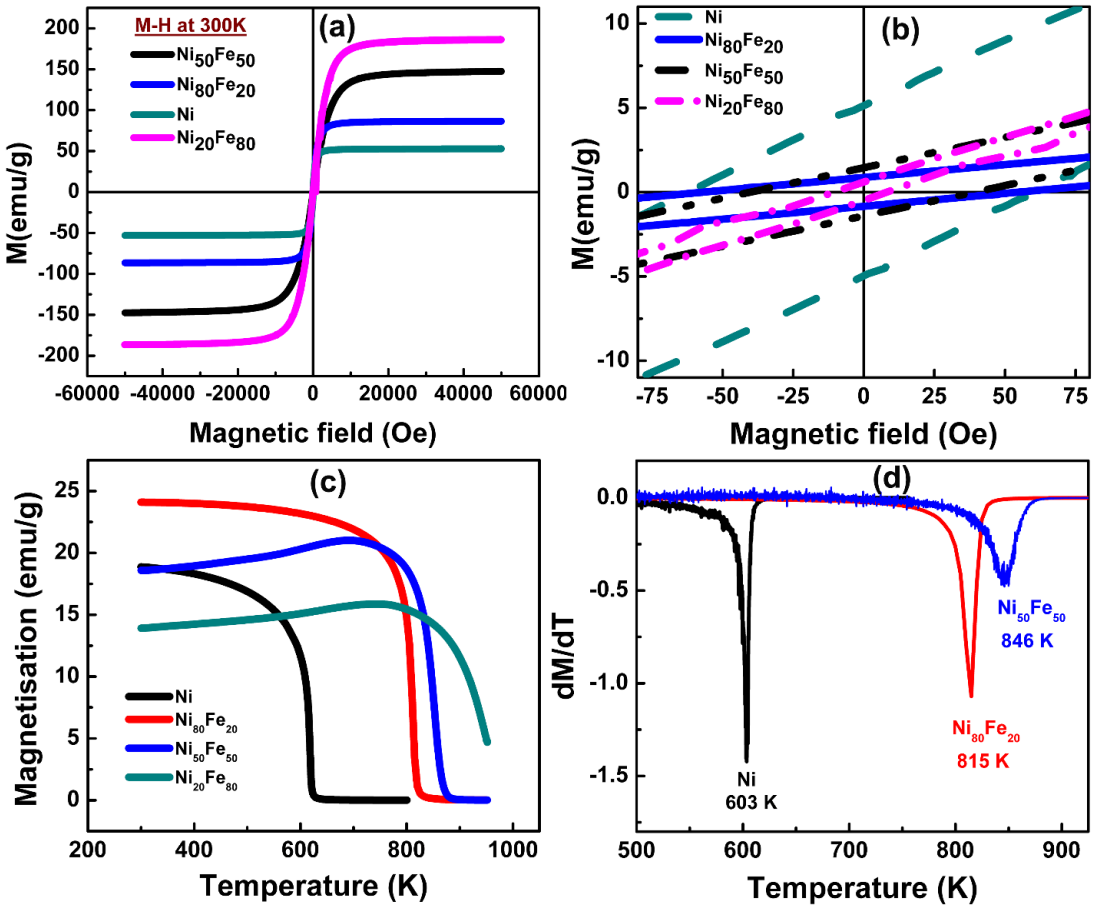

Fig. 4.9: (a) and (b) magnetization vs magnetic field (M-H) curves of Ni and NiFe alloy nanoparticles for different compositions, (c) Magnetization vs temperature curve of Ni, $Ni_{80}Fe_{20}$, $Ni_{50}Fe_{50}$ and (d) Plot of dM/dT of Ni and NiFe alloys versus temperature.

High saturation magnetization (Ms) and low coercivity (H_c) are characteristic features that promote the deployment of NiFe alloys in various soft magnetic applications.[30] EMI shielding also demands the similar properties and hence magnetic characteristics are studied for different NiFe compositions. Here, magnetic measurements were performed for magnetic field sweep between -50 kOe to 50 kOe for all the samples. Application of magnetic field causes spins to align parallel to the field.

When the field is reduced, there occurs a remnant magnetization even when the applied magnetic field reaches zero and the field required to bring the magnetization to zero is called the coercive field. As reported in the earlier literature, spherical ferromagnetic particles exhibit the same amount of magnetization in all directions and there is no shape anisotropy.[31] As shown in Fig. 4.9(c), the magnetization (Ms) is highest for $Ni_{20}Fe_{80}$ and lowest for Ni. Also one can notice from Table 4.1 that the Ms value of 52 emu/g for Ni monotonically increased to 185 emu/g for the Fe rich alloy combination i.e., $Ni_{20}Fe_{80}$. The increase of Ms with an increase in the molar concentration of Fe is due to the high inherent magnetization possessed by Fe.[15] The increased magnetization could be established by Slater-Pauling curve.[20]

Table 4.1: Magnetic properties of Ni and NiFe alloy series.

Material	Magnetic saturation Ms (emu/g)	Coercivity Hc (Oe)	Curie temperature (K)
Ni	52.90	62	603
$Ni_{80}Fe_{20}$	86.52	54	815
$Ni_{50}Fe_{50}$	147.50	38	846
$Ni_{20}Fe_{80}$	186.60	10	beyond measurable range

Fig. 4.9(c) depicts the M-T curve of nickel and nickel-iron alloy nanoparticles. The low-temperature behaviour of ferromagnetic materials could be specified by Bloch's equation ,[32]

$$M(T) = M(0)(1 - BT^{\lambda}) \quad (4.1)$$

where M(T) and M(0) denotes the saturation magnetization at temperature T K and 0 K and B is Bloch's constant and λ = 3/2. As the temperature increases, there is a reduction in saturation magnetization and beyond the Curie temperature, it undergoes a transition to a paramagnetic state.

The Curie temperature (T_C) of the spherical nickel particles was found to be 603 K which is actually less than the reported T_C for bulk Ni (627 K). The reduction in Curie temperature can be attributed to increase in the disorder of magnetic moments as well as the increase in the number of interfaces with the size reduction. Hence the thermal energy may overcome the magnetic ordering at a still lower temperature than for the bulk nickel (627 K). A T_C of 871 K was reported for the bulk $Ni_{80}Fe_{20}$ while in the present study, T_C obtained is 815 K.[33] For higher iron substituted alloys, T_C could not be estimated, since the ferro to paramagnetic transition is expected to occur above 1000 K, which is beyond the measurable temperature range of the PPMS set-up used.

In general, two factors that are found to influence the Hc of ferromagnetic nanoparticles are (i) diameter of the particles and (ii) inter-particle interaction.[31] Further, Hc also depends on the shape anisotropy constant of the nanostructure. The dependence of Hc of nanoparticles on the diameter of the particle and the critical radius,[32] R_c is defined by

$$R_c = (kA/\mu_0 {M_s}^2)^{1/2} \quad (4.2)$$

where k is 1.08 for cylindrical structures and 1.38 for spheres, the exchange constant A is 0.3 x10^{-6} erg/cm for Ni while M_s is the magnetic saturation of bulk nickel. The Hc decreases with increasing diameter after the critical radius of 13 nm for Ni.[32] As shown in Table 4.1, the apparent Hc for polyol derived nickel nanoparticle is 62 Oe, which is

lower than that reported for spherical Ni nano particles.[34] As the Fe concentration in NiFe alloy increases, there is an increase in grain size and interparticle interaction which caused a decrease in the Hc values. In the present investigation, the Hc value for $Ni_{20}Fe_{80}$ was found to be the lowest i.e., 10 Oe. Here, the size of the spherical Ni and NiFe alloy particles are approximately ~ 20 nm. The observed decrease in Hc for particles with a size above the critical radius can be attributed to magnetization reversal by curling.[35] This is because, when the diameter increases, the number of magnetic domains within the particle increases that result in lower Hc values. One has to consider the effect of grain boundaries also since grain boundaries hinder the domain wall motion in magnetic particles.[35] For smaller particles, there are only few grain boundaries and there is no sufficient restriction for domain wall motion which contributes to reduced Hc. Another major contribution to the Hc parameter arises from magnetostatic interparticle interaction.[31] A magnetic particle exerts a field around its neighbouring particles which assists them to be magnetized using a lesser field than that is actually required. As the packing density increases, the inter-particle interaction increases and hence lowering of the Hc results. The lowering of Hc as a function of Fe concentration increase, can be due to any of the reasons cited above.

4.3.3 Electrical Properties

For developing high-performance EMI shielding materials, excellent electrical conductivity is a desirable factor. This is because, when an electric field is applied to the surface of an ideal conductor, it will induce a current causing displacement of mobile charges inside the conductor that nullifies the field developed inside the conductor. The electrical conductivity of the synthesized samples at room temperature was studied using four probe

method. As shown in Fig. 4.10(a), the I-V plots are linear that is characteristic of conductors and alloys.

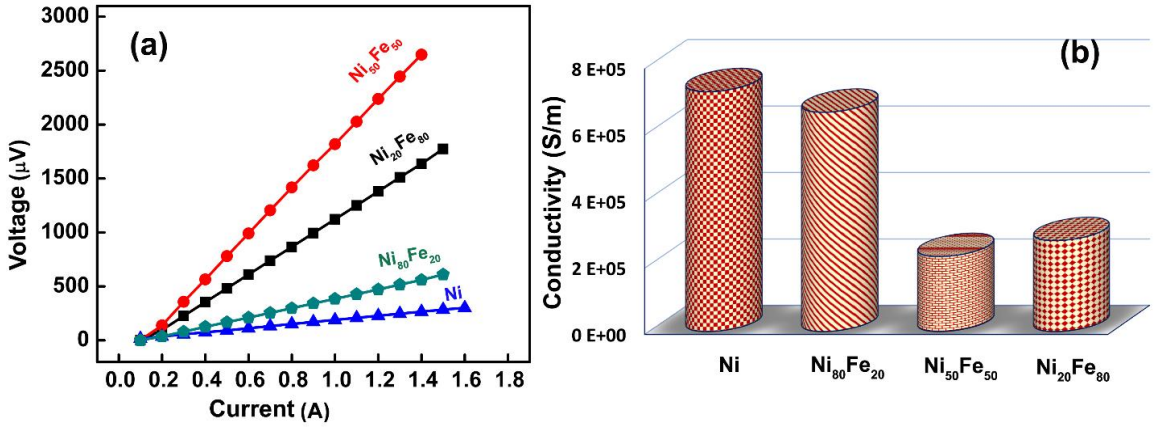

Fig. 4.10: (a) I-V plot of Ni and NiFe alloy compositions (b) DC electrical conductivity data of Ni, $Ni_{80}Fe_{20}$, $Ni_{50}Fe_{50}$ and $Ni_{20}Fe_{80}$.

Table 4.2: Electrical properties of Ni, $Ni_{80}Fe_{20}$, $Ni_{50}Fe_{50}$ and $Ni_{20}Fe_{80}$.

Composition	Resistivity (Ωm)	Conductivity (S/m)
Ni	1.39×10^{-6}	7.22×10^{5}
$Ni_{80}Fe_{20}$	1.52×10^{-6}	6.60×10^{5}
$Ni_{50}Fe_{50}$	4.42×10^{-6}	2.26×10^{5}
$Ni_{20}Fe_{80}$	3.65×10^{-6}	2.74×10^{5}

From the slope of the I-V plot, the resistance (R) was estimated and the dc electrical conductivity (σ) could be derived from the relation,

$$\sigma = \frac{l}{RA} \tag{4.3}$$

where *R* is the apparent resistance, *A* is the cross-sectional area and *l*, the distance between the voltage probe. Electrical conductivity in any system could be explained by band gap model. The electrons available near the Fermi level take part in the conduction process and electrical resistance depends on the lattice defects as well as the temperature. In ideal cases, when higher molar fractions of Fe is added to Ni, the free electrons of Fe get added to the energy levels above the Fermi level in fcc Ni and bound states are created, which in turn enhance the electrical conductivity.[20]

The electrical conductivity of Ni and its alloys are given in Table 4.2. All the observed conductivities were in the order of 10^5 S/m, but it is two orders less than their bulk counterparts.[36] This fall in conductivity could be explained based on finite size effects. As well known, the small particle size and the resultant increased number of interfaces give rise to higher surface scattering rates. This in turn, increases the mean free path for conduction electrons in the system and reduces the conductivity. Another contributing factor is the chances of surface oxidation in nickel and nickel-iron alloy nanoparticles, whose oxides are largely semiconducting. Oxide formation in polyol synthesis is inevitable since, during post-reaction processing, large amounts of the free surface are available to interact with oxygen at ambient conditions. As shown, there is a decrement in the conductivity value with Fe addition to pure Ni that reached a minimum for $Ni_{50}Fe_{50}$ composition (2.26 x 10^5 S/m) and again showed a slight improvement for $Ni_{20}Fe_{80}$. Here we have to consider the fact that Fe is more prone to oxidation and corrosion than Ni, that can reflect in the dc conductivity of the NiFe alloys. As shown in Fig. 4.4, there are slight variations in the particle size distribution for different compositions synthesized in the present study. So far as conducting composites are concerned, the connectivity of conducting fillers play a critical role in EMI attenuation. In such cases,

well-connected microstructure is preferred for high conductivity which will eventually create a micro current under the influence of an electromagnetic field. In the case of conducting composites of CNT and graphene, where hopping and migrating electrons make the way for conduction,[37,38] whereas the present system consists of pure metals and alloys. Here, the abundance of free electrons paves the way for migration of charge carriers since the conductivity is dictated by the density and mobility of charge carriers. On the other hand poor densification may adversely affect the conductivity and EMI shielding efficiency of the system, since more the porosity means lesser connectivity. Evidently, the SEM morphological analysis of heat treated Ni and its Fe alloys as depicted in Fig. 4.7, present well-connected structures with few porosities, which may contribute to an enhancement in the electron flow and generation of micro-current under the EM field. It should also be noted that a visible enhancement in the imaginary part of permittivity can also indirectly point to an enhancement in the EMI shielding effectiveness.[39,40]

4.3.4 EMI Shielding Effectiveness

From the reflection (S_{11}) and absorption (S_{21}) scattering parameters, the reflectance and transmittance can be derived from the relations, $R = |S_{11}|^2$ and $T = |S_{21}|^2$. The absorption coefficient (A) was obtained from the relation, $A + R + T = 1$. Here A, R and T are the absorption, reflection and transmission coefficients, respectively, which are representing the response of the materials towards the incident wave, i.e. the percentage of absorption, reflection, and transmission. In the present case, Ni metal nanoparticles have showed a fluctuating nature in the transmission, reflection and absorption coefficients throughout the Ku band (see Fig. 4.11). Its high absorption coefficient and lower reflection coefficient values can

be attributed to the high conducting nature as well as the slight oxide layer on the surface of Ni.

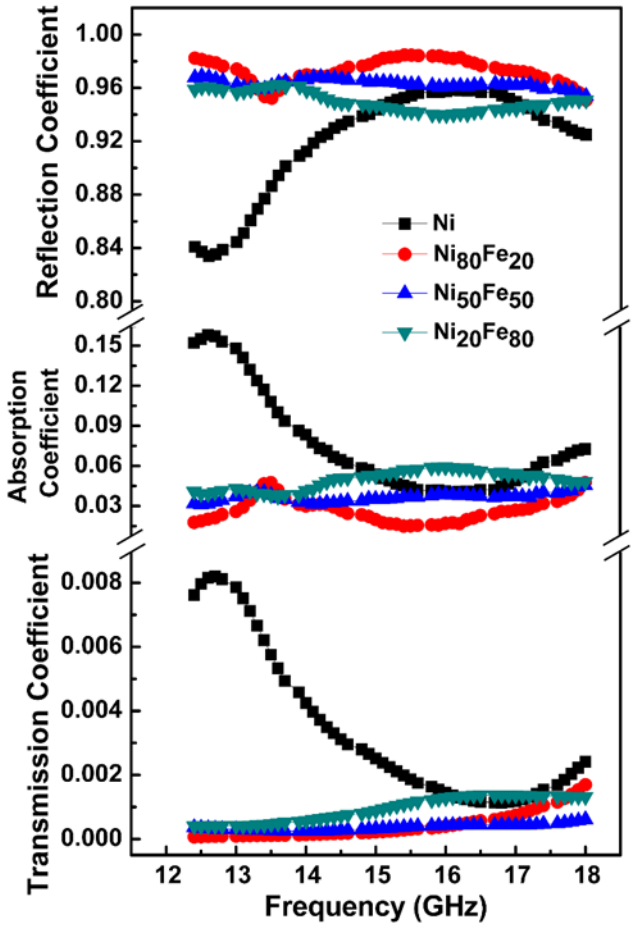

Fig. 4.11: Transmission, absorption and reflection coefficients of Ni and $Ni_{100-x}Fe_x$ [x= 20,50 and 80] alloys

A visibly high R and very low T were observed for the permalloy composition. Obviously, its high dc electrical conductivity (see Table 4.2) and permeability were favorable for achieving good R and A parameters. Interestingly, the rest of the NiFe alloys were also showing consistently high R and A with least T, throughout the Ku band. It is believed that the free electrons in the ferromagnetic metal will facilitate the reflection possible at the surface and the high value of R is a proof for its promising reflection shielding parameters. The lower T and better A values showed the capability of the alloy samples for the absorption of EM

wave inside the material. The reflection shielding efficiency (SE_R) and absorption shielding efficiency (SE_A) are calculated from the R and T as given below;[45]

$$SE_R = -10\log(1-R) \tag{4.4}$$

$$SE_A = -10\log\left(\frac{T}{1-R}\right) \tag{4.5}$$

SE_T will be the sum of (4.4) and (4.5).

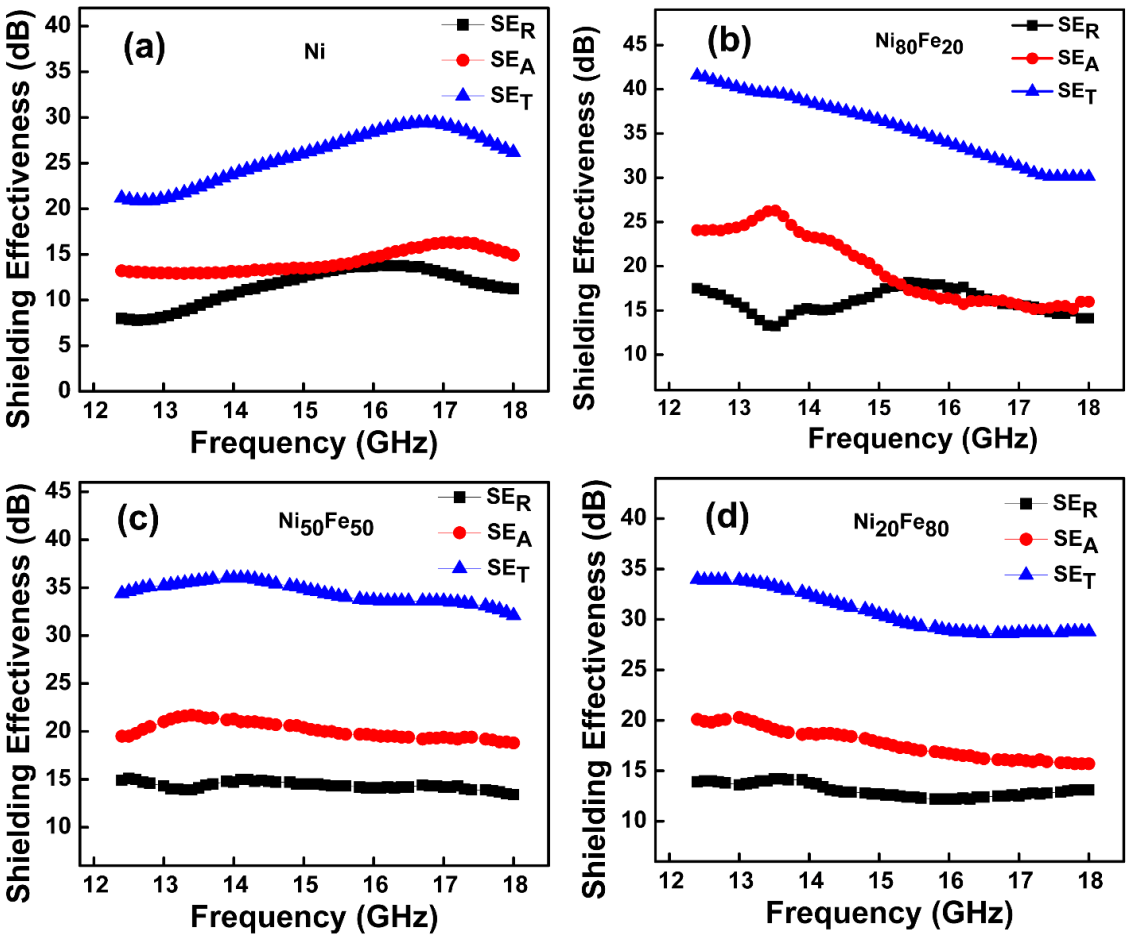

Fig. 4.12: Frequency dependent variation of total EMI shielding effectiveness (SE_T), reflection shielding effectiveness (SE_R) and absorption shielding effectiveness (SE_A) of (a) Ni (b) $Ni_{80}Fe_{20}$ (c) $Ni_{50}Fe_{50}$ and (d) $Ni_{20}Fe_{80}$ over Ku band frequency range (12.4–18 GHz).

The frequency variation of the SE_R, SE_A, and SE_T of nano Ni and NiFe alloys in the Ku band frequency range is given in Fig. 4.12. Nickel, the parent material in this study, showed an overall shielding in the range of 21 to 29 dB, at a sample thickness of 1 mm. It is understood that both reflection and absorption components have contributed to shielding effectiveness. Here, the contribution from absorption is 13 to 16 dB while that of reflection is 8 to 13 dB. Interestingly, alloys between Ni with Fe were observed to be better candidates for shielding EM wave than intrinsic Ni. For example, the permalloy composition $Ni_{80}Fe_{20}$ showed the highest shielding value of ~ 41 dB at the beginning of Ku band (see Fig. 4.12(b)) and the total shielding effectiveness falls to 30 dB when the frequency is increased from 12.4 to 18 GHz. Here the shielding mechanism is majorly contributed by absorption shielding. As given, the value for absorption shielding is in the range 16 to 26 dB while reflection shielding is in the range 14 to 18 dB, during the entire frequency band. The reason for high shielding effectiveness originates from the inherent nature of permalloy nanoparticles having higher permeability, in addition to good electrical conductivity.

In all the studied samples of Ni and its Fe alloys, the microwave attenuation is contributed by absorption and reflection, though with varying extents. Since the studied materials are conducting as well as magnetic, both dielectric loss and magnetic loss factors are active contributors towards net shielding. The appreciably good electrical conductivity results in the lowering of skin depth, which in turn makes the EM waves to reflect at the surface between materials and air. Also it creates a micro-current inside the conductor while interacting with EM wave, that may help to increase the loss factor and imaginary part of permittivity determined by the orientational relaxation loss of intrinsic dipoles and electrical conductivity.[46] Considering absorption shielding, the impedance matching conditions are vital at the interfaces

between the material and air.[47] Here in the present case, since the surface of nanoparticles possess a thin oxide layer, it will provide the required impedance matching condition at the interface for the incoming EM waves. It was reported in literature that the NiO can improve the dielectric properties of microwave absorbing materials due to its high permittivity and electronic properties.[39] For a perfect magnetic shielding material, the perfect synergy of dielectric loss and magnetic loss is an essential strategy for maximum attenuation.[48] Since the synthesized alloys possess high electrical conductivity, it may help to enhance the dielectric loss factor, according to Debye theory.[49] So, it is likely that an ideal synergy conditions like a combination of high conductivity, better permeability and impedance matching conditions might have attributed to the enhanced microwave absorption in the present batch of nickel and its alloys.

The relations connecting SE_A, SE_R, σ, f, μ and t are shown in equations 2.6 and 2.7 in chapter 2. While analyzing the conductivity parameter in those equations, it can be elucidated that the change in the permeability and conductivity values has a more direct influence to the SE_A than SE_R values. Absorption dominant shielding effectiveness for the investigated batch of alloy sheets was clearly predictable, as there is a direct relation for SE_A on permittivity and conductivity parameters. As shown in Fig. 4.12(c) and (d), with further increment in the Fe loading, there was no further enhancement in the EMI SE values, but only a marginal decrement in the SE values, in accordance with the increasing Fe content. Here it should be noted that, absorption shielding is mainly contributed by the high magnetic permeability which is directly proportional to the saturation magnetization.

Table 4.3: A brief survey of Ni or NiFe alloy-based EMI shielding studies for the last 10 years.

Sl No	Materials	Method	Frequency / Method of EMI measurement	SE(dB)	Thickness	Reference
1.	Core/shell-type iron and nickel nanoparticles	DC arc discharge method	2-18 GHz/ coaxial	> 30 dB (9 to 10 GHz)	1.7 mm	[52]
2.	Ni films deposited on cenosphere particles	Ultrasonic-assisted magnetron sputtering	80-110 GHz/ coaxial	4–27 dB (80 to 100GHz)	60 mm	[53]
3.	$Fe_{50}Ni_{50}$ powder	Mechanical milling	0.1-18 GHz/coaxial	> 10 dB (@ 0.8-1.8 GHz	2.5 – 1.2 mm	[54]
4.	Hexagonal $Ni/Ni(OH)_2$	Hydrazine reduction	2-18 GHz/coaxial	> 20 dB (@ 9 - 10GHz	2 mm	[55]
5.	Ni–Fe alloy on the helical microorganism cells	Electroplating	2-18 GHz/ coaxial	10 to 10.6 dB	1 to 1.5 mm	[56]
6.	Fe–40 wt. % Ni alloys with granular and flake shape	Mechanical alloying	0.5-4 GHz/ coaxial	> 20 dB (0.5 – 1 GHz)	4 – 5 mm	[57]
7.	Fe-50 wt. % Ni alloy	High frequency induction melting	1-18 GHz/ coaxial	6 dB (1-2 Hz)	3 mm	[2]
8.	$Ni@Ni_2O_3$ core–shell particles	Hydrogen peroxide oxidation method	0.1-18 GHz/coaxial	> 20 dB (4 GHz & 12.6 GHz)	1.8 – 4.3 mm	[58]
9.	Ni nanoparticles	Polyol route	12.4-18 GHz/ wave guide	21 to 29 dB (12.4-18 GHz)	1 mm	Present work
10.	$Ni_{80}Fe_{20}$ alloy nanoparticles	Polyol route	12.4-18 GHz/ wave guide	30 to 41 dB	1 mm	Present work
11.	$Ni_{50}Fe_{50}$ alloy nanoparticles	Polyol route	12.4-18 GHz/ wave guide	32 to 36 dB	1 mm	Present work
12.	$Ni_{20}Fe_{80}$ alloy nanoparticles	Polyol route	12.4-18 GHz/ wave guide	28 to 34 dB	1 mm	Present work

Since iron exhibits superior saturation magnetization (or permeability) compared to nickel (as shown in Fig. 4.9), the EMI shielding of iron dominant alloys, is expected to be high. In other words, in iron rich materials, we believe that the contribution of increasing permeability to EMI shielding is more prominent than a slight decrease in electrical conductivity. The optimum level of shielding for $Ni_{50}Fe_{50}$ is in the range 32 to 36 dB while that for $Ni_{20}Fe_{80}$ is 28 to 34 dB. More importantly, all the NiFe compositions are found to be good candidates for commercial EMI shielding applications with an attenuation efficiency of 99.9 %.

Here in Table 4.3, a literature study of EMI shielding solutions using Ni or NiFe alloys, from the year 2008 onwards, is given. However, those works which include a combination of ferromagnetic Ni/NiFe alloy with a conducting material, are excluded from the current survey, as the latter will have an effect on their total EMI shielding values. As shown in Table 4.3, all the NiFe alloys developed in the present study are found to be ideal for shielding purpose with SE value of above 30 dB. Further, a still better shielding of over 30 to 41 dB was achieved for permalloy composition even at a smaller thickness of 1 mm, throughout the Ku band.

4.4 Conclusions

Nickel NPs and their alloys with different molar ratios of iron were synthesized using a simple, surfactant-free polyol method, using a high boiling solvent, PEG. The concentration of the reactants was kept constant throughout the whole composition range of NiFe. From the TEM analysis, the uniform spherical nature of nickel and alloys were confirmed with an average size range of 10-30 nm. A thin oxide layer is vaguely visible in the TEM and the EDAX spectrum showed the presence of oxygen in the spectra. The XPS analysis further confirmed the formation of oxide layer associated with the nickel and its alloys that ensure prevention of further oxidation and good impedance matching conditions. A Ms of 52 emu/g

was observed for Ni NPs with a Hc range of 62 Oe. Further, with increasing Fe concentration in alloys shows an increasing trend in Ms while decreases Hc proportionally. The decrease in Hc as a function of Fe content can be due to magnetostatic interparticle interaction wherein magnetic particle exerts a field around its neighbouring particles which assists them to be magnetized using a lesser field than that is actually required. Since the packing density increases with Fe addition in the present study, the interparticle interaction increases and hence lowering of the Hc results. The dc electrical resistivity was shown to be lowest for the $Ni_{80}Fe_{20}$ (permalloy) combination, and further increment in the Fe content is helping the resistivity to increase. This trend is believed to be due to the oxidative corrosion of the Fe rich alloys where electrons have to hop at larger scales to enable conduction. The pressed precursor powder in a rectangular die was annealed at 600 ^{o}C in the H_2 atmosphere to fabricate thin sheets of the metal alloy samples of suitable dimensions for EMI shielding studies in the Ku band. The densified and hydrogen annealed samples displayed excellent microwave shielding properties ranging from 21 to 41 dB in the entire Ku bands. The lowest EMI shielding range of 21 to 29 dB was observed in the case of Ni NPs whereas the highest range was attained in permalloy (30 to 41 dB). Of the total shielding of 30 to 41 dB for permalloy, a major portion was contributed by the absorption shielding (16 to 26 dB) and the reflection shielding value was in the range of 14 to 18 dB. Unlike the parent Ni, all other NiFe alloy combinations were showing EMI shielding above 30 dB, with significant enhancements in the absorption shielding efficiency. To the best of our knowledge, no other previous studies on nanostructured NiFe alloys were indicating a consistent EMI shielding performance (> 30 dB) throughout Ku band. This high value of shielding efficiency above 99.9 %, suggests the possible commercial applicability of nano permalloy based coatings and composite structures, for magnetic

shielding applications in systems like aviation radars, video displays, magnetic proximity sensors, audio-visual recorders etc.

4.5 References

(1) Qin, G. W.; Pei, W. L.; Ren, Y. P.; Shimada, Y.; Endo, Y.; Yamaguchi, M.; Okamoto, S.; Kitakami, O. $Ni_{80}Fe_{20}$ Permalloy Nanoparticles: Wet Chemical Preparation, Size Control and Their Dynamic Permeability Characteristics when Composited with Fe Micron Particles. *J. Magn. Magn. Mater.* **2009**, *321* (24), 4057–4062.

(2) Feng, Y.; Qiu, T. Enhancement of Electromagnetic and Microwave Absorbing Properties of Gas Atomized Fe-50 Wt.%Ni Alloy by Shape Modification. *J. Magn. Magn. Mater.* **2012**, *324* (16), 2528–2533.

(3) Rao, C. N. R.; Ramakrishna Matte, H. S. S.; Voggu, R.; Govindaraj, A. Recent Progress in the Synthesis of Inorganic Nanoparticles. *Dalt. Trans.* **2012**, *41* (17), 5089–5120.

(4) Gheisari, K.; Shahriari, S.; Javadpour, S. Structural Evolution and Magnetic Properties of Nanocrystalline 50 Permalloy Powders Prepared by Mechanical Alloying. *J. Alloy. Compd.* **2013**, *574*, 71–82.

(5) Liu, Z.; Li, S.; Yang, Y.; Peng, S.; Hu, Z.; Qian, Y. Complex-Surfactant-Assisted Hydrothermal Route to Ferromagnetic Nickel Nanobelts. *Adv. Mater.* **2003**, *15* (22), 1946–1948.

(6) Zhong, Z.; Mastai, Y.; Koltypin, Y.; Zhao, Y.; Gedanken, A. Sonochemical Coating of Nanosized Nickel on Alumina Submicrospheres and the Interaction between the Nickel and Nickel Oxide with the Substrate. *Chem. Mater.* **1999**, *11* (9), 2350–2359.

(7) Ban, I.; Drofenik, M.; Makovec, D. The Synthesis of Iron-Nickel Alloy Nanoparticles Using a Reverse Micelle Technique. *J. Magn. Magn. Mater.* **2006**, *307* (2), 250–256.

(8) Suh, Y. J.; Jang, H. D.; Chang, H.; Kim, W. B.; Kim, H. C. Size-Controlled Synthesis of Fe-Ni Alloy Nanoparticles by Hydrogen Reduction of Metal Chlorides. *Powder Technol.* **2006**, *161* (3), 196–201.

(9) Dong, H.; Chen, Y.-C.; Feldmann, C. Polyol Synthesis of Nanoparticles: Status and Options Regarding Metals, Oxides, Chalcogenides, and Non-Metal Elements. *Green*

Chem. **2015**, *17* (8), 4107–4132.

(10) Viau, G.; Fiévet-Vincent, F.; Fiévet, F. Nucleation and Growth of Bimetallic CoNi and FeNi Monodisperse Particles Prepared in Polyols. *Solid State Ionics* **1996**, *84* (3–4), 259–270.

(11) Liu, C.; Wu, X.; Klemmer, T.; Shukla, N.; Yang, X.; Weller, D.; Roy, A. G.; Tanase, M.; Laughlin, D. Polyol Process Synthesis of Monodispersed FePt Nanoparticles. *J. Phys. Chem. B* **2004**, *108* (20), 6121–6123.

(12) Joseyphus, R. J.; Shinoda, K.; Kodama, D.; Jeyadevan, B. Size Controlled Fe Nanoparticles through Polyol Process and Their Magnetic Properties. *Mater. Chem. Phys.* **2010**, *123* (2–3), 487–493.

(13) Carroll, K. J.; Reveles, J. U.; Shultz, M. D.; Khanna, S. N.; Carpenter, E. E. Preparation of Elemental Cu and Ni Nanoparticles by the Polyol Method: An Experimental and Theoretical Approach. *J. Phys. Chem. C* **2011**, *115* (6), 2656–2664.

(14) Couto, G. G.; Klein, J. J.; Schreiner, W. H.; Mosca, D. H.; de Oliveira, A. J. A.; Zarbin, A. J. G. Nickel Nanoparticles Obtained by a Modified Polyol Process: Synthesis, Characterization, and Magnetic Properties. *J. Colloid Interface Sci.* **2007**, *311* (2), 461–468.

(15) Islam, M. N.; Abbas, M.; Kim, C. Synthesis of Monodisperse and High Moment Nickel-Iron (NiFe) Nanoparticles Using Modified Polyol Process. *Curr. Appl. Phys.* **2013**, *13* (9), 2010–2013.

(16) Long, N. V.; Yang, Y.; Thi, C. M.; Phuc, L. H.; Nogami, M. Polyol-Mediated Synthesis, Microstructure and Magnetic Properties of Hierarchical Sphere, Rod, and Polyhedral α-Fe_2O_3 Oxide Particles. *J. Electron. Mater.* **2017**, *46* (6), 3615–3621.

(17) Long, N. V.; Yang, Y.; Yuasa, M.; Thi, C. M.; Cao, Y.; Nann, T.; Nogami, M. Gas-Sensing Properties of p-Type α-Fe_2O_3 Polyhedral Particles Synthesized via a Modified Polyol Method. *RSC Adv.* **2014**, *4* (16), 8250–8255.

(18) Abbas, M.; Parvatheeswara Rao, S.M. Naga, Migaku Takahashi, C. K. Synthesis of

High Magnetization Hydrophilic Magnetite (Fe_3O_4) Nanoparticles in Single Reaction-Surfactantless Polyol Process. *Ceram. Int.* **2013**, *39* (7), 7605–7611.

(19) Zhang, B.; Tu, Z.; Zhao, F.; Wang, J. Superparamagnetic Iron Oxide Nanoparticles Prepared by Using an Improved Polyol Method. *Appl. Surf. Sci.* **2013**, *266*, 375–379.

(20) Guechi, N.; Bourzami, A.; Guittoum, A.; Kharmouche, A.; Colis, S.; Meni, N. Structural , Magnetic and Electrical Properties of Fe_xNi_{100-x} / Si (100) Films. *Phys. B* **2014**, *441*, 47–53.

(21) Sajanlal, P. R.; Pradeep, T. Functional Hybrid Nickel Nanostructures as Recyclable SERS Substrates: Detection of Explosives and Biowarfare Agents. *Nanoscale* **2012**, *4* (11), 3427–3437.

(22) Duo L.; Finazzi M.; Ciccacci, F. *Magnetic Properties of Antiferromagnetic Oxide Materials*; Wiley-VCH Verlag GmbH & Co. Weinheim, 2010.

(23) Cheng, W.; He, J.; Yao, T.; Sun, Z.; Jiang, Y.; Liu, Q.; Jiang, S.; Hu, F.; Xie, Z.; He, B.; et al. Half-Unit-Cell α-Fe_2O_3 semiconductor Nanosheets with Intrinsic and Robust Ferromagnetism. *J. Am. Chem. Soc.* **2014**, *136* (29), 10393–10398.

(24) Fuggle, J. C.; Hillebrecht, F. U.; Zeller, R.; Zo, Z.; Bennett, P. A. Electronic Structure of Ni and Pd Alloys. I. X-Ray Photoelectron Spectroscopy of the Valence Bands. *Phys. Rev. B* **1983**, *27* (4), 2145–2178.

(25) Nguyen, D. T.; Ferrec, A.; Keraudy, J.; Goullet, A.; Cattin, L.; Brohan, L.; Jouan, P. Ellipsometric and XPS Characterization of Transparent Nickel Oxide Thin Films Deposited by Reactive HiPIMS. *Surf. Coat. Technol.* **2014**, *250*, 21–25.

(26) Xi Li, Hengbin Zhang, Xiaoxun Liu, S. L. and M. Z. XPS Study on O (Ls) and Fe (2p) for Nanocrystalline Composite Oxide $LaFe0_3$ with the Perovskite Structure. *Mater. Chem. Phys.* **1994**, *38*, 355–362.

(27) Salou, M.; Lescop, B.; Rioual, S.; Lebon, A.; Youssef, J. Ben; Rouvellou, B. Surface Science Initial Oxidation of Polycrystalline Permalloy Surface. *Surf. Sci.* **2008**, *602*, 2901–2906.

(28) Yamashita, T.; Hayes, P. Analysis of XPS Spectra of Fe^{2+} and Fe^{3+} Ions in Oxide Materials. *Appl. Surf. Sci.* **2008**, *254*, 2441–2449.

(29) Cullity, B. D.; Graham, C. D. *Introduction to Magnetic Materials (2nd Edition)*; John Wiley & Sons, Inc., Hoboken, New Jersey, 2009.

(30) Pfeifer. F and Radeloff. C. Soft Magnetic Ni-Fe and Co-Fe Alloys - Some Physical and Metallurgical Aspects. *J. Magn. Magn. Mater.* **1980**, *19*, 190–207.

(31) Spaldin, N. A. *Magnetic Materials Fundamentals and Applications*; Cambridge University Press, New York, 2010.

(32) Zheng, M.; Menon, L.; Zeng, H.; Liu, Y.; Bandyopadhyay, S.; Kirby, R. D.; Sellmyer, D. J. Magnetic Properties of Ni Nanowires in Self-Assembled Arrays. *Phys. Rev. B - Condens. Matter Mater. Phys.* **2000**, *62* (18), 12282–12286.

(33) Wakelin, R. J.; Yates, E. L. A Study of the Order-Disorder Transformation in Iron-Nickel Alloys in the Region $FeNi_3$. *Proc. Phys. Soc. Sect. B* **1953**, *66* (3), 221–240.

(34) He, X.; Zhong, W.; Au, C.-T.; Du, Y. Size Dependence of the Magnetic Properties of Ni Nanoparticles Prepared by Thermal Decomposition Method. *Nanoscale Res. Lett.* **2013**, *8* (1), 446.

(35) Yu, R. H.; Basu, S.; Zhang, Y.; Parvizi-Majidi, A.; Xiao, J. Q. Pinning Effect of the Grain Boundaries on Magnetic Domain Wall in FeCo-based Magnetic Alloys. *J. Appl. Phys.* **1999**, *85* (9), 6655–6659.

(36) Fert, A.;Campbell, I. A. Electrical Resistivity of Ferromagnetic Nickel and Iron Based Alloys. *J. Phys. F Met. Phys.* **1976**, *6* (5), 849–871.

(37) Cao, M.; Yang, J.; Song, W.; Zhang, D.; Wen, B.; Jin, H.; Hou, Z.; Yuan, J. Ferroferric Oxide/Multiwalled Carbon Nanotube vs Polyaniline/ Ferroferric Oxide/Multiwalled Carbon Nanotube Multiheterostructures for Highly Effective Microwave Absorption. *ACS Appl. Mater. Interfaces* **2012**, *4*, 6949–6956.

(38) Lu, M. M.; Cao, M. S.; Chen, Y. H.; Cao, W. Q.; Liu, J.; Shi, H. L.; Zhang, D. Q.; Wang,

W. Z.; Yuan, J. Multiscale Assembly of Grape-Like Ferroferric Oxide and Carbon Nanotubes: A Smart Absorber Prototype Varying Temperature to Tune Intensities. *ACS Appl. Mater. Interfaces* **2015**, *7* (34), 19408–19415.

(39) Yang, H.; Cao, M.; Li, Y.; Shi, H.; Hou, Z.; Fang, X.; Jin, H.; Wang, W.; Yuan, J. Enhanced Dielectric Properties and Excellent Microwave Absorption of SiC Powders Driven with NiO Nanorings. *Adv. Opt. Mater.* **2014**, *2* (3), 214–219.

(40) Wen, B.; Cao, M.; Lu, M.; Cao, W.; Shi, H.; Liu, J.; Wang, X.; Jin, H.; Fang, X.; Wang, W. Reduced Graphene Oxides: Light-Weight and High-Efficiency Electromagnetic Interference Shielding at Elevated Temperatures. *Adv. Mater.* **2014**, *26* (21), 3484–3489.

(41) Dijith, K. S.; Pillai, S.; Surendran, K. P. Thermophysical and Microwave Shielding Properties of $La_{0.5}Sr_{0.5}CoO_{3-\delta}$ and Its Composite with Epoxy. *J. Electron. Mater.* **2017**, *46* (8), 5158–5167.

(42) Li, B. W.; Shen, Y.; Yue, Z. X.; Nan, C. W. Enhanced Microwave Absorption in Nickel/Hexagonal-Ferrite/Polymer Composites. *Appl. Phys. Lett.* **2006**, *89* (13), 132504 1-3.

(43) Saini, P.; Choudhary, V.; Singh, B. P.; Mathur, R. B.; Dhawan, S. K. Polyaniline-MWCNT Nanocomposites for Microwave Absorption and EMI Shielding. *Mater. Chem. Phys.* **2009**, *113* (2–3), 919–926.

(44) Joseph, N.; Varghese, J.; Sebastian, M. T. A Facile Formulation and Excellent Electromagnetic Absorption of Room Temperature Curable Polyaniline Nanofiber Based Inks. *J. Mater. Chem. C* **2016**, *4* (4), 999–1008.

(45) Dijith, K. S.; Pillai, S.; Surendran, K. P. Screen Printed Silver Patterns on $La_{0.5}Sr_{0.5}CoO_{3-\delta}$ - Epoxy Composite as a Strategy for Many-Fold Increase in EMI Shielding. *Surf. Coat. Technol.* **2017**, *330*, 34–41.

(46) Liu, J.; Cao, M. S.; Luo, Q.; Shi, H. L.; Wang, W. Z.; Yuan, J. Electromagnetic Property and Tunable Microwave Absorption of 3D Nets from Nickel Chains at Elevated

Temperature. *ACS Appl. Mater. Interfaces* **2016**, *8* (34), 22615–22622.

(47) Zhao, C.; Yu, Y.; Chen, Z.; Wen, G.; Wei, F.; Zheng, Q.; Wang, C.; Xiao, X. Temperature Dependent Microwave Attenuation Behavior for Carbon-Nanotube/Silica Composites Bo. *Carbon.* **2013**, *65*, 124–139.

(48) Shi, X. L.; Cao, M. S.; Yuan, J.; Fang, X. Y. Dual Nonlinear Dielectric Resonance and Nesting Microwave Absorption Peaks of Hollow Cobalt Nanochains Composites with Negative Permeability. *Appl. Phys. Lett.* **2009**, *95* (16), 10–13.

(49) Cao, M. S.; Song, W. L.; Hou, Z. L.; Wen, B.; Yuan, J. The Effects of Temperature and Frequency on the Dielectric Properties, Electromagnetic Interference Shielding and Microwave-Absorption of Short Carbon Fiber/Silica Composites. *Carbon.* **2010**, *48* (3), 788–796.

(50) Kumar, G. S.; Vishnupriya, D.; Joshi, A.; Datar, S.; Patro, T. U. Electromagnetic Interference Shielding in 1-18 GHz Frequency and Electrical Property Correlations in Poly(Vinylidene Fluoride)-Multi-Walled Carbon Nanotube Composites. *Phys. Chem. Chem. Phys.* **2015**, *17* (31), 20347–20360.

(51) Xu, Y.; Li, Y.; Hua, W.; Zhang, A.; Bao, J. Light-Weight Silver Plating Foam and Carbon Nanotube Hybridized Epoxy Composite Foams with Exceptional Conductivity and Electromagnetic Shielding Property. *ACS Appl. Mater. Interfaces* **2016**, *8* (36), 24131–24142.

(52) Lu, B.; Dong, X. L.; Huang, H.; Zhang, X. F.; Zhu, X. G.; Lei, J. P.; Sun, J. P. Microwave Absorption Properties of the Core/Shell-Type Iron and Nickel Nanoparticles. *J. Magn. Magn. Mater.* **2008**, *320* (6), 1106–1111.

(53) Yu, X.; Shen, Z. The Electromagnetic Shielding of Ni Films Deposited on Cenosphere Particles by Magnetron Sputtering Method. *J. Magn. Magn. Mater.* **2009**, *321* (18), 2890–2895.

(54) Wei, J.; Zhang, Z.; Wang, B.; Wang, T.; Li, F. Microwave Reflection Characteristics of Surface-Modified $Fe_{50}Ni_{50}$ fine Particle Composites. *J. Appl. Phys.* **2010**, *108* (12),

123908 1-5.

(55) Wang, C.; Han, X.; Xu, P.; Wang, J.; Du, Y.; Wang, X.; Qin, W.; Zhang, T. Controlled Synthesis of Hierarchical Nickel and Morphology-Dependent Electromagnetic Properties. *J. Phys. Chem. C* **2010**, *114*, 3196–3203.

(56) Lan, M.; Zhang, D.; Cai, J.; Zhang, W.; Yuan, L. Fabrication and Electromagnetic Properties of Bio-Based Helical Soft-Core Particles by way of NiFe Alloy Electroplating. *J. Magn. Magn. Mater.* **2011**, *323* (24), 3223–3228.

(57) Liu, J.; Feng, Y.; Qiu, T. Synthesis, Characterization, and Microwave Absorption Properties of Fe 40 Wt.% Ni Alloy Prepared by Mechanical Alloying and Annealing. *J. Magn. Magn. Mater.* **2011**, *323* (23), 3071–3076.

(58) Wang, B.; Zhang, J.; Wang, T.; Qiao, L.; Li, F. Synthesis and Enhanced Microwave Absorption Properties of Ni@Ni_2O_3 core-Shell Particles. *J. Alloys Compd.* **2013**, *567*, 21–25.

Chapter 5

Metallized Flexible Fabrics for Microwave Shielding Applications

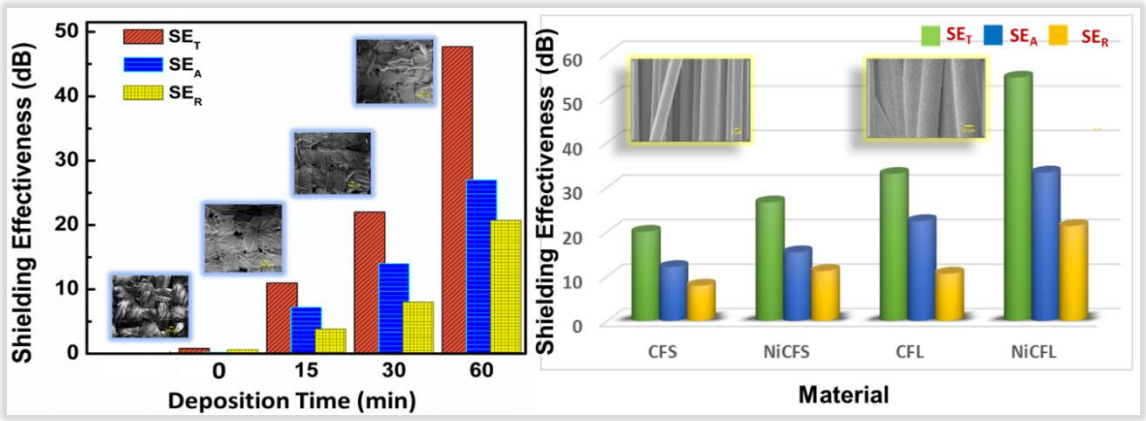

This chapter outlines the efforts to qualify woven fabrics as substrates for electrodeposition, in view of qualifying them as an EMI shield. In order to achieve this goal, surface activation of the fabric using sputtered platinum is introduced, followed by electrodeposition of nickel using Watts bath solution. Interestingly, the two step process has transformed the fabric from an EMI transparent stuff to an excellent EMI attenuator. Exceptional EMI shielding efficiency of 99.999% was achieved for Ni deposited linen fabrics. Similar electrodeposition procedure was followed in the case of carbon fabric, except the Pt sputtering step. The Ni deposited carbon fabrics have exceptional shielding efficiency of 55-58 dB, which is suitable for high performance outdoor shielding applications. The ultimate goal of this research can lead to the development of lightweight, wearable and flexible 'radar invisible fabrics', which has wide range of applicability in defense and healthcare sectors.

5.1 Nickel Electrodeposited Textile Fabrics for Microwave Shielding Applications

5.1.1 Introduction

As discussed in the previous chapters, highly conductive metals or highly permeable magnetic materials are used as microwave shields[1] where corrosion resistant metals are most preferred, due to their strength and high electrical conduction. But there are domains where high density and rigid nature of metals can be constraints in application such as wearable and portable shields. For example, RF shielding portable tents, curtains and screens are used for customised mobile laboratories and workstations. Further, shielded mobile phone and laptop pouches which is highly handy for domestic as well as police, military and security services around the globe. In defence, a microwave absorbing attire designed for a reportedly located soldier will be useful, since it can make him 'radar invisible' to the surveillance radars of the enemy. Against this background, the research on conductive textile materials as EMI shields gain rapid momentum. Ideally, the fabric shield should combine the flexibility, breathability and conformability of a textile fabric, with the RF electrical properties of a metal, like ultra-low surface resistivity and excellent shielding effectiveness.

Since most textile materials are intrinsically non-conductive and EMI transparent, there are different modification techniques that could transform them into conductive materials to be employed as EMI shields. Textiles could be structurally classified into three: woven, knitted or non-woven fabrics. In a woven fabric, warp and weft interlace at every single crossing for plain weaves and interlaces, after two or more crossings for twill. A chain of interconnected loops in the yarn creates a knitted fabric.[2] The surface modification methods and incorporation of fillers are two ways of making textiles conductive. Conductive coatings, electroless plating,

electroplating, thermal evaporation, sputtering and ion plating are different techniques adopted for modification of textile surface to conductive shields. Another way is to wrap fine yarn over metallic fibers, where the later is usually located within the core of the yarn, thereby preventing physical contact with the wearer. Nevertheless, since the electrically conductive components are internalized within yarn, yarn-to-yarn conductivity is discontinuous and therefore the fabrics formed from these yarns do not provide a sufficient level of conductivity to provide high level EMI shielding capabilities. Hence coating of fabrics with suitable metals has become the most facile option.

Conductive fillers include metallic nanoparticles, conducting polymers and carbonaceous materials. Saini *et al*. demonstrated that conductive polymer layers formed on cotton fabrics by polymerization method exhibited microwave absorption dominant shielding in X-band (8.2–12.4 GHz), where polypyrrole (PPY) grafted fabrics showed shielding effectiveness of 11.3 to 11.7 dB and polyaniline (PANI) grafted structures achieved shielding values of 9.2 to 9.6 dB.[3] Though they could be effective solutions for electrostatic charge dissipation functions, these fabrics could be qualified as efficient shields, with their efficiency reaching only 92%. Carbonaceous nanoparticles exhibit more resistivity than their metallic counterparts while employed as fillers and hence has only limited use in applications demanding high shielding efficiency > 50 dB.[4] Among the metals, silver, copper and nickel are the most widely studied ones for EMI shielding fabric applications. A wet electroless plating technique for coating silver on surface of cotton fabric, showed excellent shielding value of 71 dB at X band, which is attributed to cell-like configurations formed owing to the porous nature of non-woven fabric and cotton-silver core-shell structure.[5] Zhao et al. reported copper film developed by electroless coating on cuprammonium fabric/polypyrrole

composite, derived from in-situ polymerization technique. This multilayered structure showed shielding values as high as 30.3-50.4 dB at a frequency range of 30-1000 MHz.[6]

Among electroplatable metals, silver is a highly expensive choice considering the cost for producing large scale shielding structures whereas copper is highly corrosive and requires special inert conditions for fabrication; thus making nickel an optimum choice for fabricating microwave attenuating shields.[7] Excellent magnetic properties also make Ni based coatings effective shields against low frequency EM waves. Textiles like nylon, linen, cotton and polyester are intrinsically highly resistive materials and are reported to show poor shielding efficiency of 0.1 dB upto a frequency range of 1.5 GHz, but suitable incorporation of metallic components could enhance the shielding values to 79 dB.[8] Recently Xu et al. reported electroless Ni plated flexible Nylon membrane forming a sandwich shielding structure with excellent shielding efficiency of 77 dB in X band.[4] Polytrimethylene-terephthalate (PTT) fabric was coated with PANI by in-situ chemical polymerization and nickel was coated by electroless method, to produce shielding effectiveness of above 40 dB at 1.5 GHz.[9] Polyester fabric when coated with magnetite nanoparticles and modified with PEDOT through chemical vapour deposition technique, possessed shielding effectiveness of 13-17 dB in X band.[10] Electroless Ni plating on PPY deposited linen fabric modified with 3-aminopropyl trimethoxysilane (APTMS) self-assembled monolayers (SAMs) could attain shielding values as high as 43.5 dB whereas linen/PPY had a value of only 15 dB and linen/Ni showed about 20 dB at a frequency of 1 GHz.[11] In most of these methods polymerization step is done prior to electroless coating process.

Motivated by these earlier attempts, we designed a procedure to metallize breathable woven fabrics using nickel electroplating where the fabric templates were priorly sputtered by

Pt. Here we used nylon-a synthetic fabric and linen-a natural fabric as textile materials for developing breathable, lightweight EMI shields which are portable and shows good adhesion properties.

5.1.2. Materials and Methods

In the current investigation, we have used both a natural and an artificial fiber based fabrics. Our starting materials are; linen, which is basically a cellulosic fiber obtained from flax plant, and nylon; an artificial fiber. They are in woven form. Electrodeposition requires a conducting surface to be connected with the cathode so that metal cations can get reduced at the active surface. So, in order to convert the surface of the fabric conducting, it was sputtered with Pt using JOEL Auto coater 1600 for about 60 s in 30 mA current, and later connected to the cathode of the electroplating setup. The thickness of sputtered layer ranges 4 nm. The steps involved in the electroplating technique are shown in the Fig. 5.1. The typical electrodeposition set up consists of an electrolyte, cathode/anode and a source of electricity. Chemicals used for electrolyte preparation are hydrated salts of respective metals (Sigma-Aldrich, USA)) and boric acid (Merck). Here boric acid was used as a buffering agent. The composition of the electrolyte was 180 g/L of nickel sulphate hexahydrate ($NiSO_4.6H_2O$), 50 g/L nickel chloride hexahydrate ($NiCl_2.6H_2O$) and 30g/L boric acid (H_3BO_3) in deionized water with pH maintained at 4. The solution was prepared in deionized water to avoid the presence of unwanted ions. The electrodeposition set up (Plastomek, Kerala) consists of teflon connectors, platinum strips and borosilicate jar. The platinum sputtered fabrics were connected to the cathode with the help of a platinum strip. Another platinum strip was immersed in the electrolyte which acts as the anode. Voltage was applied between anode and cathode using a voltage source apparatus Keithley 2410 1100V Source Meter. Here, electrodeposition was

done at 4 V, for different time intervals. The microwave dielectric properties were measured in a Split Post Dielectric Resonator (SPDR) operating at 5, 10 and 15 GHz with the aid of a vector network analyzer. Conventional characterization tools described in previous chapters, were employed here to study their structural, microstructural, electric, magnetic and electromagnetic properties.

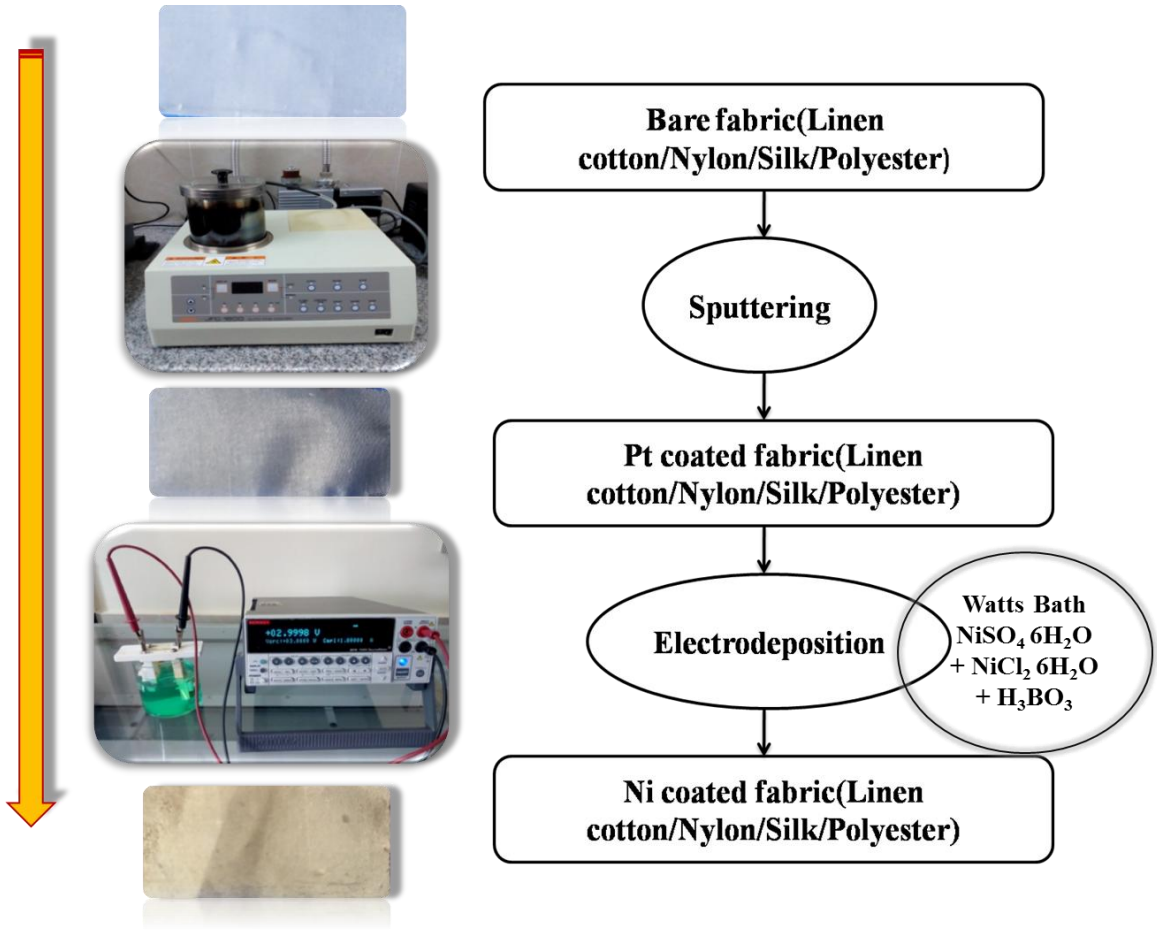

Fig 5.1: Flow chart with photograph indicates the steps involved in the electrodeposition of Ni on fabric substrates.

5.1.3. Results and Discussion

5.1.3.1 WAXS and XRD Analysis

Polymer fibers contains lamellae or small crystallites along with amorphous regions. Wide angle X-ray scattering (WAXS) is a useful tool to study these structural orientation of the crystals, and the packing of the chains within these crystals. The WAXS analysis, as shown in Fig. 5.2, displays corresponding characteristic α peaks of nylon at 20.5 ^{o} and 23.6 ^{o} and cellulosic linen fabrics have main intensity peak at 22.7 ^{o} corresponds to (002) peak. At 14.8 and 16.7 ^{o} the peaks (101) and ($10^{-}1$) are observed.

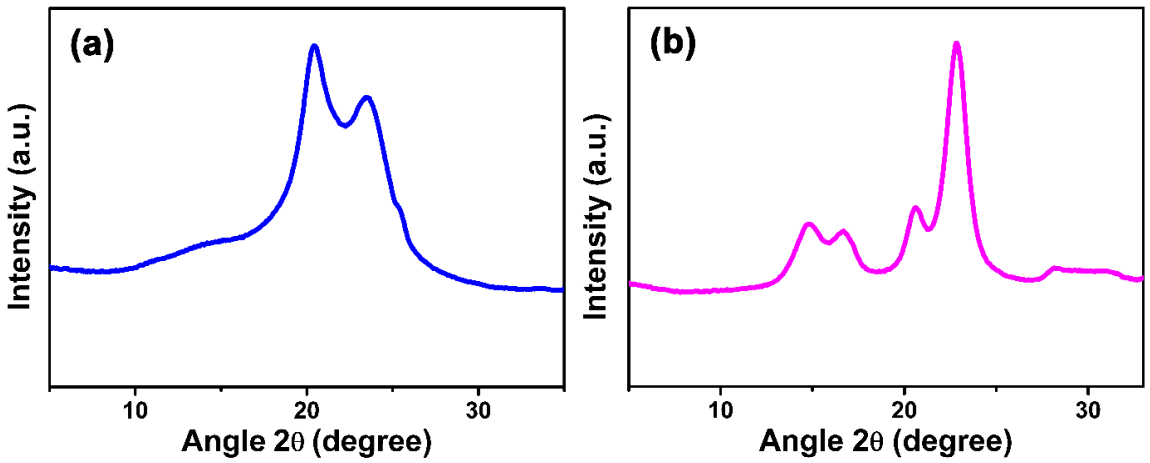

Fig. 5.2: WAXS of nylon and linen fabrics.

The X-ray diffraction patterns of bare linen (LN) and nickel electroplated linen (NEL) fabrics are shown in Fig. 5.3(a) and 5.3(b) respectively. The (002) peak at 2θ ~ 22.8° for the linen fabric could be indexed in Fig. 5.3(a). The most intense (002) peak seems like the reflection from the crystallographic planes of the glycosidic moieties.[12] All the peaks in the NEL could be indexed based on the standard JCPDS file: 00-004-0850. The XRD shows a high intensity peak at 2θ value of 44.51° which corresponds to (111) plane of fcc structured Ni. Other peaks correspond to (200) plane at 51.85° and (220) plane at 76.37°. This analysis confirmed the assumption that deposited Ni were crystalline and phase pure. On comparing the highest intensity diffraction peaks in Fig 3(b), obviously, linen exhibits low intensity peak

(002) compared to nickel (111). The metals always exhibit high intensity diffraction peaks than polymers due to their higher structure factor and the preferred orientation of their crystal planes.

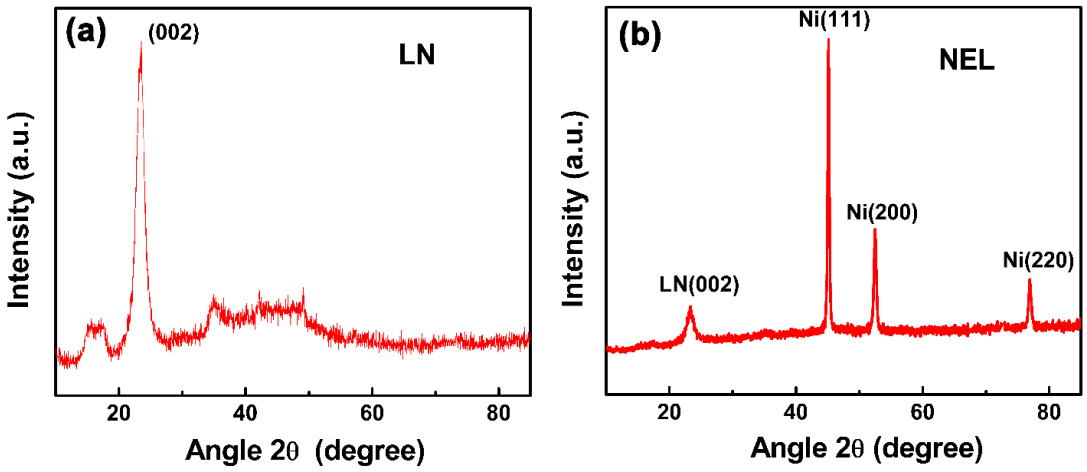

Fig. 5.3: XRD analysis of (a) bare linen and (b) Ni electrodeposited linen.

5.1.3.2 Morphological Characterizations

5.1.3.2.1 Photographic Images

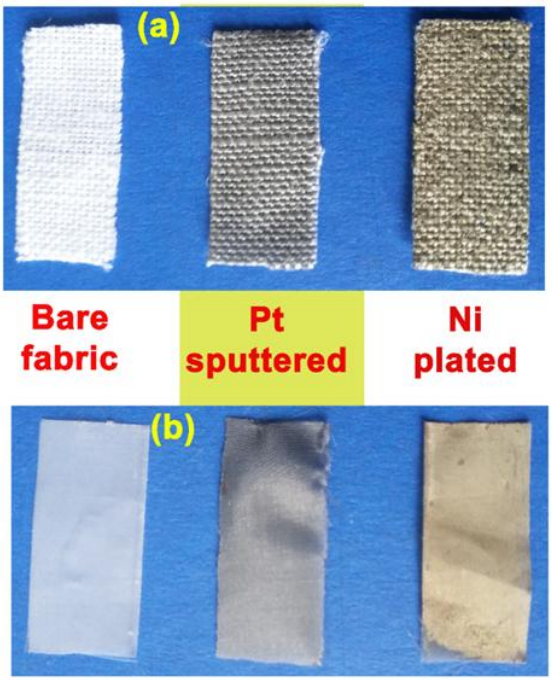

Fig. 5.4: Photographic image of (a) bare, Pt coated and Ni plated linen (b) bare, Pt coated and Ni plated nylon.

Fig. 5.4(a) shows the photographic images of bare, Pt coated and Ni plated linen (NEL) fabrics while Fig. 5.4(b) shows the photographic images of bare, Pt coated and Ni electroplated nylon (NEN) fabrics. In Fig. 5.4(a), the pure white one is representing the bare linen fabric. After coating with Pt, the fabric appears greyish in colour and the NEL fabric can be seen in metallic silvery white colour, which is characteristic of the deposited Ni metal.

5.1.3.2.2 Optical Microscopy

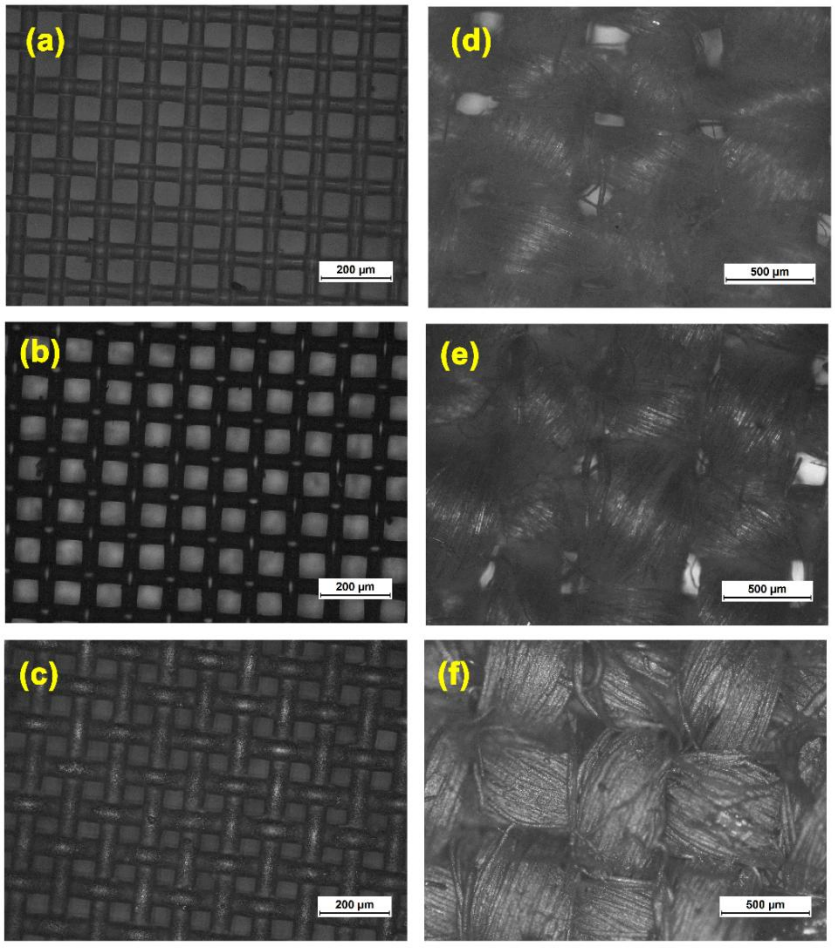

Fig. 5.5: Optical microscopic images (a) bare (b) Pt sputtered and (c) Ni plated nylon fabrics. Fig 5.5(d), (e) and (f) are bare, Pt sputtered and Ni plated linen.

Optical microscopic images of bare, Pt sputtered and Ni plated fabrics are analyzed. Fig. 5.5(a) and 5(b) shows the surface of the bare and Pt sputtered Nylon fabrics. In Fig. 5.5(c) NEN fabrics are shown after 30 min of electrodeposition. Similarly, Fig.5.5(d) and (e) shows the surface of the bare and Pt sputtered linen fabrics. In Fig. 5.5(f), NEL fabrics are shown after 30 min of electrodeposition. The peculiarity of the nylon fabric, as observed from the above optical microscopic image is that, each warp and weft consist of single strands only, while in the case of linen fabrics each warp and weft consist of several micron sized fibers assembled together. Thus the bare linen fabrics seems to be rough due to the lints, which are fibers detached or protruded outwards from the weave. Here for the electroplated structures, a uniform deposition of nickel throughout the fabric surface is clearly visible in the optical micrographs.

5.1.3.2.3 Scanning Electron Microscopic Analysis

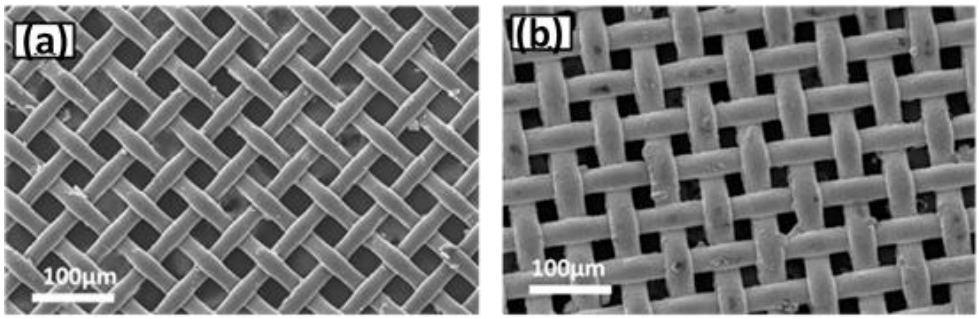

Fig. 5.6: SEM images of (a) bare and (b) Ni electroplated nylon fabric.

Fig. 5.6 shows the SEM images of bare and NEN fabrics after 30 min of electrodeposition. Each warp and weft consists of 25-30 μm sized nylon fibers, which get deposited uniformly with the nickel metal in both directions.

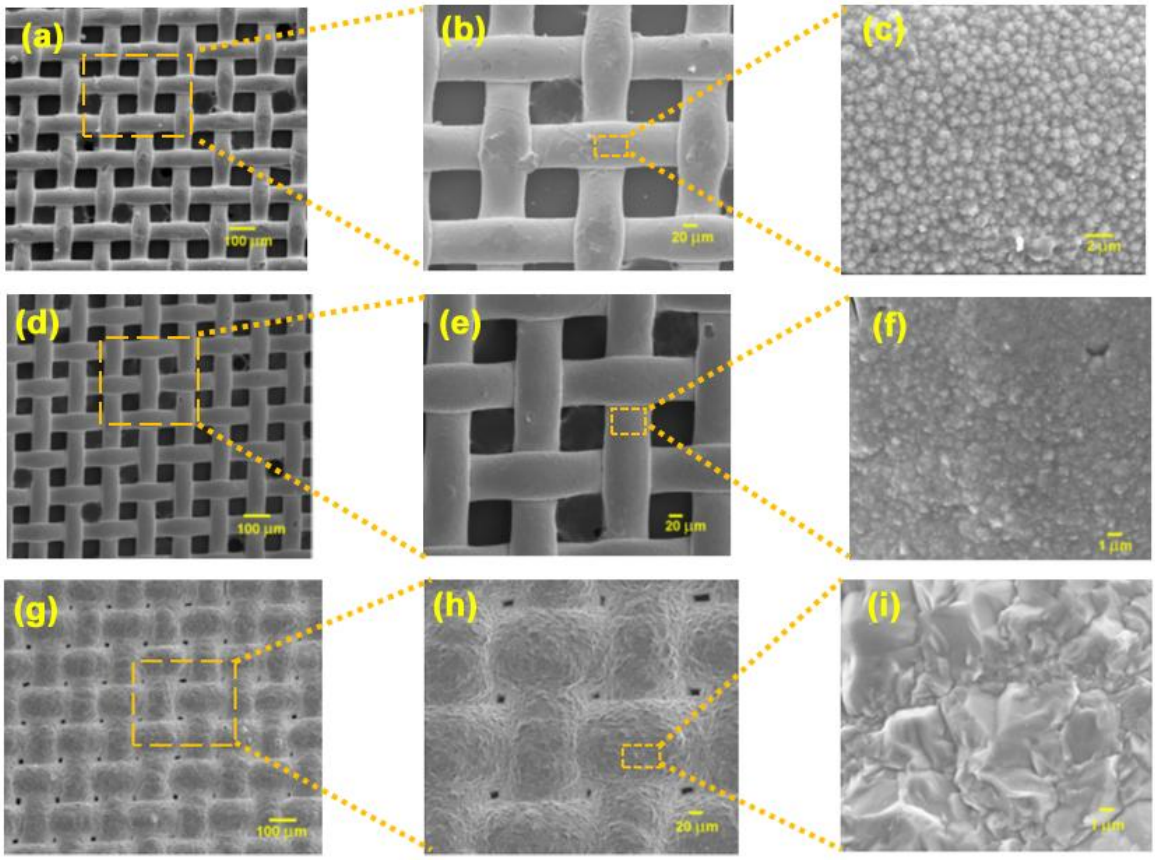

Fig. 5.7: (a) (b) and (c) are different magnification of NEN fabric for 15 min deposition. Fig. 5.7(d), (e) and (f) are NEN fabric after 30 min of deposition while Fig. 5.7(g), (h) and (i) are different magnification of NEN fabric after 60 min of deposition.

As the time interval increases, the gap between the warp and weft was periodically decreases, as seen in Fig. 5.7(b) and (h). This is due to the increase in the quantum of Ni being deposited at the cathode side. In the magnified image of Fig. 5.7(c), it is clear that the small heaps of Ni deposits initially formed got broadened (Fig. 5.7(i)), with the increase in time duration for deposition. After 60 min of Ni deposition the gap between the warp and weft approaches less than 10 μm. Fig 5.8 shows the SEM images of bare and nickel plated linen fabrics. Initially, nickel is getting deposited atom-by-atom on the surface of the fabrics, owing to the latter's large surface area which is favorable site for electro deposition.[13]

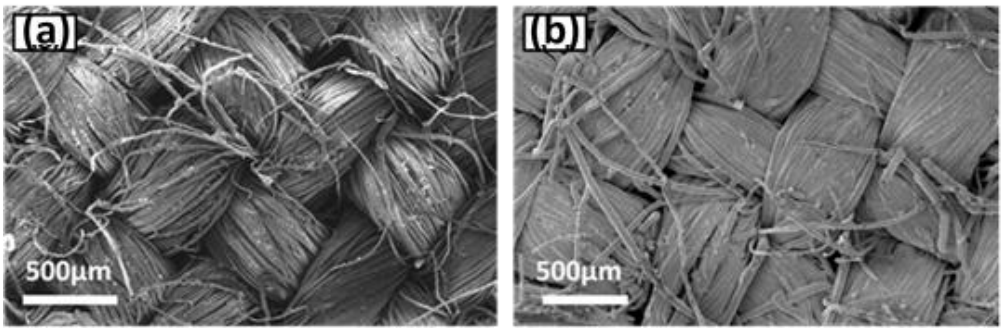

Fig. 5.8: SEM images of (a) bare and (b) NEL fabric.

The thickness of nickel coating depends on factors like the voltage, current and the time taken for the deposition. Fig. 5.9 details the morphological changes happened in the linen fabric from its bare form to various time duration of Ni deposition i.e., from 15 to 60 min. Here, unlike the case of nylon fabric, the warp and weft consists of several microfibers and the higher magnification images (see Figs 5.9(b) to 5.9(h)) clearly explains the transformation happened to each fiber. As the deposition duration increases, the thickness of the fibers are increasing and even tiny 'stick out' lints are being fully deposited with the Ni. Here, the surface seems to be rough and uneven while comparing to the nylon counterparts where it appears smooth and lint free in their bare form also. In the case of NEL, less number of voids are visible after electrodeposition, because Ni deposition seems like a cement reinforcing procedure to cover every bundle of fibers. NEL and bare linen are shown in the Fig. 5.10(c). The linen fabric exhibited dense nickel coating, thanks to the abundance of lints and high packing density of fibers. This eventually makes more surface for Ni deposition, which helps in creating a comparatively broader coating, without leaving any voids in the structure. In the case of nylon, from the cross section image Fig. 5.10(b), it is clear that a thick shell of Ni layer is wrapping each fiber individually. However, the pores are vaguely visible even after deposition, since the fiber density is low which is not having irregular lints on that surface. Also, the deposition

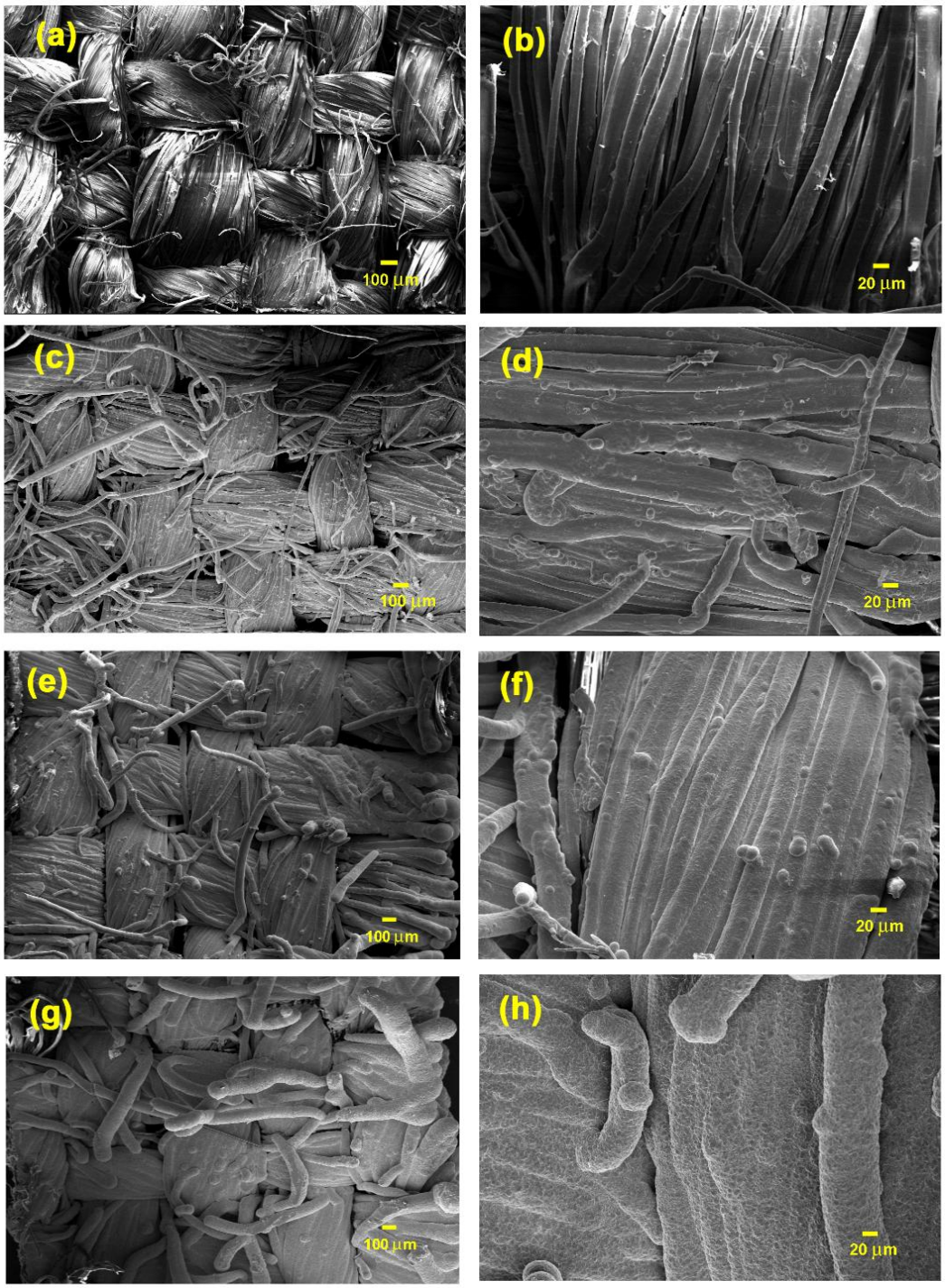

Fig. 5.9: (a) and (b) are low and high magnification of bare linen fabric, while (c) and (d) are low and high magnification of NEL fabric after 15 min. deposition. (e) and (f) are low and high magnification of NEL fabric for 30 min electrodeposition while and Figs (g) and (h) are that of NEL fabric for 60 min.

seems to be equally covering warp and weft of the fabric and extents to the entire surface which is clear from the image Fig. 5.10(a). The cross section of the nylon fabrics having Ni deposition at different time interval can be seen in Fig. 5.11. As the deposition time increases, the thickness of the coating increases from 25-35 μm at 15 min to 95-105 μm at 60 min.

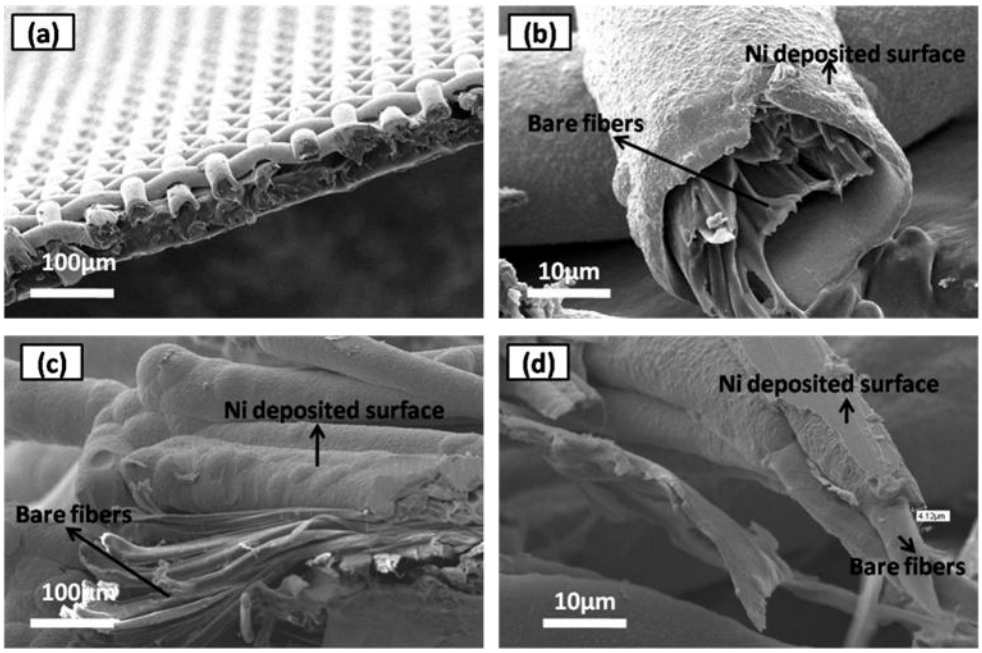

Fig. 5.10: SEM images: (a) and (b) showing cross sectional images of nylon, while (c) and (d) showing cross sectional images of linen.

The bare and Ni deposited linen fibers are clearly visible in Figs 5.10(c) and (d). The bare linen fibers are thicker after deposition of Ni. The cross sectional micrograms of the linen fabrics can be seen in Fig. 5.12. Here, instead of a smooth looking clean deposited fibers as observed in the case of nylon, a clumsy array of fibers with more protruding microfibers in bundles. These result prompt us to assume that the Ni deposited surface wavier in the initial period (Fig. 5.12(a)), which gets progressively smoothened after being deposited for 60 min, as seen in Fig. 5.12(c).

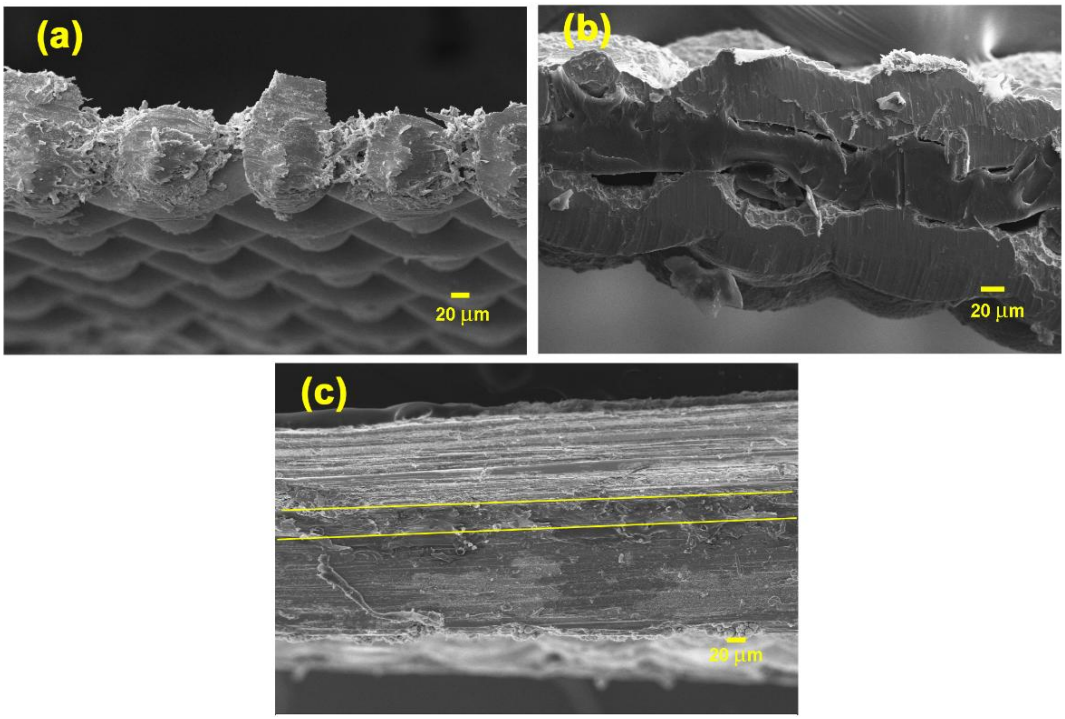

Fig. 5.11: (a), (b) and (c) are cross sectional SEM of NEN after 15, 30 and 60 min of deposition.

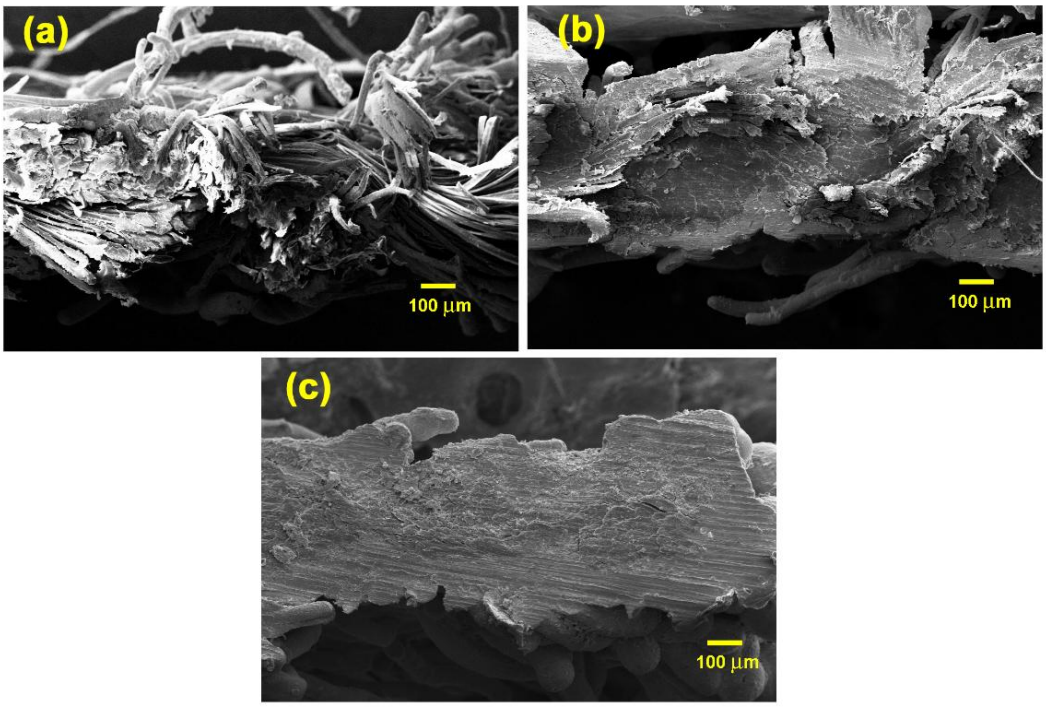

Fig. 5.12: (a), (b) and (c) are cross sectional SEM of NEL after 15, 30 and 60 min of deposition

5.1.3.2.4 Elemental mapping and EDAX

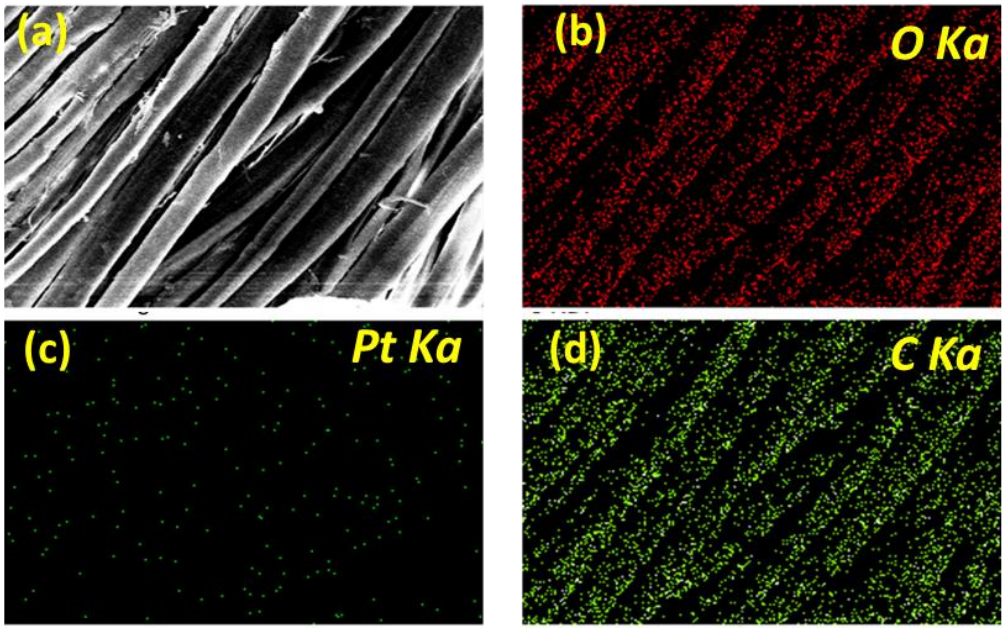

Fig. 5.13: (a), (b), (c) and (d) are elemental maps of bare linen fabric surface.

In order to illustrate the elemental distribution before and after Ni deposition on linen and nylon fabric, the elemental mapping analysis was done on a selected rectangular fiber region, as represented in Fig. 5.13. Since the linen is mainly cellulose derived composed of carbon and oxygen, the mapping clearly attests their presence in the microstructure. Here, presence of Pt comes from the sputtering. From the Pt mapping distribution it is evident that sputtering yielded a feeble but uniform distribution throughout the fabric surface. This step is essential to transform the fabric to a conductive electrode during electrodeposition, which is insulating otherwise. The elemental microstructure of post Ni deposited fabric is depicted in Fig. 5.14. Here, seemingly homogeneous Ni element distribution in the fabric substrate is seen, along with slight oxygen presence which might have come from the possible oxidation of Ni metal. The EDAX spectrum in Fig. 5.15(a) denotes characteristic energy lines of Pt which is

sputtered on the bare fabric where the carbon and oxygen energy lines take their origins from the cellulose rich nature of the fiber. After electrodeposition, the characteristic energy lines of Ni are visible in the EDAX spectrum, as shown in Fig. 5.15(b).

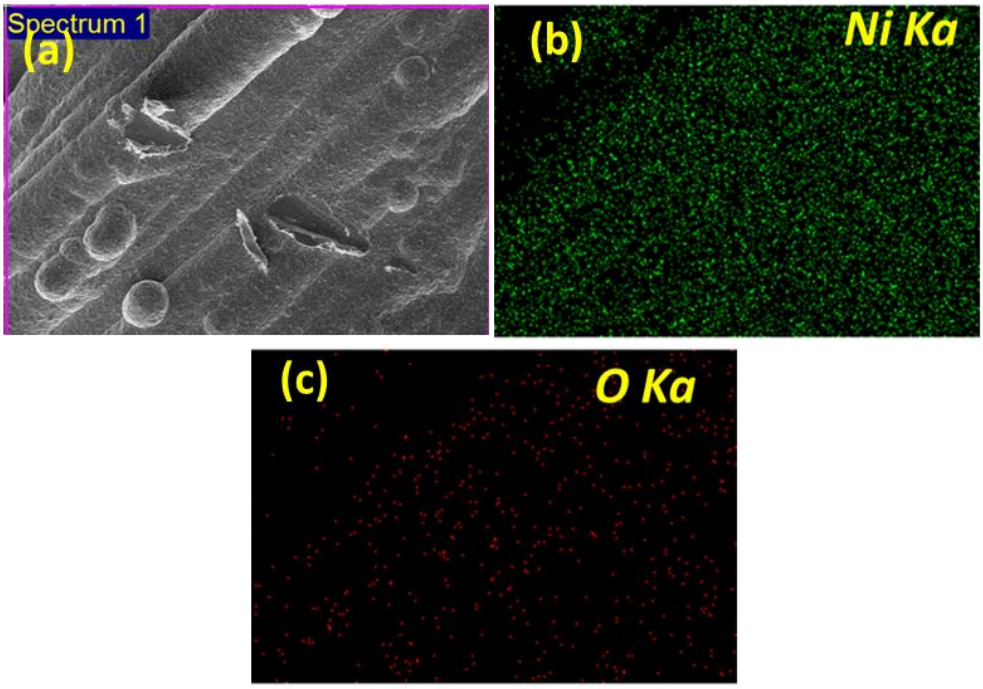

Fig. 5.14: (a), (b) and (c) are elemental maps of NEL fabric surface.

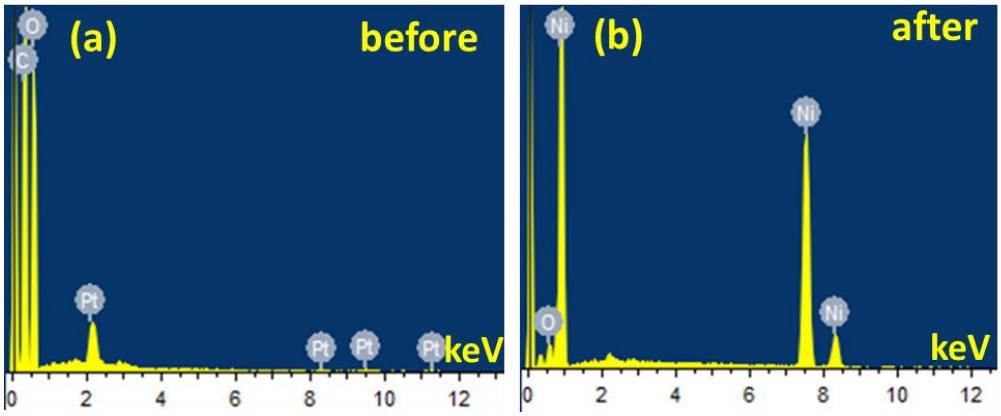

Fig. 5.15: EDAX scanning spectrum of (a) bare and (b) Ni deposited linen fabric.

Elemental distribution in NEN fabric clearly implied that Ni is uniformly deposited throughout the fabric surfaces. In order to further confirm the homogeneity of Ni distribution, linear

EDAX analysis was conducted as well. Intense and Continuous Ni signals are detected by line scanning, see Fig. 5.16(d). Even though nickel possess high corrosion resistance among soft

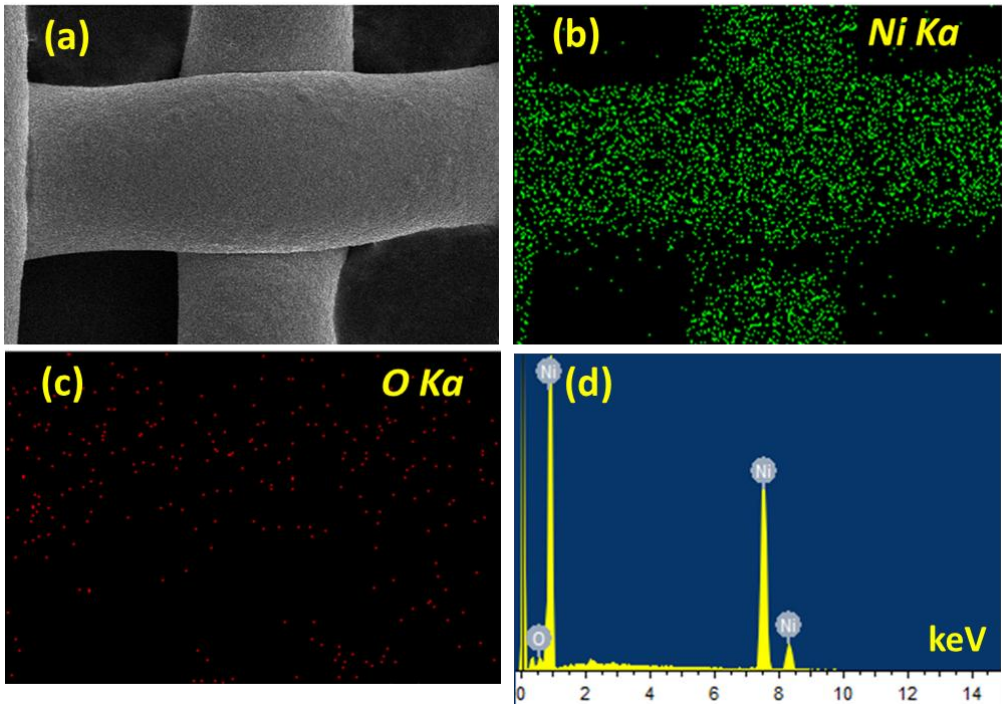

Fig. 5.16: (a), (b), (c) are elemental maps (d) EDAX scanning spectrum of NEN fabric surface.

ferromagnetic metals, they are likely to undergo marginal oxidation on ageing, which is visible in both elemental mapping and EDAX analysis.

5.1.3.2.5 Dielectric Characterization of Fabrics

The microwave dielectric properties of the bare fabrics are given in Table 5.1. Here, the permittivity and loss tangent for different fabrics varies with respect to measured frequency range. Linen cotton shows high relative permittivity (ε_r) and dielectric loss ($\tan\delta$) over different frequencies (at 5 GHz, 10 GHz and 15 GHz). The fabrics are made of fibres which are linear long chain polymers exhibiting high aspect ratios. The dielectric relaxation in polymers are associated with (a) primary chain motion of crystalline and amorphous regions (b) secondary

main chain motion in both crystalline and amorphous regions (c) side chain motions and (d) impurity motions.[14,15] On the application of an external electric field, the polymer chain causes the orientation of dipoles or strongly polarizable bonds in the direction of the applied electric field and thus polarization occurs. In polymers, the orientation of polar groups is rather a slow process. So at lower frequencies, the chains exhibit complete polarization. There are reports on the trend of decrease in permittivity with increase in frequency in the case of fabrics.[16]At higher frequencies, the contribution is from atomic as well as electronic polarization. Thus the permittivity decreases with the increase in frequency. On the other hand, the permittivity decreases as a function of frequency, which is in agreement with the theory. This is because in microwave domain, ionic and electronic polarization takes over other interfacial and orientational polarizations and hence permittivity assumes still smaller values.

Table 5.1 Microwave dielectric properties of fabrics at microwave frequency range.

Material	Thickness (mm)	5 GHz		10 GHz		15 GHz	
		ε_r	tanδ	ε_r	tanδ	ε_r	tanδ
Linen	0.3532	2.32	0.133	2.20	0.116	2.06	0.134
Nylon	0.0848	1.55	0.005	1.54	0.022	1.34	0.044

5.1.3.2.6 Electrical Conductivity

The I-V characteristics of electroplated Ni sheets were analyzed using four probe method. Current from a known source (Aplab 9710p) was passed through the fabrics and voltage across the sheet was measured using a voltmeter (Keithley 2182A nanovoltmeter). A typical I-V plot of a deposited Ni sheet is graphically represented in Fig. 5.17. The graph shows archetypal linear ohmic nature which is a typical characteristic of conductive metals. Here, the

resistivity can be obtained by the equation, $\rho = \frac{RA}{l}$ and conductivity, $\sigma = \frac{1}{\rho}$, where A is the area of cross section, l is the gap across which voltage is measured, R is the resistance measured. A Ni sheet has been strip off from the platinum plate after 60 min of deposition and is taken as the sample for four probe measurement setup.

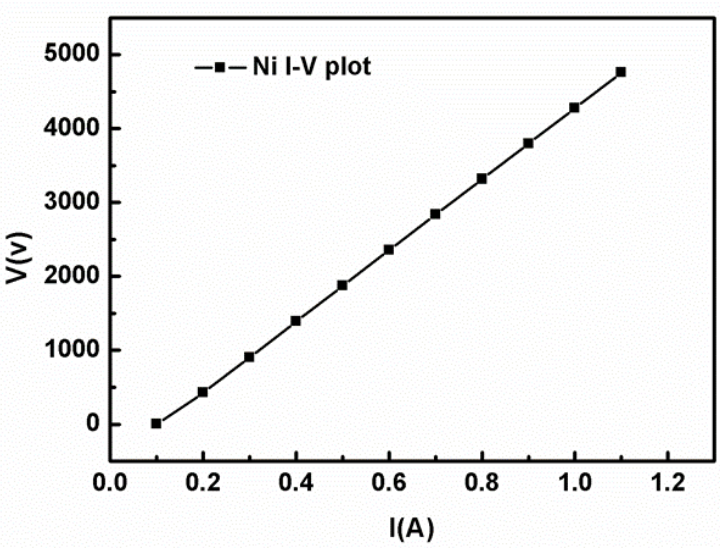

Fig. 5.17: I-V plot of electrodeposited nickel plate on platinum plate.

For electrodeposited Ni sheet sample with dimensions, l = 6 mm, A = 7.5 μm^2, the apparent resistance R is 2198.62 $\mu\Omega$, from which the conductivity is estimated as 3.5926×10^5 S/m. It should be noted that the observed conductivities are two orders less than bulk counterparts.[17] The lowering conductivity may be attributed to two possible reasons: (i) the finite porosity and surface roughness of the electroplated Ni surface and (ii) possible oxidation of Ni deposits, where feebly thin NiO can form a core-shell assembly and NiO is mostly semiconducting.

5.1.3.2.7 Magnetic Characterization

Fig. 5.18 explains the dependence of magnetization of electroplated Ni, on the applied magnetic field at 300 K. Here the studied metallic Ni was taken from the Pt strip. Magnetic

measurements were executed for magnetic field sweep between -50 kOe to 50 kOe. Usually application of a magnetic field causes spins to align parallel to the field. When the field is reduced, remnant magnetization occurs even when the applied magnetic field reaches zero. The field required to bring the magnetization to zero is called the coercive field (H_c). The analysis of magnetization versus applied field (M-H curve) clearly shows the ferromagnetic nature of nickel, with saturation magnetization (M_s) of 60 emu/g and coersivity 48 Oe. The shape of hysteresis loop certifies the typical ferromagnetic nature of a soft magnet.[18]

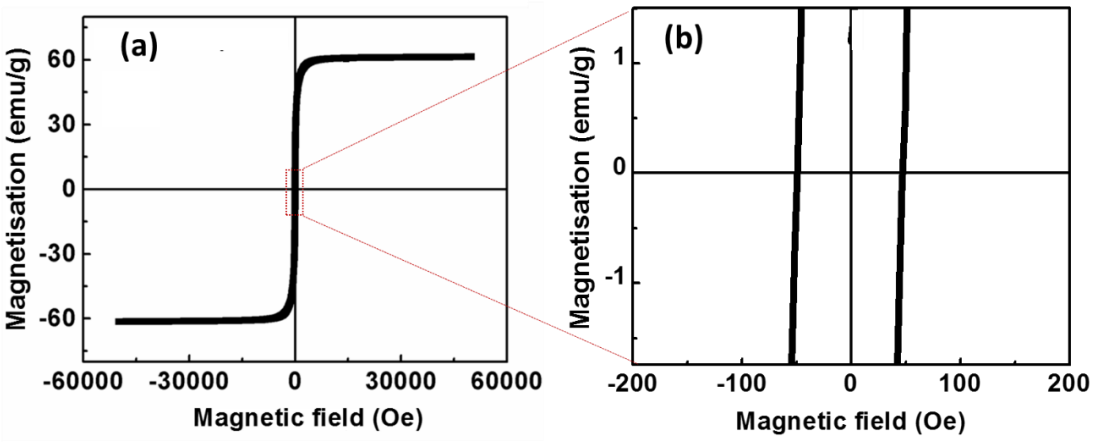

Fig. 5.18: (a) M-H curve of the electrodeposited nickel at 298 K. (b) The hysteresis loop of the electrodeposited nickel.

5.1.3.2.8 EMI Shielding Characterization

As seen in chapter 1, the reflection or absorption of the EM waves by a shield is decided by factors like the frequency of incident wave, conductivity and magnetic permeability of the material.[19] Metallic materials having good magnetic properties are great competitors for ideal magnetic shielding applications. Even though metals are widely used in shielding applications, they are usually heavy, rigid and easily prone to corrosion. A probable solution to this problem is making a thin layer of less oxidation prone material on a comparably less dense, continuous

and flexible substrate like a fabric or fiber mats. Coating with a metal is a widely applied strategy in fabrics. In that case, it is not necessary to compromise largely on properties such as flexibility, formability, mechanical properties and light weight of fabrics which are really advantageous for consumer electronics applications.[20–22] The advantage of metals like nickel is that it is electrically conducting as well as magnetic so that it can simultaneously interact with electric and magnetic components of EM wave. As stated before, naturally occurring cellulose based linen and synthetic nylon fabric are the selected substrates for electrodeposition.

Mechanism of shielding is very important as it determines the kind of applications the shield can fit in. The frequency dependence of shielding effectiveness of bare, platinum coated and nickel electrodeposited fabrics in the X-band frequency range are shown in Fig. 5.19. From the figure it is clear that the uncoated bare fabric and platinum sputtered fabrics are poor shielding materials having SE values less than 1 dB. In other words, these materials behave like EM transparent. But in the case of nickel electroplated one at various deposition durations, they showed excellent SE values. Here the $SE_{R,}$ SE_A and SE_T of the NEL in the X band frequency range are shown in Fig. 5.19 (c) to (e). An impressive total SE value of 45–52 dB was observed in the case of 60 min electrodeposited linen samples. Here, both absorption and reflection contributions come in the range of above 20 dB, with absorption slightly dominant.

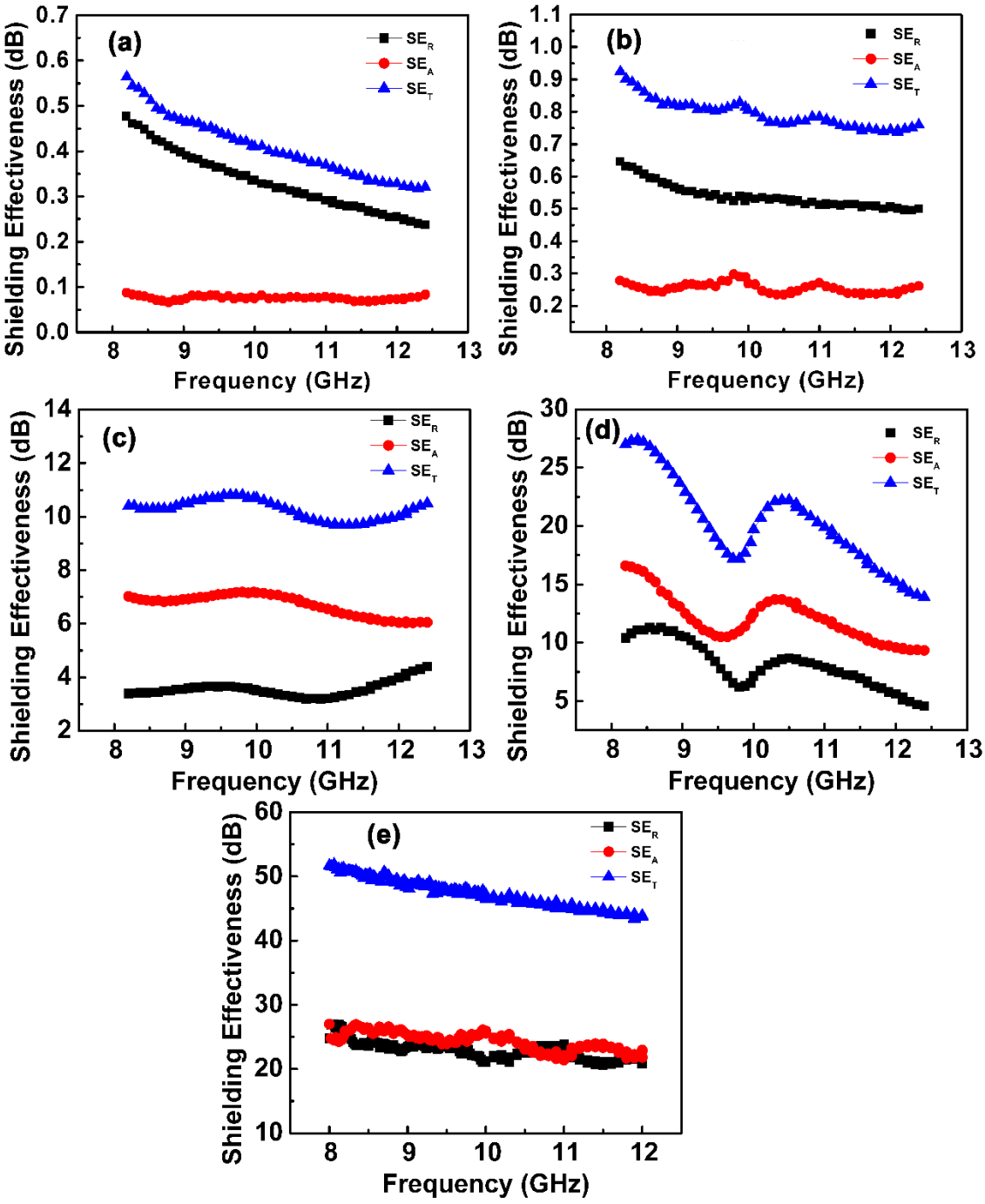

Fig. 5.19: (a) and (b) showing frequency dependent variation of total EMI shielding effectiveness (SE_T), reflection shielding effectiveness (SE_R) and absorption shielding effectiveness (SE_A) of bare and platinum sputtered fabric over X band frequency range (8.2–12.4 GHz). Fig. 5.19 (c), (d) and (e) are frequency dependent variation of SE_T, SE_R and SE_A of NEL fabric at various time intervals of 15, 30 and 60 min of deposition.

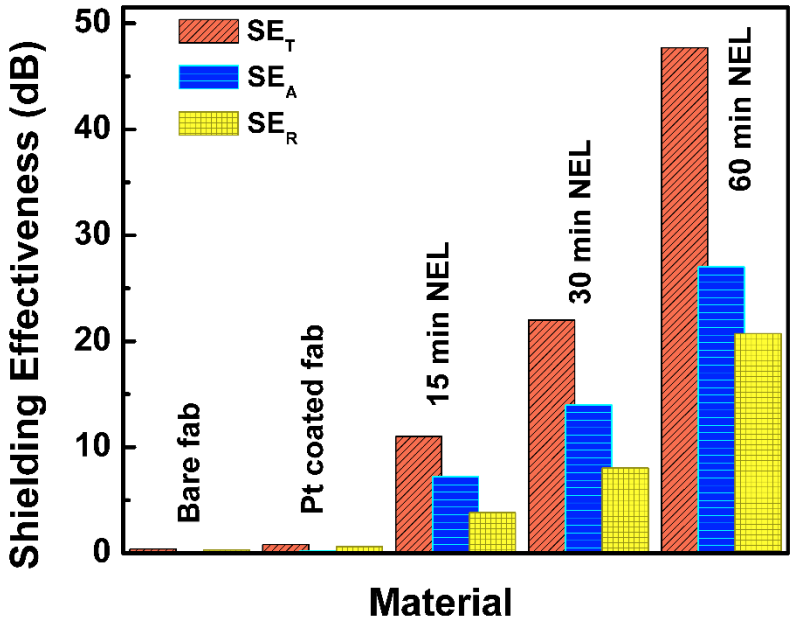

Fig. 5.20: Variation of SE_T, SE_R and SE_A of bare, platinum sputtered and Nickel electroplated Linen fabric at various time periods of 15, 30 and 60 min over mid - X band (10 GHz) range.

On the other hand, SE_T of 15 and 30 min electrodeposited samples are in the range of 10 dB and 15-25 dB respectively. In all the cases, the SE_T is majorly contributed by the absorption shielding which is around 6-7 and 10-15 dB, in the respective cases. An observation of the SE_R, SE_A and SE_T values over the mid X band (i.e., 10 GHz) is shown in Fig. 5.20, which is in agreement with the trends in SE values with increasing Ni deposits on the fabric surface. The results indicate that both SE_R and SE_A visibly enhanced with the deposition of nickel. The shielding effectiveness is intimately related to skin depth, which is the depth an electromagnetic wave takes to become 1/e th of the initial intensity. From bare fabric to nickel deposited one, the major variation is in skin depth value. The deposited nickel in the fabric is having better conductivity and permeability which can provide lower skin depth values and higher SE. Another morphological advantage of linen is that the higher lint content on its surface leads to higher areal density of spikes. Thus these spikes, in a way present an increased number of active sites for nickel to be deposited. These protuberances at the surface of linen

which is clearly seen in the SEM images (Fig. 5.9 and 5.12), are the main contributing factor for the enhanced absorption shielding in the case of linen, compared to relatively cleaved surface of NEN fabric. In other words, the effective area of coverage of deposited nickel is high in linen due to the enhanced surface area and the higher thickness. Some morphological advantages like fiber bundles in each tow are also contributing greatly to the multiple reflection possibilities and effective shielding of NEL fabric.[23]

The effect of nickel electrodeposition on the shielding effectiveness of Nylon fabric is shown in the Fig. 5.21 and Fig. 5.22. Similar to our earlier observation in the case of linen, bare and Pt sputtered nylon fabrics are also EM transparent, having less than 1 dB of SE value. It should be noted that the Pt sputtering should improve the EM wave attenuation, in principle. However, here the coating thickness is way too less and the fabric surface is highly porous which could not enable continuous electrically conducting channels on fabrics surface. After Ni deposition, here also there is a dramatic enhancement in the SE_R, SE_A and SE_T values, which increases with increasing time duration of deposition. However, NEN shielding values are lower while comparing to that of NEL fabric. An efficiency range of over 99 % is achieved in the case of 60 min NEN fabric. SE_T of 60 min NEN fabric lies in the range of 25-38 dB, with SE_R value in the range of 20-30 dB and SE_A value in the range of 8-18 dB. In contrast to the trends in the case of NEL fabric, the reflection shielding mechanism is dominating in NEN. The discrepancy can be attributed to the difference in microstructure of both the fabrics after electrodeposition for identical durations (see Figs 5.7 and 5.9). In the case of NEN, even after 60 min of electrodeposition, still there exists a lot of voids. So the EM wave can easily escape through this voids making absorption mechanism to weaken.

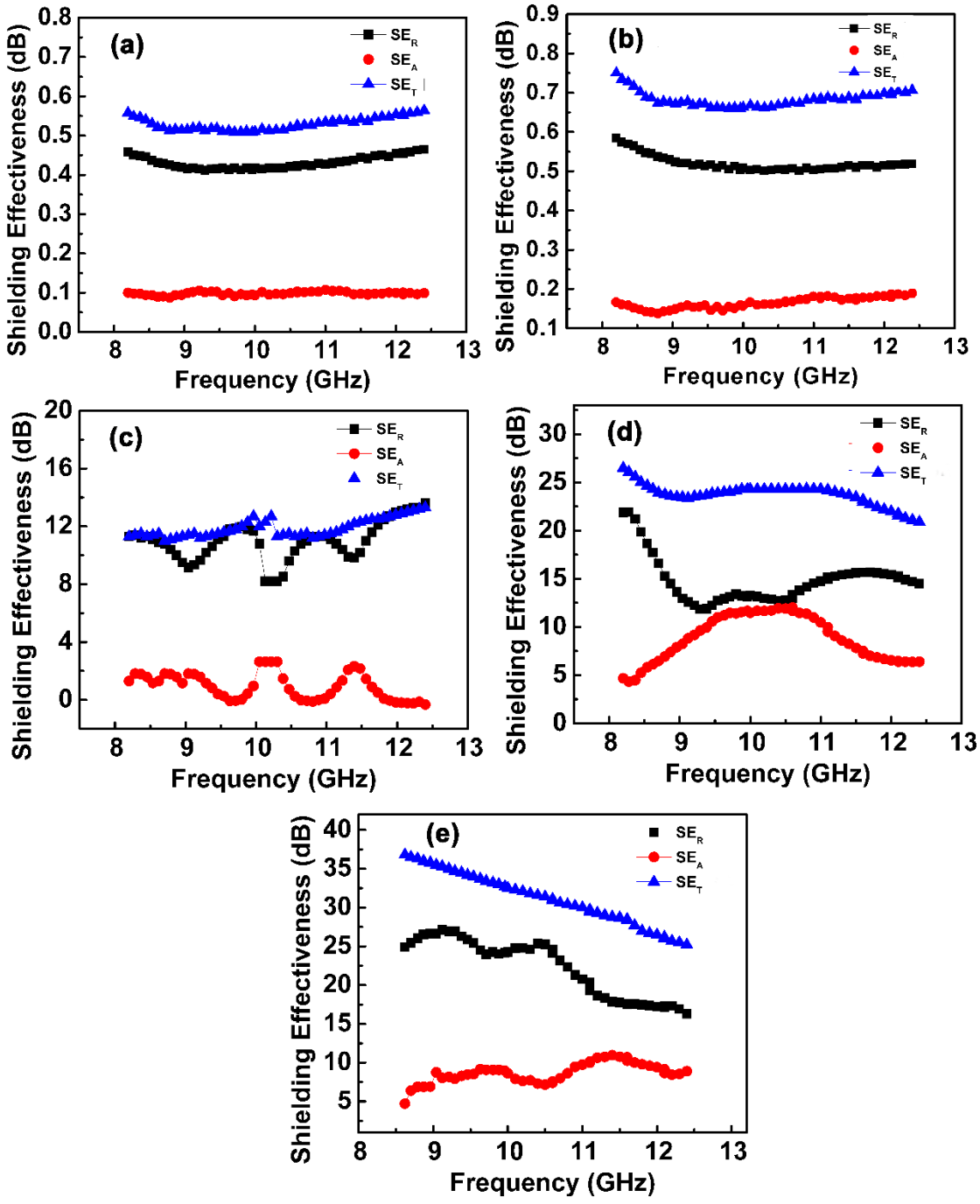

Fig. 5.21: (a) and (b) showing frequency dependent variation of total EMI shielding effectiveness (SE_T), reflection shielding effectiveness (SE_R) and absorption shielding effectiveness (SE_A) of bare and platinum sputtered Nylon fabric over X-band frequency range (8.2–12.4 GHz). Fig. 5.21 (c), (d) and (e) are frequency dependent variation of SE_T, SE_R and SE_A of NEN fabric at various time intervals of 15, 30 and 60 min of deposition.

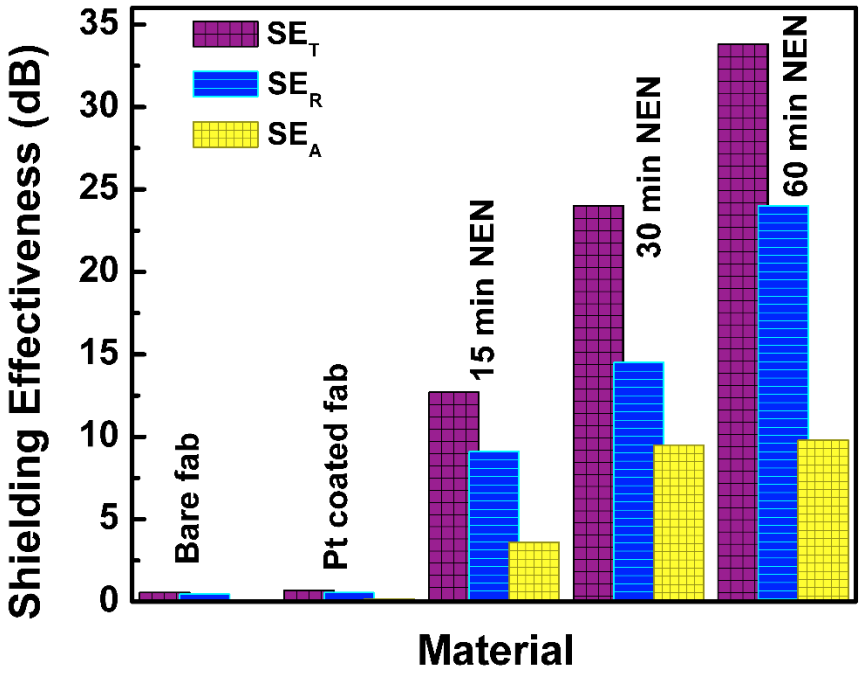

Fig. 5.22: Variation of SE_T, SE_R and SE_A of bare, platinum sputtered and nickel electroplated nylon fabric at various time periods of 15, 30 and 60 min over mid - X band (10 GHz) range.

Let us now comparatively discuss the shielding mechanisms of NEL and NEN in detail. As discussed earlier, warp and weft in linen are composed of a lot of protruding lints and bundles whose Ni coverage will be more. Such irregular but conducting surfaces will give more room for interaction with EM wave. Thus, there arise enormous possibility for multiple reflection between different interfaces in a bundle of fibers, than a single bundle in the case of NEN fabric. Also after electrodeposition, the modified fabric structure is like sandwiched between two electrodeposited Ni layers. Due to relatively thinner structure and possessing more voids between warp and weft, NEN behaves like a metallic sheet with insulating fabric mesh sandwiched in between. On the other hand, in the case of NEL, there exist two distinct layers of Ni being separated by a thick linen layer where the linen had a much higher surface area. In short, more multiple reflection possibilities and more surface coverage of Ni due to

the lints on linen fabric make it a better competitor for flexible EMI shielding applications. Such fabrics can be applied as flexible screens for absorbing electromagnetic radiation to produce cores in transformers, generators, etc., and also to produce selective filters to remove contaminants showing magnetic properties from water and air.

5.1.4. Conclusions

This subdivision of the chapter summarizes the efforts to transform conventional woven fabrics into useful EMI attenuating solutions. Linen and nylon fabrics were chosen as the substrate materials which were priorly activated by platinum sputtering. Nickel electroplating was executed on selected substrate fabrics at various time duration, keeping the concentration and voltage unchanged. Permittivity and loss factors were maximum for the linen fabric due to the higher packing density of fibers and higher thickness. The coercivity and saturation magnetization of the Ni deposits were about 48 Oe and 60 emu/g respectively, which is in agreement with literature values. The total shielding effectiveness of NEN fabric was in the range of 25-38 dB after 60 min of deposition, with an efficiency in the range of 99 %. On the other hand, excellent EMI shielding effectiveness of 45-52 dB was achieved for NEL fabric, that corresponds to 99.999 % efficiency. The contribution of absorption and reflection shielding part were above 20 dB, with the former dominating marginally. The absorption dominant shielding for linen was mainly due to its peculiar microstructure, whose higher surface area arising from large number of lints on the top of fabric which was well deposited with nickel and forms protuberances and irregularities on the Ni coated surface of fabric. Another contributing factor in NEL fabric's high attenuating properties is due to its availability of more dielectric-metal interfaces, which adds to its enhanced absorption. Since absorption is directly related to the shield's thickness, a material with greater thickness and

large interface area will enable more multiple internal reflections and eventually ended up as an excellent shield against EM wave. The high conductivity and high permeability of Ni also played a pivotal role in the current system to lower the skin depth of the shield, along with the more inter-connected coating structure, which are advantageous for better shielding. Out of the two fabrics analyzed, the highly efficient linen can be a suitable candidate for various practical applications in personal electronic, aeronautical and defense sectors, where light weight and flexibility are additional benefits.

5.2 Nickel Electrodeposited Carbon Fabrics for Microwave Shielding Applications

5.2.1. Introduction

Conventional shielding structures, as briefly seen in section 5.1, comprises of metal sheets such as stainless steel, aluminium, copper, silver and nickel. But high density and corrosive nature of metals hinder their applications in aviation sector where light weight and environmental stability are prerequisite for components. Passive intermodulation or rusty bolt effect is another drawback for metallic shields, where the shields themselves may act as sources of spurious radiation.[24,25] Similarly, multi-layered shields may suffer from galvanic corrosion when different metals are combined to form EMI shields.[26] Metal coated fabrics, as discussed in the preceding section can be a suitable platform for corrosion resistant wearable shields. Despite the suggested merits, metal-coated fabrics may sacrifice their flexibility when the coating thickness increases. Besides, metallized fabrics are subject to surface wear when worn, leading to a subsequent decrease in their electrical conductivity. This can be detrimental to their EMI shielding as well due to conduction channel breakage. Thus for outdoor protection applications, more durable platforms need to be chosen. Against this background, carbonaceous materials are recently explored, taking advantage of their durable and flexible EMI shielding capabilities. Most widely researched ones were carbon black, exfoliated graphite, carbon nanotubes (CNTs), carbon fiber, carbon nanofiber etc.[27] For customized practical applications, various polymer–carbon composites were reported with improved chemical resistance and mechanical properties.[28] Though CNTs have high aspect ratios and are useful in forming conductive pathways when loaded into a polymer matrix, they could not be efficient shields due to the contact resistance problem that decreases the effective conductivity

of the system.[29] Structural stability and processability are essential parameters for developing an ideal EMI shield. Thus the light weight carbon fabrics are emerged as excellent choice in the fabrication of shields that could be portable, bendable and could be applied on aircrafts, or space crafts as protective shields. Polypropylene/polyethylene (PP/PE) core/sheath bi-component fibers composited with nonwoven carbon fabrics achieved a maximum shielding effectiveness of 39.15 dB at a frequency range of 30~1500 MHz, for a loading of 90 wt. % carbon fabric.[30] Tang *et al*. reported a carbon fabric/polycarbonate sandwiched film fabricated by lamination method with optimum EMI shielding properties and excellent tensile properties.[31]

Carbon fabrics with highly conductive continuous fibres exhibits superior shielding properties compared to carbon mats with randomly oriented discontinuous short fibres.[32] A wearable and breathable fabric with excellent shielding efficiency is of huge interest in defence sector. Hence in the present work, carbon fabrics were chosen as the substrates for developing EMI shield due to their high tensile strength and microwave attenuation. For further enhancement of their shielding effectiveness, uniform nickel coating was applied by electrodeposition process and various properties including the effect of coating time on the thickness of the coating were studied.

5.2.2. Materials and Methods

Electrodeposition procedure is same as explained earlier in the case of Linen and Nylon fabrics in section 5.1.2. The only difference from the earlier procedure is that in the current case there was no need for any prior activation using Pt sputtering, because the carbon fabric is already electricaly conducting and can be directly connected to the cathode of the electrodeposition set up. In the present study, we have used two such kinds of carbon fabrics.

One was having warp and weft constituting 6000 microfibers of diameter in the range of 6-10 μm bundled together, termed hereafter as carbon fabric large (CFL), while the other one was having 3000 microfibers bundled in a warp or weft, termed as carbon fabric small (CFS).

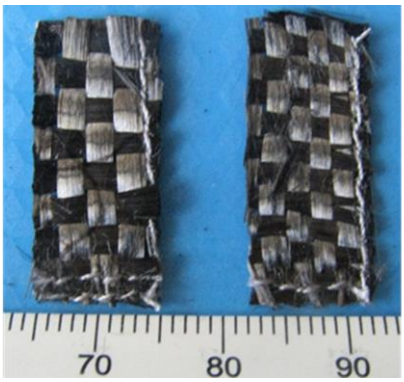

Fig. 5.23: Photographic image of CFL and CFS sheets.

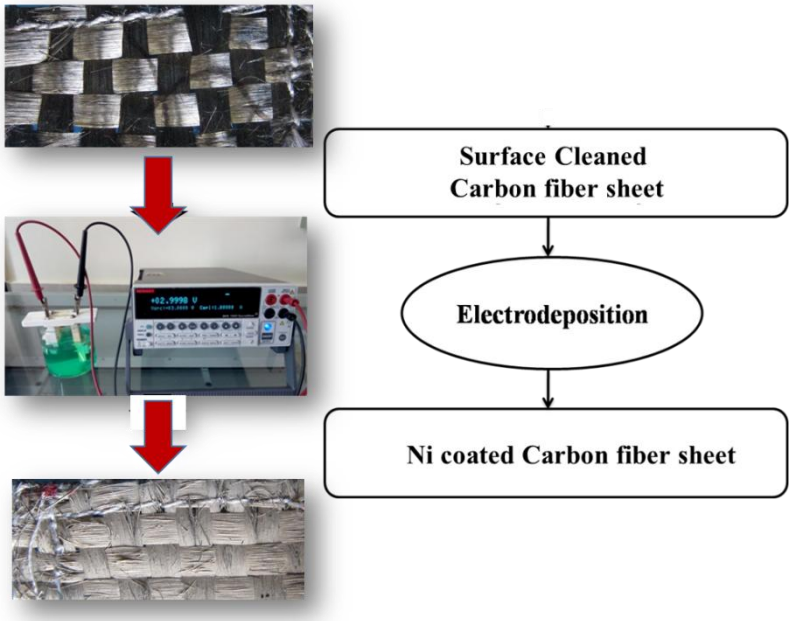

Fig. 5.24: The photographs with flow chart for each steps of the entire process involved in the electrodeposition of Ni on CF sheets.

CFL and CFS are shown in the Fig. 5.23. The steps involved in the electroplating technique are shown in the Fig. 5.24. Here as mentioned in the flow chart in Fig. 5.24, there is a desizing step done for the as purchased carbon fabrics. In order to do that the carbon fabrics

are cut in to required dimensions and put it in a soxhilation set up for 3 h, where it was washed with acetone for several times, so as to remove the polymer coating on each fiber. Conventional characterization tools described in previous chapters, were employed here too to elucidate their structure, microstructure, and electromagnetic properties.

5.2.3. Results and Discussion

5.2.3.1 Scanning Electron Microscopy

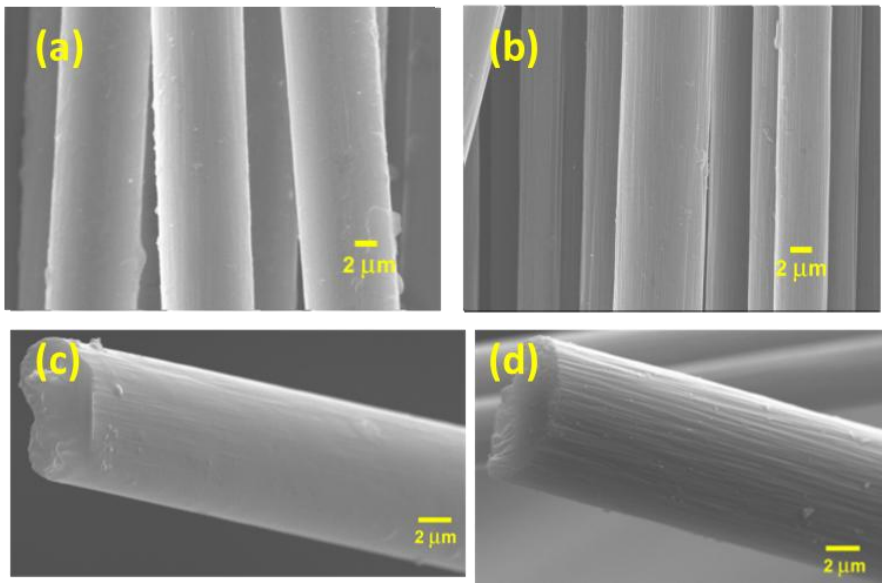

Fig. 5.25: (a) and (c) are SEM micrographs of as obtained CF, (b) and (d) are after acetone treatment.

For properly aligning and stacking of individual fibers in each bundle during factory manufacturing, they are coated with some polymers like polyethylene glycol. Those coatings, being insulating, should be avoided before undergoing the electrodeposition procedure. Herein, an acetone washing for 3 h was followed, before they were taken to the electrodeposition set up.

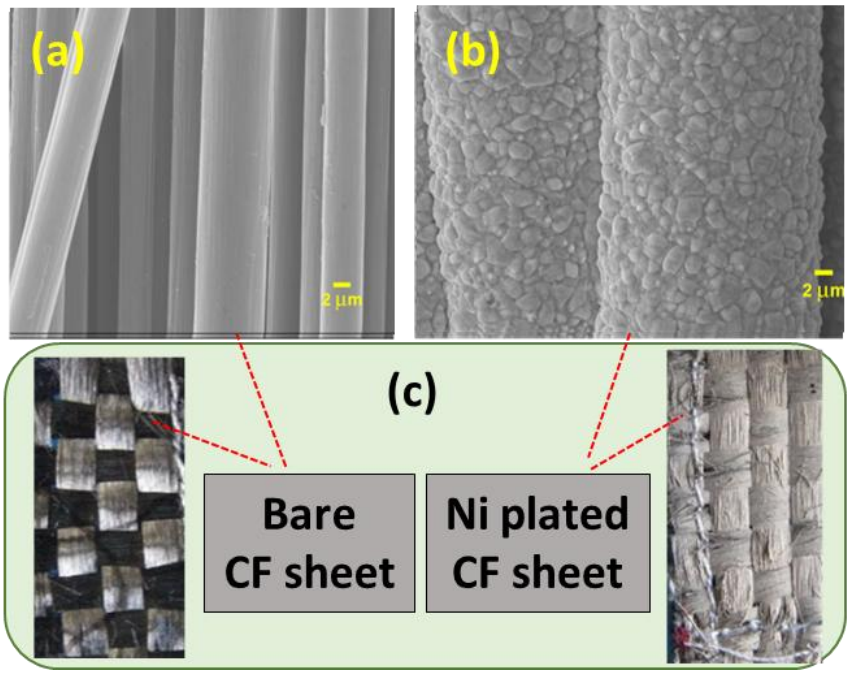

Fig. 5.26: (a) and (b) are bare and Ni deposited CF sheets (after 60 min of deposition). Fig 5.26(c) is the photographic image of the bare and Ni deposited CF.

As observed in the Fig. 5.25, there is a visible coating of sooth polymer layer on each carbon fiber (see Figs 5.25 (a) and (c)). However, after washing with acetone, it was fully removed and the surface became more rough as observed in Figs 5.25 (b) and (d).

5.2.3.2 Elemental Mapping

Elemental mapping analysis is intended to give a colour illuminated elemental distribution, before and after Ni deposition on carbon fabric. Fig. 5.27 shows the mapping of bare carbon fabric where a carbon rich illuminated area is well observed, with EDAX showing peaks corresponds to the carbon and oxygen. From Fig. 5.28 which was recorded from Ni electroplated carbon fabric surface, we see a homogeneous Ni element distribution in the carbon fabric surface, with a minor carbon and oxygen distribution. EDAX in Fig. 5.28(e) clearly indicates the energy peaks corresponding to the presence of Ni on carbon fabric surface.

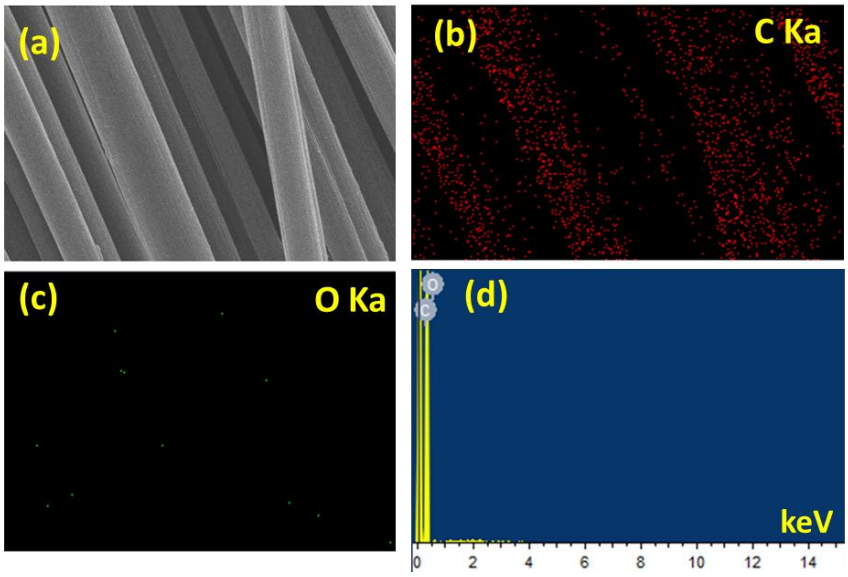

Fig. 5.27: (a), (b) and (c) are Elemental maps of bare Carbon fabric surface. (d) EDAX scanning spectrum of bare Carbon fabric.

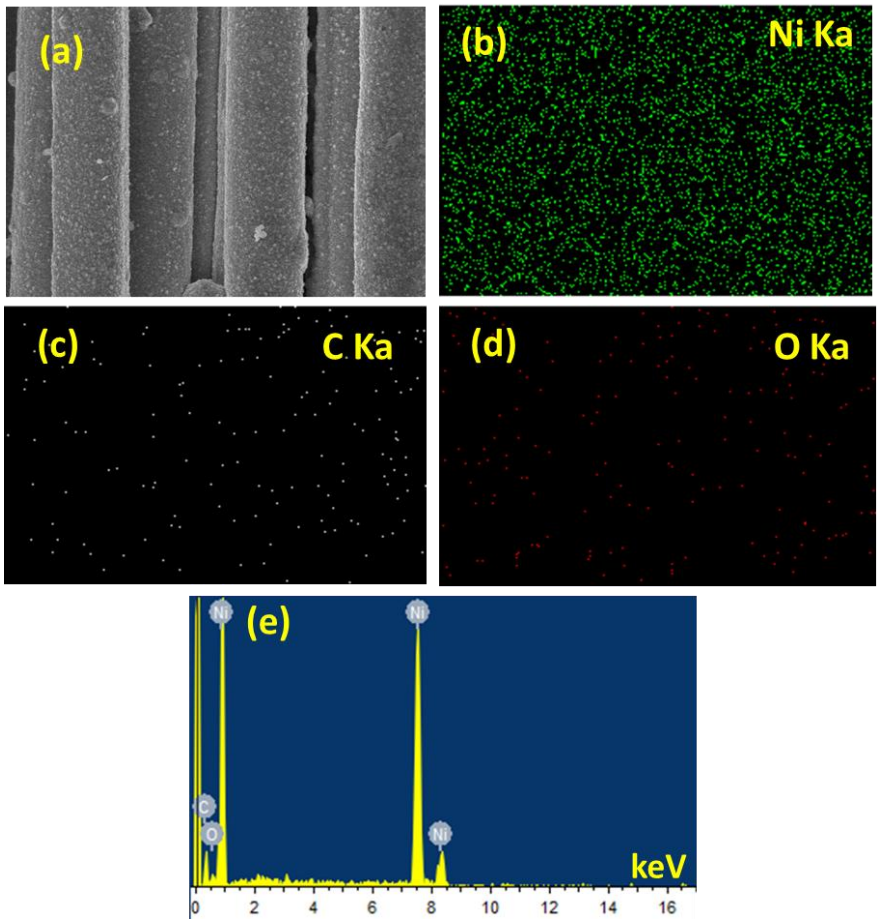

Fig. 5.28 (a)-(d) Elemental maps of Ni electroplated carbon fabric surface. (e) EDAX scanning spectrum of Ni deposited carbon fabric.

5.2.3.3 EMI Shielding Characterization

The frequency dependence of shielding effectiveness of bare and nickel electrodeposited carbon fabrics in the 8.2-12.4 GHz frequency range are shown in Fig. 5.29. Nickel electroplated carbon fabric is showing some excellent SE values, especially the CFL fabric. A promising total SE value of 22–32 dB was observed in the case of 60 min electrodeposited CFS samples, with absorption being the dominant shielding mechanism. Here, SE_A is in the range 15-18 dB, while the SE_R comes to around 7-14 dB. In fact, the bare carbon fabric samples were already known for their EMI shielding nature owing to carbon's high electrical conductivity.[22,33,34] Hence, after the surface coating using a ferromagnetic metal, an additional functionality is brought to the shielding solution since such high permeability coatings can create magnetic field attenuation by creating a low reluctance path which draws the material's magnetic field. The second system of carbon fabric we studied, CFL, i.e. the fabric with double the number of carbon fibers in every tow of warp or weft, was exhibiting excellent shielding effectiveness of 55-58 dB, after Ni deposition for 60 min. In the bare form also, CFL was showing a shielding of 34 dB, from which an enhancement of 60 % in the total shielding value was observed after Ni deposition. In the measured total SE value, the absorption shielding contributes around 35 dB while reflection part adds around 20-22 dB only. Here the enhanced SE value may be resulted from more interlayers, that act as platforms for multiple internal reflection possibilities. As the Ni comes into the picture, an obvious betterment of electrical conductivity and magnetic permeability happens to the system, which can provide lower skin depth values and higher shielding effectiveness.[35] Also, a part of the electromagnetic energy will be utilized for the magnetic dipole alignment in the Ni layer.

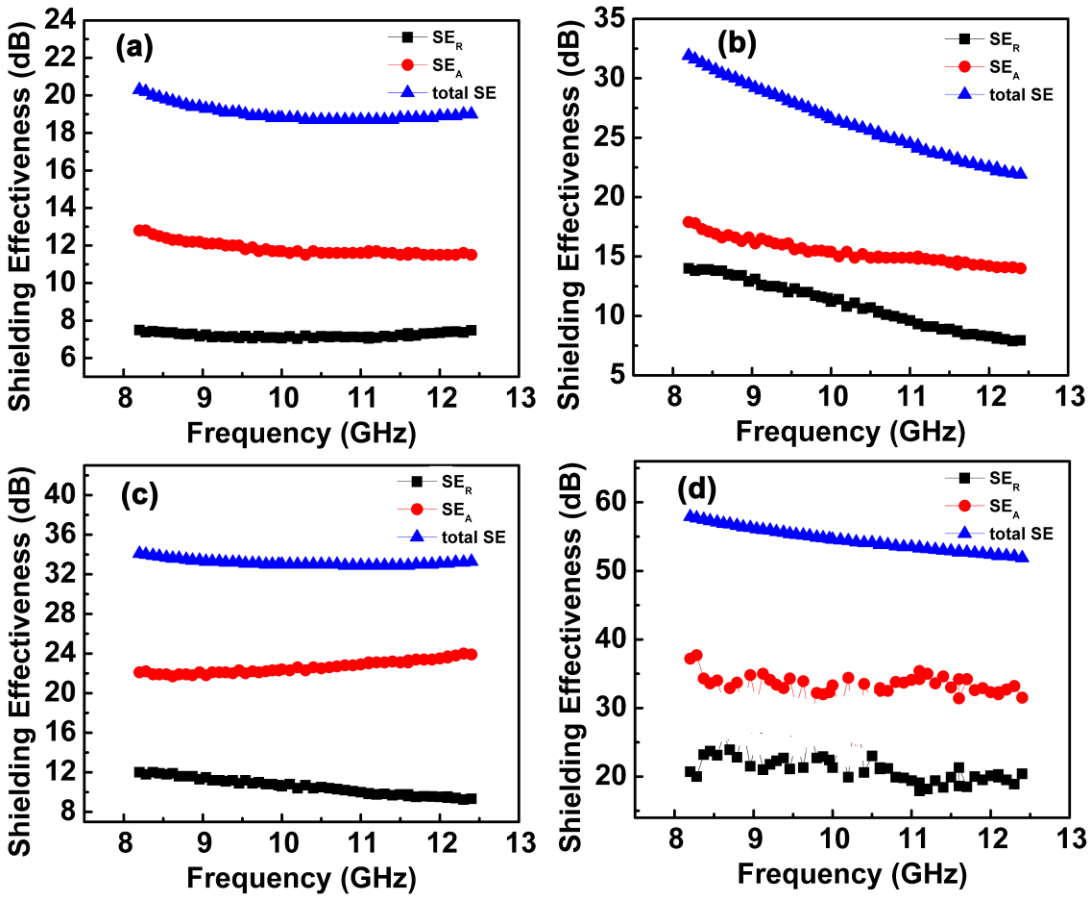

Fig. 5.29: (a) and (b) Frequency dependent variation of total EMI shielding effectiveness (SE_T), reflection shielding effectiveness (SE_R) and absorption shielding effectiveness (SE_A) of bare and Ni deposited CFS fabric @ 60 min over X-band frequency range (8.2–12.4 GHz). Fig. 5.29 (c) and (d) Frequency dependent variation of SE_T, SE_R and SE_A of bare and Ni deposited CFL fabric @ 60 min deposition.

The mechanism of shielding in such systems is a bit complex, but can be explained in the following way. When the EM wave approaches a Ni coated surface, initially it interact a high permeable and conducting Ni layer and a part of the former is reflected. Here, reflection from Ni shield results when the impedance of the incoming EM wave in free space is different from that of the EM wave in the Ni shield. This is because EM waves drives the charges in the Ni coat to oscillate in resonance with the incident wave. Thus, oscillating charges behave like an antenna which reradiates the incoming EM wave.[36]

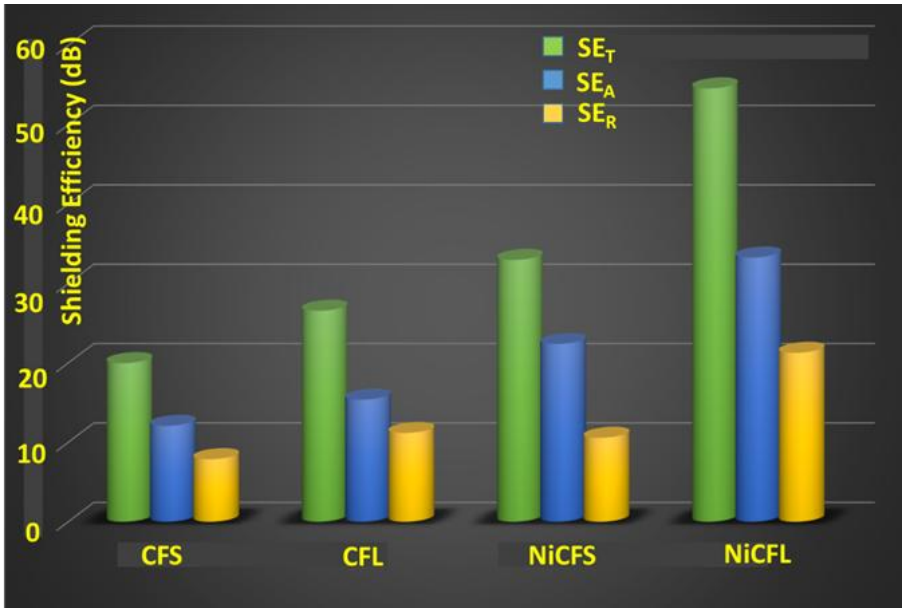

Fig. 5.30: Variation of SE_T, SE_A and SE_R of bare and Ni electroplated carbon fabric over mid - X band (10 GHz) range.

In the present case however, the dominant mechanism is absorption which happens by the attenuation of the transmitted wave to pass through the media. Lies beneath the Ni coat is a relatively lower conducting carbon fiber layer where the charge is forced to vibrate in the medium whose energy is lost in the form of heat. Again the transmitted wave meets a permeable, conducting layer at the other side of the fiber, leading to multiple reflections. In this way, the possibilities for absorption and reflection within each layer and multiple reflection possibilities among different layers, are convincingly pronounced in the Ni deposited carbon fabric case.[9] Here the SE_R, SE_A and SE_T of the bare and Ni deposited carbon fabric in the mid X-band frequency range are shown in Fig. 5.30, which clarifies the increasing trends in SE values with increasing fiber content and thickness of fabric. These results indicate that SE_A enhanced 50 % more than the initial range as a result of doubling of fiber content. Further, there is convincing enhancement in the absorption part for electrodeposited fabric as well.

5.2.4. Conclusions

The EM wave attenuating properties of carbon fabrics with and without Ni electrodeposition were investigated in this work package. Here two types of carbon fabrics were used: CFL with warp and weft constituting 6000 microfibers of diameter 6-10 μm, while CFS with half the number of microfibers. The total shielding effectiveness of CFS fabric was found to be in the range of 22-32 dB at 60 min of Ni deposition. Obviously, the efficiency of shielding has increased to the tune of 99 % with Ni deposition. On the other hand, an excellent EMI shielding effectiveness of 55-58 dB was achieved for CFL fabric, that corresponds to an impressive 99.999 % efficiency. The contribution of absorption in CFL was enormous owing to its greater thickness and lower skin depth in comparison to CFS. The absorption dominant shielding for CFL is mainly due to the higher surface area and thickness arising from large number of fibers in each warp/weft. Yet another contributing factor in Ni deposited CFL is by virtue of its greater number of interfaces. These interfaces at moderately conducting carbon fibers and magnetic Ni deposits, act as sites for enhanced absorption in the form of heat. The properties exhibited by Ni, like high conductivity and high permeability, will lower the skin depth while the moderately high conductivity and bundled structure of carbon fabric will help the multiple internal reflection of the EM waves. The useful results of this research throws light on the applicability of the developed light weight fabric structures for high performance outdoor shielding applications in aeronautical, stealth wearables domains.

5.3 References

(1) Tong XC. *Advanced Materials and Design for Electromagnetic Interference Shielding*; CRC Press. 2009.

(2) Dhineshbabu, N. R.; Behera, S. S.; Bose, S. Smart Textile Fabrics for Screening Millimeter Wavelength Radiations : Challenges and Future Perspectives. *Chemistry Select.* **2018**, *3*, 6087–6101.

(3) Saini, P.; Choudhary, V.; Dhawan, S. K. Improved Microwave Absorption and Electrostatic Charge Dissipation Efficiencies of Conducting Polymer Grafted Fabrics Prepared via in Situ Polymerization. *Polym. Adv. Technol.* **2012**, *23*, 343–349.

(4) Xu, Y.; Yang, Y.; Duan, H.; Gao, J.; Yan, D.; Zhao, G.; Liu, Y. Flexible and Highly Conductive Sandwich Nylon/Nickel Film for Ultra-Efficient Electromagnetic Interference Shielding. *Appl. Surf. Sci.* **2018**, *455*, 856–863.

(5) Tan, Y.; Li, J.; Gao, Y.; Li, J.; Guo, S.; Wang, M. Applied Surface Science A Facile Approach to Fabricating Silver-Coated Cotton Fi Ber Non-Woven Fabrics for Ultrahigh Electromagnetic Interference Shielding. *Appl. Surf. Sci.* **2018**, *458*, 236–244.

(6) Zhao, H.; Hou, L.; Lu, Y. Electromagnetic Interference Shielding of Layered Linen Fabric / Polypyrrole / Nickel (LF / PPy / Ni) Composites. *Mater. Des.* **2016**, *95*, 97–106.

(7) Ding, X.; Wang, W.; Wang, Y.; Xu, R.; Yu, D. High-Performance Flexible Electromagnetic Shielding Polyimide Fabric Prepared by Nickel-Tungsten-Phosphorus Electroless Plating. *J. Alloys Compd.* **2019**, *777*, 1265–1273.

(8) Palanisamy, S.; Tunakova, V.; Militky, J. Fiber-Based Structures for Electromagnetic Shielding – Comparison of Different Materials and Textile Structures. *Text. Res. J.* **2017**, 1–21.

(9) Jiyong, H.; Guohao, L.; Junhui, S.; Xudong, Y. Improving the Electromagnetic Shielding of Nickel / Polyaniline Coated Polytrimethylene-Terephthalate Knitted Fabric by Optimizing the Electroless Plating Conditions. *Text. Res. J.* **2016**, 1–11.

(10) Sedighi, A.; Montazer, M.; Mazinani, S. Fabrication of Electrically Conductive Superparamagnetic Fabric with Microwave Attenuation, Antibacterial Properties and UV Protection Using PEDOT/Magnetite Nanoparticles. *Mater. Des.* **2018**, *160*, 34–47.

(11) Zhao, H.; Hou, L.; Lu, Y. Electromagnetic Shielding Effectiveness and Serviceability of the Multilayer Structured Cuprammonium Fabric/Polypyrrole/Copper (CF/PPy/Cu) Composite. *Chem. Eng. J.* **2016**, *297*, 170–179.

(12) Kourkoumelis, N.; Elgaoudi, H.; Varella, E.; Kovala-demertzi, D. Physicochemical Characterization of Thermally Aged Egyptian Linen Dyed with Organic Natural Dyestuffs Physicochemical Characterization of Thermally Aged Egyptian Linen Dyed with Organic Natural Dyestuffs. *Appl. Phys. A.* **2013**, *112*, 469–478.

(13) Cao, H.; Wang, L.; Qiu, Y.; Wu, Q.; Wang, G.; Zhang, L. Generation and Growth Mechanism of Metal (Fe , Co , Ni) Nanotube Arrays. *Chem. Phys. Chem.* **2006**, *7*, 1500–1504.

(14) W. E. Morton and J. W. S. Hearle. *Physical Properties of Textile Fibres*; CRC Press Boca Raton Boston, New York, 2008.

(15) Riande, E; Diaz-Calleja, R. *Electrical Properties of Polymers*; CRC Press, Boca Raton Boston, New York, 2004.

(16) Bur, A. J. Dielectric Properties of Polymers at Microwave Frequencies: A Review. *Polymer.* **1985**, *26*, 963–977.

(17) Fert. A.; Campbell. I. A. Electrical Resistivity of Ferromagnetic Nickel and Iron Based Alloys. *J. Phys. F Met. Phys.* **1976**, *6* (5), 849–871.

(18) Cullity, B. D.; Graham, C. D. *Introduction to Magnetic Materials (2nd Edition)*; John Wiley & Sons, Inc., Hoboken, New Jersey, 2009.

(19) Roh, J.; Chi, Y.; Kang, T. J.; Nam, S. Electromagnetic Shielding Effectiveness of Multifunctional. *Text. Res. J.* **2008**, *78(9)*, 825–835.

(20) Chen, H. C.; Lee, K. C.; Lin, J. H.; Koch, M. Comparison of Electromagnetic Shielding

Effectiveness Properties of Diverse Conductive Textiles via Various Measurement Techniques. *J. Mater. Process. Technol.* **2007**, *193*, 549–554.

(21) Xu, C.; Liu, G.; Chen, H. Fabrication of Conductive Copper-Coated Glass Fibers through Electroless Plating Process. *J. Mater. Sci. Mater. Electron.* **2014**, *25*, 2611–2617.

(22) Hong, X.; Chung, D. D. L. Carbon Nanofiber Mats for Electromagnetic Interference Shielding Xinghua. *Carbon.* **2017**, *111*, 529–537.

(23) Jaroszewski, M; Thomas, S; Rane, A. V; *Advanced Materials for Electromagnetic Shielding*; John Wiley & Sons, Inc., Hoboken, New Jersey, 2018.

(24) Geetha, S.; Satheesh Kumar, K. K.; Rao, C. R. K.; Vijayan, M.; Trivedi, D. C. EMI Shielding: Methods and Materials-A Review. *J. Appl. Polym. Sci.* **2009**, *112* (4), 2073–2086.

(25) Lui, P. L. Passive Intermodulation Interference in Communication Systems. *Electron. Commun. Eng. J.* **1990**, 109–118.

(26) Jayashantha, S.; Gamage, P.; Yang, K.; Braveenth, R. MWCNT Coated Free-Standing Carbon Fiber Fabric for Enhanced Performance in EMI Shielding with a Higher Absolute EMI SE. *Materials.* **2017**, *10*, 1350.

(27) Chung, D. D. L. Electromagnetic Interference Shielding Effectiveness of Carbon Materials. *Carbon.* **2001**, *39* (2), 279–285.

(28) Thomassin, J. M.; Jérôme, C.; Pardoen, T.; Bailly, C.; Huynen, I.; Detrembleur, C. Polymer/Carbon Based Composites as Electromagnetic Interference (EMI) Shielding Materials. *Mater. Sci. Eng. R Reports* **2013**, *74* (7), 211–232.

(29) Rahman, R.; Servati, P. Effects of Inter-Tube Distance and Alignment on Tunnelling Resistance and Strain Sensitivity of Nanotube/Polymer Composite Films. *Nanotechnology* **2012**, *23* (5).

(30) Lu, L.; Xing, D.; Teh, K. S.; Liu, H.; Xie, Y.; Liu, X.; Tang, Y. Structural Effects in a

Composite Nonwoven Fabric on EMI Shielding. *Mater. Des.* **2017**, *120*, 354–362.

(31) Tang, W.; Lu, L.; Xing, D.; Fang, H.; Liu, Q.; Teh, K. S. A Carbon-Fabric/Polycarbonate Sandwiched Film with High Tensile and EMI Shielding Comprehensive Properties: An Experimental Study. *Compos. Part B Eng.* **2018**, *152*, 8–16.

(32) Kim, T.; Chung, D. D. L. Mats and Fabrics for Electromagnetic Interference Shielding. *J. Mater. Eng. Perform.* **2006**, *15*, 295–298.

(33) Eddib, A. A.; Chung, D. D. L. The Importance of the Electrical Contact between Specimen and Testing Fixture in Evaluating the Electromagnetic Interference Shielding Effectiveness of Carbon Materials. *Carbon.* **2017**, *117*, 427–436.

(34) Bhattacharjee, Y.; Bhingardive, V.; Biswas, S.; Bose, S. Construction of a Carbon Fiber Based Layer-by-Layer (LbL) Assembly-a Smart Approach towards Effective EMI Shielding. *RSC Adv.* **2016**, *6* (113), 112614–112619.

(35) Remadevi, A.; Sreedeviamma, D. K.; Surendran, K. P. Printable Hierarchical Nickel Nanowires for Soft Magnetic Applications. *ACS Omega* **2018**, *3*, 14245–14257.

(36) Maity, S.; Singha, K.; Debnath, P.; Singha, M. Textiles in Electromagnetic Radiation Protection. *J. Saf. Eng.* **2013**, *2* (2), 11–19.

Chapter 6

Conclusions and Future Prospects

This chapter summarizes the overall conclusions and scope of future work of the present thesis

6.1 Conclusions

Communication technologies simplify modern life, with the emergence of technologies like LTE, IoT etc. When devices like mobile phones, GPS, Bluetooth and Wi-Fi become increasingly compact, shielding them against inevitable electromagnetic interference (EMI) becomes more challenging. In addition to consumer electronics, devices operating in automotive transit systems, medical electronics and critical military infrastructure also face massive EMI threats that may lead to under performance of the circuit and are hazardous to human health as well. So, mitigating or blocking the interfering EM signals is inevitable for a healthy device management. Conductive and magnetic materials are the most suitable and well explored systems in EMI shielding. The development of novel EMI shielding solutions is a challenge due to the lack of suitable materials available and the complex design & engineering involved.

As discussed in previous chapters, the present day consumer electronic and defence sectors are looking for surface modified, ultra-lightweight, porous, flexible and wearable shielding structures. Against this background, the present thesis work entitled as "Novel EMI shielding strategies for hybrid functional structures", is designed as an authentic record on how some of these challenges were addressed, in a systematic way. As narrated in 4 different working chapters, our broad objectives were to develop innovative EMI shielding solutions that can meet demands of modern electronics like light weight, high temperature tolerance, portability and wearability, through some facile, novel approaches. The major scientific and technological outcomes of the present thesis, are summarized below.

In the first working chapter, a perovskite conducting oxide like $La_{0.5}Sr_{0.5}CoO_{3-\delta}$, was introduced into the vast domain of EMI shielding applications, for the first time. A traditional way of making composite of the conducting oxide with polymer seems to be ineffective for high end

applications. Here we put forward a scheme of introducing screen printing strategy of silver designs on an optimized composite, which are already qualified owing to better dielectric, mechanical and thermal characteristics. Modification brought a dramatic 4-fold increase in *SE* with visible enhancements in the SE_R and SE_A values. An efficiency enhancement from 90 to even 99.9 % was observed after the modification. For silver designs printed on top of composites, this high shielding has been authenticated by visible increments in the ac conductivity, relative permittivity, and dielectric loss, as well as a corresponding lowering of skin depths. The present strategy of introducing screen printing based design structures on composites can be used as a precursor for achieving the high *SE* values on materials with mediocre shielding.

The subsequent chapter describes a promising strategy in developing a material with lower density and thermal conductivity with good EMI shielding characteristics, which was made possible through the approach of foaming. In this way, creative introduction of systematic porosity augments the use of conductive ceramic oxides in lightweight shields. This is an example of how multiple reflection of EM waves help to attenuate them in porous material. Here we focused on developing LSCO foams through an emulsion route which is simple, low cost and environmental friendly. Compared to the dense counterpart, the electrical conductivity values were inferior in foams, yet showed SE_T in the range of > 30 dB in the X-band. Such foams can be qualified for light weight EMI shielding applications including satellite and aeronautical applications that are subjected to under harsh environmental conditions. LSCO nanowires investigated in this contest are also showing the best EMI shielding characteristics owing to the special morphology and interconnectivity. These conductive and corrosion resistant nanowires could be proposed as ideal candidates for nanoscale EMI shielding coatings under corrosive environments and high temperature conditions, where most metallic and polymer based nanowires fail.

Chapter 4 makes a candid insight into the performance of nanostructured Ni and NiFe alloys including permalloy, for EMI shielding applications. Here we adopted a facile polyol method for the nanoparticle synthesis wherein the polyol, i.e. PEG, plays multiple roles as a versatile dispersant, high boiling solvent, effective reductant, and also as a stabilizer which control the particle growth and avoid aggregation of precursors. Uniform spherical nanoparticles with an inevitable oxide layer was formed, where the latter will eventually prevent further oxidation and makes it suitable for biological applications. High magnetic saturation and low coercivity are peculiar with Fe incorporation, while DC electrical conductivity follows a decreasing trend with Fe addition. All the alloy combinations are excellent in microwave attenuation in the Ku band with shielding effectiveness exceeds 30 dB even with a thickness of 1mm. The better conductivity and permeability ranges are the main contributors for the higher shielding values. The prominent candidate of the series is permalloy ($Ni_{80}Fe_{20}$) that showed the best EMI SE in the range of 30 dB to 41 dB, which is ideal for commercial level applications. A brief survey of Ni or NiFe alloy-based EMI shielding studies indicates that the consistent EMI shielding performance (> 30 dB) throughout the frequency range (12.4–18 GHz) is unique for the developed samples. Shielding efficiency is above 99.9 % and there is scope for developing the alloy based coatings and composite structures for magnetic shielding applications.

Developing a flexible and wearable fabric which can have direct applicability in defense and consumer electronics is the central theme of Chapter 5. A simple procedure of electrodeposition brought the conventional woven fabrics like linen and nylon to the domain of high EMI shielding materials. After electrodeposition the electric, magnetic and electromagnetic characteristics of the fabrics were excellent to meet the criteria for a good flexible shield. The EMI SE of nickel electrodeposited nylon fabric is in the range of 25-38 dB while that of linen fabric is

in the range of 45-52 dB with efficiency of > 99.99 %. The absorption dominant shielding for linen is influenced by the peculiar microstructure, higher surface area, thickness and availability of more dielectric-metal interfaces. The high conductivity and permeability of Ni also played a pivotal role in the current system to lower the skin depth of the shield, along with the more inter-connected coating structure, which are advantageous for better shielding. A similar investigation on nickel deposited carbon fabric shows excellent EMI SE of 55-58 dB that corresponds to an impressive 99.999 % efficiency. The useful results of this research throws light on the applicability of the developed fabric structures for high performance outdoor shielding applications in aeronautical, stealth wearables domains where light weight and flexibility are additional benefits.

6.2 Scope for Future Works

The results obtained in the present study provide an excellent scope for the further research, as discussed below.

- Real case study of all the microwave absorbers developed in the present research, through free-space testing using horn antennas with dielectric lenses in an anechoic chamber. The free-space testing will give further authenticity to the EM wave attenuation habits of such materials.
- Predesigned metamaterial conducting patterns can be printed on the developed hybrid absorbers and their property enhancement can be tested. A modelling can be done for the same for suitable implication of the patterns with required level of attenuation.
- Develop LSCO inks suitable for 3D printing, to form various porous structures whose shielding parameters can be evaluated, against theoretical modelling. Other perovskite oxides like $LaCo_{0.5}Ni_{0.5}O_{3-\delta}$ (LCNO) can also be developed for similar applications.

- The ceramic foams derived in the current study can be explored for their applicability under high temperature conditions. Also the possibility of incorporation of other functional fillers in the macropores of ceramic foams, that can be subjected to further research.
- The derived permalloy nanoparticles can be developed into an ink. They can be incorporated as part of any high aspect ratio carbonaceous materials to see the conjugation of both components and further analyze the feasibility of application. Such inks can also be explored for the printing of bank checks on blank stock, in magnetic ink character recognition applications.
- Fabric based shielding materials can be made into flexible wearable apparels, and can be tested in an anechoic chamber and compare their performance with currently available shielding fabrics in the market. Further, the jackets and military wear made out of these fabrics can be tested as ‘radar invisible fabrics’, in real battle field applications.

List of publications related to thesis

1. **K. S. Dijith**, S. Pillai, K. P Surendran, Screen Printed Silver Patterns on $La_{0.5}Sr_{0.5}CoO_{3-\delta}$ - Epoxy Composite as a Strategy for Many-Fold Increase in EMI Shielding, *Surface & Coatings Technology*, 330 (2017) 34–41. doi : 10.1016/j.surfcoat.2017.09.063.

2. **K. S. Dijith**, S. Pillai, K. P. Surendran. Thermophysical and Microwave Shielding Properties of $La_{0.5}Sr_{0.5}CoO_{3-\delta}$ and Its Composite with Epoxy, *Journal of Electronic Materials*, 46 (2017) 5158–5167. doi:10.1007/s11664-017-5520-y.

3. **K. S. Dijith**, R. Aiswarya, M. Praveen, S. Pillai, K. P. Surendran. Polyol Derived Ni and Nife Alloys for Effective Shielding of Electromagnetic Interference. *Materials Chemistry Frontiers*, 2 (2018) 1829-1841. doi: 10.1039/C8QM00264A.

4. **K. S. Dijith**, S. Vijayan, K. Prabhakaran, K. P. Surendran. Conducting $La_{0.5}Sr_{0.5}CoO_{3-\delta}$ Foams for Harsh Condition Microwave Shielding. *Journal of Industrial and Engineering Chemistry*, 78 (2019) 330-337. doi: 10.1016/j.jiec.2019.05.037

5. **K. S. Dijith**, R. Aiswarya, C. V. Sruthy, S. Pillai, K. P. Surendran. Nickel Electrodeposited Linen and Nylon Fabrics for Microwave Shielding Applications. Manuscript under preparation.

6. **K. S. Dijith**, R. Aiswarya, S. Pillai, K. P. Surendran, Nickel Plated Carbon Fabrics for Effective Shielding Electromagnetic Waves. Manuscript under preparation.

7. **K. S. Dijith**, R. Aiswarya, S. Pillai, K. P. Surendran, Micron, Submicron and Nano Sized $La_{0.5}Sr_{0.5}CoO_{3-\delta}$ Based EMI shielding Structures. To be communicated.

List of publications not related to thesis

8. R. Narasimman, S. Vijayan, **K. S. Dijith**, K. P. Surendran, K. Prabhakaran. Carbon Composite Foams with Improved Strength and Electromagnetic Absorption From Sucrose and Multi-Walled Carbon Nanotube. *Materials Chemistry and Physics*, 181 (2016) 538-548. doi:10.1016/j.matchemphys.2016.06.091.

9. R. Aiswarya, **K. S. Dijith**, K. P. Surendran. Printable Hierarchical Nickel

Nanowires for Soft Magnetic Applications. *ACS Omega*, 3 (2018) 14245−14257. doi: 10.1021/acsomega.8b01422.

10. R. Aiswarya, **K. S. Dijith**, K. P. Surendran. Magnetic Nanowires for Sensor Applications, *Materials Science Forum*, 830-831 (2015) 565-568. doi: 10.4028/www.scientific.net/MSF.830-831.565.

11. J. B. Anooja, **K. S. Dijith**, K.P. Surendran G. Subodh, A Simple Strategy for Flexible Electromagnetic Interference Shielding: Hybrid rGO@CB Reinforced Polydimethylsiloxane. *ACS Omega*, Under Review.

List of Conference Proceedings

Contributory Talks

1. **K. S. Dijith**, R. Aiswarya, M. Praveen and K. P. Surendran, Polyol Derived Ni and NiFe Alloys for Effective Shielding of Electromagnetic Interference, IIM Trivandrum Chapter, Thiruvananthapuram 2018

2. **K. S. Dijith**, R. Aiswarya, M. Praveen and K. P. Surendran, Nano-Permalloy for Enhanced EMI Shielding in Ku band, International Conference on advanced Materials for Power Engineering (ICAMPE 2015), Mahatma Gandhi University, Kerala, August 9-11, 2015.

Poster Presentations

1. **K. S. Dijith**, C.V.Sruthy, K.P.Surendran, Nickel Electroplated Linen and Nylon Fabrics for X-band Shielding Applications, National Conference on "Critical and Strategic Materials for Advanced Technologies" (CSMAT), Munnar, March 9, 2017.

2. **K. S. Dijith**, C.V.Sruthy, K.P.Surendran, Electromagnetic Interference Shielding of Nickel Electroplated Fabrics, International Conference on Polymer Science and Technology (MACRO 2017) Thiruvananthapuram, January 9-11,2017.

3. **K. S. Dijith**, S. Pillai, K. P. Surendran, $La_{0.5}Sr_{0.5}CoO_{3-\delta}$ – Epoxy Composites for Electromagnetic Interference Shielding Applications. International Conference on

Science, Technology and Applications of Rare Earths (ICSTAR 2015), Thiruvananthapuram, April 23-25, 2015.

4. R. Aiswarya, **K. S. Dijith**, K. P. Surendran, Magnetic Nanowires for Sensor Applications, International Conference on Advanced Materials and Manufacturing Processes for Strategic Sectors (ICAMPS 2015), Thiruvananthapuram, May 13-15, 2015.

5. R. Aiswarya, **K. S. Dijith**, M.T. Sebastian, K. P. Surendran, Formulation of Perovskite Conducting Oxide Inks for Printed Electronics, International Conference on Science, Technology and Applications of Rare Earths (ICSTAR 2015). Thiruvananthapuram, April 23-25, 2015.

6. Nina Joseph, **K. S. Dijith,** M T Sebastian, K. P. Surendran, Functional Composites for Electromagnetic Shielding Applications International Conference on Advanced Functional Materials (ICAFM 2014) Thiruvananthapuram, February 19-21, 2014.